Alveoli-on-a-chip

Alexandra [sasha] Laniece

To cite this version:

Alexandra [sasha] Laniece. Alveoli-on-a-chip: A close-contact dynamic model of the alveolar capillary barrier: micro-engineering, microfluidics and induced pluripotent stem cells. Biomechanics [physics.med-ph]. Université Paris Diderot; École Normale Supérieure de Paris, 2018. English. NNT : 2018USPCC132 . tel-02050336

HAL Id: tel-02050336

https://hal.science/tel-02050336

Submitted on 27 Feb 2019

Thèse de doctorat de
L'Université Sorbonne Paris Cité
Préparée à l'Université Paris Diderot
Ecole doctorale Physique en Ile-de-France (ED 564)
Institut Pierre-Gilles de Gennes

Ecole Normale Supérieure de Paris, Laboratoire PASTEUR, UMR 8640
Laboratoire Matière et Systèmes Complexes, UMR 7057

Alveoli-on-a-chip

A close-contact dynamic model of the alveolar capillary barrier: micro-engineering, microfluidics and induced pluripotent stem cells

Thèse de Doctorat de Physique

par Alexandra LANIECE

Dirigée par Dr. Jean-François Berret et Pr. Yong Chen

Présentée et soutenue publiquement à l'Institut Pierre-Gilles de Gennes le 5 Octobre 2018

Président du jury : Baeza-Squiban, Armelle / Professeur / Université Paris-Diderot

Rapporteur : Descroix, Stéphanie / Directeur de recherche / Institut Curie

Rapporteur : Di Fabrizio, Enzo / Professeur / King Abdullah University of Science and Technology

Examinateur : Fattaccioli, Jacques / Maître de conférences / Ecole Normale Supérieure de Paris

Directeur de thèse : Berret, Jean-François / Directeur de recherche / Université Paris-Diderot

Co-directeur de thèse : Chen, Yong / Professeur / Ecole Normale Supérieure de Paris

Membre invité : Quignard, Sandrine / Docteur / Institut Pierre-Gilles de Gennes

Alvéoles-sur-puce
Modèle dynamique au contact de la barrière alvéolo-capillaire: micro-fabrication, microfluidique et cellules souches pluripotentes induites

Résumé

Les particules issues de la pollution sont responsables de millions de morts prématurées. Les nanoparticules (au diamètre inférieur à 100 nm) atteignent les alvéoles où elles rencontrent la barrière alvéolo-capillaire. Cette barrière est composée d'un épithélium alvéolaire et d'un endothélium, dos à dos contre une membrane ultrafine (environ 0.2 μm), soumis à une stimulation constante exercée par l'inflation cyclique des alvéoles et par le cisaillement dû à la circulation sanguine. Nous nous sommes appliqués à développer un modèle *in vitro* innovant de cette barrière alvéolo-capillaire afin d'observer les interactions des nanoparticules avec cette barrière.
Dans un premier temps, nous avons développé un substrat micro-fabriqué qui reproduit les propriétés géométriques et physiques de la membrane alvéolo-capillaire. Sur cette membrane, nous avons mis en place une co-culture de cellules épithéliales alvéolaires (A549) et endothéliales (HUVEC). Grâce à une étude de microscopie confocale, nous avons observé le comportement de ce modèle en termes d'étanchéité et de fonctions biologiques. Finalement nous avons observé les interactions entre des nanoparticules de silice et notre modèle en termes de toxicité, d'internalisation et de translocation.
Dans une seconde partie, nous avons développé une puce microfluidique à deux chambres qui permet de reproduire autour de notre modèle de co-culture le microenvironnement spécifique des alvéoles pulmonaires. Des études de conception mécanique et l'optimisation de méthodes de microfabrication nous ont permis de générer une puce réversible compatible avec de la culture à long-terme et de l'observation en live par microscopie confocale.
Dans une troisième partie, nous avons commencé un travail préliminaire visant à intégrer des cellules pluripotentes induites différenciées dans notre modèle *in vitro*. Nous avons travaillé à optimiser deux protocoles de différentiation sur une lignée commerciale: vers un endothélium et vers un épithélium alvéolaire.
Finalement, nous proposons ici un modèle *in vitro* offrant de nombreux avantages: une importante communication intercellulaire via leur co-culture sur une membrane ultrafine, une culture long-terme observable au quotidien, la reproduction des stimuli dynamiques de l'environnement alvéolo-capillaire *in vivo* et la possibilité d'effectuer des tests d'interaction et de translocation de nanoparticules.

Mots-Clefs

Poumon, Alvéole, Barrière, Modèle *in vitro*, Organe-sur-puce, Microfluidique, Cellules souches pluripotentes induites, Nanoparticules, Translocation, Internalisation, Silice, A549, HUVEC.

Alveoli-on-a-Chip

A close-contact dynamic model of the alveolar capillary barrier: micro engineering, microfluidics and induced pluripotent stem cells

Abstract

Pollutions particles are responsible for millions of premature death. Nanoparticles (with a diameter below 100 nm) reach the alveolar sacs where they encounter the alveolar capillary barrier. This barrier is constituted of an alveolar epithelium and an endothelium back to back on an ultra-thin membrane (about 0.2 μm), submitted to constant stimuli due to cyclic alveolar inflation and blood flow shear stress. We focused here on developing an innovative *in vitro* model of the alveolar capillary barrier to study the interactions of the nanoparticles with this barrier.

Firstly, we have developed a micro-engineered substrate reproducing the geometrical and physical properties of the alveolar capillary membrane. We implemented the co-culture of an alveolar epithelium (A549) and an endothelium (HUVEC) on this membrane. We used confocal microscopy to observe the behavior of our model regarding barrier integrity and specific phenotypes. Finally, we observed the interactions between Silica nanoparticles and our model in terms of toxicity, internalization and translocation.

Secondly, we developed a two-chamber microfluidic chip reproducing the specific microenvironment of the alveoli around our co-culture model. Studies of mechanical design and fabrication processes optimization allowed for the generation of a reversible chip compatible with long-term culture and live observation with a confocal microscope.

Thirdly, we launched preliminary experiments aiming at the integration of differentiated induced pluripotent stem cells in our *in vitro* model. We worked on optimizing two directed differentiation protocols: towards an endothelium and towards an alveolar epithelium.

Finally, we present here an *in vitro* model with numerous features: a close-contact co-culture on an ultra-thin membrane enabling important intercellular communication, a long-term culture allowing for live monitoring, mimicking the *in vivo* dynamic stimuli of the alveolar capillary barrier microenvironment and the possibility for nanoparticles interaction and translocation studies.

Keywords

Lung, Alveoli, Barrier, *In vitro* modeling, Organ-on-a-chip, Microfluidic, Induced pluripotent stem cells, Nanoparticles, Translocation, Internalization, Silica, A549, HUVEC.

To my parents and my sisters, for their unconditional love,
And to my friends, for their constant support.

Acknowledgments

First and foremost, I wish to thank the jury participating in this project, especially the two reviewers, Dr. Stéphanie Descroix and Pr. Enzo Di Fabrizio. I also wish to thank my two PhD directors, Pr. Jean-François Berret and Pr. Yong Chen for giving me the opportunity to prepare this thesis, even without having any scientific background in biology.
I would also like to express my very great appreciation to Dr. Jacques Fattaccioli, Pr. Armelle Baeza-Squiban and Dr. Sandrine Quignard for their regular mentoring and their constructive suggestions during the planning and development of this research work. I also wish to thank Pr. Onnik Agbulut for his support and his contribution to the thesis committee.
I wish to thank various people for their contribution to this project: Chloé Puisney for her competent advice in cell biology, Lauriane Gérémie for her help in immunostaining and confocal microscopy and Alison Tebo for the use of the plate-reader.

I wish to thank all of my coworkers for their daily support and for accepting to investigate various scientific issues with me:

- My labteam: Léa Pinon, Lorraine Montel, Kaori Sakai, Olivier Mesdjian and Mathilde Bernard
- From Ecole Normale Supérieure: Bin Wang, Xiaolong Tu, Yadong Tang, Ayako Yamada, Jian Shi, Elrade Roofani, Jin Wei and Li Wang
- From Paris-Diderot: Chloé Puisney, Fanny Mousseau, Evdokia Oikonomou and Fred Loosli

I also wish to thank all the PhD students from Institut Pierre-Gilles de Gennes for our scientific discussions, for their friendly company at the lab on the week-ends and late evenings, and their emotional support around rooftop barbecues: Lauriane Gérémie, Ismaïl Hajji, Sarah Myram, Amine M'Barki, Lucie Barbier, Charles Cavaniol, Elian Martin, Mizah Cognart, Rafaele Attia, Damien Cuvelier, Nicolas Carpi and Marco Serra.
It would not be right to mention IPGG without acknowledging the tremendous help given by our engineering team: Guillaume Laffite, Olivier Lesage and Nawel Cherkaoui. Your dedication enabled us to work in a high-quality environment with great technical advising, and your constant smiles and joke created the most enjoyable environment to work in.

I also wish to thank my closest friends for their constant support these past three (and more) years: a warm thank to my dearest Caroline Cantin, Marion Cosson and Poppy Ryland. And to my only companions in this ordeal, Nicolas Virgaux and Alice Moutenet. I also thank Anne-Sophie Noël, Arthus Audousset, Caroline Robey, Augustin Planty, Guillaume Sautière, Marine Raveleau, Henri Bouillon, Gaël de Percin, Luc Larroumet, Marie de Percin, Valentine des Rieux (ainsi que Bertrand et Gustave), Maxim Van Den Abbeele, Amaury de Cassan, and Daphné Wibaux-Kerbaul.

I also wish to give a special thanks to two former coworkers, friends and mentors, who followed me during this adventure: David Brauge and Remi Villenave.

I wish to thank my family for their unconditional support through my studies, and for trying all these years to understand what I am doing. I wish to apologize for all the family reunions I missed because I was in the lab. I especially thank my GrandMa for asking me everyday for three years if my cells were still growing.

Finally, I wish to thank Camille Kerbaul, for his immense support in this adventure. Thank you for your constant patience, your generosity, your care and for all the wine and the good laughs. I apologize for all the evenings and the week-ends stuck in the lab, for the time missed together, and for all of the stress. This achievement is dedicated to you.

Contents

Résumé en français (French summary)

0.1 Introduction

Introduction générale En 2010, la pollution de l'air a causé 1,2 millions de morts en Chine [1]. Même face à de telles observations, il apparaît que les mesures prises par la communauté internationale ne sont pas suffisantes: la course à la croissance continue, au détriment de notre environnement et de notre santé. Cependant, la pollution atteignant des niveaux records dans l'atmosphère et dans les océans, désormais tous les pays sont directement concernés.

Même en prenant immédiatement des mesures drastiques, il y faudra attendre un certain délai avant de pouvoir observer une diminution de la pollution de l'air. Il est donc indispensable de penser à la protection de notre santé, tout en continuant de chercher des méthodes préventives contre la pollution. Afin de protéger les populations, il apparaît qu'il faut d'abord approfondir les connaissances actuelles sur cette pollution et les mécanismes pathologiques associés, pour pouvoir ensuite développer des équipements de protection ou des traitements pharmaceutiques adaptés.

Un contexte de pollution de l'air Les polluants de l'air sont originaires de sources naturelles telles que les cendres volcaniques, la poussière ou le pollen, ainsi que de sources anthropogéniques telles que la combustion d'énergies fossiles (pour l'industrie, les transports ou les chauffages personnels), l'incinération, les particules issues de l'abrasion de freins ou de pneus ou encore d'autres particules générées par diverses industries. Ces particules voyagent et se déposent selon leur taille. Ainsi les particules les plus petites sont les plus mobiles et les plus toxiques, car leur construction atomique leur confère des propriétés très réactives, pouvant ainsi causer un stress oxydant dans les cellules, voire une internalisation et/ou une toxicité élevée(s). Ces petites particules, sont donc extrêmement dangereuses, et pourtant l'Organisation Mondiale de la Santé annonçait en 2015 que les limites fixées en termes de concentration en particules étaient dépassées dans la majorité des zones urbaines [2].

Trajet d'une particule dans les poumons Les poumons sont les organes responsables de la respiration chez l'humain: ils oxygènent le sang via un procédé d'échange gazeux situé dans les alvéoles pulmonaires. Les poumons sont organisés autour de deux structures de canaux respiratoires en arborescence depuis la trachée (voir Figure 1). Composés de deux lobes, les poumons sont enclavés dans une membrane bicouche, la plèvre. La couche inférieure est intimement connectée aux poumons, suivant sa surface jusque dans les moindres fissures des lobes et la couche supérieure est connectée aux muscles intercostaux. Ainsi le procédé de respiration résulte d'une contraction de ces muscles, gonflant la cage thoracique et créant une dépression dans la plèvre, ce qui va déployer le tissu pulmonaire, aspirant ainsi de l'air dans les canaux respiratoires.

L'air ainsi inhalé peut contenir des particules de pollution qui vont alors se déposer le long de l'arbre bronchique selon leur taille. Ainsi, les particules de diamètre supérieur à 5 µm se déposent dans la bouche et la gorge par inertie. Entre 1 et 5 µm les particules se déposent dans l'arbre bronchique jusqu'au bronchioles par sédimentation gravitationnelle. Les particules inférieures à 0.5 µm avancent dans les bronchioles par convection et se déposent dans les alvéoles par diffusion ([3], [4]).

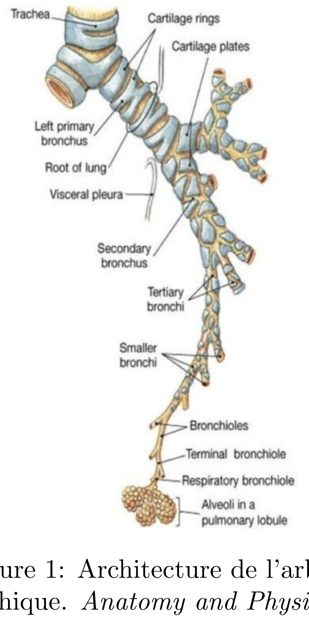

Figure 1: Architecture de l'arbre bronchique. *Anatomy and Physiology*

Le long de ce trajet, il existe différents mécanismes de protection. Pour les particules déposées sur l'arbre bronchique, elles s'agrègent dans le mucus produit par l'épithélium bronchique et sont évacuées jusque dans la trachée par un mouvement synchronisé des cellules ciliées: c'est l'escalator muco-ciliaire. Pour les particules atteignant les alvéoles pulmonaires, elles peuvent ainsi rencontrer le surfactant, un liquide visqueux composé principalement de phospholipides et de protéines, qui va réagir différemment avec différentes particules [5] pour former différents types d'agrégats, selon une règle qui n'est pas encore connue. Ceux-ci peuvent ensuite être digérés par les macrophages pulmonaires ou entrer en contact avec la barrière alvéolaire.

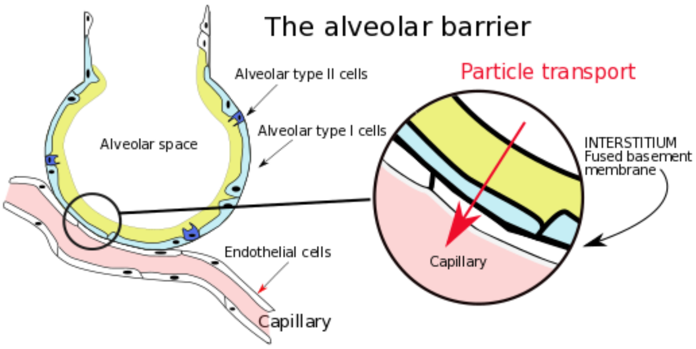

Figure 2: Schéma de la barrière alvéolo-capillaire

La barrière alvéolaire est composée de l'épithélium alvéolaire et de l'endothélium des capillaires sanguins irriguant les alvéoles dos à dos contre une membrane extracellulaire appelée interstitium (voir Figure 2). Cette membrane a une épaisseur inférieure à 0,2 μm, et le cytoplasme des cellules épithéliales et endothéliales atteint souvent moins d'un micron d'épaisseur, ce qui permet des échanges importants de part et d'autre de la barrière, que ce soit pour transporter des nutriments, du CO_2 ou des particules.

Cette barrière est soumises à des stimulations mécaniques en continu: d'une part les forces de cisaillement dues à la circulation du sang dans les capillaires alvéolaires, et d'autre part les contraintes de déformation qui résultent en un agrandissement linéaire de 8 à 12% [6] de la paroi alvéolaire. Ces forces jouent un rôle important mais pourtant encore mal connu dans le développement des cellules et dans l'expression de leurs différentes fonctions. Ainsi, il semble que la déformation cyclique des alvéoles jouent un rôle dans l'internalisation des particules en contact avec l'épithélium alvéolaire [7]. Le devenir des particules en contact avec la barrière alvéolaire n'est pas encore assez connu pour pouvoir être prévisible. Ainsi, selon la dose inhalée, la taille, la composition chimique ou la charge électrique de la particule, elle peut former divers agrégats avec le surfactant qui à leur tour peuvent avoir différentes interactions avec la barrière alvéolaire: une certaine toxicité sur l'un ou les deux types cellulaires, une internalisation (avec une exocytose possible dans le surfactant ou dans les capillaires) ou une translocation (active ou passive).

Constat Nous avons fait le constant d'un contexte alarmant au regard de la concentration de la pollution dans l'air. Actuellement aucun pays n'a pris des mesures suffisamment répressives pour réduire cette pollution dans les prochaines années: il faut donc se préparer à vivre avec. Afin de développer des méthodes innovantes de protection, il est essentiel de comprendre les mécanismes qui entrent en jeu lors de l'interaction entre les particules de l'air et la barrière alvéolo-capillaire. En effet, il existe une multitude de devenirs d'une particule dans les alvéoles. Afin de mieux les connaître et peut-être de les comprendre, il est essentiel de faire un important travail de recherche dans ce domaine.

Les méthodes actuellement utilisées pour un tel travail de recherche sont limitées: la culture traditionnelle de cellules en 2D ne peut reproduire les phénomènes et interactions complexes que l'on observe *in vivo* et les modèles sur animaux sont coûteux et peu précis au regard des phénotypes spécifiques à l'humain. Nous proposons un modèle intermédiaire, qui pourrait reproduire la barrière alvéolo-capillaire *in vitro* afin de servir à des études de toxicité des particules dans les alvéoles. Ce modèle reproduit l'architecture, les composantes cellulaires ainsi que les contraintes dynamiques observées *in vivo*. En effet, grâce à de nouvelles avancées en microfabrication, de nouvelles techniques permettent de cultiver des cellules sur des supports d'architectures en 3D, avec une géométrie contrôlée. L'intégration de ces supports dans des puces microfluidiques permet alors de reproduire le microenvironnement spécifique au tissu ainsi cultivé, contraintes dynamiques comprises. De plus, nous proposons d'utiliser une nouvelle source de cellules pour modéliser notre tissu humain: les cellules souches pluripotentes induites. Ces cellules sont obtenues à partir de cellules somatiques que l'on fait revenir au stade pluripotent par l'utilisation de facteurs de transcription spécifiques: c'est la reprogrammation. Ces cellules peuvent ensuite être différentiées en divers types cellulaires grâce à des protocoles spécifiques nouvellement mis au point et encore en cours d'optimisation. Les cellules ainsi obtenues présentent de nombreux avantages par rapport aux lignées utilisées en biologie cellulaire: elles ne comportent pas de mutations les rendant immortelles, et ne souffrent pas du vieillissement inhérent à ces cellules. Enfin, comme elles peuvent être obtenues de n'importe quel donneur, elles ouvrent la voie à la modélisation de maladies spécifiques et à la personnalisation de certains traitements.

Conclusion et objectifs L'objectif de ce projet de recherche est le développement d'un outil pour la recherche sur la toxicité des polluants de l'air. Il s'agit d'un modèle *in vitro* amélioré qui reproduit les fonctions complexes de la barrière alvéolo-capillaire, c'est-à-dire sa structure membranaire fine, la co-culture d'un épithélium et d'un endothélium exprimant des phénotypes comparables aux observations *in vitro*, et la reproduction des stimuli dynamiques propre au microenvironnement alvéolaire.

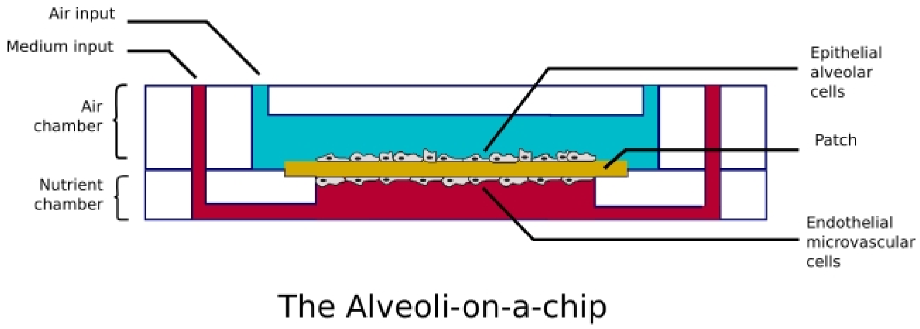

Figure 3: Objectif technique du projet: **the Alveoli-on-a-chip**

Ce manuscrit comporte trois chapitres décrivant le développement de ce modèle. Le premier chapitre détaille la génération d'un modèle statique micro-fabriqué qui reproduit la barrière alvéolaire *in vitro*. Dans le second chapitre nous détaillons la fabrication d'une puce microfluidique qui inclut ce premier modèle statique pour l'intégrer dans un microenvironnement contrôlé pouvant reproduire les stimuli dynamiques locaux (voir Figure 3). Enfin, le dernier chapitre récapitule nos efforts pour optimiser les protocoles de différentiation dirigée d'une lignée d'iPSC commerciales en endothélium et en épithélium alvéolaire.

0.2 Modèle statique de la barrière alvéolo-capillaire

Modéliser la barrière alvéolaire Comme mentionné précédemment, la barrière alvéolaire est composé de deux épithéliums adossés à un interstitium. L'épithélium alvéolaire est composé de deux types cellulaires: les AET I (alveolar epithelial type I ou pneumocyte I) et les AET II (voir Figure 2). Les premières sont des cellules squameuses couvrant 95% de la surface alvéolaire, et jouant principalement un rôle dans les échanges à travers la barrière, qu'elles régulent activement par leurs jonctions serrées. Les types II sont des cellules cuboïdales qui composent 65 à 90% des cellules épithéliales mais ne couvrent que 5% de la surface. Ces cellules jouent un rôle dans la défense de l'alvéole: elles produisent les phospholipides du surfactant, ainsi que la protéine SP-B qui régule l'organisation et le recyclage du surfactant.
Les cellules endothéliales sont des cellules squameuses qui forment un épithélium lâche, avec des jonctions communicantes. Elles jouent un rôle dans la régulation du flux sanguin (action de vasoconstriction ou vasodilatation, gestion de la thrombose) et dans la protection des tissus environnants (par exemple en recrutant des plaquettes ou en contrôlant les inflammations localement).
Les modèles existants en terme de biologie cellulaire sont soit des cellules primaires, obtenues directement sur un sujet *in vivo*, soit des cellules de lignées, souvent cancéreuses ou modifiées génétiquement pour être immortelles. Ces dernières présentant l'avantage d'un coût d'utilisation réduit ainsi que d'une expression phénotypique largement caractérisée, nous avons choisi d'utiliser deux lignées dans notre modèle: les A549 (cellules AET II cancéreuses humaines) et les HUVEC (cellules endothéliales du cordon ombilical humain).
Ces deux types cellulaires, ainsi que la membrane qui les supporte sont les principales composantes de la barrière alvéolaire. Nous allons présenter ici le modèle de membrane que nous avons mis au point via des techniques innovantes de microfabrication, ainsi que la méthode développée pour obtenir la co-culture des A549 et HUVEC.

Modèle microfabriqué La membrane présentée ici est une amélioration du patch proposé par Liu *et al* [8] and Tang *et al* [9]. Ce "patch" est composé d'une grille rigide avec des trous hexagonaux qui supporte une couche de nano-fibres de gélatine réticulée. Dans ce résumé nous allons présenter la version finale de ce patch, en décrivant les méthodes fabrication spécifiquement mises au point.

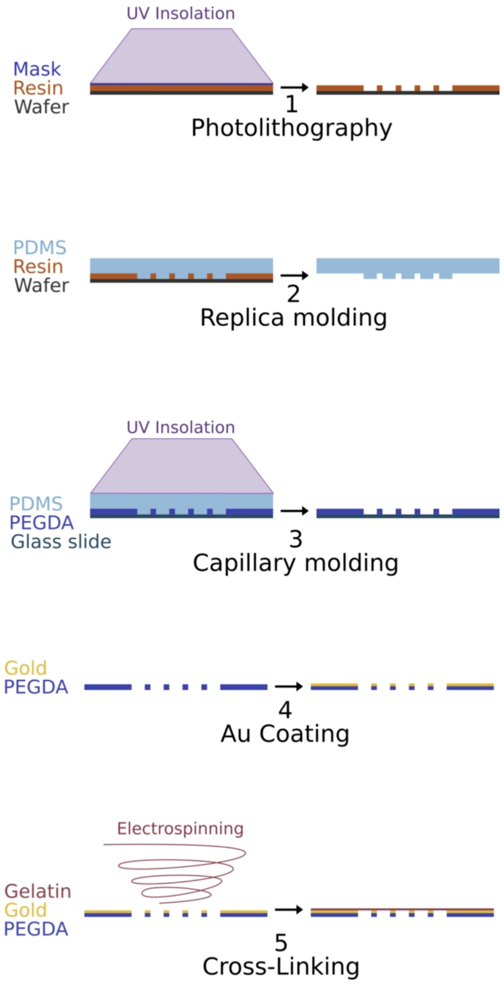

Figure 4: Etapes de microfabrication du patch

La première étape de fabrication est la génération d'une grille de PolyEthylène Glycol Diacrylate (PEGDA). Elle est composée de trous hexagonaux (diamètre interne 400 μm) séparés par des travées (120 μm de large), entourée par une large couronne (diamètre intérieur 4 mm / extérieur 13 mm). La grille est obtenue par photolithographie d'une couche de 50 μm. Sur cette couche nous effectuons une deuxième photolithographie de 50 μm, de la couronne seulement (voir Figure 4, étape 1). Cette couche de résine est ensuite utilisée comme moule pour générer des pièces de PDMS (voir Figure 4, étape 2). Ces pièces servent à leur tour de moule pour la réticulation par capillarité du PEGDA (voir Figure 4, étape 3). La couche de PEDGA ainsi moulée est détachée et nettoyée (avec de l'isopropanol puis un bain d'eau de 48 h). Elle a une épaisseur totale de 100 μm.

La grille de PEGDA est ensuite recouverte d'une mince couche d'or (voir Figure 4, étape 4) afin de la rendre conductrice. Cela nous permet ensuite d'utiliser la méthode d'électrospinning (voir Figure 2.11, étape 5) pour déposer un réseau aléatoire de nanofibres de gélatine grâce à un champ électrique entre notre substrat et une seringue contenant une solution de gélatine avec un solvant à évaporation rapide (acide acétique, acétate d'éthyle et eau). Ce réseau de fibres est ensuite séché sous vide et réticulé chimiquement pendant quatre heures. Après de multiples rinçages à l'éthanol, le patch est séché sous vide, stérilisé aux UV et est prêt à être utilisé. Un grand travail d'optimisation a été réalisé pour obtenir un protocole reproductible et efficace. Ainsi, le protocole amélioré triple la production de grilles de PEGDA en une journée et génère 99% de patches plat (contre 10 à 20% avec l'ancienne méthode). Une étape de fabrication reste cependant sensible: c'est l'électrospinning, qui est très dépendant de l'humidité de l'air, et qui doit donc être réalisé préférentiellement à basse humidité.

Finalement, le substrat que nous avons mis au point présente des propriétés intéressantes, que nous avons pu observer au microscope électronique à balayage (voir Figure 5). En effet, il comporte des pores qui permettent le transport de molécules signalétiques entre les cellules, sans pour autant permettre aux cellules de le traverser (aire maximale des pores: 57,76 μm^2, aire moyenne: 1,72 μm^2, et aire minimum 0,055 μm^2). De plus, une fois ces fibres réticulées, elles fusionnent en une seule couche d'épaisseur moyenne d'environ 1 μm. Cette membrane est la plus fine que nous ayons pu recenser dans la littérature, ce qui présente une avancée non négligeable pour l'étude des communications intracellulaire.

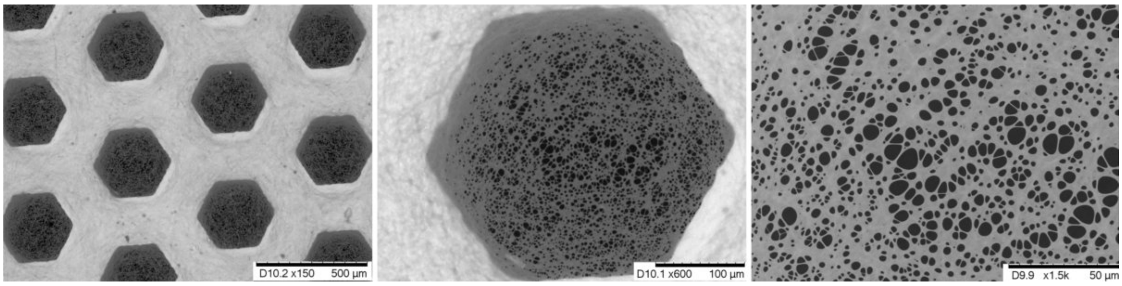

Figure 5: Images au MEB du patch, zoom sur les nanofibres de gélatine

Reproduction de la barrière alvéolaire La co-culture de l'épithélium alvéolaire et de l'endothélium est obtenue grâce au développement de chambres spécifiques de PDMS qui permettent de cultiver les patches en suspension. Les cellules HUVEC sont ensemencées d'abord (200 000 cellules dans 200 μL par patch), puis après 24h les patches sont retournés et les A549 sont ensemencées (180 000 cellules dans 200 μL par patch). Le jour suivant, les cellules sont passées en interface air-liquide (ALI), toujours dans du milieu ECGM (endothelial cell growth medium). Finalement, le jour suivant (J+3) puis un jour sur deux, le milieu est renouvelé et supplémenté en Dexamethasone, un corticoïde qui force la maturation des cellules. Cela nous permet d'induire la génération de jonctions serrées dans l'épithélium alvéolaire, ainsi que de réduire la prolifération des cellules. De nombreuses analyses d'immunofluorescence nous ont permis d'observer la présence de protéines alvéolaires spécifiques des AET I (Cavéoline 1) ou des AET II (SP-A, SP-B, proSP-C, NKX2.1) exprimées par les A549. Cette dualité de phénotype n'est pas surprenante car elle a déjà été observée. De plus, si les A549 ne produisent pas de Mucine 1 comme *in vivo*, elle produisent du MUC5AC, une autre mucine, ce qui indique qu'il y a bien une production type surfactant. Nous avons observé que cette production est d'autant plus importante en culture ALI.

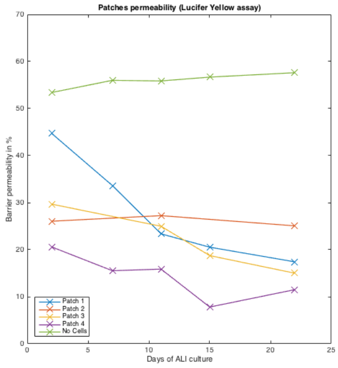

Figure 6: Evolution de la perméabilité du patch au cours du temps d'après l'analyse du transport de Lucifer Yellow à travers la barrière alvéolaire.

Les cellules épithéliales, elles, ont montré une expression de VE-Cadhérine et de PECAM1 mais il semblait que cette production n'était pas assez mature pour se localiser aux jonctions entre les cellules. Il semble donc que nos conditions de co-culture puissent être encore améliorées pour les cellules endothéliales. Cependant ces conditions permettent déjà des premiers essais de translocation sur notre modèle de barrière alvéolo-capillaire. En effet, l'expression soutenue de N-Cadhérine, d'Occludine et de ZO-1 dans les deux types cellulaires indique une forte intégrité de la couche cellulaire. Nous avons aussi travaillé sur la quantification de l'étanchéité membranaire via le transport de molécules au transport paracellulaire mais la variabilité inter-patches (due à l'étape d'électrospinning) ne nous a pas permis d'obtenir une valeur précise. Cependant nous avons pu observer une claire diminution du transport au cours du temps avec le traitement à la Dexamethasone, atteignant quasiment une faible perméabilité autour de 15 jours de traitement (voir Figure 6). Il serait intéressant de refaire cette expérience avec un plus grand nombre de patches et sur une plus grande durée afin de préciser les résultats obtenus et d'avoir une vision d'ensemble sur le comportement du patch à long terme.

Analyse de la translocation de nanoparticules Afin d'effectuer un premier test sur notre modèle, nous avons étudié la translocation de nanoparticules de Silice de 50 nm de diamètre à travers notre modèle de barrière alvéolaire. Un premier test (analyse du cytosquelette des cellules par immunofluorescence après 24 h d'incubation) a montré que ces particules sont toxiques pour les A549 et les HUVEC à partir d'une concentration proche de 50 $\mu g/mL$ (voir Figures 7a et 7b). L'analyse de la translocation des particules en une heure montre un transport inversement lié à la concentration en nanoparticules. Nous avons aussi incubé des cellules A549 avec le milieu basal afin d'observer les particules ayant traversé, et nous avons pu constater qu'elles ne sont pas dissoutes au cours du passage. De plus, une observation confocale montre que les particules sont majoritairement agrégées à la surface de l'épithélium alvéolaire, et qu'une très faible partie seulement est internalisée dans les cellules A549 (voir Figure 7c) . Nous n'avons cependant pas observé d'internalisation dans les cellules endothéliales, ce qui était pourtant le cas en culture sur verre.

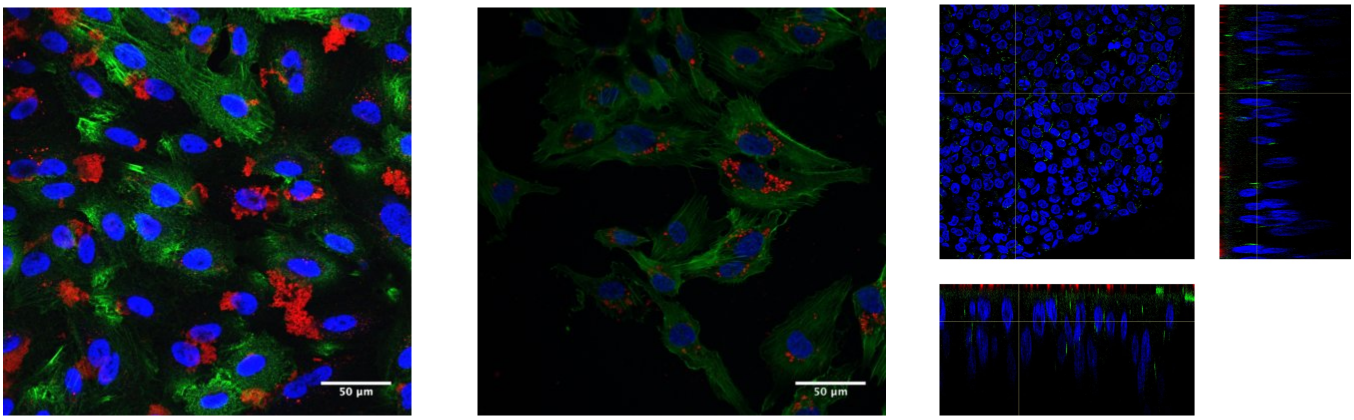

(a) Toxicité sur les A549

(b) Toxicité sur les HUVEC

(c) Translocation des particules

Figure 7: Observation de la toxicité des nanoparticules à 50 $\mu g/mL$ après 24 heures d'exposition et observation de la translocation à travers le patch *(Bleu: Noyaux, Vert: ZO-1, Rouge: Nanoparticules de* SiO_2*)*

Nous faisons l'hypothèse que les cellules favorisent la translocation à l'internalisation. Afin de vérifier cela, il serait intéressant de refaire ces expériences en observant la translocation à différents temps (1 h, 2 h, 12 h, 24 h, 48h, 72 h) afin d'observer si différents mécanismes (transport passif ou actif, para ou intracellulaire) prennent place au fur et à mesure du temps. Finalement, effectuer la translocation à 4 °C permet de séparer le transport actif du transport passif. Nous désirons aussi refaire ces expériences avec des particules de taille et de charge différentes pour observer l'effet de ces paramètres sur la translocation.

Conclusion Ces premiers travaux nous ont permis de présenter un modèle de barrière alvéolo-capillaire innovant, avec une membrane extrêmement fine permettant une importante communication intercellulaire. Ce modèle micro-fabriqué utilise des lignées simples à cultiver et permet de faire des tests de toxicité et de translocation de nanoparticules. En conclusion, nous avons développé un modèle de part en part et nous sommes allés jusqu'aux tests préliminaires faisant ainsi la preuve de concept de l'utilité de ce modèle dans les recherches de nanotoxicité. Cependant, il serait intéressant de prendre le temps de s'arrêter sur divers aspects du modèle pour en améliorer les performances ou mieux en caractériser les propriétés (notamment en termes de phénotypes exprimés et de perméabilité).

0.3 L'alvéole-sur-puce

Introduction et objectifs Afin d'améliorer notre modèle, nous avons décidé de fabriquer une puce microfluidique capable d'intégrer le patch et de reproduire les stimuli mécaniques propres à l'alvéole pulmonaire. En effet, ces stimuli jouent un rôle dans le comportement des cellules et influent ainsi sur la perméabilité de la barrière alvéolaire ([10], [11]). La technologie de puce microfluidique appliquée à la culture de tissu vivant a été présentée par le Wyss Institute au début des années 2010 [12] et a été depuis largement appliquée, d'abord à différents tissus humains, puis pour générer des modèles de maladies. Rapidement, des techniques de microfabrication sont utilisées pour fabriquer une puce biocompatible, souvent en PDMS, à l'intérieur de laquelle sont ensemencées des cellules (parfois jusqu'à cinq ou six types différents). Des machines viennent ensuite activer les différentes chambres de la puce, par exemple avec un flux de liquide nutritif, ou un apport électrique ou encore un étirement des parois. Le tout est dimensionné en taille et en effort pour reproduire au plus près les conditions observées *in vivo*. Cela permet non seulement de créer un modèle humain extrêmement précis et fidèle, mais ces puces sont aussi d'une grande praticité en laboratoire: elles sont petites, faciles à utiliser, peu coûteuses et permettent un suivi en temps réel de l'évolution des cellules en culture (imagerie live, suivi des activités biochimiques, génétiques ou métaboliques, etc.). Ces puces ont de nombreuses applications, permettant l'avancement de la recherche sur des mécanismes fondamentaux (physiologiques ou pathologiques) encore inconnus, ou servant de cobaye pour des tests de toxicité de certaines molécules et pour le criblage de médicaments.

Design de la puce Au vu de la revue de littérature qui est présentée dans ce manuscrit, nous avons fixé des objectifs clairs pour le développement de notre puce. Ainsi, elle doit: incorporer notre patch de PEGDA-gélatine, comprendre deux chambres (une supérieure pour l'air et une inférieure pour le milieu de culture), être étanche entre ces deux chambres, permettre la survie des cellules dans ce milieu confiné, être réversible pour permettre de prendre et de retirer le patch à convenance, permettre une observation en live au microscope confocal à au moins 40x, résister au flux continu de milieu dans la chambre inférieure (à cisaillement contrôlé), résister aux variations de pression induites dans la chambre supérieure (pour déformer le patch) et enfin être un objet robuste et reproductible.

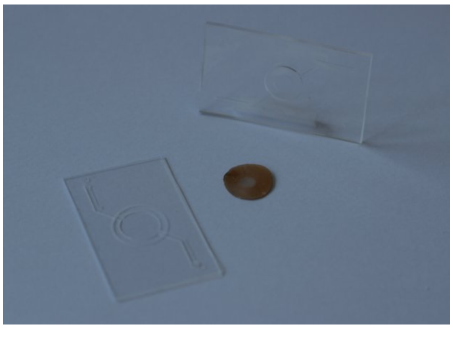

Figure 8: Les deux parties de la puce

Après 6 versions, nous proposons le modèle suivant: une puce en deux parties (voir Figure 8), maintenue serrée par une structure sur-mesure (nommée ici "clamp") qui vient l'encadrer et se ferme magnétiquement (voir Figure **??**). Rapidement, la partie inférieure de la puce comprend une lamelle de verre sur laquelle est collée par plasma une mince feuille de PDMS (0.2 mm) qui contient une chambre alimentée par deux canaux (entrée/sortie). Une seconde feuille de PDMS est collée sur la première, fermant ainsi la partie supérieure des canaux.

Cette seconde feuille contient en son centre un trou circulaire de la taille du patch, centré au-dessus de la chambre, ce qui permet de positionner le patch au-dessus de la chambre tout en obtenant une surface supérieure parfaitement plate. Cela permettra ensuite l'étanchéité lorsqu'elle sera maintenue en pression par la clamp contre la partie supérieure de la puce. Cette partie supérieure est composée de deux couches de PDMS. La partie supérieure est en PDMS moulé et contient une chambre et deux canaux d'alimentation, et la partie inférieure est une feuille de PDMS contenant un trou central de 5 mm de diamètre (légèrement plus grand que la zone du patch où se situent les cellules). Cette feuille ferme la partie inférieure des canaux tout en assurant un joint flexible entre la chambre supérieure et le patch, qui s'adapte au patch. Elle contient aussi des trous situés au-dessus des entrée et sortie des canaux de la chambre inférieure pour permettre de facilement aligner les tuyaux. Regardant la fabrication, les feuilles de PDMS ont été achetées (Silex.Co) et découpées via un Cutter Plotter (GraphTec), et le PDMS moulé l'a été dans un moule réalisé par impression 3D (FormLabs 2).

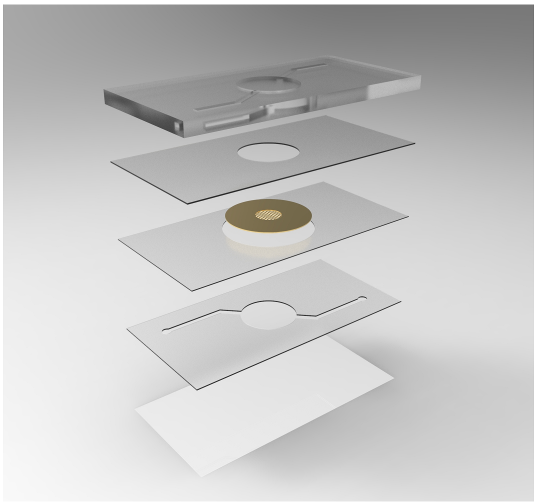
Figure 9: Vue éclatée de la puce (rendering)

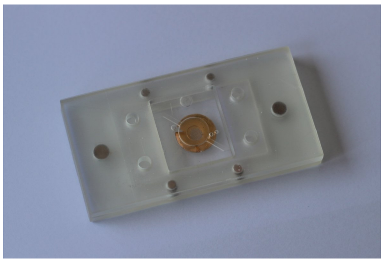
Figure 10: Photo de la puce dans sa clamp

Cette puce est ensuite enserrée dans une clamp: cette pièce imprimée en 3D est faite aux dimensions de la puce et comprend 6 aimants par face afin de serrer les deux parties de la puce, assurant ainsi l'étanchéité de l'ensemble (voir Figure 10). Des tuyaux sont ensuite connectés aux entrées/sorties des chambres, permettant ainsi une alimentation en milieu nutritif dans la chambre inférieure, et en air pressurisé dans la chambre supérieure.

Nous avons développé un modèle de puce microfluidique réversible intégrant parfaitement notre patch, lequel est visible dans sa clamp à 40x au microscope confocal, et sans fuite interne ou externe, et ce, même avec un air pressurisé à 100 mbar. Il s'agit maintenant de mettre les cellules en culture pour observer leur survie, en conditions statiques puis dynamiques.

Activation de la puce Comme détaillé dans le manuscrit, la mise en service de la puce est une étape extrêmement technique car il s'agit d'assembler tous les composants en les maintenant stériles, secs et sans poussière, le tout dans un laps de temps minimal pour garantir la survie des cellules hors de l'incubateur. Une fois cette opération effectuée, il s'agit ensuite de paramétrer le flux de milieu pour obtenir des propriétés comparables aux observations *in vivo*, notamment un taux de cisaillement compris entre 1 et 10 $dynes/cm^2$ [13]. Avec la taille de nos canaux et la viscosité du milieu de culture, il nous a été impossible d'obtenir un tel cisaillement. Nous proposons cependant différentes solutions à explorer pour remédier à cela. Nous avons cependant observé la survie des cellules après 18 jours de culture sous un flux de 100 $\mu L/min$.

Afin de reproduire la déformation cyclique induite par la respiration, nous avons décidé d'utiliser une pression positive dans la chambre supérieure. Il s'agit alors, pour chaque cycle (0,2 Hz) d'obtenir 8 à 12 % de déformation linéaire de la couche de cellules. Nous avons donc mis au point un dispositif expérimental permettant de calculer la déformation en fonction de la pression imposée par un contrôleur de pression (MFCZ-EZ, Fluigent), comme montré sur la Figure 11. Des résultats préliminaires nous ont permis d'observer que notre couche est trop rigide, et que la pression nécessaire à sa déformation est trop importante pour permettre la survie des cellules. Il faudrait donc travailler à améliorer les propriétés mécaniques du patch pour en augmenter son élasticité.

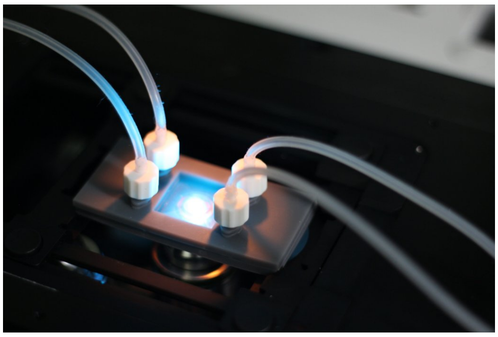
Figure 11: Puce connectée sur le microscope

Conclusion Nous avons présenté ici une puce microfluidique qui permet de reproduire les efforts mécaniques présents au niveau des alvéoles pulmonaires. Si pour le moment nous n'avons obtenu que des résultats préliminaires, nous avons démontré que cet objet est capable de remplir ses fonctions, moyennant encore un peu d'optimisation.

0.4 Différentiation des iPSC

Introduction Dans cette dernière partie, nous avions pour objectif d'améliorer notre modèle en changeant le modèle de cellules. En effet, utiliser des cellules souches pluripotentes induites différenciées plutôt que des lignées permet d'obtenir un comportement cellulaire plus proche de ce qui est observé *in vivo*. Cependant, la recherche sur les différents protocoles de différentiation de iPSC étant encore jeune, il s'agit de réussir à optimiser ces protocoles pour un type d'iPSC donné. Ainsi, nous reportons ici nos efforts pour optimiser deux protocoles de différentiation (en endothélium et en épithélium alvéolaire) afin de les implémenter sur notre patch.

Comportement des iPSC sur le patch Dans un premier temps, nous avons vérifié que notre lignée commerciale d'iPSC (Human Episomal iPSC Line, Gibco, Ref. A18945) pouvait être cultivée sur le patch sans que cela n'induise de différentiation inopinée des cellules. Nous avons donc observé l'expression de plusieurs marqueurs de pluripotence sur nos iPSC après quinze jours de culture sur Geltrex et sept jours de culture sur le patch et avons pu confirmer une expression soutenue de ces différents marqueurs (NANOG, SSEA-4, OCT4 sur Geltrex et SOX2, TRA-1-60 et SSEA-4 sur le patch).

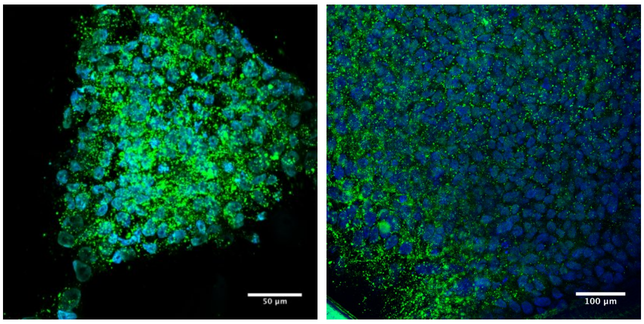

Figure 12: Immunomarquage de la protéine de pluripotence SSEA-4 sur des iPSC en culture (gauche) et sur le patch (droite)

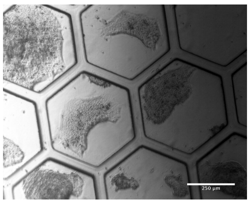

Figure 13: Formation de corps embryonnaires à partir d'iPSC sur le patch

Une deuxième étape a été de travailler à la formation de corps embryonnaires sur le patch. En effet, certains protocoles de différentiation commencent par ces agrégats de cellules, et nous voulions observer si cela était possible sur le patch. Nous avons réussi à mettre au point un protocole pour obtenir la formation de ces corps, même s'ils reste des améliorations à faire en termes d'homogénéité de forme, de taille et de distribution.

Différentiation en endothélium Le protocole de différentiation des iPSC en cellules endothéliales a été optimisé à partir de celui de Patsch *et al* [14]. Il s'agit d'un protocole en 5 étapes:

1. **Préparation** : Les cellules sont ensemencées en singleton, à densité contrôlée, et laissées 24 h pour adhérer (voir Figure **??**).
2. **Induction du mésoderme** : Les cellules sont incubées trois jours avec du CHIR99021 et du BMP4 (à respectivement 6 μM et 25 ng/mL). Le premier est un inhibiteur de $GSK3 - \beta$ qui active la voie de signalisation canonique des protéines Wnt, et le second est activateur potentiel du mésoderme. Au bout de trois jours, on obtient la formation de colonies denses (voir Figure **??**).
3. **Obtention des progéniteurs endothéliaux et spécification en cellules endothéliales** : Le milieu est remplacé au jour 4 par un milieu enrichi en Forskolin (2 μM) qui augmente la production de AMP-cyclique ce qui active la protéine kinase A, une voie qui pousse la différentiation des cellules du mésoderme en progéniteurs endothéliaux. Le milieu contient aussi du VEGF (200 ng/mL) qui pousse la différentiation vers des cellules endothéliales seulement. Ce milieu est renouvelé le lendemain. On observe alors des colonies de cellules très allongées (voir Figure 14c).
4. **Purification** : Les cellules sont ensuite triées par MACS (Magnet-Activated Cell Sorting) d'après un marqueur endothélial (ici la VE-Cadhérine ou CD144). Elles sont ensuite ensemencées pour la maturation.
5. **Maturation** : Les cellules sont cultivées encore avec du VEGF (50 ng/mL) jusqu'à confluence (3 à 5 jours) puis peuvent être utilisées.

Après plusieurs tentatives, nous avons obtenu la différentiation de nos iPSC en cellules endothéliales, et nous avons effectué une séparation magnétique. Malheureusement, celle-ci n'était pas proprement optimisée et les cellules ainsi séparées ont été tuées dans le process. Cependant nous avons pu mesurer que notre différentiation avait été efficace à 50% pour le marqueur CD144. Si nous n'avons pas pu aller plus loin, nous avons mis en place une liste de choses à tester et à améliorer pour obtenir à la fois un taux de différentiation plus élevé et une séparation magnétique efficace, afin de pouvoir ainsi continuer la maturation des cellules obtenues.

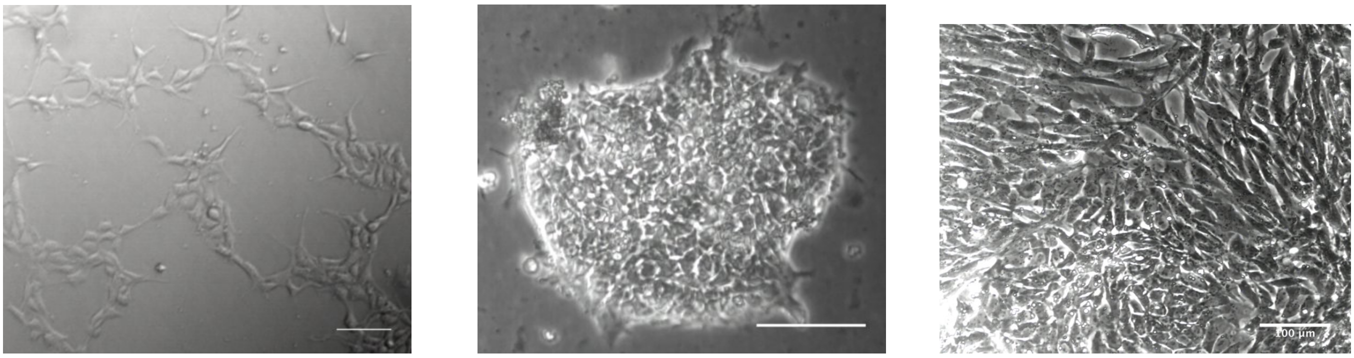

(a) Jour 1 : Ensemencement (b) Jour 2 : Mesoderme (c) Jour 5 : Progéniteurs

Figure 14: Résultats de la différentiation des iPSC en endothélium

Différentiation en épithélium alvéolaire La différentiation des iPSC en épithélium alvéolaire a été effectuée d'après le protocole proposé par Huang *et al* [15]. Ce protocole comporte de nombreuses étapes, pour 25 jours de différentiation et 25 jours ou plus de maturation. Chaque étape comprends de nombreux points à optimiser, que ce soit le timing, la concentration de certains facteurs de différentiation, la densité des cellules ou la façon dont les cellules sont manipulées. Ces étapes ont donc été essayées et optimisées plusieurs fois, tout en continuant à avancer pour essayer un maximum d'étapes. Ainsi les premières étapes sont plus optimisées que les dernières. Nous avons donc procédé ainsi:

1. **Formation de la ligne primitive** : Les cellules sont cultivées sous forme de corps embryonnaires dans un milieu comportant du ROCK inhibitor (à 10 µM, pour la survie des cellules), du Wnt3a (à 10 ng/mL, pour activer la voie canonique WNT) et du BMP4 (à 3 ng/mL), ce qui active la formation de la ligne primitive (voir Figure 15a).
2. **Induction définitive de l'endoderme** : Les corps embryonnaires sont cultivés pendant 3 jours avec un milieu enrichi en ROCK (à 10µM), en Activine A (à 100 ng/mL) pour simuler la voie Nodale et induire la formation d'endoderme définitif , en BMP4 (à $0,5ng/mL$) qui favorise la formation d'endoderme (mais doit être stoppé ensuite sous peine de pousser les cellules vers une destinée hépatique) et en FGF-2 (à $2,5ng/mL$) qui est crucial pour ne pas obtenir de l'ectoderme. L'efficacité de la différentiation en endoderme définitif est mesurée par cytométrie de flux, en observant l'évolution de la co-expression des marqueurs CXCR4 et c-Kit. En fonction de leur pic d'expression, nous pouvons déterminer le timing optimal pour commencer l'étape suivante. Après plusieurs tests, un résultat préliminaire nous permet de choisir le jour 4 pour avancer dans la différentiation (voir Figure 15b).
3. **Spécification en Anterior Foregut Endoderm (AFE)** : Au jour 4, les cellules sont dissociées et ensemencées (voir Figure 4.27a), puis cultivées 24 h avec un milieu enrichi en NOGGIN (à 100 ng/mL) un antagoniste qui sert à inhiber les signaux de BMP4 pour éviter la direction hépatique, et en SB431542 (à 10 µM) qui inhibe les signaux $TGF-\beta$. Le milieu est ensuite changé pour 24 h à nouveau, étant cette fois enrichi en IWP2 (à 1 µM) qui inhibe le signalement WNT et en SB431542 (à 10 µM) à nouveau.
4. **Induction des progéniteurs pulmonaires** : Le milieu des cellules est ensuite changé et renouvelé un jour sur deux jusqu'au jour 15. On utilise ici un milieu enrichi en CHIR99021 (à 3 µM) activateur de WNT, en KGF (à 10 ng/mL), en FGF-10 (à 10 ng/mL) , en BMP4 (à 10 ng/mL), en EGF (à 20 ng/mL) et en Acide Rétinoïque (à 50 nM), qui sont toutes des molécules nécessaires à l'induction d'une spécification pulmonaire chez la souris. La concentration en Acide Rétinoïque doit être ajustée à chaque lignée cellulaire pour obtenir une expression maximale du marqueur pulmonaire NKX2.1. Nous avons ici testé différentes concentrations et obtenue une meilleure viabilité et croissance cellulaire pour une concentration de 0.0625 µM, observant même la formation de bourgeons pulmonaires (voir Figure 15d) et une large expression du marqueur NKX2.1 (voir Figure 15e). Nous avons pu observer par immunofluorescence l'engagement de nos cellules en faveur d'un destin endodermal, malgré la présence de quelques cellules neuronales (voir Figure 15f).
5. **Expansion des progéniteurs pulmonaires** : Au jour 15, les cellules sont dissociées délicatement et ensemencées à nouveau. Cette étape demande une optimisation des gestes de l'expérimentateur, pour pouvoir dissocier partiellement les cellules en singleton (qui sont le plus souvent des cellules neuronales) et garder les autres, sans trop casser les agrégats mais en estimant correctement la densité d'ensemencement. Ensuite, entre le jour 16 et le jour 25, le milieu utilisé est enrichi en CHIR99021 (à 3 µM), et en KGF et

FGF-10 (tous deux à 10 ng/mL). Le BMP4 est retiré car il induit plutôt des cellules proximales. Pour nous, le protocole s'est arrêté ici, et nous avons caractérisé les cellules à la fin de cette étape d'expansion (voir Figure 16a).

6. **Maturation en cellules pulmonaires distales** : Au jour 25 le milieu est changé tous les deux jours pour les 25 prochains jours, avec un milieu enrichi en CHIR99021 (à 3 μM), en KGF et FGF-10 (tous deux à 10 ng/mL), en Dexamethasone (à 25 ng/mL), en IBMX (à 0,1 mM) et en cAMP (à 0,1mM). Ce cocktail a été testé et approuvé pour l'obtention de cellules alvéolaires de type II. Malheureusement, nous n'avons pas pu atteindre cette étape du protocole, et n'avons donc pas de résultats à présenter pour cette partie.

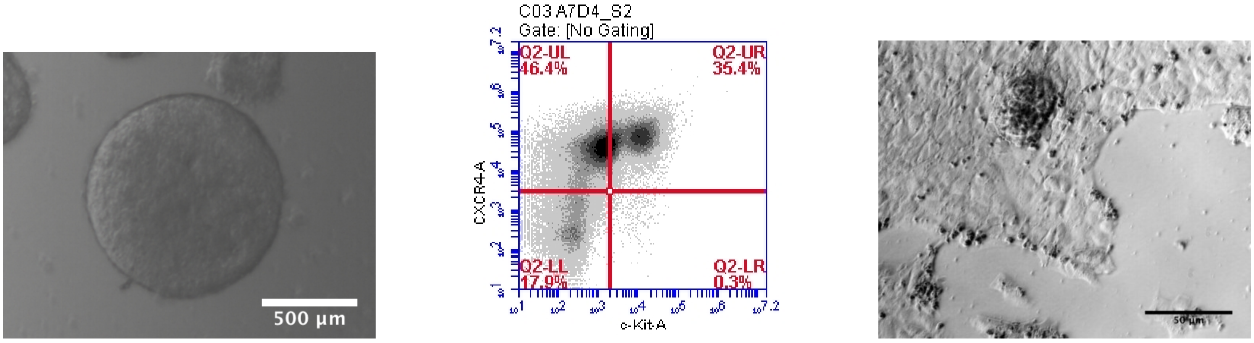

(a) Jour 1: ligne primitive (b) Engagement endodermal (c) Jour 4: Endoderme

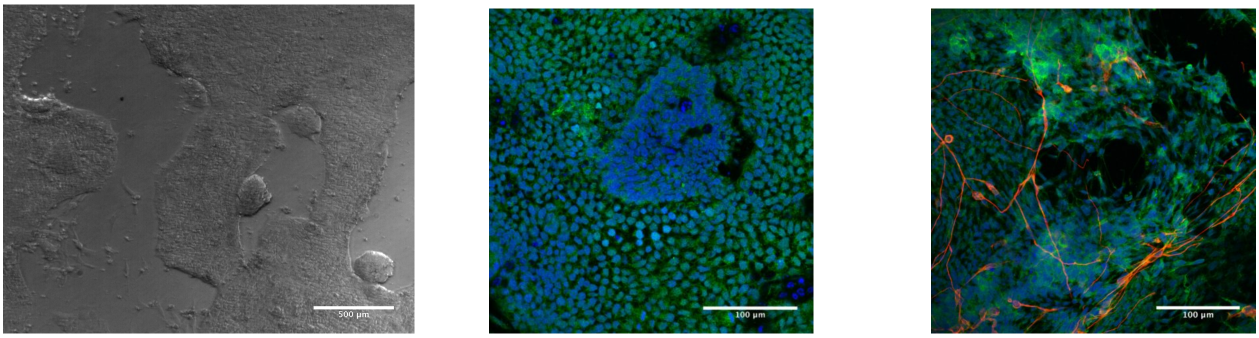

(d) Jour 10: Bourgeons pulmonaires (e) Jour 15: Expression de NKX2.1 (f) Jour 15: quelques neurones

Figure 15: Etapes de la différentiation des iPSC en épithélium alvéolaire

Après 32 jours de culture et sans avoir utilisé le cocktail de maturation, nous avons observé les phénotypes exprimés par nos cellules à cet instant de la différentiation (voir Figure 16). Tout d'abord, les cellules sont encore organisées en colonies, avec toujours la formation de bourgeons pulmonaires (voir Figure **??**), et elles forment un épithélium pulmonaire caractérisé par l'expression du marqueur NKX2.1 et maintenu par de fortes jonctions serrées (voir ZO-1 (vert) et NKX2.1 (rouge) sur la Figure 16b). De plus nous avons pu observer l'expression de deux marqueurs des cellules distales pulmonaires: la production de MUC5AC (voir Figure 16c) et de Podoplanine (voir Figure 16d). L'expression de marqueurs plus spécifiques aux cellules alvéolaires tels que AQP5, SP-A, SP-B ou proSP-C n'a pas été observé, ce qui indique qu'il faut effectivement poursuivre l'étape de maturation de ces cellules avec le cocktail préconisé.

Conclusion Nos expériences de différentiation en épithélium alvéolaire ont posé les bases de l'optimisation nécessaire à l'adaptation du protocole à la lignée commerciale avec laquelle nous travaillons. Si le temps nous a manqué, nous avons cependant commencé à optimiser plusieurs étapes, resserrant les fourchettes autour des valeurs optimales, que ce soit pour le jour idéal de d'induction de l'AFE, pour la concentration idéale en Acide Rétinoïque, pour la densité idéale d'ensemencement aux jours 4 et 15, etc. De plus, en avançant ainsi jusqu'à l'avant-dernière étape de la différentiation, nous avons pu confirmer qu'il est possible d'obtenir des cellules pulmonaires distales avec ce protocole et cette lignée. Cela nous donne confiance dans la suite: il s'agit désormais de répéter les expériences en optimisant chaque étape.
Dans le manuscrit nous décrivons aussi nos essais de différentiation *in situ*, c'est-à-dire directement à partir de cellules iPSC sur le patch. Comme ces essais n'ont pas été concluants pour aucun des deux protocoles, j'ai

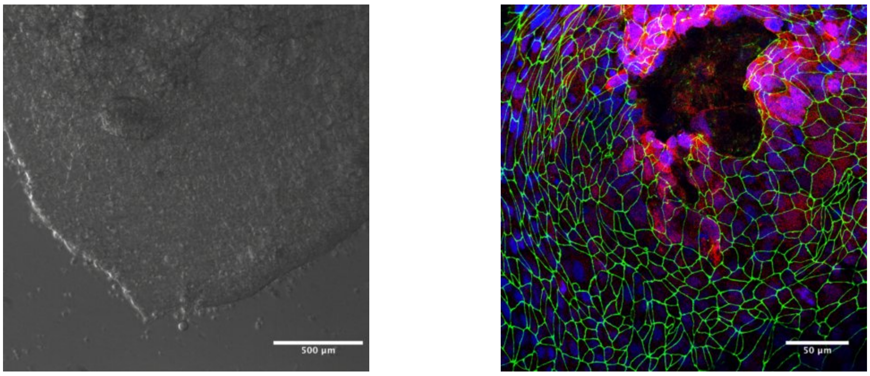

(a) Jour 26 (b) NKX2.1 (Rouge), ZO-1 (Vert)

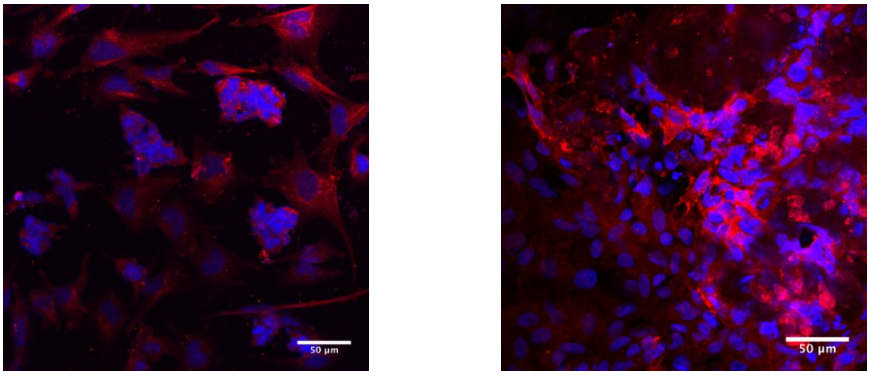

(c) MUC5AC (d) Podoplanine

Figure 16: Résultats de la différentiation en épithélium alvéolaire. Les colonies révèlent une forte présence de cellules de poumons au marquage positif pour le marqueur pulmonaire NKX2.1, avec une pluralité de phénotypes: Type I (Podoplanine) et Type II (MUC5AC). Les tissus sont joints par des jonctions serrées (ZO-1)

fait le choix de ne pas les détailler ici. Ces essais seront à refaire une fois les deux protocoles complètement optimisés avec le mode de culture traditionnel.

0.5 Conclusion et perspectives

Conclusion Dans ce manuscrit, nous présentons un modèle de la barrière alvéolo-capillaire. Ce modèle est obtenu à travers plusieurs approches: nous avons d'abord réalisé un modèle statique, avec pour objectif d'obtenir une co-culture des deux types cellulaires viable sur plusieurs mois, et de pouvoir utiliser ce modèle pour faire des tests de translocation. Ce modèle micro-fabriqué possède le grand avantage d'avoir une membrane entre les types cellulaires jusqu'à dix fois plus fine que ce que la littérature proposait alors. Ensuite, nous avons voulu intégrer les stimuli mécaniques propres à l'environnement alvéolaire pour reproduire les signaux locaux et voir quelle influence ils avaient sur notre modèle et sur sa capacité à internaliser ou transloquer des particules. Pour cela nous avons développé une puce microfluidique novatrice car réversible. Finalement, dans l'objectif d'intégrer des iPSC à ce modèle, nous avons travaillé à l'optimisation de deux protocoles de différentiation en endothélium et épithélium alvéolaire afin de les appliquer à une lignée commerciale.

Perspectives Différents éléments de discussion ont été soulevés, et dressent ainsi une liste des prochains axes de recherche nécessaires à l'avancement de ce projet. Ainsi, le comportement des cellules endothéliales sur notre modèle statique peut être amélioré, par exemple en optimisant la concentration en Dexamethasone. Les essais de translocation de nanoparticules peuvent être élargis pour tester de nombreux paramètres: cela permettra de comprendre au mieux les différents mécanismes qui ont lieu au cours du transport de ces nanoparticules à travers la barrière alvéolo-capillaire. De plus, la mise en place des stimuli mécaniques n'est pas encore tout à fait optimisée: l'obtention de la déformation du patch doit être revue au profit de la survie des cellules, et le flux de milieu doit être modifié pour pouvoir induire la contrainte de cisaillement voulue. Enfin, les protocoles de différentiation des iPSC comportent de nombreux points d'amélioration, déjà cités précédemment, à mettre en oeuvre patiemment.

Chapter 1

Introduction

1.1 General introduction

In 2010, outdoor air pollution alone contributed to 1.2 million premature deaths in China [1], *i.e.* nearly 40% of the world total. When faced with such reality, one would hope to see a radical awakening of all nations. However, if some measures to limit air pollution were taken, they only concerns a minority of countries, and more often than not, these feel like a droplet in the ocean. The global race for growth, unregulated, is happening at the expense of our environment and our health. If developing countries seem more directly concerned, eventually pollution travels in the air or through the oceans, reaching even the most deserted parts of our planet and leaving no place untouched. In 2018, air pollution is not a forthcoming complication, or a present technicality, it is an impending fate for all living, breathing, things.

Even if major preventive actions were to be taken right away, it will take a long time to implement them, and even longer to reverse the current trend. Air pollution will inevitably increase in the years to come. Faced with this realization, we need to develop solutions to cope with it. One thing is to find how we can protect human health. In order to do so, the scientific community needs to have a deeper understanding of air pollutants but also of the human lungs, its protection mechanisms and its reaction when faced with air pollutants. Gaining this knowledge is the first basis for the development of dedicated protection equipment or therapeutic solutions. This is exactly what this project aimed at.

Our objective was to develop a tool for research in air pollution toxicology. This tool is an *in vitro* model recapitulating most of the complex features of the alveolar capillary barrier. We have worked on enhancing the different aspects of our model to always go further and improve its accuracy.

This manuscript reports our efforts in designing and validating this model. In this first introductory chapter, we will briefly introduce the current context of air pollution as well as describe the air pollutants. Then we will follow the transport of an inhaled pollution particle in the lung to get acquainted with this complex organ and its protective features. We will then try and understand the pathological mechanisms by which air pollution damages the lungs. Finally, we will see that, currently, we cannot implement preventive solutions to air pollution, and that we have to turn to designing protective solutions. We will explain the interest of making *in vitro* models to help contribute to this issue, and we will introduce our own project.

At the end of this introductory part, we will detail the technical objectives of this project, and unfold the organization of this manuscript.

1.2 Ongoing concerns: when air pollution reaches the alveoli

1.2.1 A dramatic situation: current air pollution issues

a. Snapshot of the current situation

Air pollution is a dramatic environmental and social issue and, at the same time, it is a complex problem posing multiple challenges in terms of management and mitigation. Air pollutants are emitted both from anthropogenic and natural sources; they may be either emitted directly or formed in the atmosphere. They have numerous impacts on health, ecosystems, built environment and climate and because they are transported or formed over long distances, they affect large areas. Effective action to reduce the impacts of air pollution requires a good understanding of its causes, and of how pollutants are transported and transformed in the atmosphere, and how they impact on humans, ecosystems and the climate.

Effective air quality policies call for action and cooperation on global, national and local levels. These actions should extend across most economic sectors as well as engage the public [2]. It is baffling to realize that the EU limit value for PM2.5 (particulate matter of size below 2.5 μm), applying from 2005, continues to be exceeded in large parts of Europe in 2013 according to the data of the European air quality database (Air Quality e-reporting database, EEA, 2015, [2]). Figure 1.1 shows concentrations of PM2.5 in relation to the daily limit value, which is more stringent than the annual limit value and, therefore, more frequently exceeded. The limit was fixed to 10 $\mu g/m^3$ for the World Health Organization, and 25 $\mu g/m^3$ by the EU Air Quality Directive. The exceedances occurred for 95% of the cases in urban or suburban areas. This non-compliance is all the more problematic that air pollution is the single largest environmental health risk in Europe. Recent estimates suggest that the disease burden resulting from air pollution is substantial [16]. Heart disease and stroke are the most common cases of premature death attributable to air pollution and are responsible for 80% of cases of premature death; lung diseases and lung cancer follow (WHO report, 2014). In addition to causing premature death, air pollution increases the incidence of a wide range of diseases (e.g. respiratory and cardiovascular diseases and cancer), with both long and short term health effects. Air pollution as a whole, as well as particulate matter as a separate component of air pollution mixtures, have recently been classified as carcinogenic by the International Agency for Research on Cancer (in 2013).

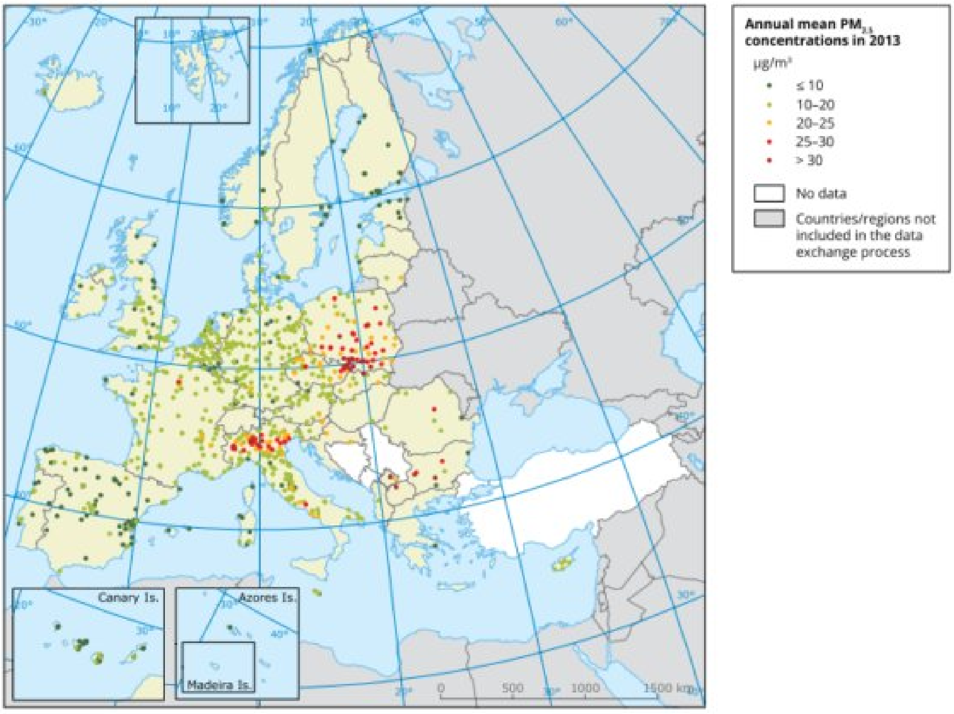

Notes: The dark-red dots indicate stations reporting exceedances of the EU annual target value (25 µg/m³) plus at least 5 µg/m³.
The red dots indicate stations reporting exceedances of the EU annual target value (25 µg/m³).
The orange dots indicate stations reporting exceedances of the 2020 EU indicative annual limit value (20 µg/m³).
The light-green dots indicate stations reporting exceedances of the WHO AQG for $PM_{2.5}$ (10 µg/m³).
The dark-green dots indicate stations reporting values below the WHO AQG for $PM_{2.5}$ (10 µg/m³).
Only stations with > 75 % of valid data have been included in the map.

Source: Based on Air Quality e-reporting database (EEA, 2015a).

Figure 1.1: Incidence of PM2.5 pollution in Europe in 2013. The WHO limits for air pollution are often exceeded, especially in urban areas.
2015 Report on Air quality in Europe [2]

b. Getting acquainted with pollution particles

Origins Particulate matter is both directly emitted to the atmosphere (primary PM) or formed in the atmosphere (secondary PM). The main precursor gases for secondary PM are NH_3, SO_2 and NO_x, reacting in the atmosphere to form ammonia, sulfate and nitrate compounds. The latest are responsible for the acidification of the oceans that is currently causing the destruction of the coral reefs and their biodiversity. These compounds form new particles in the air or condense onto pre-existing ones and form so-called secondary inorganic aerosols. Primary PM originates from both natural and anthropogenic sources. Natural sources include sea salt, naturally suspended dust, pollen and volcanic ash. Anthropogenic sources, which are predominant in urban areas, include fuel combustion in thermal power generation, incineration, building construction, domestic heating for households and fuel combustion for vehicles, as well as vehicle (tyre and brake) and road wear and other types of anthropogenic dust. Black carbon is one of the constituents of fine PM and has a warming effect. Black carbon is a product of incomplete combustion of organic carbon as emitted from traffic, fossil fuels and biomass burning, and industry.

Properties Air pollutants are categorized according to their size. The smaller they are, the more damage they produce. Indeed, smaller particles have a greater proportion of atoms or molecules oriented on the surface, hence interacting more readily with the adjacent atoms. In a human body, these highly reactive particles can cause cellular toxicity, instability, increased uptake or induce oxydative stress [17]. That is why the nanoparticles (particles with a diameter below 100 nm) are mostly studied: they are the most dangerous.

Deposition in human lungs After inhalation, the particles deposit in the respiratory track according to three different mechanisms, depending on their size. All particles reach the lung by a convective transport due to mechanical breathing.
Firstly, the particles of a diameter superior to 5 μm will deposit in the mouth and throat by inertial impaction. For diameters from 1 to 5 μm, the particles deposit along the bronchial tree and the first airway divisions up to the bronchioles due to gravitational sedimentation. Indeed, as convective transport depends on local flow patterns, the equilibrium between convection and inertia forces changes over the bronchial tree [3].
Finally, the particles below 0.5 μm are deposited mostly by diffusion, due to their Brownian motion [3]. A fluid mechanics analysis by Tsuda *et al* [4] underlined that although it is often thought that nanoparticles deposit in the lung solely by diffusion, in fact convective transport dominates over diffusive transport by far (for all generations but the terminal sacs).
In the following section, we will follow a particle down the lungs in order to understand their architecture and learn about their functional organization. We will elaborate on the alveolar capillary barrier, which is the focus of this project.

1.2.2 A particle's journey down the human lung

The lungs are the primary organs of the respiratory system in human beings. They replace the carbon dioxyde in our blood with oxygen, thus powering all other organs and muscles. In order to achieve this oxygenation, the lungs need to connect outside air directly to the blood flood, via a complex route, which serves as a key entry point to the human body. In order to establish this connection while still protecting the human body, the lung architecture is convoluted, with multiple divisions and complex protective features. We will present here this very structure, from the macro to the nano-scale, that is detailed in this part, with the help of the work of Ali *et al.* [18] and the *Gray's Anatomy* [19]. All the architecture, and actuation of the lung will first be depicted, then a focus on the alveolar capillary barrier will portray the specifics of this part of the human body.

a. The respiratory system: global architecture

Actuation The trachea and both lungs compose the respiratory system, which is responsible for all the respiration process, from the air inhalation to the final gas exchange in the alveoli. The lungs are contained in the rib cage, enveloped by two lubrified membranes that reach deep into the fissures of the lung, and that can slide along each other (the pleurae). The rib cage acts as a protection, but also as the main actuator of the respiration mechanism. Indeed, when the intercostal muscles and the lower diaphragm, separating the lungs from the abdominal cavity, contracts, it extends the rib cage, creating a depression between the two membranes enveloping the lung. These membranes will thus unfold, deploying the lung and aspirating air inside the airways: this is the inspiration. When the diaphragm relaxes, the opposite mechanism takes place: this is the expiration.

Breathing dynamics A normal human being at rest has a respiration rate of about 12 breaths per minute. This rate can increase up to 30 or 60 breaths per minute during exercise. During normal breathing at rest,

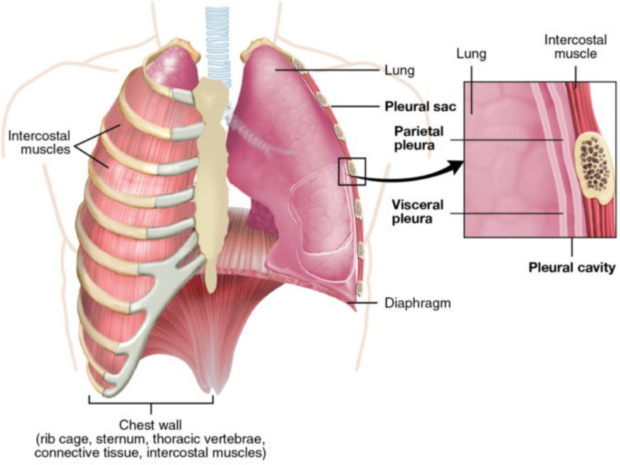

Figure 1.2: Complex integration of the lung in the human body: the intercostal muscles and the diaphragm are responsible for the expansion of the ribcage, deploying the lungs through a complex mechanism of intertwined membranes, the pleurae.

the tidal volume (volume inhaled during a single breath) is 500 mL [20], inhaled in about 1.5 to 2 seconds, and exhaled in the same time, with a one second pause [21]. The respiratory system commences to work the minute we are born, and continues subconsciously all along our life.

Architecture The left and right lobes of the lungs are divided into bronchopulmonary segments based on the locations of bronchioles. This segmental anatomy is different in both lobes, and is useful clinically for localizing disease processes in the lungs. As can be seen on Figure 1.3, the entry point from the trachea to each lobe are the bronchus, each leading to a bronchial tree. The bronchus then divides into the secondary and tertiary bronchi, going into smaller and smaller bronchioles until they become the respiratory bronchioles. It comports 23 generations of divisions. The respiratory bronchioles lead to terminal bronchioles, which end in clusters of alveolar sacs. The bronchioles supply air through alveolar ducts into each alveolus, where the gas exchange finally takes place. The lungs have a total surface area of about 50 to 75 square meters. This impressive surface area is crucial to optimize gas exchange.

Internal constitution Surrounding the trachea and bronchi are cartilage rings, which help to maintain stability. As we go along the bronchial tree, the stability is preserved by cartilage plates, allowing for more flexibility (see Figure 1.3). The bronchioles are not surrounded by cartilage rings: they are encircled by a layer of smooth muscle actin.

The bronchi are lined with columnar epithelial cells that possess cilia: small frond-like projections. Interspersed with these epithelial cells are Goblet cells which produce mucus, and club cells (or Clara cells), which are nonciliated bronchiolar secretory cells with actions similar to macrophages (see Figure 1.4). The bronchioles possess the same columnar epithelial lining.

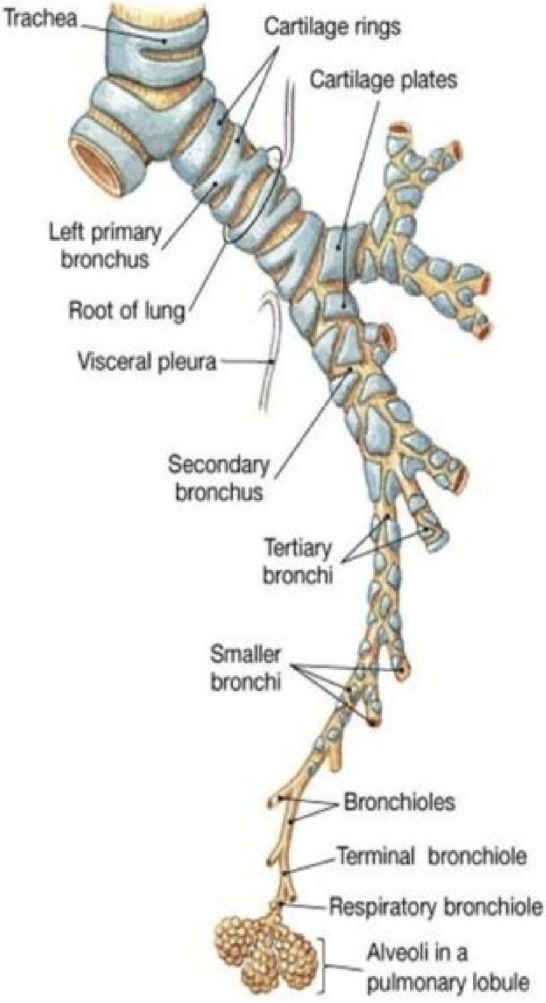

Figure 1.3: Architecture of the bronchial tree: the trachea divides into bronchi, bronchioles and finally end in small alveolar sacs. *Anatomy and Physiology*

b. The mucociliary barrier

All along the respiratory tract, the nanoparticles will encounter the defense mechanism of the bronchi to protect the epithelia against particle deposition and interactions: the mucociliary barrier.

The mucus The epithelial cells throughout the respiratory tract secrete epithelial lining fluid or mucus, the composition of which is tightly regulated. The mucus continously produced in the bronchial tree acts as a protective layer on the epithelium: it will physically protect the bronchial epithelium, and will trap the bigger particles inhaled. It comes essentially from the chorion glands, called Goblet cells, at a quantity of 10 to 20 mL per day. It is mostly composed of mucins (viscous proteoglycans) and some proteins with playing a role against infectious agents. The mucus humidifies the ambient air by partially evaporating, thus regulating the local hygrometry.

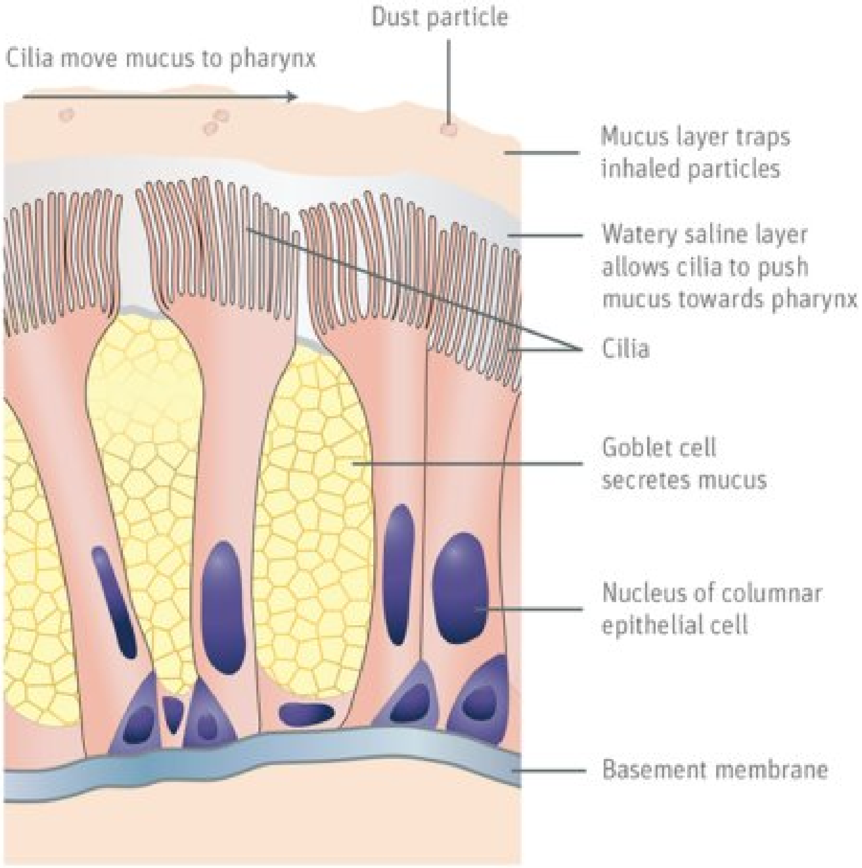

Figure 1.4: The mucociliary escalator is a defense mechanism of the bronchi: the ciliated cells beat in rythm to push the mucus upwards and down the oesophagus to discard any particles trapped in this mucus. *Courtesy of teva.com*

The mucocilary escalator The mucus is evacuated through the mucociliary escalator: the ciliated cells of the bronchial epithelium (see Figure 1.4) move their cilia upwards at a mean frequency of 15 to 20 Hz, and this motion pushes the viscous mucus toward the trachea. The cilia height and beating frequency increase as we move up the bronchial tree. They contract in a wave that propagates along the respiratory epithelium via gap junctions. In the trachea, the mucus reaches a speed of 10 to 15 mm per minute, before being discarded in the digestive system. This clearance system evacuates all the inhaled particles that were large enough to sediment in the bronchial tree.

c. The alveolar capillary barrier

Particles that were not trapped by the mucociliary barrier, will continue diffusing down until they reach the alveolar sacs.

Structure of the alveoli At the end of the bronchial tree, the alveoli form clusters of thin-walled, inflatable grape-like sacs at the terminal branches of the conducting airway. They are surrounded by a dense network of microvascular capillaries (see Figure 1.5). There are about 500 million alveoli in the lungs, ranging from about 200 to 300 μm in diameter.
Inside an alveolar sac, the alveoli are connected by minute pores called pores of Kohn (about 10-15 μm diameter), which allow pressure distribution in the sac, and also provide an alternative air entry for diseased or blocked alveolus.
The alveolus is composed of monolayer of two epithelial cells (see Figure 1.5): type I and type II alveolar cells (also referred to as pneumocytes). They form the alveolar wall, and are responsible for all the functions performed by the alveoli. Type I cells are extremely thin cells that cover 95% of the alveolar surface and are

responsible for homeostasis and particle transport across the epithelium. Type II cells are round-shaped cells responsible for immune defense through a secretory activity. Indeed, they produce the surfactant, a protective fluid composed mainly of phospholipids, which contains specific surfactant proteins. Each of those proteins has a specific role in the immune defense of the alveoli. The role of each type of cells, as well as the surfactant's will be extensively detailed further in this manuscript.

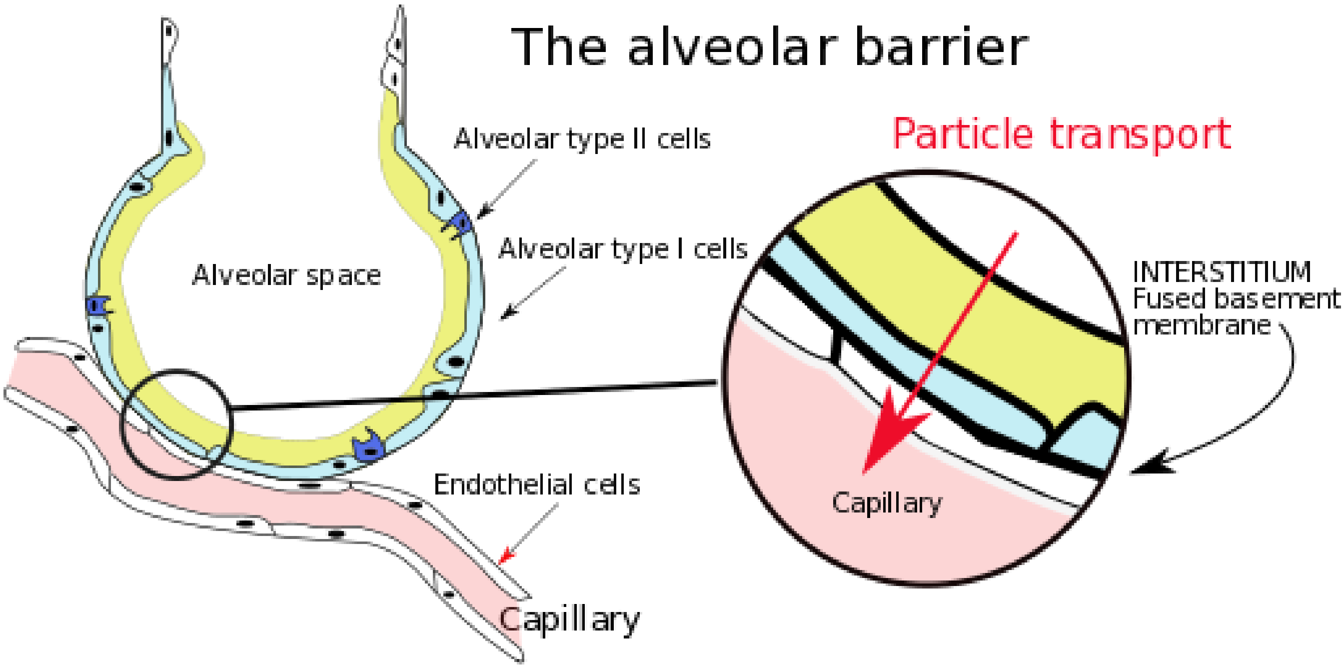

Figure 1.5: Schematic of the alveolar capillary barrier. The alveoli are surrounded by capilaries. The alveolar capillary barrier is composed of four main layers: the surfactant, the alveolar epithelium, the interstititum and the microvascular endothelium.

The alveolar interstitium The alveoli are held in a macrostructure: the interstitium, the connective tissue of the alveolar sacs. This supportive tissue is actually the fusion of the basal laminas of the alveolar epithelium and the capillary endothelium (see Figure 1.5). The microscopic composition of this tissue determines for the macroscopic mechanical properties of the lung. The interstitium is a loose, elastic, and highly vascularized extra-cellular matrix (ECM) tissue, composed mainly of elastic fibers and collagen [22]. These fibers are made of elastin, a fibrous elastic protein produced by the fibroblasts present in this interstitial space. It is a stable component with a turn-over lower than that of collagen. These fibers represent a third of the total lung dry mass.

Endothelium Each of those alveoli is enclosed in a network of pulmonary micro-capillaries. This network is so dense that alveoli nearly bathe in a continuous blood flow. These capillaries are also lined by a monoloayer of endothelial cells called the endothelium. The alveolar epithelium and endothelium are back to back on the same extra-cellular matrix: the complete alveolar capillary barrier separating the inhaled air from the blood is about 0.2 to 0.5 μm thick (see Figure 1.5).

1.2.3 Fate of the nanoparticles that reached the lung

a. Encounter with the alveolar capillary barrier

The particles involuntarily inhaled deposit along the respiratory tract depending on their size and mass. The smaller particles, below 100 nm in diameter reach into the alveolar sacs where the they encounter the alveolar capillary barrier.

Reaction with the alveolar surfactant Depending on their physico-chemical properties, these particles might react with the surfactant [5] and form different types of aggregates (see Figure 1.6). Some might be opsonized by the dedicated surfactant immune proteins, SP-A and SP-C. These clusters can either be deposited back to the mucociliary escalator to be discarded in the digestive system, or they can be phagocytized by the pulmonary alveolar macrophages.

Crossing the alveolar capillary barrier The remaining clusters, or surfactant-particle formations will deposit on the alveolar epithelial cells. From there, there are two possible routes of entry: either through the cells (intracellular transport), via endocytic and/or nonendocytic pathways; or between the cells (paracellular transport) if the viability of the epithelial barrier has been compromised. Depending on the type of particle, all of these outcomes are possible, and currently, we fail to be able to predict which will occur. For this reason, there is a need to gain knowledge on translocation and toxicity analyses on the alveolar barrier, to predict the fate of inhaled nano-particles and anticipate their effect on the human body.

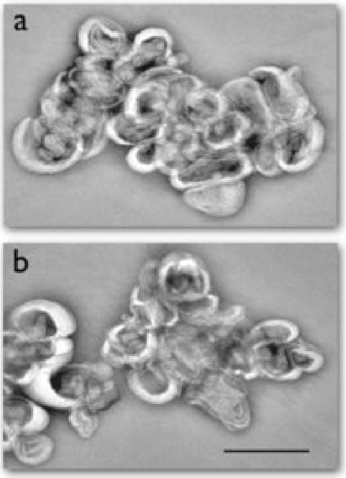

Figure 1.6: Transmission electron microscopy image of the aggregation of surfactant and alumina particles *Scale bar: 200 nm. Mousseau et al, 2015*

b. Pathological mechanisms

As a multi-tissue organ, the lung is exposed to a great variety of diseases. These conditions can either be triggered by external factors such as pollution, allergic pathogens or cigarette smoke, or they can arise from a dysfunction of any of the multiple cells and tissues present in the lung. We are interested here in the pathologies associated with air pollution exposure, and their mechanisms.

Nanoparticles generate oxydative stress Important toxicity of nanoparticles in the lung was observed and could be linked to an important production of reactive oxygen specifces (ROS) as well as oxidative stress [23]. Research later showed that particle exposure could lead to pro-inflammatory signaling ([24], [25]). These responses were particle and dose-dependent, but in the worst case scenario, researchers would observe prolonged or excessive ROS generation leading to cell death. Moreover, oxidative stress is known to play an important role in inflammation- based chronic degenerative diseases such as pulmonary fibrosis or cancer in the case of the lung. These mechanisms are the primary responses of the human lungs to nanoparticle exposure. Depending on the duration and frequency of the particle exposure, the development that follows might trigger different sorts of diseases.

Associated diseases Nanoparticles are affecting the lungs in three manners: cellular stress, local inflammation or indirect tissue weakening. For example, the airway and the alveolar epithelia are very sensible to stress. High stress leading to cell death can result in a leakage of the epithelium (emphysema) or the endothelium (pulmonary edema).

Moreover, the airway and the alveoli are thin structures, sensible to many inflammation-based pathologies such as Chronic Bronchitis, Pneumoconiosis, Acute Respiratory Distress Syndrome or Asthma. Asthma is one of the most common lung diseases, as it affects 385 million people (for 397 000 deaths) each year [26]. It is a long-term condition with sudden crisis which can lead to death by asphyxia. There is no cure for asthma, only a life-long treatment to reduce day-to-day symptoms.

Finally, some lung diseases are not directly caused by particles, but the weakening of the lungs due to particle exposure greatly influence the chances of survival. For example, bacterial inflammations such as COPD (Chronic Obstructive Pulmonary Disease) and pneumonia are also quite frequent disorders, with respectively 174.5 millions affected (3.2 millions deaths) and 450 millions affected (4 millions deaths) each year [26]. Any type of lung cancer will also be worsened by particle exposure. According to the National Cancer Institute (*Surveillance, Epidemiology and End Results Program, 2015*), it affected 3.3 million people in 2015, with a five-year survival rate of 17.4% in the US. If most cases of lung cancer occur on long-term smokers, it is unsettling to realize that 10 to 15% happen to non-smokers, generally sickened by chemicals or urban pollution.

Conclusion We have a better understanding of the fate of inhaled particles: how they enter the lung and interact with its different structures, how they impact the cellular tissues, and what are the possible outcome.

All of these diseases are either life-long conditions or potentially lethal. This underlines the urge to come up with a solution to air pollution: could we stop it or do we have to be thinking about designing a medical treatment for nanoparticle exposure ?

1.2.4 The contribution of science

Faced with this dramatic ascertainment that not only does pollution alter all humans on Earth, but that it is becoming the major threat over human life, we cannot help but wonder what can science do to help ?

a. Upstream action against air pollution: an impossible challenge ?

A first contribution of science resides in prevention: reducing the emissions of air pollution is the most direct way to contain pollution-associated lung diseases.

A solution: pollution-free energies In the past decades, awareness on the soon-ending fossil energy resources has triggered an interest in renewable or, even better, sustainable energy sources. Projects all over the world have developed machines powered by wind (wind turbines, as in Figure 1.7), hydraulic power (dams, hydro-turbines, wave or tide-based turbines), solar power (photo-voltaic systems), geothermal energy or biomass-based energies. However these machines receive intermittent input submitted to the laws of nature. This greatly hinders the development of sustainable technologies, dependent on improvements in energy storage and energy efficiency.

Figure 1.7: Wind turbines in Rio Vista, California. (National Geographic Photography Award)
Courtesy of: Aya Okawa, 2017

Reality check: who can really change the game ? As good as they may be, green energies will take time to develop, and current trends need to be changed. When facing large-scale pollution sources such as industries or power generation infrastructures, the possibility for personal contribution seems slight. Leading causes of air pollution are motor vehicle emissions, agriculture (pesticides and herbicides), chemical plants, coal-fired power plants, oil refineries, petrochemical plants, nuclear waste disposal activity, incinerators, large livestock farms, metals production factories, plastics factories, and other heavy industry. These major pollution sources can only be controlled by strict environmental policies.
This is were pollution prevention is limited: it is highly dependent on politics, which are in turn relying on economics. This is a vicious circle: implementing strict environmental policies would weakened industries based on polluting technologies, thus destabilizing the economy and raising distress in the population. Few politicians are willing to take that risk. One way out of this circle is education: if the people are demanding an environmental policy, they might put enough pressure on the politicians to see drastic changes.

Hope for the future: education, new initiatives and changing behaviors Indeed, with the emergency of the situation, it is important that people take their survival into their own hands. Contrarily to the general thinking, actions at the individual scale can have a major impact. For example, it was recently shown that meat production is one of the largest sources of greenhouse gases and one of the leading causal factors in the loss of biodiversity because of the important deforestation to create pastures or plant crops to grow animal food. This means that switching to vegan, vegetarian or flexitarian diets can have an important impact on air pollution emission. Indeed, in 2016, Springmann *et al*, published a study revealing that " transitioning toward more plant-based diets that are in line with standard dietary guidelines could reduce global mortality by 6–10% and food-related greenhouse gas emissions by 29–70% compared with a reference scenario in 2050" [27].
Raising awareness on how the individual can play a role in protecting the environment is our best hope in reducing air pollution. But this comes with a shift in education policies; by teaching the new generations how to live while respecting the planet. In modern countries, a shift towards environment-friendly habits is already in place: new generations are reducing their consumption, their use public or green transportation systems, get informed on the products they use, tend to buy local, and encourage sustainable trade. In schools too, kids are sensitized to water saving, waste reducing, recycling or other day to day behaviors.

Conclusion Finally, pollution prevention relies on limiting the emission of air pollutants. However the pollution machinery is an extremely complex mechanism with intertwined politic and economic interests. Change may come with population's rising awareness, but this process can only be slow, whilst millions of people are dying every year of pollution-related diseases. A preventive approach is the key to implement sustainable change for future generations, but with the current state of things it is not sufficient to reduce air pollution to a non-harming level.

b. Downstream action: gaining knowledge and acting

With this conclusion, when faced with the already happening dramatic incidences of air pollution on human health, we understand the urgent need to act. In order to come up with solutions, we first need to understand the mechanisms by which air pollution kills millions. Only with this knowledge could we start to develop protective equipment or medical treatments.

Understanding the mechanisms involved: a need for models Among the various lung diseases that we have presented here, most are not fully understood yet: if we know the causes and the symptoms, we still lack a deeper understanding at the cellular level. This lack of awareness on pathological mechanisms prevents science from designing efficient treatments for those widespread conditions. As the rising pollution issues will only amplify the incidence of lung diseases, there is clearly an urge to understand the complex lung physiology, both for physiological and pathophysiological conditions.
With this comes a immense work on pollution testing, which has already begun. Links between pollutants and diseases were made either by using epidemiology records, or by direct testing on animals or cell cultures. Such analyses are extremely complex, because we have seen that each pollutant can provoke different cellular responses and trigger different pathological pathways depending on its inherent properties. Therefore, researchers would need to test the different air pollutants in order to understand which mechanism they activate and be able to design specific drugs. Depending on the pollutant, targeted drugs could hinder pathological pathways or enhance specific immune reactions.

Current models are limited However, currently, drug development is a costly, long-term process that is still dependent on animal testing. Drug discovery can take up to 20 years with an average of 12 years, and its cost can reach several **billion** dollars [28]. Moreover, the clinical phase success rate is only of 10 to 20% [28], which does only increase the time and money required to complete the development process. When facing urgent problems such as the pollution-related diseases, it is crucial to find ways to optimize that process.
In order to optimize drug discovery processes, pharmacologists need tools. However, the tools at hand are very limited: conventional cell culture does not account for the complex environment and mechanisms in place in a whole tissue. Animal models do account for these features but they do not properly replicate human-specific interactions. These poor models fail to bridge the gap between the lab and the clinical trial phases.
Moreover, the classic cell culture technology has not evolved much since the 19th century, when it was discovered by the English physiologist Sydney Ringer: 2D cells cultured in a dish, topped with specific cell culture medium.

This 2D culture does not reproduce the 3D structure of the organ, nor does it allow for the co-culture of different cells in an organized matrix.

New technologies to the rescue Recent advances in microfabrication techniques enable the development of new culture methods. Indeed, in the beginning of the seventies, novel miniaturization technologies appeared, such as photolithography, sputtering, micro-molding or microprinting. They allowed for the development of MEMS (Micro-Electro-Mechanical Systems), *i.e.* complex micro-machines the size of which is comprised between 200 and 1 μm. These technologies were so advanced and so precise that they allowed for impressive achievements, such as writin two pages of a book on the head of a pin (Thomas Newman, CalTech, 1985) or designing a gear that could fit on the leg of an ant (Karlsruhe Institute of Technology, 1992), which is shown on Figure 1.8.

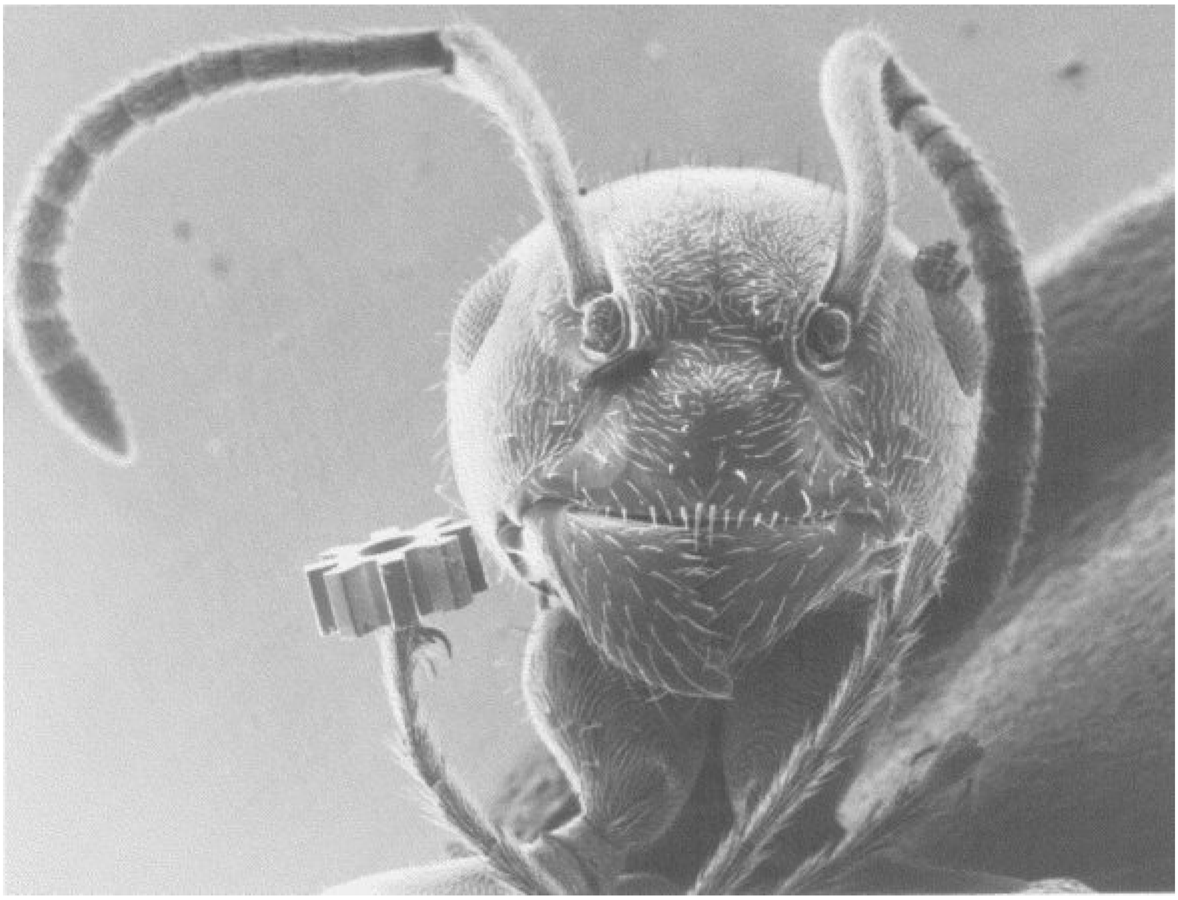

Figure 1.8: Advances in microfabrication technologies: SEM image of an ant holding a gear microfabricated at Karlsruhe Institute of Technology in 1992

A great interest of these technologies is that the micro-world is not submitted to the same physical forces than the macro-world that we know. Indeed, in microfluidics, capillary forces will predominate over gravity, meaning that we can generate passive dynamic systems that do not require energy inputs. Moreover, they allow for the generation of specific micro-architectures, with patterns of sizes that are relevant to cellular biology (down to a few nanometers). In the beginning of the century, these techniques became cheaper and more user-friendly, and were applied to the field of biology by innovative engineers.

1.2.5 Integrating three novel technologies in an *in vitro* model

Building on these new technologies, different methods have been developed, opening the door for multiple fields of research. I will now introduce three modeling technologies that we will use in our project.

a. Micro-engineered scaffolds to mimic the alveolar interstitium

We have underlined the important role of the alveolar interstitium in the global structure of the alveolar capillary barrier. Indeed, not only does this membrane support both cell types, but it is extremely thin (about 0.2 µm) and possess elastic properties as it deforms along with the breathing motion.

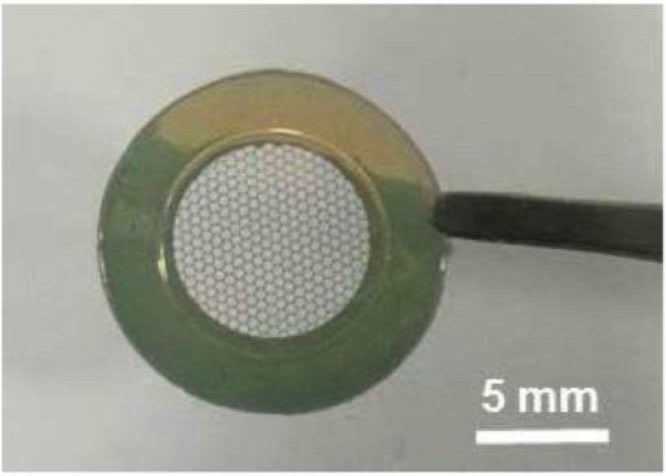

Figure 1.9: The patch: a microengineered substrate for cell culture
Courtesy of Yadong Tang et al, 2015.

Replicating the features of this membrane is the first challenge of our model. In order to do so, we will adapt an existing technology: a microengineered substrate developed in our team by Liu *et al* [8] and Tang *et al* [9]. Briefly this "patch" is constituted of a rigid frame (made with a plastic polymer) supporting a network of gelatin nanofibers (see Figure 1.9). The novelty of this substrate resides in its precision, which allows us to design specific patterns at the size of the *in vivo* alveoli, as well as its composition: the natural ECM bio-polymer that is gelatin.

b. Organs-on-chip to mimic the alveolar dynamic micro-environment

With these new microfabrication techniques, we can also design complex microfluidic chips, that can reproduce a tissue's specific microenvironment. The Organs-on-Chips are microfluidic cell culture devices that recapitualte different features of a tissue's environment, such as its 3D organization, its chemical properties or the dynamic forces exerted on this tissue. These devices proved to produce an accuracy of tissue and organ functionality that was not possible with conventional 2D or 3D culture systems. They are highly accurate *in vitro* models of a fonctional organ tissue ([29], [30]).

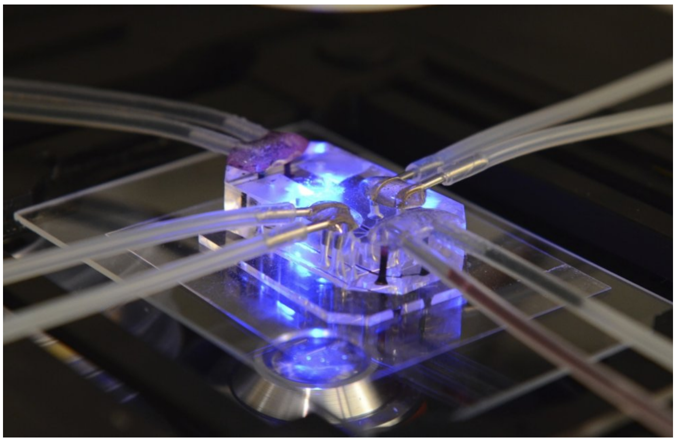

Figure 1.10: Example of a microfluidic Organ-on-a-chip.
Courtesy of the Wyss Institute.

c. iPSC to mimic the complex features of the cells of the alveolar capillary barrier

In 2001, when President George Bush put a hold to embryonic stem cell research with a severe financial restriction ban, it encouraged researchers to investigate alternative sources of stem cells. Indeed, in 2006, Yamanaka's group in Japan obtained an astonishing result: they successfully transformed adult mouse fibroblasts into pluripotent stem cells using specific factors (see Figure 1.11). These were called iPSC and this process is called reprogramming. After a couple of years this reprogramming was successfully implemented for human fibroblasts and human iPSC were born.
iPSC possess all the advantages of embryonic stem cells (ESC), without their major inconvenients. Indeed, they are pluripotent too, hence they can differentiate into any sort of tissue of the human body. Moreover, stem cells have the capacity to renew indefinitely as long as they are maintained in a pluripotent condition. Furthermore, iPSC do not cause ethical concerns related to embryo sourcing and manipulation.

iPSC are a revolution in biology because they allow for the fabrication of models that are not based on cell lines. Indeed, most cell lines are cancerous or genetically modified, which can induce phenotypes that are not observed *in vivo* and therefore biased the *in vitro* model. Moreover, because these cells are "home-made", they can be specifically directed towards a certain phenotype (for example distal lung rather than airway epithelia) or purified to retain only cells exhibiting a specific behavior. They are often preferred to primary cells as experiments can be designed without the issue of lot-to-lot variations.
Finally these cells can be obtained from any living human, therefore using iPSC paves the way towards the generation of personalized or disease-specific *in vitro* models.

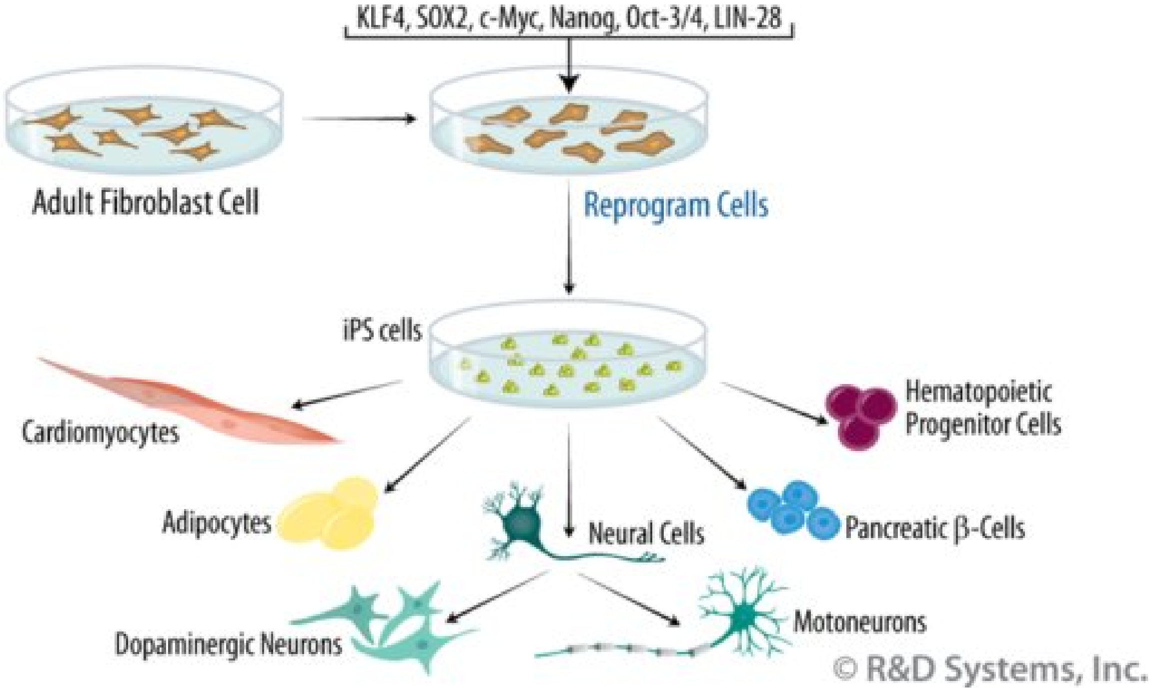

Figure 1.11: Obtained for any donor, iPSC can be reprogrammed to an embryonic state and differentiated into any type of mature tissue, allowing for model personalizing. *R&D Systems.*

We offer here to use these three state-of-the-art techniques to design our *in vitro* model of the alveolar barrier. Enhanced models as this one could help bridge the gap from the lab to the patient during drug development. Moreover, they could become a standard for pollution toxicity testing.

1.3 Conclusion and project objectives

In this first part, we have presented the context that prompts us to launch this research project. We have introduced the global functions of the lung, from its integration in the human body to its cellular organization and functions. Our objective was to give the reader a full comprehension of the intricate mechanisms that define the alveolar barrier from the air inhaled up to the circulating blood, as well as a good knowledge of the different cells of distal airway and alveolar capillary barrier. We pointed out that current preventive actions are not sufficient to reduce air pollution concerns in the immediate future. Therefore we have identified a clear need to prepare protective actions. In order to do so, researchers need to gain knowledge on the interactions of the nanoparticles with the alveolar capillary barrier. We believe in the development of enhanced *in vitro* models that would enable both a deeper understanding of the lung's physiology and the possibility to improve drug development processes to help protecting humans against air pollution.

Our objective is to develop an *in vitro* model combining microfabrication, microfluidic and advanced biology techniques to recreate the micro-environment of the alveolar capillary barrier. We will design this model particularly for translocation assays. This object, that we named the **Alveoli-on-a-chip** (see Figure 1.12), will have multiple applications in fundamental research, toxicity assay or drug screening.

This manuscript consists of three chapters describing our *in vitro* model. We first developed a static model of the alveolar capillary barrier, then integrated this model in a three-dimensional dynamic environment, and finally tried to improve our cellular model by using directed differentiation of induced pluripotent stem cells into an alveolar epithelium and endothelium. This project is at the interface of different domains of physics and biology, therefore each chapter requires a different technical background. That is why each chapter starts with an introductory part that contains a brief summary of the pre-required knowledge, as well as a description of the current state of the art in this domain. Finally, because we started this project from scratch, there was a lot of protocol development and optimization, which are detailed in the Appendix for an easier reading of this manuscript.

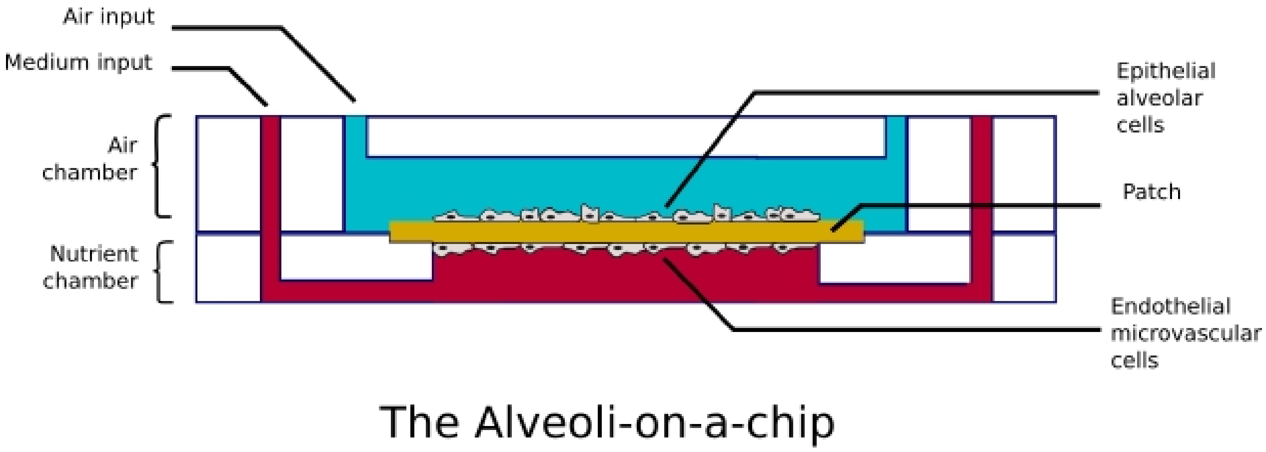

Figure 1.12: Technical principles of our project: **the Alveoli-on-a-chip**, a reversible microfluidic dynamic chip integrating the patch with two chambers for air liquid interface culture, allowing for live confocal observation.

In the first Chapter, we introduce the different models the alveolar barrier in static conditions. We then present our achievement in developing a revolutionary micro-engineered cell-supporting membrane to model the alveolar interstitium. The implementation of the culture of the model and its optimization will be described. We then analyzed the behavior of the model and compared it to *in vivo* observations. Finally, we performed a translocation assay with silica nanoparticles across our alveolar capillary barrier.

The second Chapter introduces the different microfluidic *in vitro* models of the alveolar capillary barrier. We describe the development of our microfluidic chip that can recapitulate the complex *in vivo* micro-environment of the alveolar capillary barrier *in vitro*. We explain the technical features of this microfluidic chip, as well as characterize its mechanical properties. Finally, the impact of this technology on our alveolar capillary barrier model is analyzed.

The third and last Chapter introduces the recent technology that are induced pluripotent stem cells (iPSC). It explains how they are obtained and how they can be used for many different applications. We then explored the possibility of using differentiated iPSC as a more accurate model of human cell in our model. We will present our efforts in obtaining directed differentiation of iPSC into an alveolar epithelium as well as an endothelium.

The final part will summarize the work presented in this manuscript. We will also discuss these results and offer perspectives for improvement or further research.

Chapter 2

Alveolar Capillary Barrier : Static Model - Development and validation of a co-culture model of the alveolar barrier

2.1 Introduction

In this first chapter, we present the static version of our alveolar model. We have seen previously that there is an urge to make progress in research concerning the different types of pollution and their possible impact on a human lung. However, *in vivo* experiments are only possible on animal models and these often fail to accurately predict the specific reactions of the human body. Moreover, they do not allow for a precise understanding of the mechanisms involved at the cellular level. In order to deeply comprehend the response of the alveolar capillary barrier when encountering pollution particles, researchers need to work on models.

We will first detail the different features of the alveolar barrier, as well as its different roles in the human body. We will then present the different cell models currently available to reproduce an alveolar capillary barrier *in vitro*. Finally, we will introduce the different static models of the alveolar capillary barrier that can be found in the literature.
We will then introduce our micro-engineered cell culture substrate: its design and optimization for a highly precise manufacturing. Then we will present the co-culture technique that we optimized to obtain an advanced *in vitro* model replicating the functions of the alveolar barrier. Finally, we will explain how we used this model to perform assess the impact of silica nanoparticles on the alveolar capillary barrier.

2.2 Modeling the alveolar barrier

2.2.1 The alveolar barrier: histology and immune functions

We have seen previously that the alveolar barrier is composed of an endothelium and an alveolar epithelium, back to back on a thin membrane. Each cell type in this structure plays a specific role, that we will detail here.

a. Alveolar Type I cells (AET I)

Cell morphology Type I are squamous epithelial cells that make up most of the alveolar wall surface. Although they represent about 10 to 35% of the alveolar cells, they cover about 95% of the alveolar surface (see Figure 2.1). Type I cells are extremely flat cells, mostly invisible under a microscope, excepted in the nuclear region. The type I cell contains an endoplasmic reticulum, a Golgi apparatus, mitochondria and lysosomes in the perinuclear region. Type I cells are responsible for particle translocation, gas exchange and local homeostasis.

Cellular functions The AET I epithelium stands on the sceptum (or alveolar wall), a type of chorion which serves as a basement membrane of the alveoli. Their cytoplasm can be as thin as 0.1 to 0.2 μm. They are complex branched cells with multiple cytoplasmic plates. They can have up to ten plates, making it impossible for them to divide: they can only be replaced by differentiation of type II cells. The endothelial cells of the pulmonar micro-capillaries are in close contact with the AET I, as their basal laminae fuse with the interstitium, forming a extremely thin barrier: about 0.2 to 0.5 μm ([31], [22]). Being so flat, the AET I cells are designed for passive diffusion (see Figure 2.1).

Whereas endothelial junctions (maculi adherentes) are known to be leaky, the alveolar epithelial junctions are highly selective. Indeed the AET I form tight junctions (zonuli occludentes) without gaps. However, some particles (such as albumin and globulin) are known to cross this epithelium, suggestive that the AET I can perform selective translocation by slow transport.

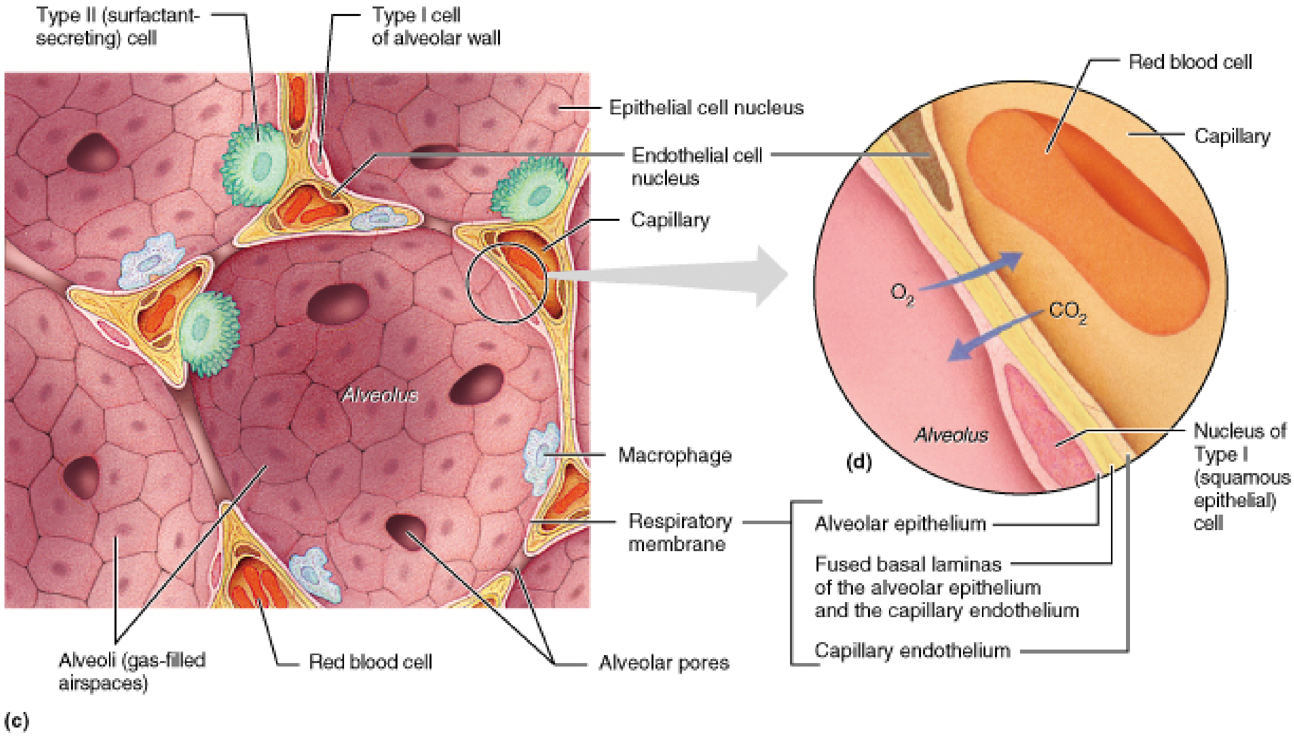

Figure 2.1: Histology of the alveolar capillary barrier. The alveolar walls are lined by alveolar cells of Type I and Type II, and contain alveolar macrophages. They are responsible for gas exchange as well as particle and nutrient transport across the interstitium and through the endothelium of the capillaries.

b. Alveolar Type II cells

Cell morphology The cuboidal AET II cells form clusters generally localized at the corners of the alveolus, a position inducing a high distortion during inflation: this is a stimuli for surfactant release. They cover only 2 to 5% of the alveolar surface, but play a crucial role in its immune defense (see Figure 2.1). Their most characteristics features are their microvilli around their apex and their abundant lamellar bodies in the cytoplasm.

Cellular functions AET II produce the surfactant, a viscous liquid that lines the alveoli. It is mostly composed of phospholipids (mainly DDPC, Dipalmitoylphosphatidylcholine) and four main proteins called surfactant proteins A, B, C and D (also named SP-A or SFTPA, SP-B or SFTPB, etc...). The surfactant is synthesised by the AET II cells and released upon appropriate stimuli by exocytosis from an intracellular storage organelle (the lamellar bodies). These bodies are a group of lipids and protein. The lipids of the lamellar body structure are arranged by the SP-B protein. Basically, SP-B plays a role in the organogenesis (formation of structure) of lamellar bodies. These lamellar bodies are then secreted into the fluid lining the interior of alveoli, and release the tubular myelin. This myelin associates in a meshwork that forms the surfactant.

Alveolar surfactant has a half life of 5 to 10 hours once secreted. It can be both broken down by macrophages and/or reabsorbed into the lamellar structures of type II pneumocytes. Up to 90% of surfactant is recycled from the alveolar space back into the type II pneumocyte. The other 10% is taken up by alveolar macrophages and digested.

The AET II have an almost unlimited potential to proliferate. They renew continuously, creating a great progeny for the tissue. These cells either replace injured or dead epithelial cells by differentiating into AET

I cells, or are regulated by apoptosis. They are responsible for the conservation and repair of the alveolar epithelium [32].

c. Alveolar defense systems: the surfactant and the pulmonary macrophages

The surfactant secreted by AET II is a key feature of the alveolar capillary barrier, and not only for its immune functions. It plays

Surface tension regulation The surface tension at the border between the surfactant and the inhaled gas (air-liquid interface or ALI) in an alveolus determines the motion of the alveolus as a whole. Lipid arrangement in the surfactant is the primary determining factor of this surface tension since the lipids form a thin film (monolayer) on the surface of the surfactant at the ALI. Different lipids will allow for different ranges of motion, as they can be arranged differently.

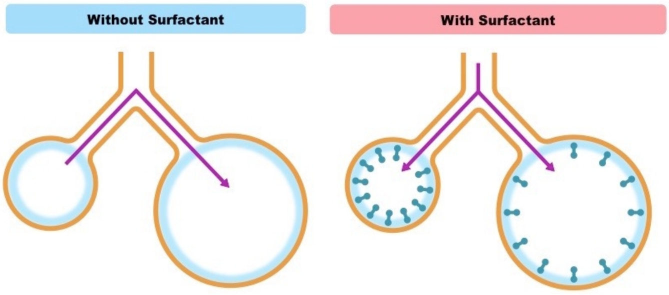

Figure 2.2: Importance of the surfactant in alveolar inflation: by reducing the surface tension of the alveolar walls, it allows for a pressure equilibrium within both small and large alveoli.

Indeed, the Laplace law states that surface tension is inversely proportional to the radius of the bubble. Therefore, the surface tension of the walls of small alveoli is greater than that of the walls of large alveoli, which means that the small alveoli should deflate in the larger ones (see Figure 2.2 Top). This is the main role of the surfactant: allowing for alveolar inflation by minimizing the surface tension at the ALI (see Figure 2.2 Bottom).

Surfactant protein functions The four-surfactant proteins are highly interconnected in their functions in surfactant. For example, though the mechanism is not yet understood, SP-B functions in the post-translational modification of SP-C, and mature SP-C is not formed without SP-B. SP-C assists in the functions of SP-B, and is the most similar to SP-B of the two other surfactant proteins. However, each of these proteins has a specific role.

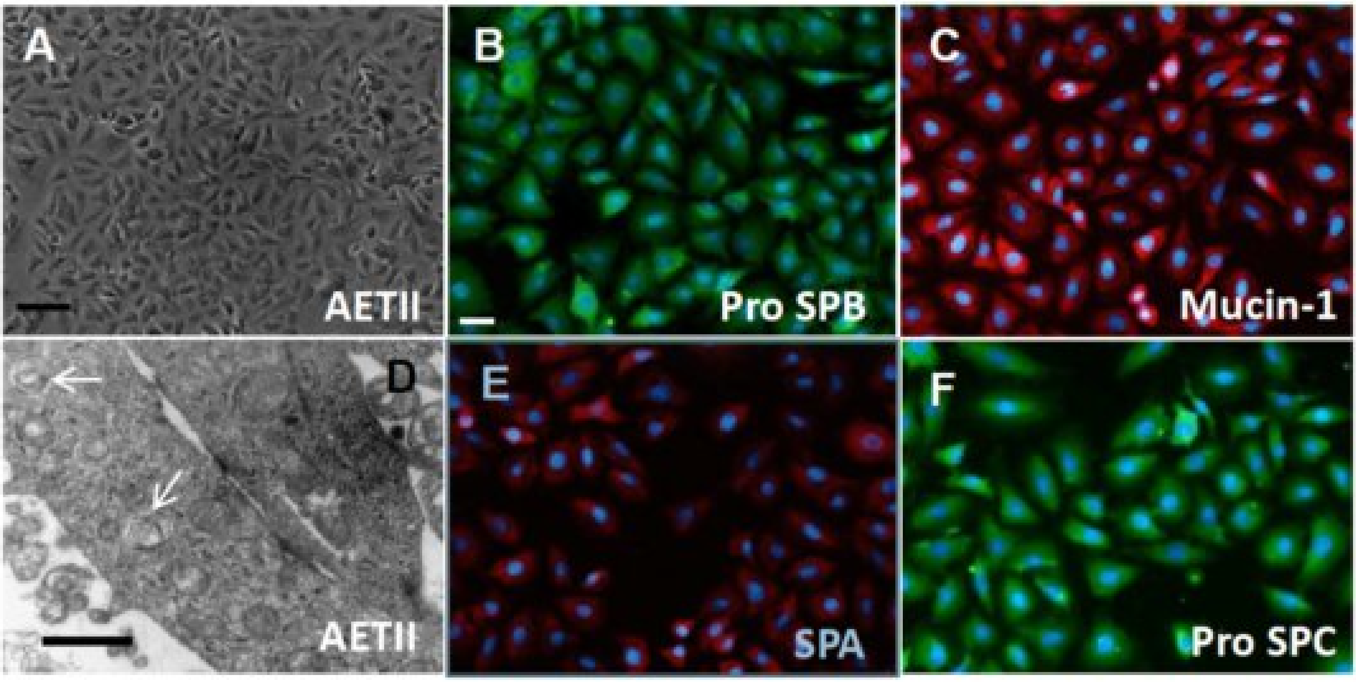

Figure 2.3: Immunostaining examples of several alveolar markers, on C2 iPSC lines differentiated towards distal lung cells *(Ghaedi et al. [33])*.**(A)** Phase-contrast images AET II cells. Immunofluorescent staining of alveolar type II markers; **(B)** pro-SP-B, **(C)** Mucin-1, **(E)** SP-A, **(F)** pro SP-C Scale bar, 63 μm.**(D)** Transmission electron microscopy: AET II containing characteristic cytoplasmic laminar bodies (scale bar, 1 μm).

SP-A and SP-D are collectins Surfactant protein A is an innate immune system collectin. It is water-soluble and has collagen-like domains similar to SP-D. It is part of the innate immune system and is used to opsonize bacterial cells in the alveoli marking them for phagocytosis by alveolar macrophages. SP-A may also play a role in negative feedback limiting the secretion of pulmonary surfactant. SP-A is not required for pulmonary surfactant to function but does confer immune effects to the organism. Two genes encode SP-A: SP-A1 and SP-A2. SP-A2 is expressed only in airway cells, whereas SP-A1 and SP-A2 are expressed in AET II [34]. SP-A is also present in bronchiolar nonciliated Clara cells, AET II and alveolar macrophages (AM). It has also been observed in other epitheliums (colon, prostate, etc.) ([35], [36], [37], [38]).

Surfactant pulmonary-associated protein D, also known as SFTPD or SP-D, is a protein encoded in humans by the SFTPD gene. It is also an innate immune system collectin. SP-D is present in bronchiolar nonciliated Clara cells and AET II ([35], [36], [37], [38]).

SP-A and SP-D proteins have several functions:

- Aggregation of the microorganisms
- Opsonization and activation of the phagocytosis of microorganisms
- Inhibition of microbial growth
- Modulation of inflammatory responses
- Modulation of the adaptive immune system
- Inhibition of allergic response
- Activation of the clearance of apoptotic cells by macrophages.

SP-B Pulmonary surfactant-associated protein B is a protein that in humans is encoded by the SFTPB gene. Surfactant protein B is an essential lipid-associated protein found in lung surfactant, hence SP-B is highly hydrophobic. Without it, the lung would not be able to inflate after a deep breath out. It rearranges lipid molecules in the fluid lining the lung so that the alveoli, can more easily inflate due to an optimized surface tension ([35], [36], [37], [38]).

SP-B is the mature form of a large precursor protein called proSP-B. Synthesized in the endoplasmic reticulum of type II pneumocytes, proSP-B is cut down to the size of mature SP-B in the Golgi apparatus through post-translational modification. ProSP-B is also created in another type of lung cell called a Club cell, but these cells are unable to edit proSP-B into SP-B. This is why SP-B is a specific marker of alveolar type II cells. ProSP-B is found in the endoplasmic reticulum, Golgi complex and lamellar bodies whereas the mature SP-B can only be found in the lamellar bodies ([35], [36], [37], [38]).

SP-B has several functions:

- Indirect surface tension reduction via lipid selection
- Direct surface tension reduction
- Formation of lamellar bodies

SP-C Surfactant proteins C are a family of related pulmonary surfactant proteins. It is smaller, and is found embedded in lipid structures much like SP-B (see Figure 2.3). SP-C is specific to AET II cells in the whole body [37].

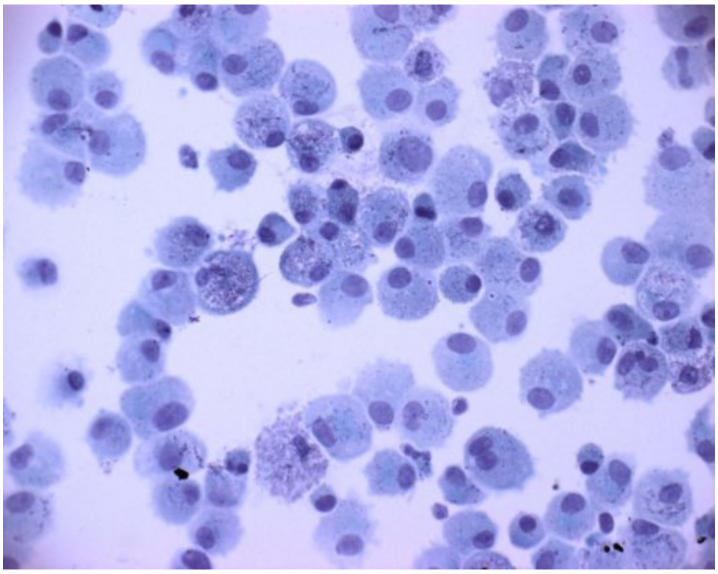

Figure 2.4: Microscope photography of pulmonary alveolar macrophages, *Hocking,et al, 1979*

The pulmonary macrophages The pulmonary alveolar macrophage (PAM) is a component cell of the mononuclear phagocytic system (see Figure 2.4). The PAM is resident within the alveolus, where it lies within the alveolar lumen on the alveolar epithelium, coated with alveolar fluid. The cell therefore occupies a relatively unique position within the body, being exposed directly to a relatively hyperoxic environment, and in intimate contact with airborne and blood-borne materials. The macrophages have three main functions: clearance by migration or phagocytosis; modulation of the immune system (using lymphokines); and modulation of the surrounding tissue (including by direct cytotoxicity) [39].

d. Endothelial cells

The pulmonar circulatory system is a complex network of microcapillaries that densely irrigates the lungs, performing a nutritive role for lung cells, as well as an important area for gas and particle exchange with the blood. These capillaries are lined with a monolayer of endothelial cells, which complete many functions. Endothelial cells are squamous cells, involved in many aspects of vascular biology. These cells act as a semi-selective barrier between the vessel lumen and surrounding tissue, controlling the passage of materials and the transit of white blood cells into and out of the bloodstream.

Passive functions Endothelial cell structure and functional integrity are important in the maintenance of the vessel wall and circulatory function. As a barrier, the endothelium is semi-permeable and controls the transfer of small and large molecules.

Active functions The vascular endothelium is versatile and multifunctional having many synthetic and metabolic properties. These cells exert significant paracrine and endocrine actions through their influence on the underlying smooth muscle cells or on circulating blood elements, such as platelets and white blood cells [40]. They also regulate thrombosis and thrombolysis, modulation of vascular tone and blood flow, and regulation of immune and inflammatory responses by controlling leukocyte, monocyte and lymphocyte interactions with the vessel wall [40]. It also modulates the vasoconstriction and vasodilatation of the capillaries, hence the control of blood pressure.

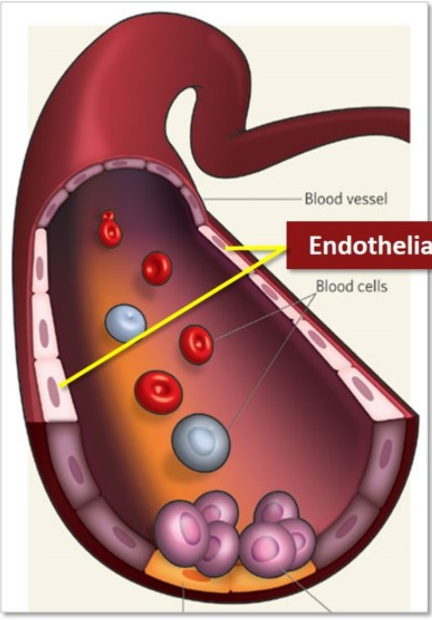

Figure 2.5: Endothelial cells in a capillary. *cellapplications.com*

2.2.2 Modeling the human body with cell biology: cellular models

Now that we have a deeper knowledge of the multiple cellular phenotypes observed in the alveolar capillary barrier, we can look into how we wish to model them. Indeed, in making *in vitro* models, the researchers need to choose the cells that best model the tissue that they are interested in. The first choice to make is deciding between using primary cells or immortalized cell lines.

Primary cells Primary cells are cells that were extracted from a live patient and isolated for cell cultures. They have a finite life span, that varies according to the cell type. Except for the enzymatic and/or physical dissociation required for extracting the cells from their tissue of origin, they are not altered in any way. They can present diverse phenotypes as they can come from a variety of people. Having a variety of primary cell types from many different donors is especially useful when carrying out early drug testing, but can be confusing if our aim is to understand a specific physiology. Primary cells can change and differentiate in culture; therefore experiments should be carried out only on earlier passages.

Immortalized cell lines The other opportunity to study cellular biology is to use immortalized cell lines. They are cells that would normally not proliferate indefinitely but, due to a mutation (natural or intentionally induced), has evaded normal cellular senescence and instead can keep undergoing division. These cells can therefore be grown for prolonged periods *in vitro*. However, immortalized cell lines often demonstrate phenotypes that they would not show *in vivo*.

I will present the different models that are available to model the alveolar epithelium and endothelium. This will allow to explain which model we chose and why, as well as define the different models are found in the review of the literature presented at the end of this section.

a. Alveolar epithelial cells models

Primary cells Primary alveolar cells, usually referenced to as **hAECS** or **pHAECs** (primary human alveolar epithelial cells) are the most representative of *in vivo* tissue behavior. Several research groups harvest and isolate the cells themselves from non-tumor lung tissue, usually obtained from patients undergoing a lung lobectomy. Obtaining cells directly from patients seems ideal but it actually requires a very complex know-how and specific technique.

Immortalized cell lines Another solution is to use cell lines to model the alveolar epithelium, such as:

- **A549**, adenocarcinomic human alveolar basal epithelial cells as a model of AET II cells [41];
- **NCI-H441**, isolated from the pericardial fluid of a patient with papillary adenocarcinoma of the lung,
- **16HBE14o-**, human bronchial epithelial cells isolated from a 1-year old male heart-lung patient,
- **Calu-3**, adenocarcinomic human bronchial epithelial cells.

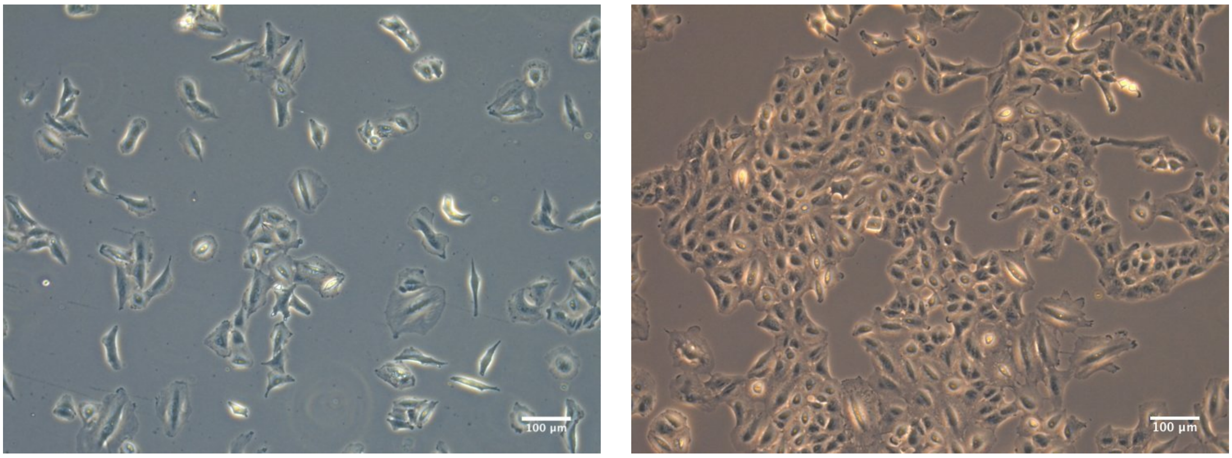

(a) A549 cell line in DMEM. *Scale bar: 100* µm

(b) Confluent A549 cells in DMEM. *Scale bar: 100* µm

Each of these cell lines have different specifities. In our effort to model the alveolar epithelium **16HBE14o-** and **Calu-3** were not be considered, as they are known to exhibit characteristics of bronchiolar pulmonary epithelium cells. In particular, the **NCI-H441** were considered as a model of the alveolar epithelium because they express surfactant protein and generate a tight epithelium but were reported to express a Clara-like phenotype [42]. A549 on the other hand, express a phenotype closer to AET II cells (or even AET I after normal [43] or induced [44] maturation). A549 were also reported to form weak junctions, and therefore are said to be a poor epithelium model ([34], [45]). However, recent studies showed that it can be improved by culturing cells with a glucocorticoid supplement, such as Dexamethasone ([46], [47], [44]). Because A549 cells are easy-to-handle and well characterized cells, it was decided that I should use them as our alveolar epithelium model.

b. Other cells of the alveolar environment

Endothelial cells models A first upgrade of alveolar models is the inclusion of endothelial cells. Indeed, they form the secondary element of the alveolar capillary barrier. Most common endothelial cell lines are:

- **SK-HEP-1**, human liver adenocarcinoma endothelial cells;
- **HUVEC**, human umbilical vein endothelial cells;
- **HMEC-1**, human dermal endothelial cells transfected with pSVT vector;
- **HULEC-5a**, human lung microvascular endothelial cells transfected with pSVT vector;
- **EA.hy 926**, a human umbilical vein cell line, established by fusing primary human umbilical vein cells with a thioguanine-resistant clone of A549

Cells models can also be primary cells, extracted from donor tissue, such as **HPMEC**, human pulmonary microvascular endothelial cells or **HMVEC-L**, human lung microvascular endothelial cells.

As for the choice of our epithelial model, donor-extracted cells were not retained due to budget reasons. We decided to use HUVEC cells, which are not cancerous nor were transfected, and were extensively characterized in the literature.

Other cells Several research groups improved their alveolar models with the addition of several types of cells such as dendritic cells [48], pulmonary macrophages [49], or mast cells [50] in culture. We have seen that these cells play different roles in the alveolar space, especially regarding immune functions, and it is an interesting challenge to study their influence on the alveolar barrier.

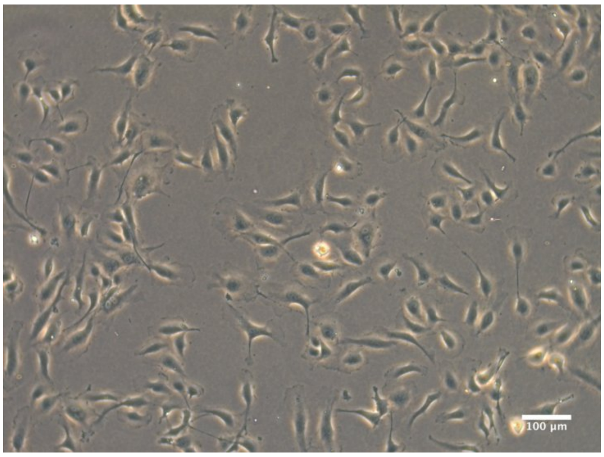

(a) HUVEC in ECGM. *Scale bar: 100 µm*

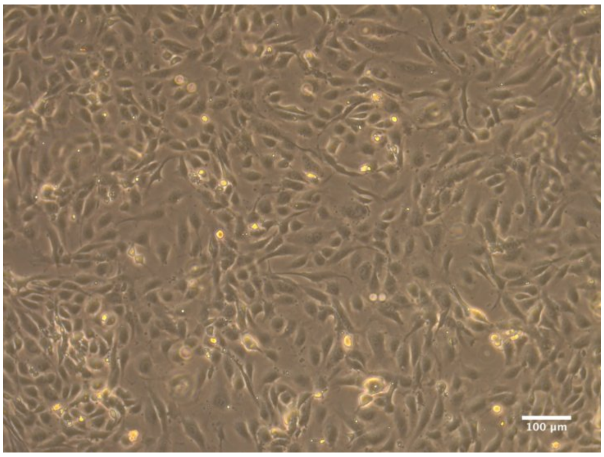

(b) Confluent HUVEC in ECGM. *Scale bar: 100 µm*

2.2.3 A review of current Alveolar Barrier models

In this section, I will present several models of the alveolar capillary barrier. This review is stricly restricted to human alveolar models (bronchial epitheliums are not included), and presents an overview of different static models, as well as the different methods used to characterize them.

a. Different designs

Cells In the literature, we can find different models of the alveolar capillary barrier with either one cell type ([51], [52], [42]), or a combination of an epithelium and an endothelium cultured onto a speficic insert ([34], [53], [54], [55]). A549 are the more popular epithelial model, followed by NCI-H441 cells. Regarding the endothelial type, HPMEC were often chosen.
Finally, there are also models with several other cells in addition, such as alveolar macrophages ([49], [50], [48], [56], [57]), dendritic cells ([48], [56]) or mast cells ([49], [50]). These are especially important for particle exposure as the alveolar macrophages may absorb an important quantity of these pathogens before they even reach the alveolar barrier. The addition of these cells is a significant step towards reproducing accurate *in vivo* conditions but it also introduces more complexity in the design and the culture of the model.

Surfactant Another addition to these models is the use of surfactant. As I did not integrate surfactant in my model, I decided not to review all the different methods used to model the surfactant. Quickly, it can be modeled by an addition of either exogenous models (drugs like AlveoFact [55] or Curosurf [5] or synthetic models (DDPC, DDPC with proteins, etc..). Studying the role of surfactant is extremely interesting, especially when looking at particle transport, because it can modify the external surface of the particles before they access the alveolar cells. The recent work of Fanny Mousseau [5] underlined the role of surfactant in particle interaction with the alveolar epithelium.

Culture substrates As can be seen in the review (Figure 2.8), the use of Transwell inserts is a popular method for cellular co-culture. They provide a robust and user-friendly co-culture method, but are limited by the thickness of their membranes. Indeed, these PET (polyethylene terephthalate) or polycarbonate membranes are offered with different pore sizes (from 0.4 to 8 μm), but they are all 10 μm thick, which is 50 times higher than the estimated *in vivo* distance between the alveolar epithelium and the endothelium.
In order to improve this specific aspect of the model, several groups have worked on developing adequate micro-engineered substrates. These can be produced with pierced polymer thin sheets such as PDMS [58] or PET [59], or with electrospun polymers such as PCL [60] or PLGA [61]. However, these complex substrates are usually included in a much complex microfluidic environment, (the *Organs-on-chip*), and therefore are not included in this static review. They will be presented in the introduction of the next chapter.

b. Characterization and validation

In order to be used for research or drug development, an *in vitro* model should validated, meaning that their accuracy should be demonstrated. For the alveolar capillary barrier, the usual features analyzed are:

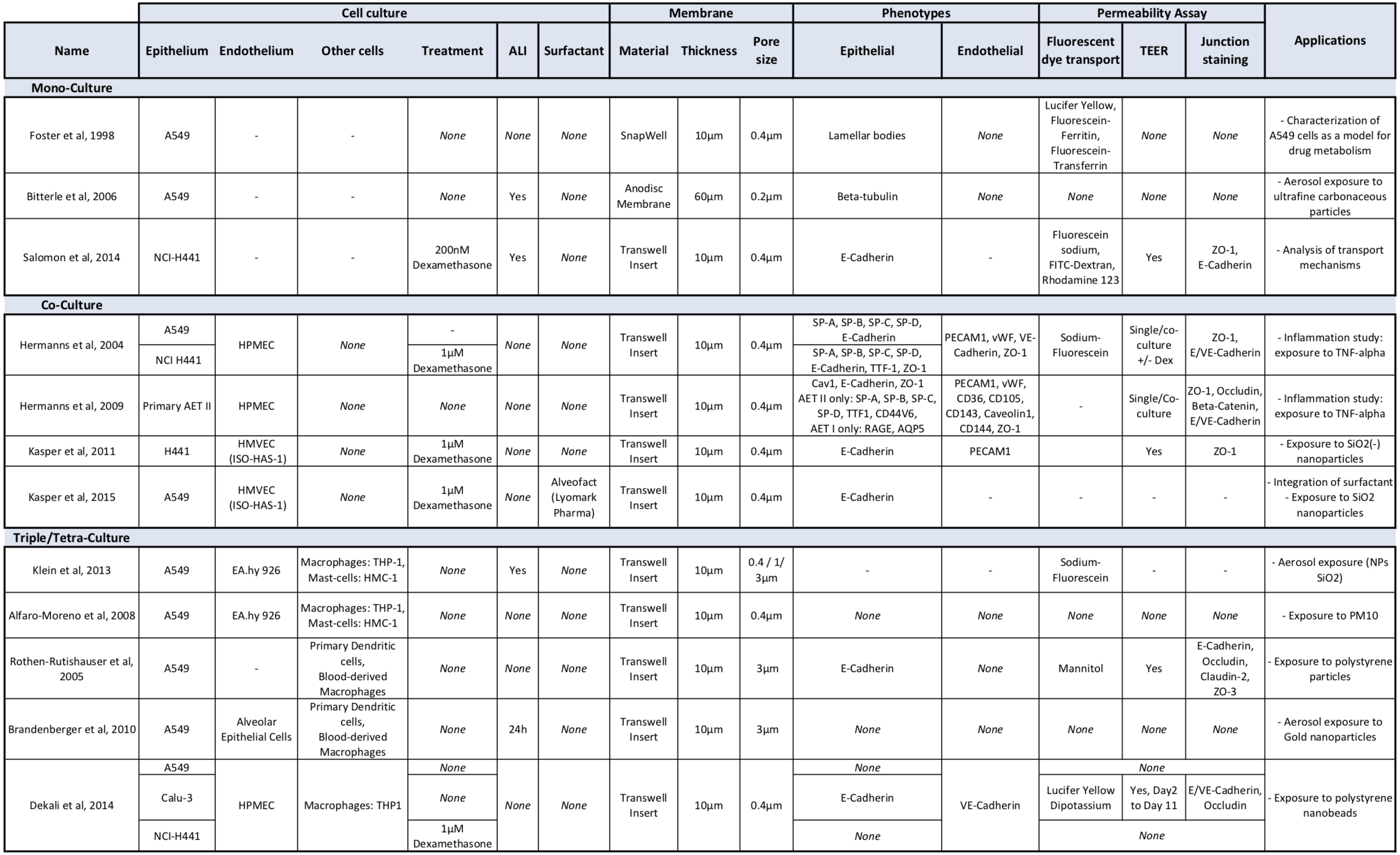

	Cell culture						Membrane			Phenotypes		Permeability Assay			
Name	**Epithelium**	**Endothelium**	**Other cells**	**Treatment**	**ALI**	**Surfactant**	**Material**	**Thickness**	**Pore size**	**Epithelial**	**Endothelial**	**Fluorescent dye transport**	**TEER**	**Junction staining**	**Applications**
Mono-Culture															
Foster et al, 1998	A549	-	-	*None*	*None*	*None*	SnapWell	10µm	0.4µm	Lamellar bodies	*None*	Lucifer Yellow, Fluorescein-Ferritin, Fluorescein-Transferrin	*None*	*None*	- Characterization of A549 cells as a model for drug metabolism
Bitterle et al, 2006	A549	-	-	*None*	Yes	*None*	Anodisc Membrane	60µm	0.2µm	Beta-tubulin	*None*	*None*	*None*	*None*	- Aerosol exposure to ultrafine carbonaceous particles
Salomon et al, 2014	NCI-H441	-	-	200nM Dexamethasone	Yes	*None*	Transwell Insert	10µm	0.4µm	E-Cadherin	-	Fluorescein sodium, FITC-Dextran, Rhodamine 123	Yes	ZO-1, E-Cadherin	- Analysis of transport mechanisms
Co-Culture															
Hermanns et al, 2004	A549	HPMEC	*None*	-	*None*	*None*	Transwell Insert	10µm	0.4µm	SP-A, SP-B, SP-C, SP-D, E-Cadherin	PECAM1, vWF, VE-Cadherin, ZO-1	Sodium-Fluorescein	Single/co-culture +/- Dex	ZO-1, E/VE-Cadherin	- Inflammation study: exposure to TNF-alpha
	NCI H441			1µM Dexamethasone						SP-A, SP-B, SP-C, SP-D, E-Cadherin, TTF-1, ZO-1					
Hermanns et al, 2009	Primary AET II	HPMEC	*None*	*None*	*None*	*None*	Transwell Insert	10µm	0.4µm	Cav1, E-Cadherin, ZO-1 AET II only: SP-A, SP-B, SP-C, SP-D, TTF1, CD44V6, AET I only: RAGE, AQP5	PECAM1, vWF, CD36, CD105, CD143, Caveolin1, CD144, ZO-1	-	Single/Co-culture	ZO-1, Occludin, Beta-Catenin, E/VE-Cadherin	- Inflammation study: exposure to TNF-alpha
Kasper et al, 2011	H441	HMVEC (ISO-HAS-1)	*None*	1µM Dexamethasone	*None*	*None*	Transwell Insert	10µm	0.4µm	E-Cadherin	PECAM1		Yes	ZO-1	- Exposure to SiO2(-) nanoparticles
Kasper et al, 2015	A549	HMVEC (ISO-HAS-1)	*None*	1µM Dexamethasone	*None*	Alveofact (Lyomark Pharma)	Transwell Insert	10µm	0.4µm	E-Cadherin	-	-	-	-	- Integration of surfactant - Exposure to SiO2 nanoparticles
Triple/Tetra-Culture															
Klein et al, 2013	A549	EA.hy 926	Macrophages: THP-1, Mast-cells: HMC-1	*None*	Yes	*None*	Transwell Insert	10µm	0.4 / 1/ 3µm	-	-	Sodium-Fluorescein	-	-	- Aerosol exposure (NPs SiO2)
Alfaro-Moreno et al, 2008	A549	EA.hy 926	Macrophages: THP-1, Mast-cells: HMC-1	*None*	*None*	*None*	Transwell Insert	10µm	0.4µm	*None*	*None*	*None*	*None*	*None*	- Exposure to PM10
Rothen-Rutishauser et al, 2005	A549	-	Primary Dendritic cells, Blood-derived Macrophages	*None*	*None*	*None*	Transwell Insert	10µm	3µm	E-Cadherin	*None*	Mannitol	Yes	E-Cadherin, Occludin, Claudin-2, ZO-3	- Exposure to polystyrene particles
Brandenberger et al, 2010	A549	Alveolar Epithelial Cells	Primary Dendritic cells, Blood-derived Macrophages	*None*	24h	*None*	Transwell Insert	10µm	3µm	*None*	*None*	*None*	*None*	*None*	- Aerosol exposure to Gold nanoparticles
Dekali et al, 2014	A549	HPMEC	Macrophages: THP1	*None*	*None*	*None*	Transwell Insert	10µm	0.4µm	*None*	VE-Cadherin	*None*			- Exposure to polystyrene nanobeads
	Calu-3			*None*						E-Cadherin		Lucifer Yellow Dipotassium	Yes, Day2 to Day 11	E/VE-Cadherin, Occludin	
	NCI-H441			1µM Dexamethasone						*None*		*None*			

Figure 2.8: Review of current static models of the alveolar capillary barrier

its capacity to form a tight barrier with selective permeability, as well as the expression of different *in vivo* phenotypes.

Barrier permeability assay A widely-used method to accurately estimate the permeability of a tissue is to use a chemical compound labeled with a tracer that is not carried by a healthy cell monolayer and follow its transport across our cell layers. These compounds are usually very small molecules (about 1-10 Å), that do not enter the cellular cytoplasm and can only cross the epithelium through intercellular space in between the cells (paracellular transport). These molecules are usually Dextrans, Albumin, Inulin, Sodium, Isothiocyanate or others, coupled with fluorophores such as Texas Red, FITC, Evans Blue, etc. This technique is quite straightforward: the tracer is placed in the apical chamber, and after a determined incubation period, it is sampled from the basal chamber and observed with a fluorescent plate reader. This technique was used by a majority of the papers listed in the review (see Figure 2.8).

Epithelium integrity and TEER measurement Another gold standard method is the measurement of Trans-Epithelial Electric Resistance (TEER) with electrodes [62]. It is a valuable non invasive technique that can be applied to quantify the integrity of the cells. The electrodes can also be integrated in micro-engineered susbtrate, which allows for direct *in situ* measurement. However, this technique requires an important system reproducibility because the probes need to be placed at exactly the same positions between two measurements, therefore it not often used in complex micro-engineered substrates.

Fluorescent staining Finally, fluorescent staining of certain proteins allows for the visualization of expressed phenotypes. It can also be used to observe cellular junctions, therefore indicating which type of junctions are formed, where, and their relative level of expression in the cells. For example, the staining of ZO-1 or Claudin proteins allowed to easily observe the induction of tight junctions in Dexamethasone-treated cells ([34], [53]). Immunostaining is also used to characterize the behavior of the cells in the model. Hermanns *et al* ([34], [53]) did an extensive analysis of the alveolar phenotype expression, observing both AET I and AET II specific behavior (such as surfactant production or transport protein expressions). Protein level expression can also be monitored by PCR, RT-PCR or flow cytometry but since these are techniques that we could not use in our lab, I will not elaborate on this subject.

2.2.4 Discussion and conclusion

In order to perform *in vitro* toxicity analyses, researchers have developed various models of the alveolar capillary barrier, each with its own advantages and disadvantages. Most models are based on a specific membrane supporting either a culture or a co-culture of cells. Some enhanced models even account for the influence of surfactant, or the presence of other cell types in the alveolar space. A common issue, however, is the important thickness of the culture membrane used: at least 10 μm thick. This technical detail is the main drawback of such models. Indeed, they do not account for inter-cellular exchanges, which are crucial in recapitulating a tissue-like environment.

2.3 Mimicking the alveolar extracellular membrane

We have seen that the cell-supporting membrane plays a crucial role in the alveolar capillary system. Thus, replicating it will be key in mimicking the alveolar functions. We should try and replicate an interstitium as thin as possible, with pores for intercellular communication, whilst providing a deformable surface. This membrane also needs to be biocompatible and to promote cell growth. Our objective here was to design a membrane thinner than all of those existing in the literature, that would allow for intercellular interactions. In order to design such a membrane, I started with a microfabricated substrate developed in our team by Liu *et al* [8] and Tang *et al* [9]. This substrate is referred to as a ”patch” and I will detail here its main characteristics, as well as the main fabrication steps. I will then present the changes made to this original design and my optimization of the fabrication process. Please note that in this part, all protocols are summarized for improved readablity. They are further detailed in the dedicated section.

2.3.1 Original patch

a. Fabrication process

The patch consists of a solid frame supporting a thin network of gelatin nanofibers (see Figure 2.9). This frame supports the fibers so that they can be easily handled. The fibers provide an extra-thin biocompatible substrate with micro-pores for intercellular interactions.

The rigid frame is made of two layers of PEGDA (PolyEthylene Glycol Di-Acrilate) bonded together. The first layer (50 μm thick) is a grid of honeycombs (internal diameter 500 μm, honeycomb wall size 50 μm) of about 13 mm diameter. The second layer (50 μm thick) consists of a PEGDA ring of 9 mm internal diameter and 13 mm outer diameter. This second layer is used to thicken the global patch for easier handling.

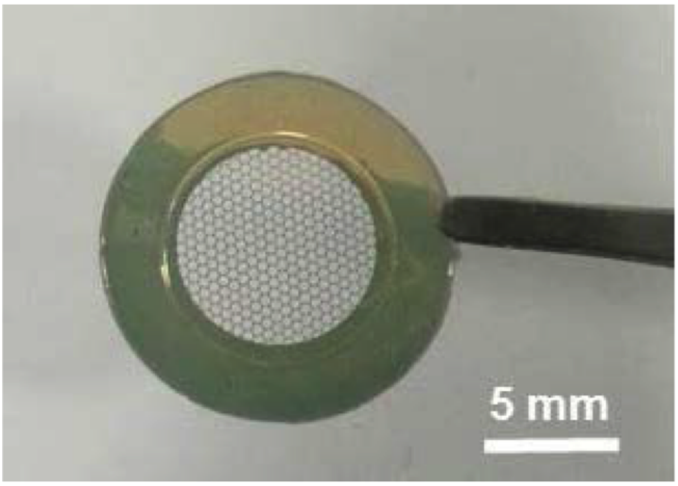

Figure 2.9: Original patch

Both PEGDA layers are obtained through a 4-step process: we first generated a patterned chromium mask and replicated the patterns onto a three-dimensional resin by photolithograpy, then used this wafer to produce PDMS parts by replica molding, and finally these parts were used to pattern the PEGDA via vacuum casting. A final step will be the deposition of the gelatin fiber network and its cross-linking.

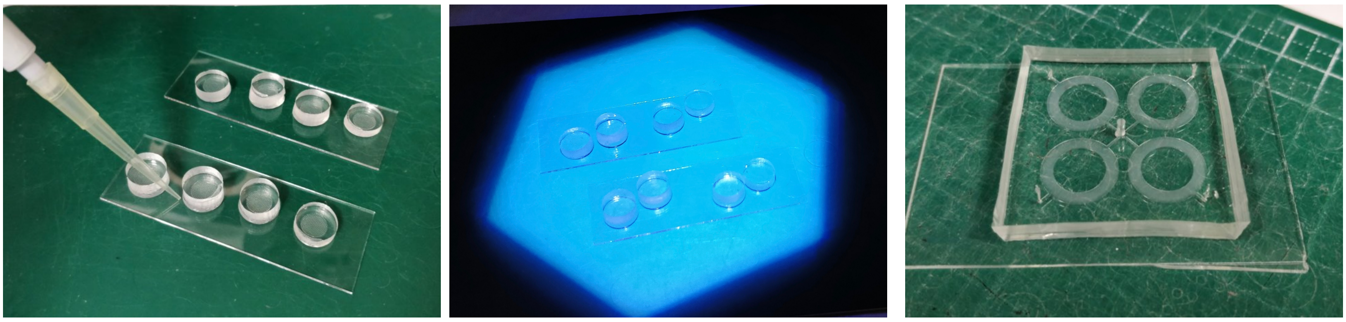

(a) Grid molding (b) UV polymerization (c) Ring molds

Figure 2.10: Pictures of the microfabrication process

Generation of the patterned substrate for PDMS molding Our photolithography mask is obtained by laser-engraving and developing a chromium mask with (μPG 101, Heidelberg Instruments). The photolithography is then carried on a silica wafer with a positive resin (AZ 40 XT). The resin is then pre-baked into a three-step process: 1 minute at 65 °C, 1 minute at 95 °C and 8 minutes to 126 °C. The resin in insolated with UV light for 75 seconds. Post-baking steps are: 30 seconds at 65 °C, 30 seconds at 95 °C and 2 minutes at 105 °C. After cooling down, the non-reticulated resin is washed out with a 3 minutes bath of AZ 726 MIF Developer, and we obtain our pattern in three-dimensions (see Figure 2.11, step 1).

Generation of the PDMS molds The PDMS reagents are mixed at a 1:10 ratio, poured on our patterned wafer, degassed and cured for at least 3 hours at 80 °C. Then it is pealed off. Regarding the grid molds, they are cut into a circular shape (13 mm diameter) with a metal puncher. We obtain a PDMS mold with the negative volume of our future grid (see Figure 2.11, step 2).

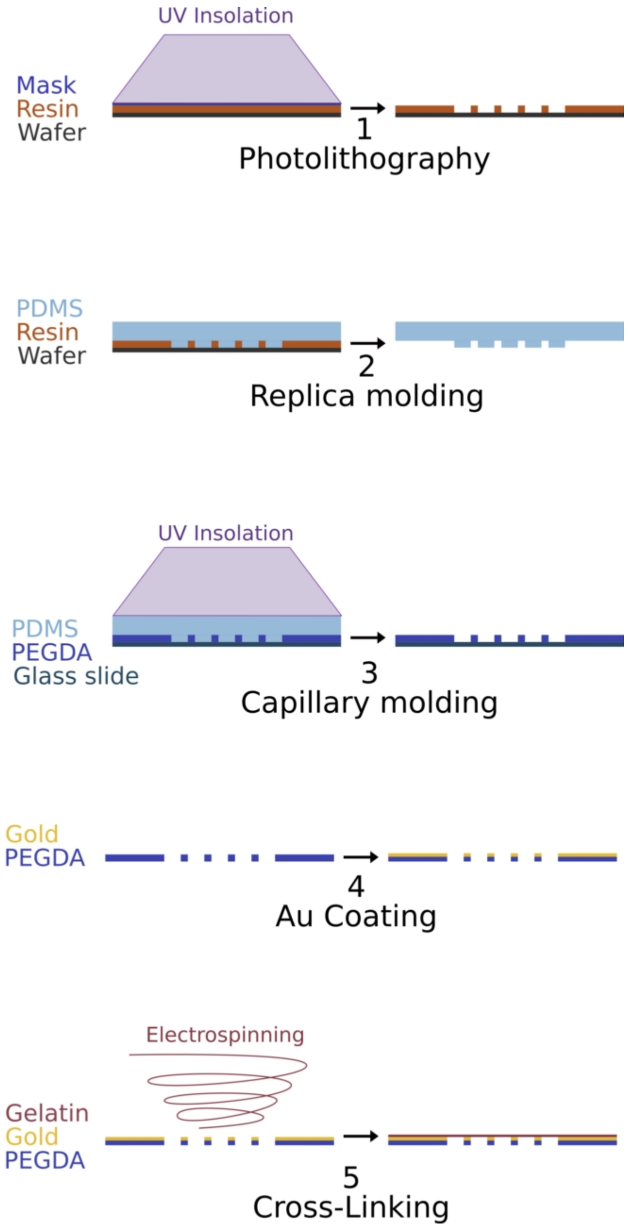

Figure 2.11: Our patch is obtained via 5 different microfabrication steps

Obtaining the supporting frame The honeycomb grid is obtained by vaccuum casting a solution of PEGDA and a photo-initiator into PDMS molds pressed onto a glass slide (see Figure 2.10a). This solution is then polymerized with UV-light through the molds (see Figure 2.10b). PDMS molds are peeled off and the PEGDA frames are detached from the slides (see Figure 2.11, step 3). The process is repeated with the PDMS ring molds (see Figure 2.10c). Finally a small amount of PEGDA solution (about 20 μL) is deposited on the rings and these are placed on the honeycomb substrates. The ensemble is reticulated and peeled off. The frames obtained are bathed in IPA for a couple of hours to dissolve potential residues of photo-initiator. Finally, frames are placed in water overnight to clean all chemicals. This last step is crucial to assure the overall bio-compatibility of the patch.

Gelatin nanofiber network fabrication In order to homogeneously receive the gelatin nanofiber network, the PEGDA frames are dried and coated with a 10 nm thick gold layer using a sputter-coater (K675X, EMITECH, Germany) (see Figure 2.11, step 4). Then, a solution of gelatin (dissolved in a solvent mixture of DI water, ethyl acetate, and acetic acid at a volume ratio of 10:14:21) is electrospun on the frames. The electrospinning is performed at 11 kV at 10 cm distance for an ejection rate of 0.2 mL/h during 15 minutes with a syringe pump. The samples are then dried overnight in a dessicator to remove solvent residues.

Finally, the nanofiber network is cross-linked with a solution of ethanol containing 0.2 M N- hydroxysuccinimide and 0.2 M 1-ethyl-3-(3 dimethylaminopropyl) carbodiimide hydrochloride for 4-6 h (see Figure 2.11, step 5). The samples are then washed three times in ethanol and dried in vacuum overnight to eliminate the residual solvent. Patches are sterilized under UV-light for 30 minutes before use.

b. Patch characterization and problem-solving

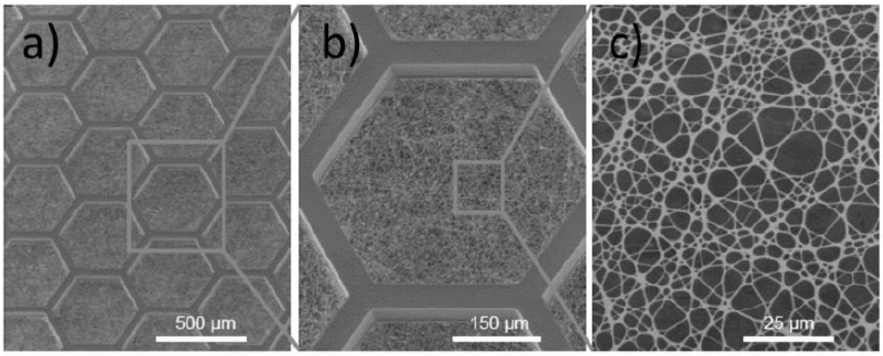

Figure 2.12: SEM images of the initial patch show the structure of the PEGDA honeycomb grid supporting the reticulated network of gelatin nanofibers. (*Courtesy of Yadong Tang*)

Characterization The patch obtained with this protocol was a total of a 100 μm thick, with a very thin layer of nanofibers. This patch was characterized by Yadong Tang in her doctoral dissertation [63]. She demonstrated that a 15 min electrospinning duration was optimal to obtain a pore size inferior to the area of the cells (below 20 μm^2), as can be seen on Figure 2.12. She also demonstrated that the gelatin network offered growth-enhancing properties.

Flatness issue During the fabrication process, I often observed that they would shrivel up (see Figure 2.13). This prevents correct cell seeding, as the droplet of cell solution tends to cascade down the patch, and it also prevents a correct integration of the patch in our microfluidic chip. Indeed, as detailed in the next part describing the design of our chip, the patch must be flat for the chip to be correctly sealed. This issue was therefore extremely important to tackle. Moreover, I had also observed that PEGDA tends to swell in water. However, the overnight water immersion of the patches could not be skipped, as it is a crucial step of the protocol, ensuring that there are no chemical residues, hence guaranteeing the bio-compatibility of the patch.

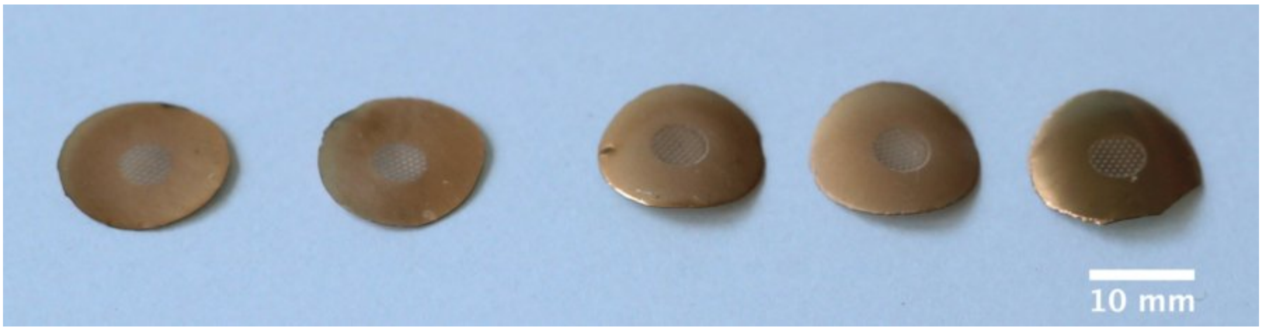

Figure 2.13: Depending on the fabrication process, the patches can be more (right) or less (left) flat. This was an important focus in our optimization of the fabrication process.

I decided to force the patches to stay flat during their water immersion. My solution was to press the patches flat during that time. I tried several methods but the optimal one was sandwiching the patches between glass slides, and putting weight on the top slide. The whole ensemble was then immersed in water for several days. Because such technique was reducing the patch-to-water exchange surface, I increased the immersion duration from overnight to a minimum of 48 hours (usually over the week-end).
This technique was promising, as the patches were clearly flatter at the end of their immersion. However, when finishing drying, some were still shrivelling. Therefore I re-instaured the 'sandwiching procedure' but with clean room paper this time. The patches were allowed to dry overnight in between paper and under weight in the dessicator. This new protocol resulted in an output of 99% flat patches, against 10 to 20% previously.

Cell layer integrity When inserting the patch in our microfluidic chip (detailed in the the next chapter), we observed that the patch, swelling with the medium tends to arch and touch the roof or the floor of the chip. This is all the more important when we apply pressure to deform the patch. The grid deforms and reaches the bottom of the chip where the cells may be damaged, thus destroying the cell layer. Moreover, any hole in the fibers means that the sample can no longer be used in the chip. Indeed, the separation of the two chambers of the chip completely relies on the integrity of the alveolar barrier. Moreover, if the cell layer contains holes, we can no longer apply pressure to deform the barrier.
Solving the PEGDA frame rigidity issue was simple: reducing the honeycomb size and increasing the distance between honeycombs automatically results in a more rigid frame. These modifications also changed the way we consider the patch. Indeed, with a now important honeycomb distance, the patch should no longer be seen as a sheet of epithelial-endothelial tissue, but as a collection of multiple independent alveoli.
Furthermore, as we can observe only a few honeycombs at a time on a microscope, there was no point in having so many (over a hundred) honeycombs on one patch. We decided to reduce the number of honeycombs to about 50. This was achieved by reducing the inner diameter of the outer ring of the PEGDA frame from 9 mm to 4 mm. The smaller the cell layer, the smaller the surface potentially undergoing tears and damages.

2.3.2 Final patch

As a result of all the issues we encountered in our use of the patch, I came up with a modified version of the initial patch, which was optimized for the specifics of the Alveoli-on-a-chip. Its new design and optimized fabrication process are detailed hereafter.

a. Fabrication process

Final design The final design retained was a honeycomb grid (internal diameter 400 μm and honeycomb distance 120 μm) inside a 4 mm inner diameter / 13 mm outer diameter ring, as can be seen on Figure 2.14).

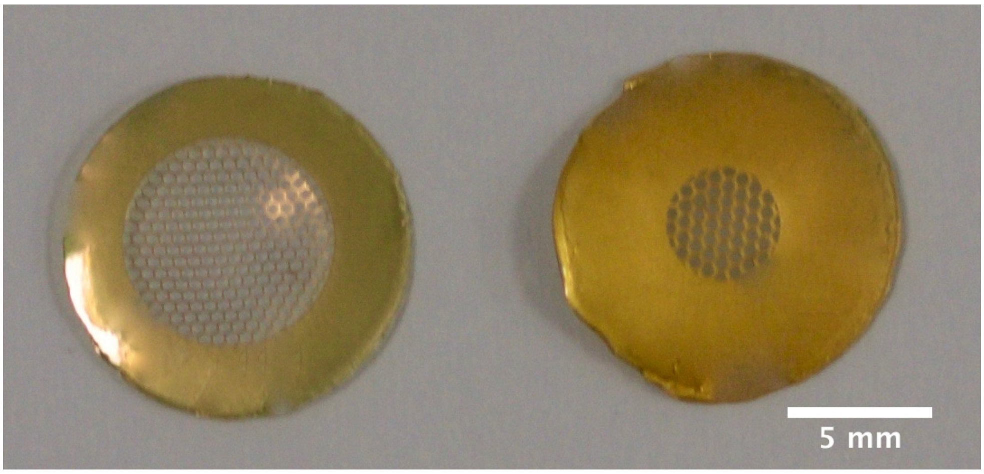

Figure 2.14: Left: Initial version of the patch (from Tang *et al*,2015). Right: our version of the microfabricatied gelatin patch

Process optimization In order to reduce the fabrication process time, the two parts (honeycomb network and outer ring) were integrated into a single PDMS mold. This was done by performing a double-layer photolithography to obtain a resin substrate with the two layers of the pattern included.

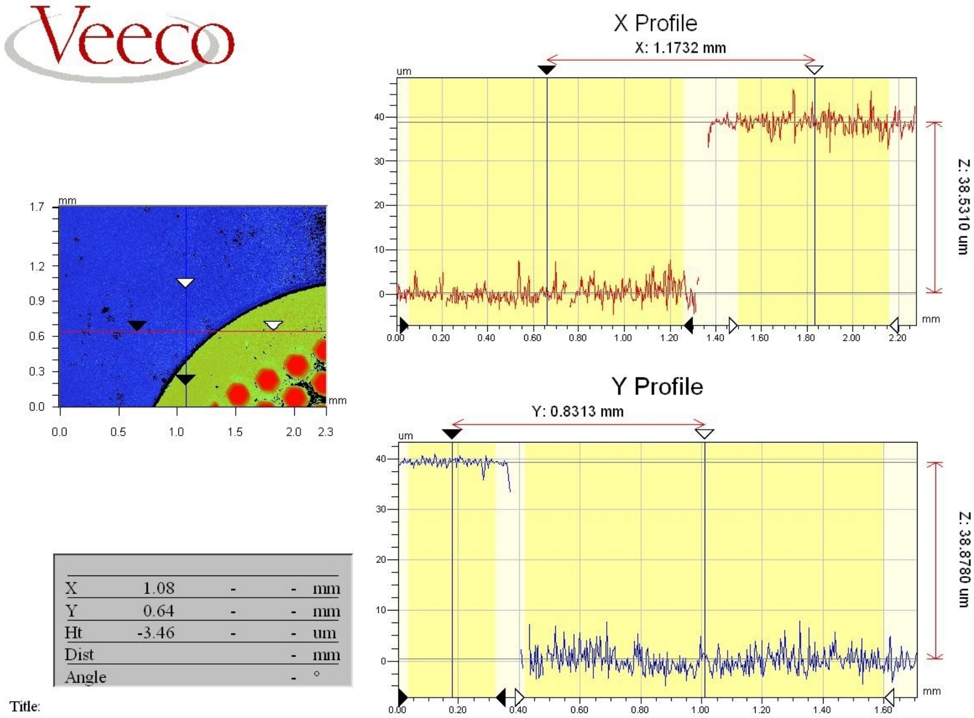

X	1.08	-	-	mm
Y	0.64	-	-	mm
Ht	-3.46	-	-	um
Dist			-	mm
Angle			-	°

Title:

Figure 2.15: Thickness measurement of the two layers of SU8 resin on our wafer using a profilometer: the two successive layers are about 38 μm each.

This photolithography was obtained by deposing a first layer of SU8-3050 at 3000 rpm onto a silica wafer followed by a soft bake: 1 minute at 65 °C, 20 minutes at 95 °C and 3 minutes of cooling down. We then exposed the wafer for 21 seconds. Then we moved on to a post-bake: 1 minute at 65 °C, 3 minute at 95 °C and 5 minutes of cooling down. The ensemble was then bathed in SU8 developer (MicroChem) for 8 minutes. Then the second layer was deposited similarly and after the same soft bake step, we aligned the second mask onto the first layer using a MJB4 mask aligner (SUSS MicroTec), and proceeded to the same exposure, post-bake and developing steps. The ensemble was hard baked for 15 minutes at 190 °C, and cooled down for 10 minutes.

We used TMCS (TriMethylChloroSilane, Sigma-Aldrich) evaporation as a silinization treatment.
The PDMS stamps molded on this substrate were then used for PEGDA vacuum casting in a single step. The rest of the microfabrication protocol was almost unchanged, with small optimization steps detailed in the Appendix.

Results We used an interference based optical profiling system (Wyko NT9100) to measure the thickness of our two layers of resin. After a few attempts and some optimization, the protocol was validated as we obtained a consistent thickness of 38 µ*m* for both layers (see Figure 2.15). This means that our patch will have a total thickness of less than 80 µ*m*.

b. Characterization

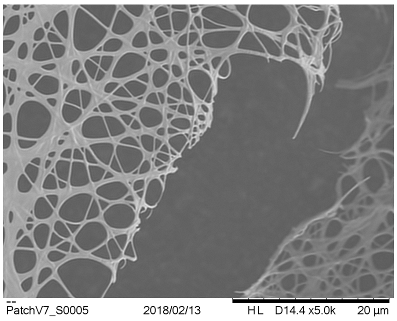

Figure 2.16: SEM images of a tear in the patch shows that the architecture of the gelatin nanofiber network is fused in a monolayer.

Nanofiber network analysis In order to analyze our new patch, we coated the nanofibers with a thin gold layer (10 nm, Sputter coater K675X, EMITECH, Germany)in order to observe them with a Scanning Electron Microscope (Hitachi, S-800) (see Figure 2.17). By creating a tear in one of the patches, we managed to obtain a side-view of the nanofibers. This gives us an idea of the 3D structure of the nanofiber network: it forms a single mono-layer (see Figure 2.16). Indeed, the chemical reaction of cross-linking the electrospun gelatin fibers causes them to merge together, thus creating a plane sheet. The thickness of this sheet was measured on the SEM images and is comprised between 600 nm and 1200 nm, with a mean size of about 1 µ*m*.

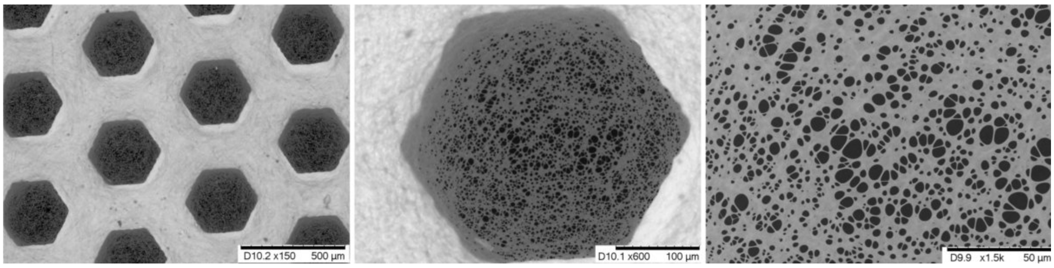

Figure 2.17: SEM images of the final patch show the thickening of the honeycomb walls and the structure of the gelatin network of merged nanofibers.

Pore distribution An extensive analysis of the patch was performed to assess pore distribution. It was important to make sure that the cells would not cross the nanofiber network, hence assuring that the different cell types seeded on each side would not mingle. Using a Scanning Electron Microscope (SEM) the nanofiber network was extensively photographed (see Figure 2.18a). A statistic analysis was run to analyze the pores via the *Analyze Particles function (ImageJ software)* (see Figure 2.18b). This analysis demonstrated that the pores were smaller than what cells could cross (max area 57.76 μm^2, mean area 1.72 μm^2, and min area 0.055 μm^2), and could also enable particle transport, with an average pore diameter of about 2 μm. On the Figure 2.18c, different colors show measurements for different patches. All data show similar trend, which demonstrates the relative reproducibility of the nanofiber network properties from one patch to another, even with the *semi random* step that is electrospinning.

2.3.3 Conclusion

We used the patch developed in our team by Liu *et al* [8] and Tang *et al* [9] and adapted it to our needs. Firstly, I had to get acquainted with the several microfabrication techniques used to compose the different elements of the patch. Then I gained some experience with the repeated fabrications and by using this patch for my experiments. With this knowledge I was able to modify the dimensions of this patch to create a microfabricated membrane that would fit my specific needs. Moreover, because I needed to prepare so many

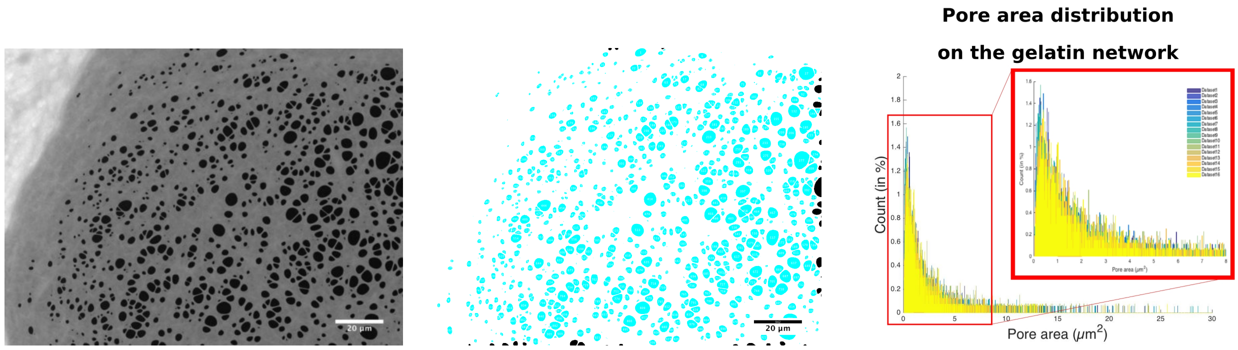

(a) SEM image of patch (b) Analyze particle function (c) Distribution of pores

Figure 2.18: Analysis of the pore distribution on the gelatin nanofiber network. The analysis of pore area over 16 honeycombs (1300 pores analyzed per honeycomb) demonstrates that the distribution is homogeneous over the honeycombs of a same patch

of these patches for my experiments, I also took the time to improve and accelerate the fabrication processes. Finally, we have presented here our model for the alveolar capillary membrane: a microengineered network of gelatin nanofibers. We designed a biocompatible membrane with a natural polymer of the extra-cellular matrix. This membrane presents dimensions close to the *in vivo* measurements in terms of alveolar size (here a diameter of 400 µ*m*) and a thickness (less than 1 µ*m*) that is currently (and to our knowledge) the thinnest available in the literature.

2.4 Developing an *in vitro* model of the alveolar barrier

2.4.1 Off-ground patch culture technique

a. Culture methods

Cell models and culture method As explained previously, we chose to model our alveolar epithelium with A549 cells (adenocarcinomic human alveolar basal epithelial cells) and our endothelium by HUVEC (human umbilical vascular endothelial cells). All culture protocols are extensively detailed in the Appendix. Rapidly, A549 cells were cultured with DMEM supplemented with 10% FBS and 1% Penicillin-Streptomycin, whereas HUVEC cells were cultured with specific Endothelial Cell Growth Medium (Lonza). HUVEC were used at or below passage 4.

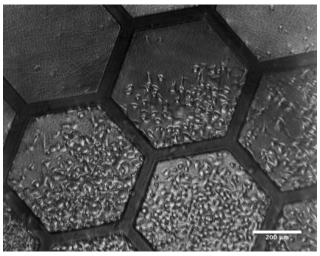

Figure 2.19: Heterogeneous cell growth on the patch (A549 cells, Seeding+24h). *Scale bar 200 µm*

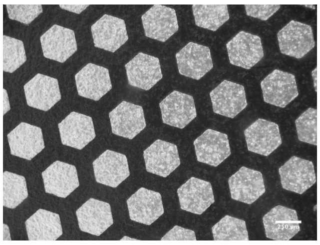

Figure 2.20: Homogenous cell growth on the patch (A549 cells, Seeding+48h). *Scale bar 250 µm*

Co-culture The co-culture on the patch is quite technical and required some testing and optimization.
The first issue was obtaining an homogeneous layer of cells. Since the cells do not grow on PEGDA, they can only spread on the side where the gelatin is electrospun. Therefore on the other side, obtaining an homogeneous seeding is extremely important, otherwise some honeycombs become confluent whereas others will stay empty of cells, no matter for how long the cells grow (see Figure 2.19).

Adding 50 µL of medium on the patches for about 10 minutes prior seeding the cells does did help cell adhesion by coating the surface. Then, when seeding the cells in a droplet (usually 100 to 200 µL), they immediately spread over the whole patch. With this and a properly homogenized cell solution, we could obtain homogeneous cell seeding (see Figure 2.20).

HUVEC in mono-culture During culture experiments I often observed holes forming in the patch (see Figure 2.21b). This would happen to some patches and not others, and at different time points in culture. I tested whether the gelatin fibers were dissolving over time by putting them either in water or in the specific medium for two months and obtained negative results. Long-term incubation at 37 °C did not induce holes either, hence the temperature was not responsible for the holes.
I tried to increase the density of the fiber network by performing electospinning for up to 25 minutes and obtained high-density patches with only pores smaller than 5 μm diameter (see Figure 2.21c). However, after a few days in culture, I also observed holes in such patches.

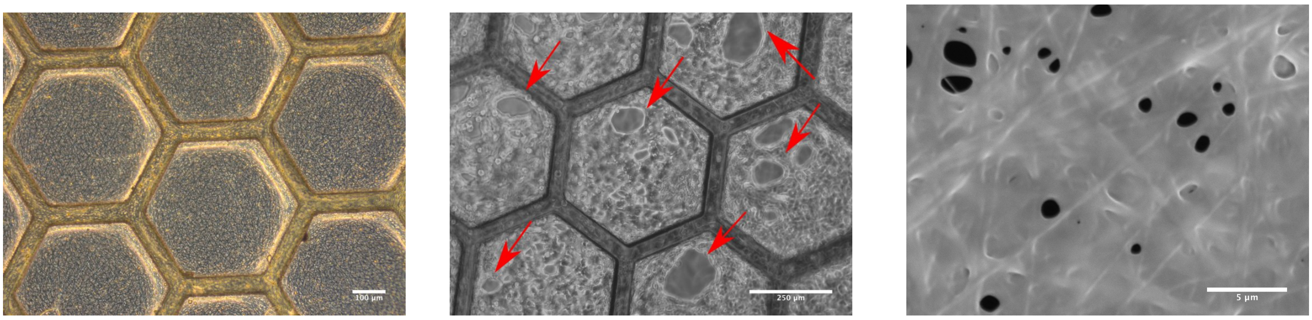

(a) Patch before seeding
Scale bar 100 μm

(b) Same patch after 5 days
Scale bar 250 μm

(c) High density patch (SEM)
Scale bar 5 μm

Figure 2.21: Investigation over the holes appearing in the culture patch.

Finally I tried seeding either HUVEC or A549 or both, at different densities, on several patches and observed them for several days. After one week, all the patches with only HUVEC were completely holey. After some research, I learned that HUVEC produce gelatinases, enzymes designed to digest the gelatin components of the extracellular matrix for when the cells perform in the angiogenesis process [64]. Because HUVEC are expensive cells, most of the patch-testing experiments were done with A549 cells, and as barrier-testing experiments were done with both cells in culture, I had rarely observed HUVEC in 'solo' for a long period of time. As it appears, the HUVEC are digesting the gelatin fibers, thus destroying the patch (see Figure2.21b). We suppose that this phenomenon is not observed in co-culture because the HUVEC can rest against the A549 cells for support. This hypothesis is supported by the fact that A549 cells produce extracellular matrix elements ([65], [66]).

b. Long-term culture: to a mature alveolar barrier

Development of PDMS rings included well plates In order to grow the cells on the patch, it was necessary to design a specific 'co-culture device' that could support the patch and prevent it from sinking to the bottom of the well and weighing on the lower layer of cells. Moreover, we wanted to tightly separate the two sides of the patch so that only the lower chamber could be filled with medium for ALI culture (Air-Liquid interface), or in order to perform translocation analysis with completely distinct chambers.

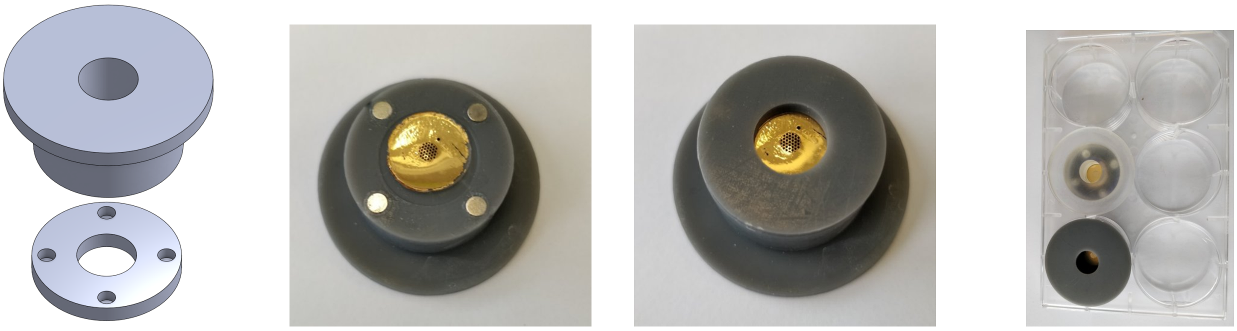

(a) CAD of the Co-culture device

(b) Step 1: Place the patch

(c) Step 2: Close with magnetic part

(d) Step 3: Place in 6-well plate

Figure 2.22: Different views of the 3D-printed co-culture device. The patch is inserted between the two parts, and the whole device is placed in a 6-well plate.

A first solution was to design a device similar to well-known Transwell inserts, holding the patch suspended in the well (see Figure 2.22a). This device was 3D-printed to the exact dimensions of a 6-well plate (the protocol for 3D-printing is detailed in the Appendix). In culture the patch was placed on the bigger part (see Figure 2.22b), then the smaller part was positioned on top with the help of magnets glued in both parts (see Figure 2.22c). Figure 2.22d shows the whole ensemble placed in a 6-well plate, with one device printed with clear resin, so that we can see the patch and the magnets. However, it was a complete failure as it was not watertight, and, once the device positioned in the well, a big bubble would form just under the patch. This bubble could not be avoided, and all the cells would dry and die. Moreover, the biocompatibility of both the glue and the resin would have to be tested, as well as their resistance in a warm aqueous medium. This technique was abandoned for a simpler, cheaper, more reliable method.

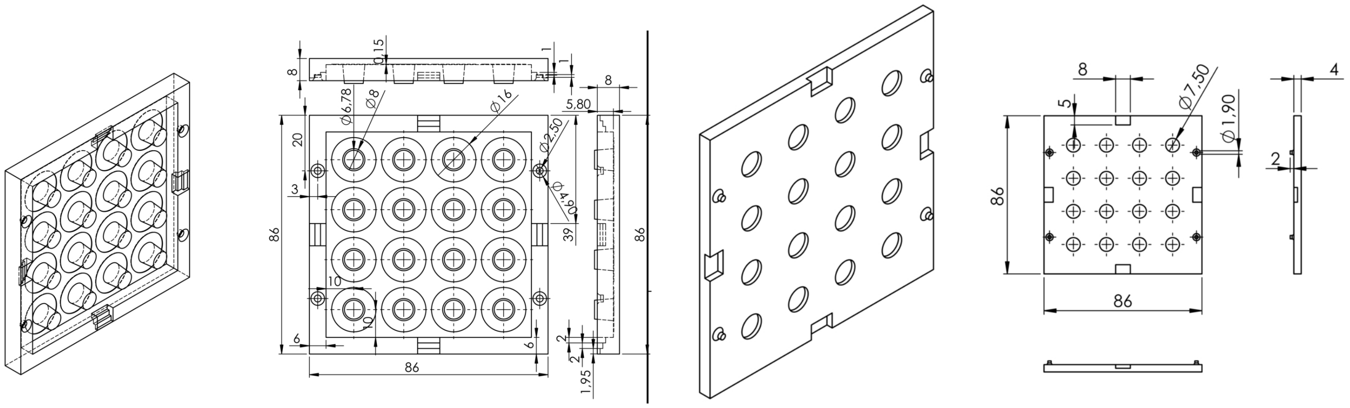

(a) Technical specifications of the bottom mold (b) Technical specifications of the top mold

Figure 2.23: Technical specifications of the 3D-printed PDMS ring mold for co-culture experiments.

The next solution I imagined was to use PDMS rings as a support for the patch. This technique is easy-to-make and quite cheap. However, in order to obtain reproducible culture conditions, it was important to prepare all the plates similarly. This meant that each PDMS ring should contain exactly the same volume. Reproducibility was obtained by preparing a 3D-printed mold, which would generate rings of controlled dimensions.

A mold with ring-shaped holes was the first idea, but friction of the PDMS against the resin was too important to remove the PDMS rings from the mold without destroying them, even with a relief angle of 2 degrees I had planned in anticipation. Therefore the mold was designed to generate a simple PDMS sheet with controlled-dimension holes pierced inside (see Figures 2.23a and 2.24a). In this mold, the PDMS is poured and degassed for about 2 hours, then the mold is closed and tightened with metal clamps. The ensemble is cured overnight at 80 °C. Afterwards, the PDMS sheet can be easily stripped off (see Figure 2.24a), and the rings are cut separate with a razor blade. The surface that corresponds to the bottom of the mold is smooth with a ring engraved: this is the part that will be in contact with the patch (see Figure 2.24b). This cutting step is not precisely reproducible because controling the external dimensions of the rings was not important: only the inside volume is decisive.

(a) PDMS sheet in the mold (b) PDMS ring in well (c) Full 6-well plate

Figure 2.24: Pictures of the implementation of precise PDMS rings in culture plates.

Finally, the rough surface of these rings is dipped into liquid PDMS, and placed inside a well of a 6-well plate (see Figure 2.24b). The plate is degassed for 30 minutes and cured at 80 °C for 2 h. The plates are sterilized with UV light before use (see Figure 2.24c).

I computed that, for cells cultured in 24-well plates (where the well surface is twice the surface of the patch, *i.e.* 1 cm^2), I had to renew the medium of about 400 µL every other days. Therefore, for a patch, 200 µL every other day should be sufficient. In order to fit with the dimensions of the patch, the rings were designed with an interior diameter of 8 mm and an outer diameter of 16 mm (to fit in a 12-well plate), as can be seen on Figure 2.23. With a controlled height of 5.8 mm, each ring contains a final volume of 223 µL. Since we are using a FormLabs2, and we print without re-orienting the parts (*i.e.* bottom of the mold on the platform), we have a resolution of 25 µm in the vertical direction, and of 140 µm in the horizontal directions. Finally, with these spatial resolutions we can compute that our mold enables us to produce PDMS rings with a final volume with a precision of about ±10 µL. Controlling the volume was highly important for following experiments with nanoparticles, as we will be working with high concentrations

c. Obtaining a mature tissue

As detailed previously, A549 cells are cancerous cells, therefore they have a high and unlimited proliferation rate. Moreover, they form poor epithelial junctions. These are two issues that we need to solve in order to produce an alveolar capillary barrier with a good tissue integrity, and that can be cultured for a long time.

A solution to stop cell proliferation and to induce their maturation is the use of Dexamethasone. We have seen that several *in vitro* models use it ([12], [7], [34], [59]), with usually a concentration of 1 µM. However, some groups demonstrated that 200 nM [42] can be sufficient. Some groups even used only 50nM [67], but they combined it with other products such as 8-bromoadenosine 3,5-cyclic monophosphate (8-Br-cAMP) and 3-isobutyl-1-methylxanthine (IBMX), which play a role in the maturation of the alveolar epithelium [46]. We decided to use 250 nM of Dexamethasone treatment on our cells. Immunostaining observations confirmed that is was sufficient to limit cell proliferation. Indeed, we observed the expression of KI67 (a protein only present in the nuclei of proliferating cells) without Dexamethasone or with 15 days of Dexamethasone treatment. On A549 cells the proliferation was completely stopped (see the lack KI67 staining in red on the blue nuclei on Figure 2.25 on the right) and on HUVEC it was highly reduced (see Figure 2.26). We also confirmed with our following experiences that Dexamethasone treatment promotes the formation of tight junctions (see following section).

Finally, my optimized co-culture technique is the following:

- Sterilize the patch with UV light for 15 minutes on each side. Similarly, sterilize a 6-well plate with integrated PDMS rings.
- Delicately place the patches on top of these rings, nanofiber networks face down
- Add 50 µL of ECGM on each patch. Incubate 10-20 min at 37 °C.
- Seed HUVEC at a density of 200 000 cells in a 200 µL droplet of warm ECGM. Carefully place the plates back in the incubator overnight.
- The next morning, aspirate the droplet, and fill the PDMS rings in the plates with warm ECGM. Return the patches to put the HUVEC face down.
- Seed A549 at a density of 180 000 cells in a 250 µL droplet of warm complete DMEM.
- Allow cells to grow for 48 h, and then remove the top medium to switch to Air-Liquid Interface (ALI) culture. Replace the ECGM medium in the lower chamber with ECGM supplemented with 250 nM of Dexamethasone.
- Renew the medium with Dexamethasone every other day.

This protocol was followed for all co-culture experiments, unless mentioned otherwise. With this technique, we could culture cells for at least three months (we did not try longer).

2.4.2 Alveolar barrier phenotype expression

We are able to obtain long-term culture of our barrier model (over three months). In order to validate our model we will now work on characterizing the phenotypes expressed by the cells. I will present here a few proteins expressed *in vivo* by the cells of the alveolar capillary barrier, detail their role in the barrier functions. Then we will present our results as we observed the different protein expression in our model. The objective of this part is to demonstrate that our model (co-culture of A549 and HUVEC cells on the patch with 15 days of Dexamethasone treatment) exhibited typical behaviors of the alveolar capillary barrier.

Some proteins secreted by alveolar cells are used to distinguish these cells in culture. These markers can either be completely specific to one type (**specific** marker), or can only help distinguish them from the other alveolar cells (**selective** marker), meaning that these proteins can be expressed elsewhere in the human body. Only the markers that we will use in this work are detailed here.

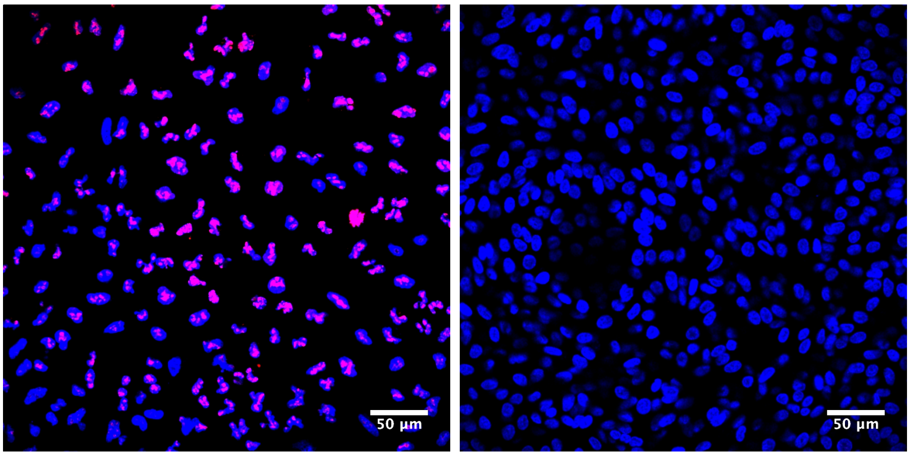

Figure 2.25: Dexamethasone treatment halts the proliferation of A549 cells. Left: A549 cells cultured for 48 hours without Dexamethasone and fixed at their confluence. Right: A549 cells cultured for 7 days with Dexamethasone before fixation. *Scale bars: 50* µm

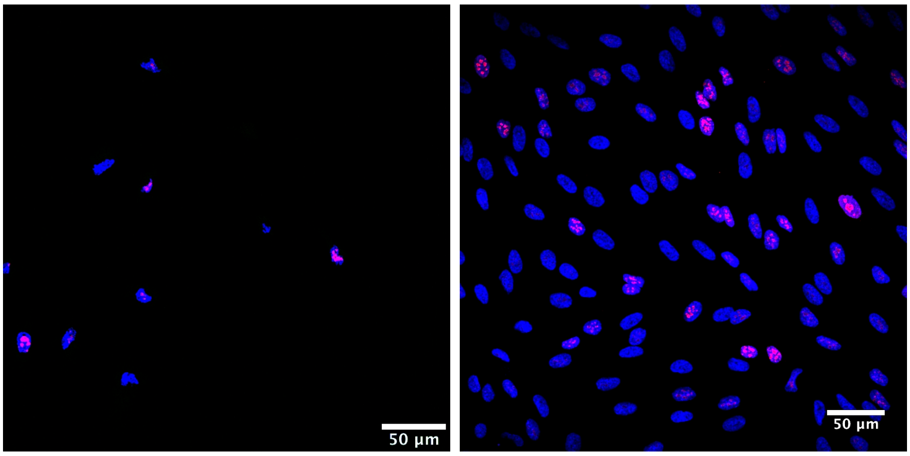

Figure 2.26: Dexamethasone treatment hinders the proliferation of HUVEC. Left: HUVEC cells cultured for 48 hours without Dexamethasone and fixed at their confluence. Right: HUVEC cells cultured for 7 days with Dexamethasone before fixation. The detachment of the cells cultured without Dexamethasone during the staining process does not allow for a pertinent comparison, however the proportion of KI-67 positive cells is smaller with Dexamethasone treatment (17%) than without (30%). *Scale bars: 50* µm

a. Observing AET I specific phenotype expression

There is no marker that is specific of AET I cells in the whole body. However, there are several selective markers.

Podoplanin One of them is Podoplanin (PDPN), an apical membrane protein said to have a role in protecting the surface of AET I cells from proteases. We observed negative PDPN staining in A549 cells, either with or without Dexamethasone. The production of PDPN was not induced on the patch either.

Endocytic transport protein: Caveolin1 Another selective marker is Caveolin1, which is not supposed to be expressed in AET II cells[68]. The protein Caveolin1 is a protein constitutive of the small flask-shaped microvesicle found in abundance in AET I and endothelial cells in the lungs [69]: the caveolae. Caveolin 1 plays an important role in endocytotic transport.

Our observations confirmed that A549 cells produce Caveolin1 (see Figure 2.27a, on a 2D coverslip), and that this expression did not decrease when switching to our co-culture model with Dexamethasone cultured at an ALI interface (see Figure 2.27b, on the patch with Dexamethasone). Moreover, we also noticed that HUVEC cells produce Caveolin1 (see the staining of the two cell layers in Figure 2.27c), which is actually coherent because HUVEC cells are also responsible for transport accross the endothelium [70].

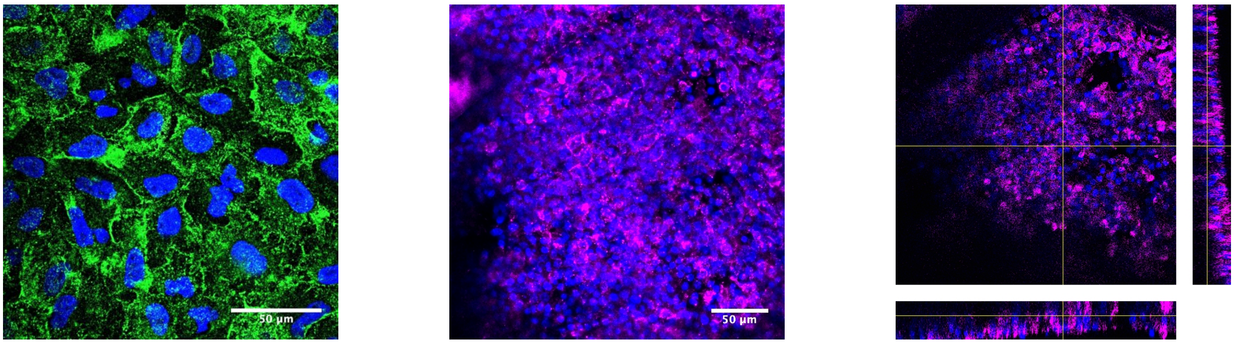

(a) Caveolin1 expression in A549 on glass

(b) Caveolin1 expression on the patch

(c) Caveolin1 expression on the patch (Side view)

Figure 2.27: Immunostaining of the endocytosis protein Caveolin1 to assess the ability of the model to perform particle transport. The confocal images show the expression of Caveolin1 in A549 cells (after 2 days in culture without Dexamethasone), and on the patch (Co-culture for 15 days with Dexamethasone). The side-view of the confocal stack demonstrates that both cell type express Caveolin1. *Scale bars: 50* µm

Water transport proteins: AQP5 The AQP5 protein is a water channel protein, and is a selective markers of the AET I cell, as it is not expressed in AET II cells [68]. It is located in the apical membrane of AET I cells and bronchiolar epithelial cells in the lung. AQP5 is essential for the movement of water from the airspaces to the capillary bed in response to an osmotic gradient generated from the vascular bed. However, AQP5 does not appear to be crucial in water absorption out of the airspaces under normal conditions or under conditions in which alveolar fluid clearance is upregulated by specific agonists. Nor is AQP5 decisive in lung extravascular fluid accumulation in acute injury. It has been proposed that AQP5 may be influential in the regulation of AET I cell volume [69].
We could not observe the expression of AQP5 in our model, neither in 2D nor on the patch. This was not changed by the addition of Dexamethasone. The absence of APQP5 by A549 was confirmed by other research, but it was recently demonstrated that they produce AQP3 [71], which indicates that they should still be able to perform osmotic equilibrium.

b. Observing AET II specific phenotype expression

Surfactant protein The only marker that is absolutely specific to AET II cells is the SP-C protein of the surfactant that is synthesized and transporter in the lamellar bodies of the type II cells.
We observed the production of proSP-C (SP-C protein that is not yet mature, therefore not exocytosed) in our A549 cells. This protein was naturally expressed without the Dexamethasone treatment (see Figure 2.28a). After Dexamethasone treatment, the staining was still important in a dish (see Figure 2.28b) or on the patch (see Figure 2.28c). This indicates that our cells are producing surfactant proteins.

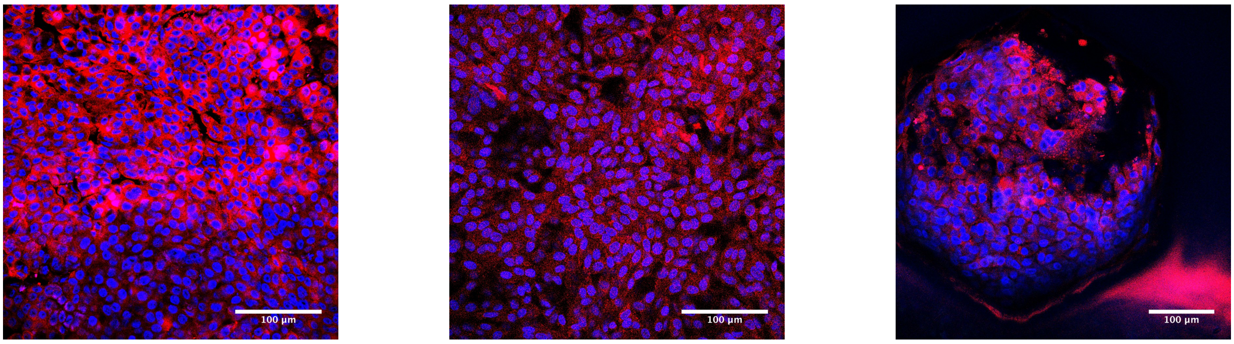

(a) proSP-C expression on A549

(b) proSP-C expression on A549 with Dexamethasone

(c) proSP-C expression on the patch

Figure 2.28: A549 cells produce future surfactant protein C in (a) regular dish culture (2 days in culture), (b) in a dish with 15 days of Dexamethasone treatment and (c) in co-culture for 15 days with Dexamethasone. *Scale bars: 100, 50 and 100* µm*.*

The other surfactant proteins (SP-A, SP-B and SP-D) are expressed by both AET II and distal bronchial pulmonary cells.

Our immunostaining experiments confirmed the production of SP-A and SP-B by A549 cell with Dexamethasone on the patch (see Figures 2.29d and 2.29e). Interestingly, in a dish, we could not observe any expression without using Dexamethasone (see Figures 2.29a and 2.29b). On our patch, however, we did not need the Dexamethasone to induce SP-B production (see Figure 2.29c). This was not the case for SP-A. This means that either the ALI culture condition or the patch itself has an influence on SP-B expression.

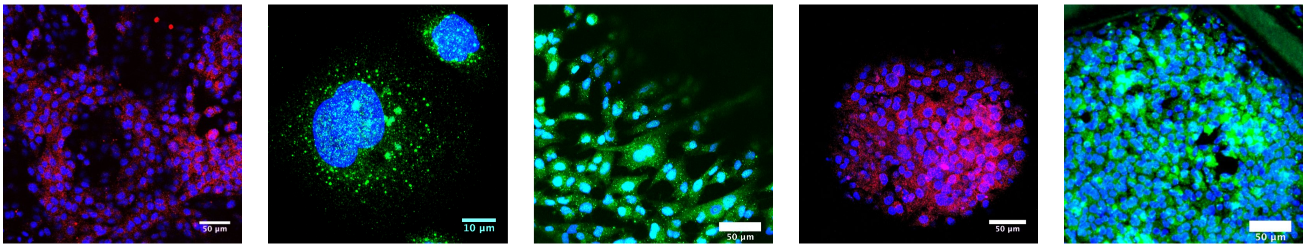

(a) SP-A expression in A549 with Dexamethasone
(b) SP-B expression in A549 with Dexamethasone
(c) SP-B expression on patch (No Dexamethasone)
(d) SP-A expression (patch + Dexamethasone)
(e) SP-B expression (patch + Dexamethasone)

Figure 2.29: A549 cells produce (a) SP-A and (b) SP-B in culture only with the Dexamethasone treatment (15 days). On the patch, only (c) SP-B can be expressed without Dexamethasone (4 days), but both proteins (d) SP-A and (e) SP-B were expressed on the patch in co-culture with Dexamethasone (15 days) *Scale bars: 50, 10, 50, 50 and 50* µm

Similarly, the AET II cells and epithelial cells of the respiratory bronchioles are known to produce MUC1, a mucin protein, but not in AET I, Goblet cells or mucous cells of the bronchial glands. Mucins are a family of heavily glycosylated proteins (glycoconjugates) produced by epithelial tissues in most organisms, serving functions such as lubrication, cell signaling or forming chemical barriers.

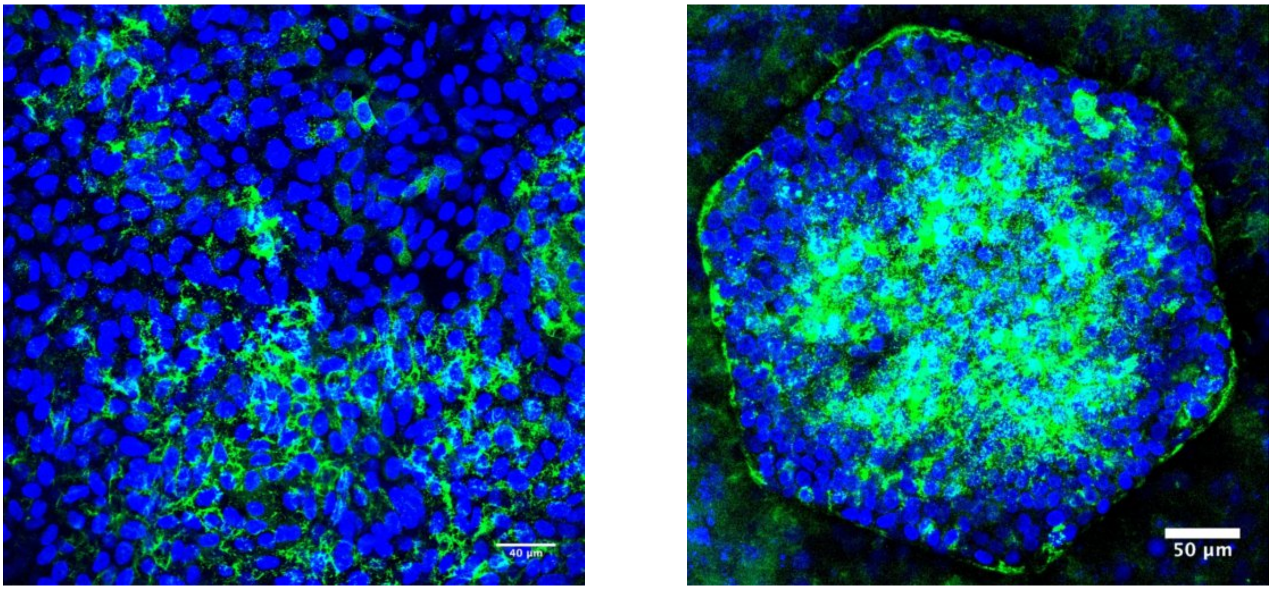

(a) MUC5AC expression in A549 in culture with Dexamethasone
(b) MUC5AC expression in A549 on the patch with Dexamethasone

Figure 2.30: A549 cells produce the surfactant protein MUC5AC, both in (a) regular culture (4 days) and (b) on the patch in co-culture with Dexamethasone (15 days). *Scale bars: 40 and 50* µm.

It is widely observed that A549 fail to produce MUC1, and this was confirmed in our experiments. However, they still produce a mucin protein: MU5AC. This protein is expected to be produced by Clara cells, but was often observed in A549 [72]. We were able to observe consistent expression in 2D and on our patch (see Figures2.30a and 2.30b) with the Dexamethasone treatment.

Finally, we investigated whether our A549 cells expressed the lung-associated marker NKX2.1 or TTF1. This thyroid transcription factor-1 is found in AET II and club cells of the lung. It is also overexpressed in

adenorcarninomas, which explains its presence in A549 cells.
We observed consistent expression in A549 cells, with or without Dex, and on the patch too (see Figure 2.31).

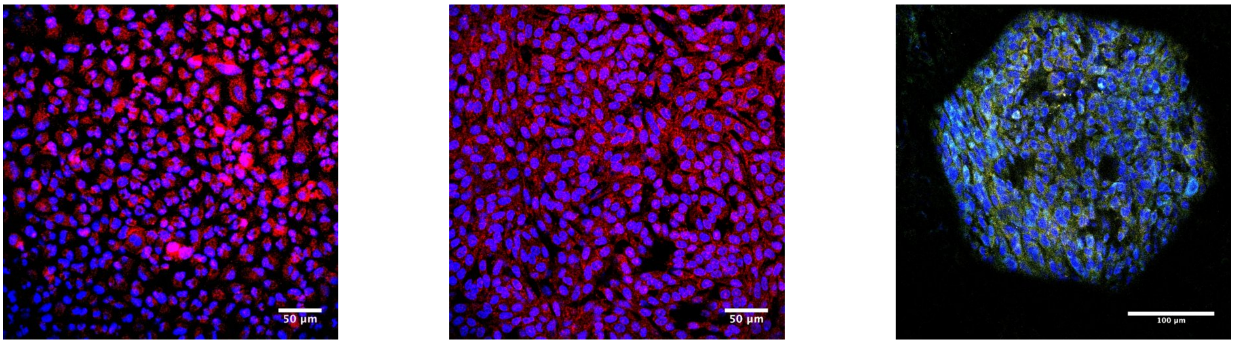

(a) NKX2.1 expression on A549 (No Dexamethasone)

(b) NKX2.1 expression on A549 with Dexamethasone

(c) NKX2.1 expression on the patch with Dexamethasone

Figure 2.31: A549 cells produce the lung marker NKX2.1 both in (a) regular culture (4 days) and (b) on the patch in co-culture with Dexamethasone (15 days). *Scale bars: 50 and 100* µm

c. Observing specific endothelial phenotype expression

Amongst the many endothelial cell proteins, I will present two that play important roles in the accomplishment of endothelial functions: VE-Cadherin and PECAM1.

Vascular Endothelial cadherin Ve-Cad or CD144 is a protein of the cadherin superfamily. Cadherins impart to cells the ability to adhere in a homophilic manner. Therefore, VE-Cadherin helps control of the cohesion and organization of the intercellular junctions [73]. Integrity of intercellular junctions is a major determinant of permeability of the endothelium, and the VE-cadherin-based adherens junction is thought to be particularly important. VE-cadherin is known to be required for maintaining a restrictive endothelial barrier: early studies using blocking antibodies to VE-cadherin increased monolayer permeability in cultured cells and resulted in interstitial edema and hemorrhage *in vivo*.
We were able to observe VE-Cadherin expression in HUVEC cells under Dexamethasone treatment (see Figure 2.32a). On the patch we could see some protein expression but they were not localized in at the cellular junctions (see Figure 2.32b).

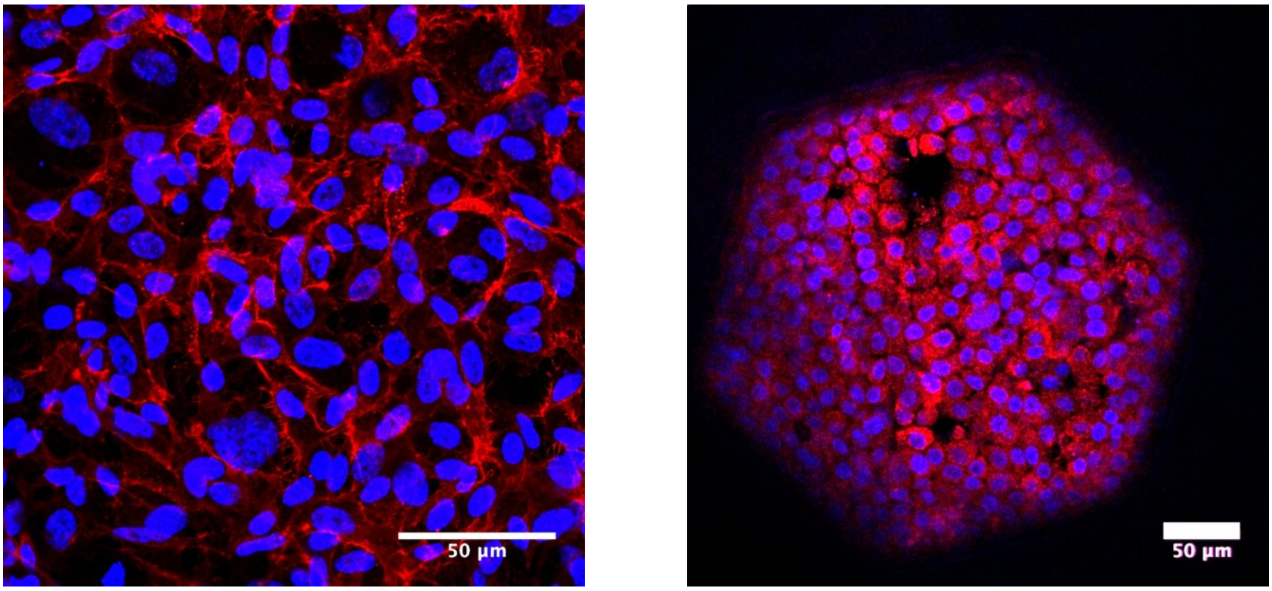

(a) Ve-Cadherin expression in HUVEC with Dexamethasone treatment

(b) Ve-Cadherin expression in HUVEC on the patch with Dexamethasone treatment

Figure 2.32: HUVEC cells produce VE-Cadherin both in (a) culture with Dexamethasone (15 days) and (b) on the patch in co-culture with Dexamethasone (15 days). *Scale bars: 50* µm

Platelet endothelial cell adhesion molecule (PECAM1 or CD31) is a protein found on the surface of platelets, monocytes, neutrophils, and some types of T-cells, and make up a large portion of endothelial cell intercellular junctions [74]. The encoded protein is a member of the immunoglobulin superfamily and is likely involved in leukocyte transmigration, angiogenesis, and integrin activation.
Similarly to VE-Cadherin, we could observe PECAM1 expression in HUVEC cells under Dexamethasone treatment (see Figure 2.33a) and on the patch too but they were not localized in at the cellular junctions (see Figure 2.33).

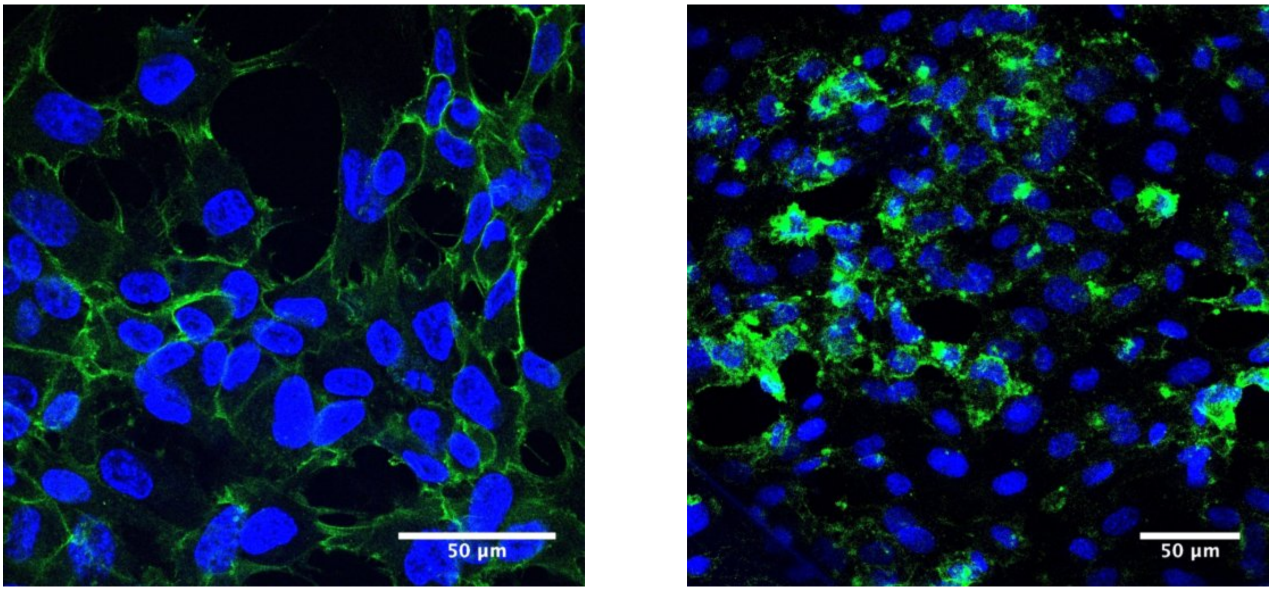

(a) PECAM1 expression in HUVEC with Dexamethasone treatment

(b) PECAM1 in HUVEC on the patch with Dexamethasone treatment

Figure 2.33: HUVEC cells produce PECAM1 both in (a) culture with Dexamethasone (15 days) and (b) on the patch in co-culture with Dexamethasone (15 days). *Scale bars: 50* µm

d. Tissue organization

Cadherin expression We have seen that endothelial cells produce VE-Cadherin (CD144), a cell adhesion molecule that allows the formation of intercellular adherens junctions. Similarly, the alveolar epithelial cells produce E-Cadherin (CDH1).
We were able to observe E-Cadherin production in A549 cells (see Figure 2.34a). The protein expression was upregulated with the Dexamethasone treatment (see Figure 2.34b), and was still expressed in patch culture conditions (see Figure 2.34c).

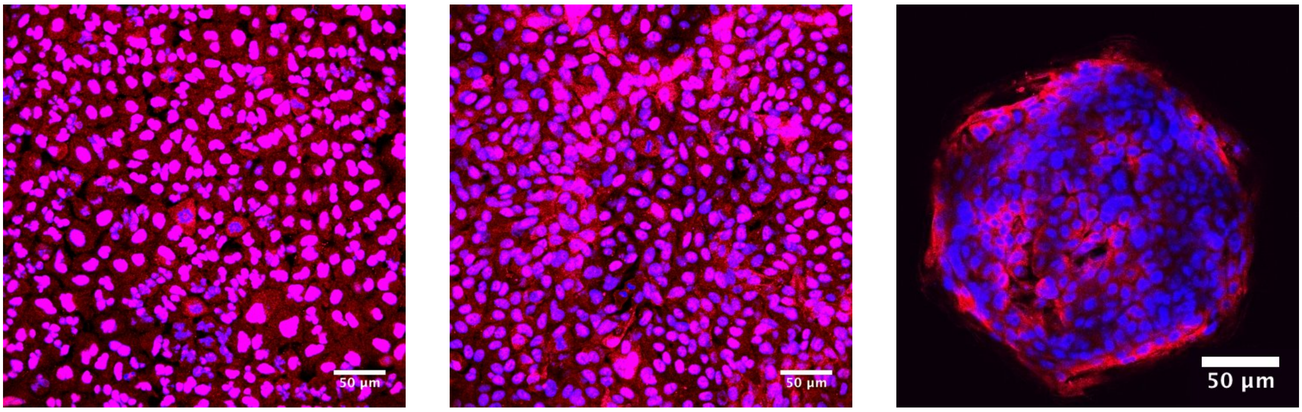

(a) E-Cadherin expression in A549 without Dexamethasone treatment

(b) E-Cadherin expression in A549 with Dexamethasone treatment

(c) E-Cadherin expression in A549 on the patch with Dexamethasone

Figure 2.34: A549 cells produce E-Cadherin *Scale bars: 50* µm

Another cadherin protein, the N-Cadherin is expressed in epithelial and endothelial cells. This Neuronal Cad-

herin or Cadherin-2 (CDH2).
RESULTS For both A549 and HUVEC, N-Cadherin was expressed and enhanced with Dexamethasone treatment (see Figure 2.35). On the patch we could observe N-Cadherin expression on both cell layers (see Figure 2.35e side views).

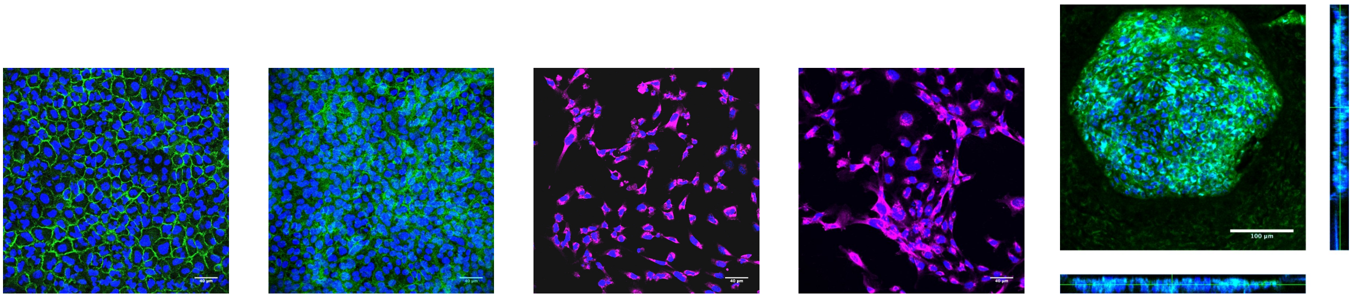

(a) N-Cadherin expression in A549 (no Dex)

(b) N-Cadherin expression in A549 with Dex treatment

(c) N-Cadherin expression in HUVEC (no Dex)

(d) N-Cadherin expression in HUVEC with Dex

(e) Dual N-Cadherin expression in the model on the patch with Dex

Figure 2.35: A549 and HUVEC cells produce N-Cadherin *Scale bars: 40, 40, 40, 40 and 100 microm*

Formation of tight junctions If the Cadherins expression indicates that our cells form layers of adherent cells, we do not know how tight are these sheets. Indeed, adherens junctions are permeable and their presence does not indicate a good barrier integrity. In order to assess this integrity, we will now look at tight junction proteins: Occludin and ZO-1 [75]. ZO-1 is a protein encoded by the TJP1 gene. It is located on the cytoplasmic membrane surface of intercellular tight junctions. The encoded protein may be involved in signal transduction at cell–cell junctions. ZO-1 links the actin of the cytoplasm to the occludins or the claudins that cross the cellular membrane and bond to each other [76].
We observed the expression of occludin in our A549 cells (see Figure 2.36a), with an important upregulation due to the Dexamethasone treatment (see Figure 2.36b). In HUVEC, Occludin expression was extremely weak, and not mature enough to be localized at the membrane of the cells. On the patch we obtained a present but low expression (see Figure 2.36c). This could be due to the antibody used (we did not have enough time to repeat the experiment at a lower dilution).

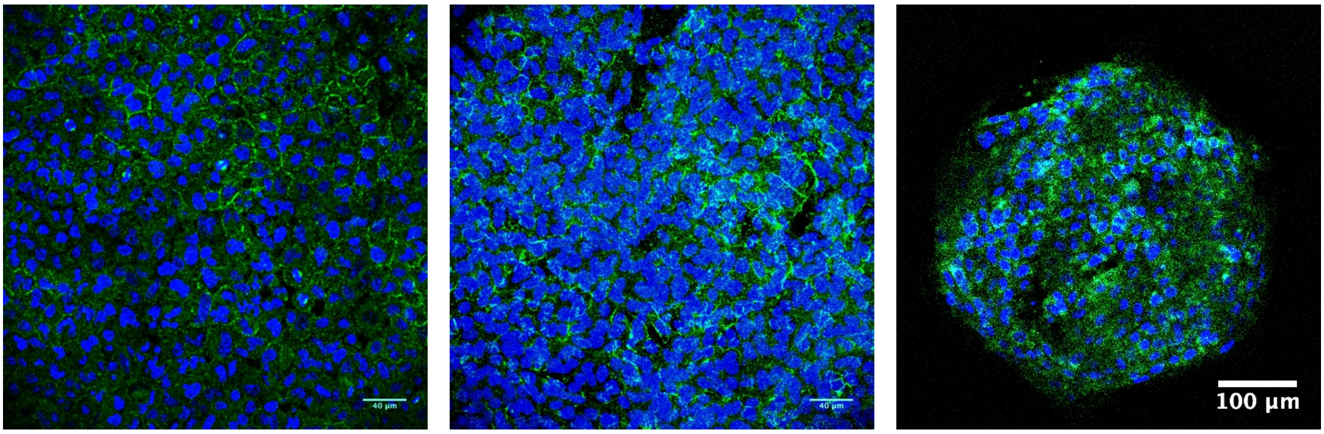

(a) Occludin expression in A549 without Dexamethasone treatment

(b) Occludin expression in A549 with Dexamethasone treatment

(c) Occludin expression in A549 cells with Dexamethasone treatment

Figure 2.36: Occludin expression in A549 cells *Scale bars: 40, 40 and 100* µm

The expression of ZO-1 in A549 was low and immature (the proteins were still in the cytoplasm) without Dexamethasone treatment (see Figure 2.37a), but 15 days of Dexamethasone treatment were enough to induce strong commitment of the ZO-1 protein to the membrane regions (see Figure 2.37b). In HUVEC cells, the expression was more important than in A549 for no-Dexamethasone condition (see Figure 2.37c). However the Dexamethasone treatment also induced a maturation of this protein expression as we could observe a better localization of the protein at the cellular junctions (see Figure 2.37d). On the patch with Dexamethasone treatment, the expression of ZO-1 was observed in both cell layers (see Figure 2.37e) and widespread all over the patch (see Figure 2.37f).

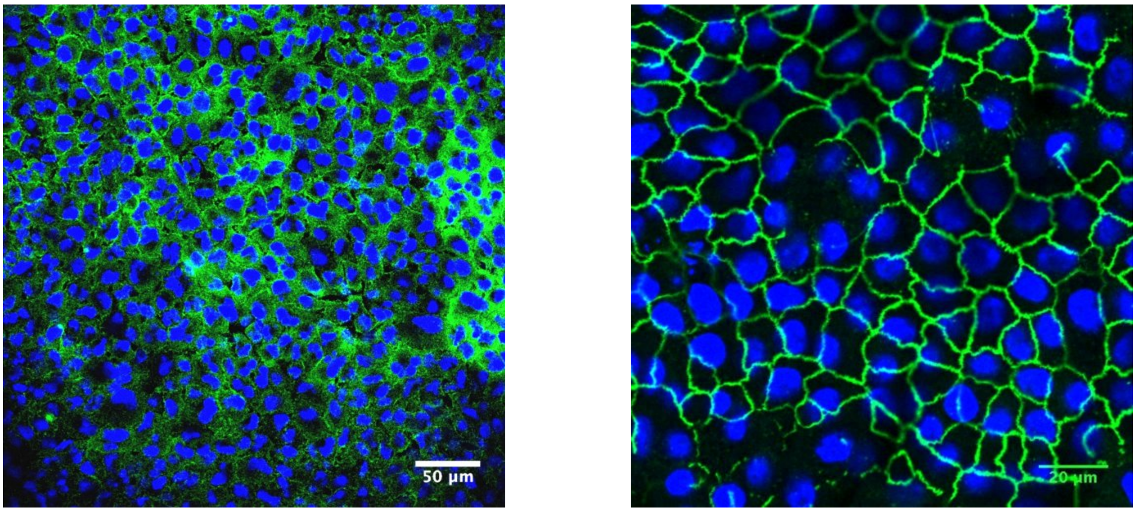

(a) ZO-1 expression in A549 without Dexamethasone treatment

(b) ZO-1 expression in A549 with Dexamethasone treatment

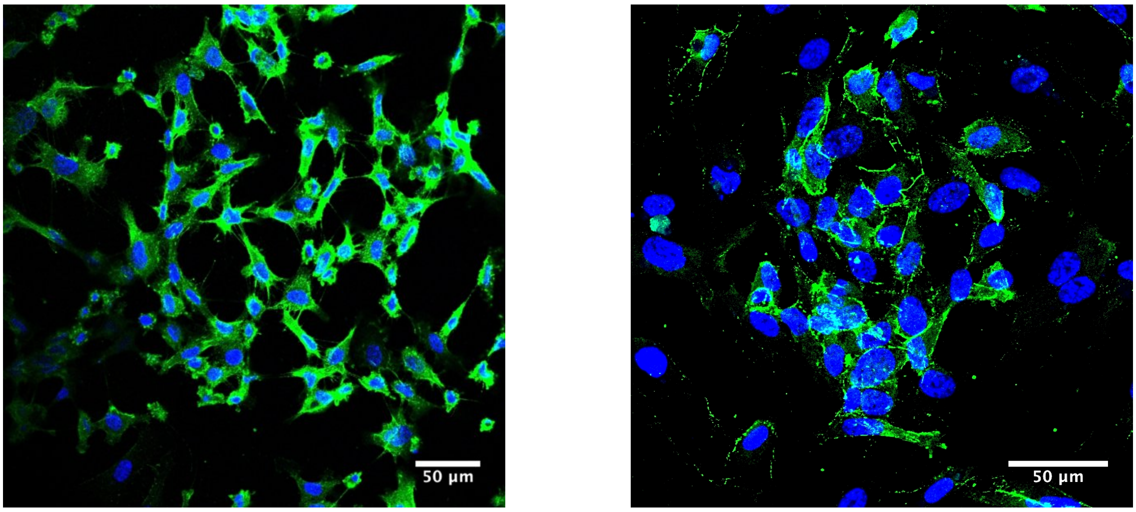

(c) ZO-1 expression in HUVEC without Dexamethasone treatment

(d) ZO-1 expression in HUVEC with Dexamethasone treatment

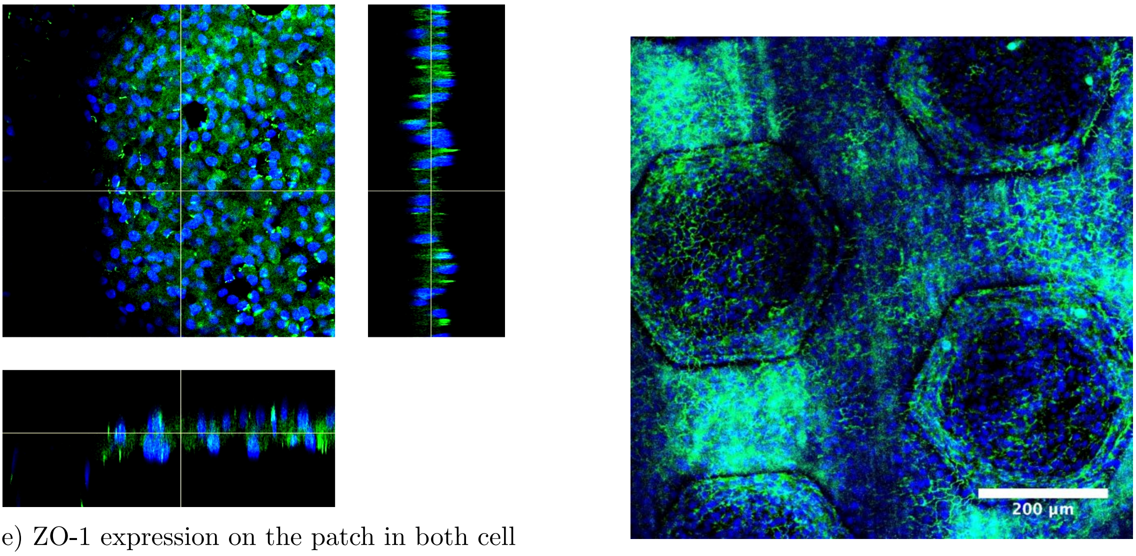

(e) ZO-1 expression on the patch in both cell layers (with 7 days of Dexamethasone treatment)

(f) Widespread ZO-1 expression on the patch (with 32 days of Dexamethasone treatment)

Figure 2.37: A549 and HUVEC cells produce N-Cadherin *Scale bars: 40, 40, 40, 40 and 100* µm

e. Conclusion

Alveolar epithelium: a multiple phenotype In A549 cells we observed the expression of markers of Type I (Caveolin1) and Type II markers (proSP-C and NKX2.1) as well as other markers normally expressed in both cell type (SP-A and SP-B) or even other lung cells (MUC5AC). Some of these markers are enhanced by Dexamethasone (SP-B and NKX2.1 [44]). This indicates that the air liquid interface culture with th Dexamethasone treatment seems to enhance the production of surfactant proteins. This variety of phenotype was observed in the literature: A549 cells are known to a have a large phenotype, exhibiting properties of AET I, AET II and Clara cells ([72], [44], [43]).

Epithelium: a weak phenotype Our HUVEC cells exhibit a normal behavior in regular culture conditions, as well as with the Dexamethasone treatment. However, we were suprised to observe the poor expression of both PECAM1 and VE-Cadherin. On the patch, these cells express both markers but these are not properly localized, as if they had just been synthesized. This behavior is concerning because it indicates that HUVEC cells are not able to properly perform their adhesion and immune functions on the model. This could be explained possibly by the Dexamethasone concentrations that should be optimized, or by the lack of shear stress exerted on the cells, which is a crucial for their survival [11].

Barrier formation We are designing a model specifically for nanoparticle translocation assays, therefore it is very important for us that our alveolar capillary model presents a good barrier integrity. In order to establish whether its integrity was acceptable, we looked into the expression of junction proteins. We observed E-Cadherin expression from the epithelial cells, as well as consistent N-Cadherin from both cell types with a dual staining on both cell layers. This indicates the formation of a tissue structure. The integrity of this tissue was verified by the observation of tight junction protein expression: Occludin and ZO-1. We had a more consistent expression of ZO-1 than Occludin, but this could be due to the antibodies used for Occludin staining. Interestingly, the use of Dexamethasone proved necessary for the production of both tight junction proteins at a mature level, *i.e.* localized at the cell membranes.

2.4.3 Barrier permeability quantification

In developing an *in vitro* model of the alveolar barrier, an imperative function to recreate is the selective permeability of the alveoli. The observation of cellular junctions (E-Cadherin, VE-Cadherin) allowed us to ensure that our cells formed a tissue-like structure. Moreover, the strong formation of tight junctions (ZO-1, Occludin) suggests a good barrier integrity ([76], [77]). Because our objective is to study nanoparticle translocation through the alveolar barrier, it is crucial to have a barrier with a limited permeability. In this part, I will explain the method used to quantify this permeability, as well as the materials that were specifically developed for such end.

a. Lucifer Yellow assay

As detailed in the introduction, one of the methods used to assess barrier integrity is to follow the transport of hydrophilic molecules across the barrier. The protocol for this assay is usually performed with Transwell inserts. The cells are grown on the inserts and, at different timepoints, the permeability can be measured. In this regard, a solution containing the labeled compound in a low-fluorescence buffer solution is placed in the apical chamber, while the basal chamber is filled with the same buffer. Cells are incubated at 37 °C for 45 minutes to 2 hours (depending on the protocol), and then the solution of the basal chamber is sampled and analyzed with a fluorescence reader. This can be repeated daily to follow the evolution of tissue permeability over time.

Developing impervious chambers In order to analyze the transport of these labeled compounds, we had to design a Transwell-like system, with two distinct chambers and our patch as the separating membrane. My design for this device was based on the PDMS rings used for co-culture. As we had already designed a chamber for the lower side of the patch, we only needed to add another chamber on top of the patch. My method was to use the same 3D-printed mold generating PDMS rings, but this time, I casted a magnet in each PDMS ring . I chose neodymium magnets with a coating of cupronickel (reference R-12-09-1.5-N, Supermagnete), so that they could resist to the corrosive conditions of the incubator. They were rings of 9 mm inner and 12 mm outer diameters with an adherence force of about 14.7 N.

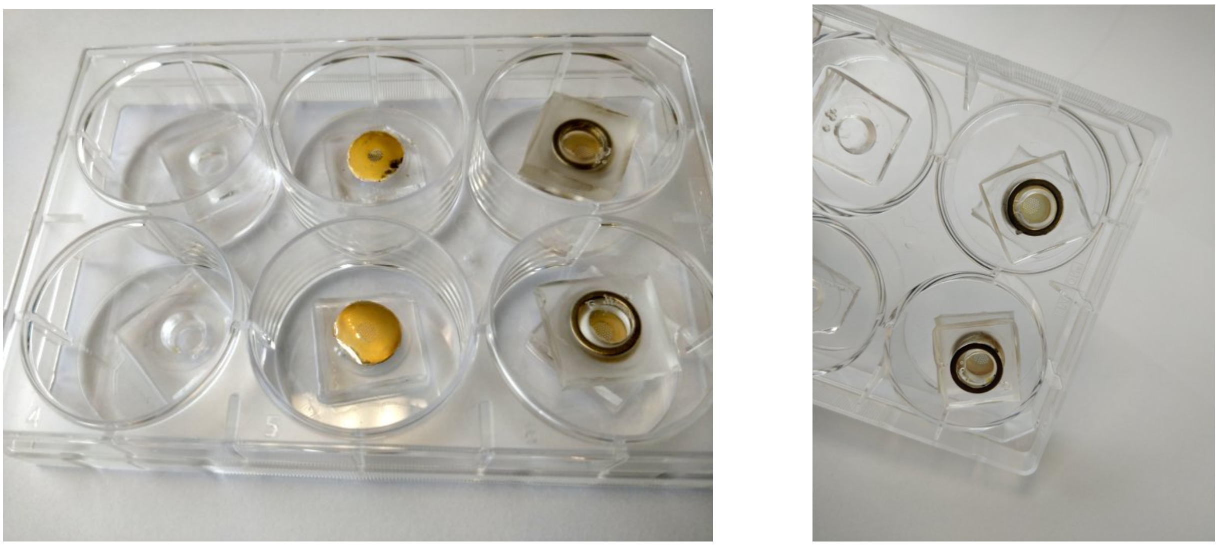

(a) Mounting PDMS-magnetic chamber: first three steps (b) Magnets placed below the plate

Figure 2.38: Technical setup designed for translocation assays on the patch. The PDMS rings used for patch co-culture are used as the basal chamber. For the apical chamber, a magnet is cast in one of these PDMS rings, and held in place by a second magnet placed below the well.

In order to mount the chambers, one would have to place the patch on the PDMS ring glued at the bottom of a 6-well-plate, then place these magnet-containing PDMS rings on top (see Figure 2.38a). Then, they would place a corresponding magnet below the plate to hold the top chamber in position (see Figure 2.38b). This system has the advantage to be strong enough to have watertight chambers, but the positioning process is gentle enough to avoid tissue destruction. Indeed, I tried placing the second magnet directly into the lower chamber PDMS ring, but it generated a particularly strong attraction but when placing another magnetic ring on top, and it would 'jump' into place and damage the network of nanofibers. Finally, the solution with only one cast magnet and another magnet below the chamber was retained (see Figure 2.38).

Protocol optimization In order to evaluate the integrity of our barrier, we performed a translocation assay of Lucifer Yellow CH Dipotassium Salt (Sigma-Aldrich, Ref.L044), in a home-made buffer that I will present here. I had observed that prolonged 1 h-incubations of HUVEC cells in PBS or HBSS (recommended buffers) resulted in consequent cell detachment, therefore I decided to use some nutritive medium in the buffer. To reduce parasitic fluorescence, I chose white DMEM medium (without Phenol Red). Its autofluorescence was still important, therefore I decided to mix it with DPBS, and to assure the nutritive aspect of the medium, I used the High Glucose formulation (4500 mg/L). The final buffer, that I named '**5050 White Buffer**', consists of 50% DPBS and 50% High Glucose White DMEM (LifeTech, Ref.31053-028).
Before using this buffer, we had to assess that it did not interact with the Lucifer Yellow and change its emission/excitation spectrums. We used a spectrometer to measure this, and the Figure 2.39 shows that Lucifer Yellow has the same spectrum in DPBS and in our homemade buffer. In further experiments, the Lucifer Yellow was always excited at 426 nm and its fluorescence was observed at 440 nm.
Before starting any experiments, we wanted to determine the optimum volume to sample for fluorescence analysis. We used 96-well plates, therefore we tested volumes between 10 and 150 μL. As demonstrated by the observations in Figure 2.40a, the fluorescence varies extremely importantly with the volumes for volumes below 50 μL, whatever the concentration of LY used. This variation stabilizes for volumes around 100 μL. Therefore, we chose to work with 100 μL samples so that potential errors of pipetting would have a minimal effect on the overall measured fluorescence.
We also established a standard curve using known concentrations of Lucifer Yellow solution to correlate the intensity of the fluorescence with the concentration. We observed that the correlation was quasi-linear below 100 $\mu g/mL$, therefore we chose to work with a maximum concentration of 100 $\mu g/mL$ for future experiments. We could also confirmed that the fluorescent plate reader (Tecan Spark) was able to detect concentration as low as 0.5 $\mu g/mL$ (detected fluorescence of about 150-200 a.u. where the blank buffer is about 100 a.u., for samples of 100 μL). With 150 μL samples, the precision could be up to 0.01 $\mu g/mL$. However, a precision of 0.5 $\mu g/mL$ corresponds to 0.5% of the initial LY concentration, which is largely sufficient for our needs, as

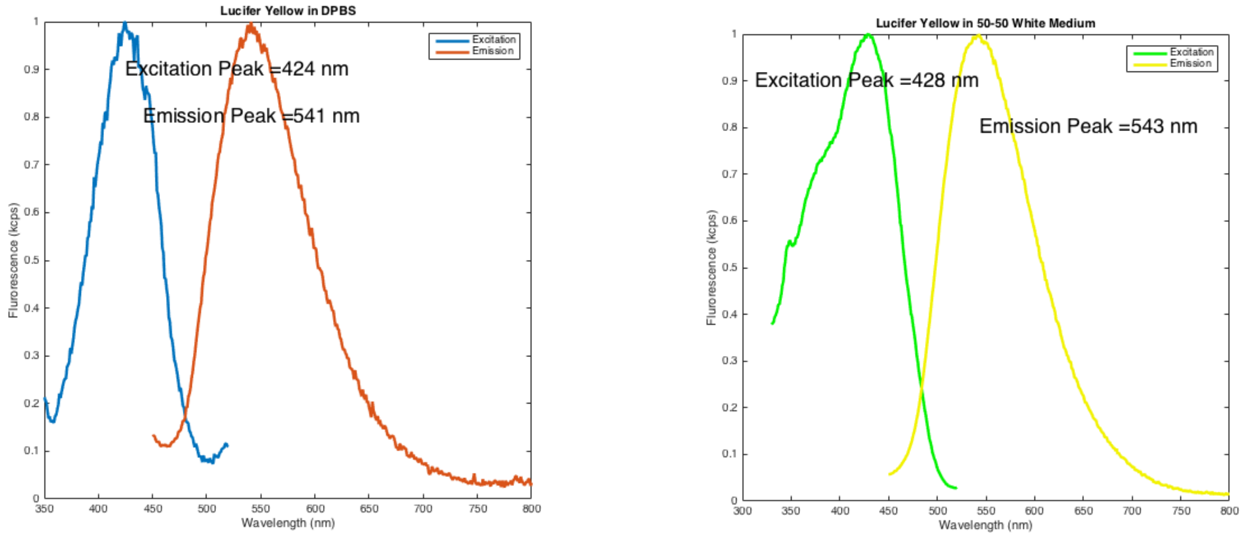

(a) Lucifer Yellow in DPBS

(b) Lucifer Yellow in 5050 Buffer

Figure 2.39: Excitation/Emission spectra of Lucifer Yellow in PBS and in the 5050 Buffer. The change of buffer does not change the fluorescence spectrum of the Lucifer Yellow. This experiment was done to set up the reading parameters of the plate reader.

we usually consider that a barrier integrity is confirmed as long as less than 3% of solution has crossed the barrier [45].

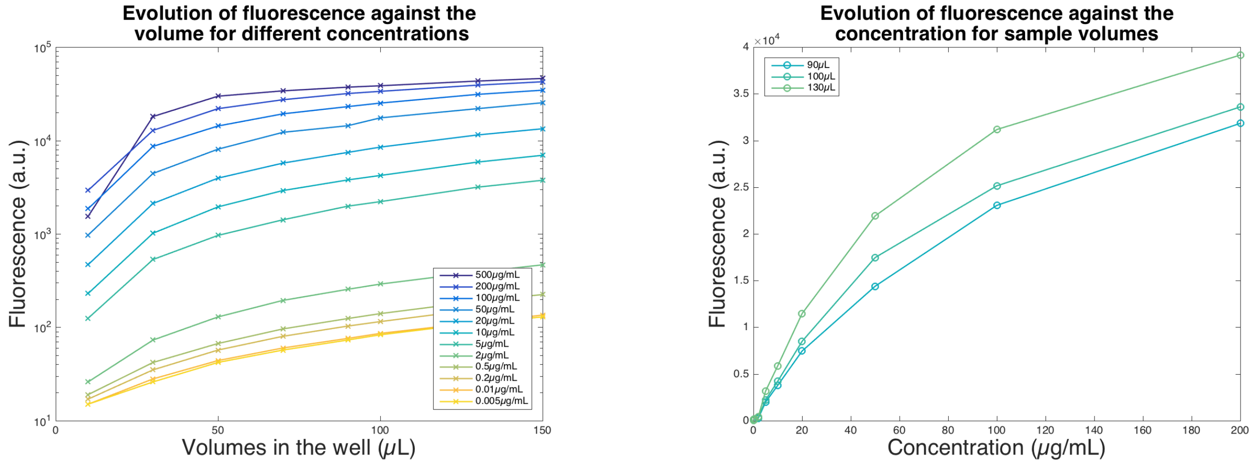

(a) Effect of volume on the fluorescence

(b) Standard curve for 3 different sample volumes

Figure 2.40: Influence of sample volume and sample concentration on the overall measured fluorescence

b. Tests and Results

First testing As a first attempt, we decided to measure the permeability of our alveolar tissue on Transwell inserts, as a control. We used 0.4 μm-pore Transwells. The study was performed with 400 μL of a 100 $\mu g/mL$ solution of LY deposited in the top chamber. After 1 h of incubation at 37 °C, two samples of 100 μL of the lower chamber were placed in a 96-well plate and observed with our plate reader. This was repeated every other day for 21 days on 8 different conditions: A549, A549 with Dexamethasone treatment, A549 in ALI, A549 in ALI with Dexamethasone treatment, HUVEC, HUVEC+Dex, A549+HUVEC and A549+HUVEC+Dex. The results can be observed in Figure 2.41. Each point is the mean of the two 100 μL samples, and the standard deviation is plotted.

Surprisingly, there is no trend over time, neither is there any difference between the conditions tested (see Figure 2.41). For all conditions, including the blank Transwell (no cells), the detected fluorescence varies randomly over time. We can still observe a difference between the control and the inserts with cells, which means that there is a difference in permeability that we are able to detect, but the variations from one day to another are in the range of the noise of our experiment.

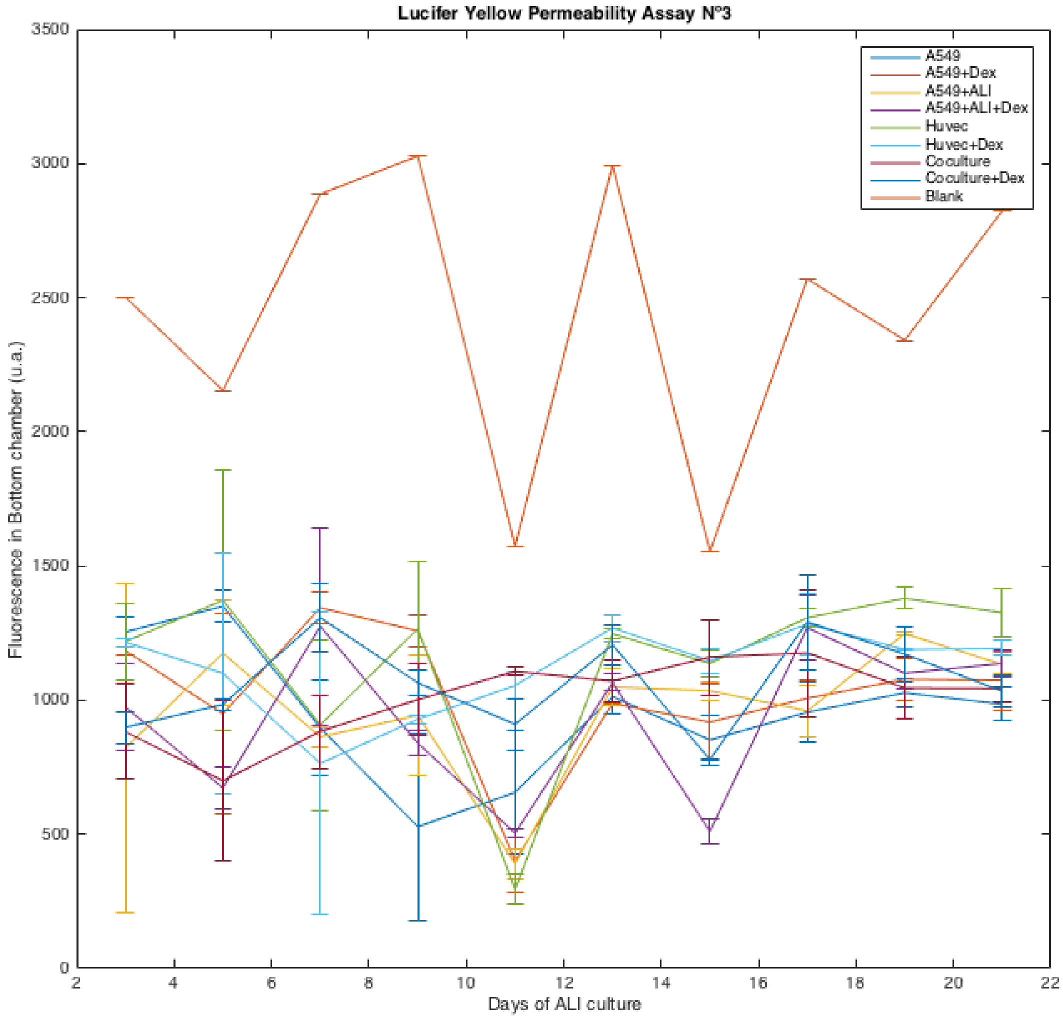

Figure 2.41: Results of a failed experiment to follow the evolution of the transport across the alveolar capillary barrier model cultured on 0.4 µm pores Transwell inserts. Measure of the fluorescent intensity of Lucifer Yellow particles incubated on the apical surface for an hour.

In order to accurately monitor the evolution of LY translocation over a few days, we need to reduce the noise. The first source of noise is the possible variation of fluorescence of the Lucifer Yellow solution used every day. This can be explained by possible variations in preparations (the stock solution is 10X) or by loss of fluorescence over time. For further experiments, it was decided to prepare once the exact volume required for all the experiment, and to store the solutions in opaque bottles at all times. This solution will be measured as a control every day and the measured fluorescence will be standardized over this control.
Another explanation for such important noise is the importance of the incubation time. Indeed, with so several samples at a time, they cannot be collected exactly 60 minutes after the beginning of the incubation. There is bound to be a few minutes variation. We wondered whether a few minutes difference would have an important impact on the quantity of Lucifer Yellow that will have crossed the inserts. Moreover, the fluorescence observed were extremely low (about 1500 a.u., whereas the initial solution reached 50 000 a.u.), therefore we wondered whether 1 h of incubation was relevant to observe a minimum of LY transport. In order to study such matter, we performed an analytical computation of Lucifer Yellow transport mechanism across both the Transwell inserts and our microengineered patch.

Lucifer Yellow diffusion process computation We will equate the diffusion of a small molecule, our Lucifer Yellow Dipotassium Salt in water, from one chamber to another, through a porous membrane. Our

buffer is approximated as water, as they have very similar density and viscosity.
Firstly, the diffusion coefficient D of LY in water can be computed as follows:

$$D = \frac{\kappa_B \times T}{6 \times \Pi \times \eta \times r} \tag{2.1}$$

$$\text{With} \begin{cases} \kappa_B = 1.38 \times 10^{-23} J/K, \text{ Boltzmann's constant} \\ T = 310.15K, \text{ the temperature (37°C)} \\ \eta = 1 \times 10^{-3} Pa.s, \text{ the dynamic viscosity of water} \\ r = 5 \times 10^{-10} m, \text{ the radius of Lucifer Yellow} \end{cases}$$

Therefore:

$$\begin{aligned} D &= \frac{1.38 \times 10^{-23} \times 310.15}{6 \times \Pi \times 1 \times 10^{-3} \times 5 \times 10^{-10}} && (2.2) \\ &= 4.5 \times 10^{-10} m^2/s && (2.3) \end{aligned}$$

When diffusing through a porous medium, the diffusion coefficient is changed. According to Grathwohl [78], the effective diffusion coefficient D_{eff} can be computed as:

$$D_{eff} = \frac{D \times \varepsilon \times \delta}{\tau} \tag{2.4}$$

$$\text{With} \begin{cases} D = 4.5 \times 10^{-10} m^2/s, \text{ the diffusion coefficient of Lucifer Yellow in water} \\ \varepsilon, \text{ the porosity of the porous media} \\ \delta, \text{ the constructivity of the porous media} \\ \tau, \text{ the tortuosity of the path through the porous media} \end{cases}$$

The **constructivity** δ accounts for the fact that the cross section of a pore space segment varies over its length. It is viewed to depend on the ratio of the diameter of the diffusing particle to the pore diameter [79]. Here, for both the patch and the Transwell inserts, the membranes have straight and constant pores in the vertical direction, therefore we can estimate that:

$$\delta = 1 \tag{2.5}$$

The **tortuosity** τ assesses the tortuous property of the diffusion path through the pores. The main direction of the diffusion paths is the same as that of the concentration gradient. The tortuosity is equal to 1 if the diffusion paths wind through the pore space as straight streamlines in the porous media. Therefore,

$$\tau = 1 \tag{2.6}$$

The **porosity** ε is defined as the fraction of the volume of voids over the total volume of the media, a dimensionless number comprised between 0 and 1.
For the Transwell inserts, we can compute it as follows:

$$\begin{aligned} \varepsilon_{Transwell} &= \frac{\text{Volume of voids}}{\text{Total volume}} && (2.7) \\ &= \frac{\text{Total Number of pores} \times \text{Volume of one pore}}{\text{Total volume}} && (2.8) \\ &= \frac{\text{Total Number of pores} \times (\text{Area of one pore} \times \text{Thickness of one pore})}{\text{Total area} \times \text{Total thickness}} && (2.9) \\ &= \frac{(\text{Number of pores}/cm^2 \times \text{Total area}) \times (\text{Area of one pore} \times \text{Membrane thickness})}{\text{Total area} \times \text{Membrane thickness}} && (2.10) \\ &= \text{Number of pores}/cm^2 \times \text{Area of one pore} && (2.11) \end{aligned}$$

$$\text{With} \begin{cases} 4 \times 10^6 \text{ pores per } cm^2 \\ 0.4 \mu m, \text{ the mean pore diameter} \end{cases}$$

Hence for a $0.4\mu m$ pore Transwell insert:

$$\varepsilon_{Transwell} = 4 \times 10^6 \times \Pi \times (\frac{4 \times 10^{-5}}{2})^2 \tag{2.12}$$

$$\varepsilon_{Transwell} = 0.005 \tag{2.13}$$

For our microengineered patch, thanks to its extensive characterization (detailed in subsection b.), we can also use the Analyze Particle Function of the ImageJ software in order to directly compute the area of the voids over the total area, and we obtained the following measurement (if we neglect the pores of the gelatin fibers themselves):

$$\varepsilon_{Patch} = 0.006 \tag{2.14}$$

Finally we can compute the effective diffusion coefficient of Lucifer Yellow in water for both membranes:

$$\begin{cases} \text{Transwell}: \ D_{eff_T} = \frac{D \times \varepsilon_{Transwell} \times \delta_{Transwell}}{\tau_{Transwell}} \\ \text{Patch}: \ D_{eff_P} = \frac{D \times \varepsilon_{Patch} \times \delta_{Patch}}{\tau_{Patch}} \end{cases}$$

$$\Rightarrow \begin{cases} \text{Transwell}: \ D_{eff_T} = D \times \varepsilon_{Transwell} \\ \text{Patch}: \ D_{eff_P} = D \times \varepsilon_{Patch} \end{cases}$$

$$\Rightarrow \begin{cases} \text{Transwell}: \ D_{eff_T} = 4.5 \times 10^{-10} \times 0.005 \\ \text{Patch}: \ D_{eff_P} = 4.5 \times 10^{-10} \times 0.006 \end{cases}$$

$$\Rightarrow \begin{cases} \text{Transwell}: \ D_{eff_T} = 2.25 \times 10^{-12} \ m^2/s \\ \text{Patch}: \ D_{eff_P} = 2.7 \times 10^{-12} \ m^2/s \end{cases}$$

Now that we have computed key parameters describing our system, we will focus on the evolution of the diffusion process along the membranes. Our system consists of two chambers of same volume, one above the other. The top chamber is filled with a solution of Lucifer Yellow (C_{max}), whereas the bottom chamber is filled with the empty buffer. At t=0, the separation between the two chambers is removed. We work with the diffusion of a solute (i) in an incompressible fluid (j) therefore we can use Fick's Law of diffusion:

$$j_i = -D_{ij} \times \bigtriangledown C_i$$

$$\text{With} = \begin{cases} j_i, \ \text{the molar diffusion flux of i} \ (mol.m^{-2}.s^{-1}) \\ D_{ij}, \ \text{the diffusion coefficient of i in j} \\ C_i, \ \text{the molar concentration of solute i}(mol.m^{-3}) \end{cases}$$

In our case, we will use the following notations:

$$j = -D \times \bigtriangledown C$$

The mass of solute is also conserved, therefore we can assume that:

$$\frac{\partial C}{\partial t} + \bigtriangledown j = 0$$

Therefore from the previous equation, we can induce:

$$\frac{\partial C}{\partial t} + \bigtriangledown(-D \times \bigtriangledown C) = 0 \tag{2.15}$$

$$\frac{\partial C}{\partial t} - D \ (\bigtriangledown.\bigtriangledown)(C) = 0 \tag{2.16}$$

$$\frac{\partial C}{\partial t} - D(\frac{\partial^2 C}{\partial x^2} + \frac{\partial^2 C}{\partial y^2} + \frac{\partial^2 C}{\partial z^2}) = 0 \tag{2.17}$$

We define the $\vec{u_z}$ as the vertical direction, perpendicular to the membrane. This is also the direction of the diffusion gradient. Because both the Transwell inserts and the patch are round-shaped, our problem is symmetrical in the $\vec{u_x}$ and $\vec{u_y}$ directions, therefore $\frac{\partial^2 C}{\partial x^2} = \frac{\partial^2 C}{\partial y^2}$. Moreover, we assume that the concentration of Lucifer Yellow is homogeneous in each chamber, therefore the concentration is constant along the $\vec{u_x}$ and $\vec{u_y}$ directions, therefore $\frac{\partial^2 C}{\partial x^2} = \frac{\partial^2 C}{\partial y^2} = 0$. We can now resume our computations with:

$$\frac{\partial C}{\partial t} - D(\frac{\partial^2 C}{\partial z^2}) = 0 \tag{2.18}$$

We approximate the diffusion gradient along $\vec{u_z}$ as follows:

$$\begin{aligned} \frac{\partial C}{\partial z} &= \frac{\triangle C(t)}{\triangle z} && (2.19)\\ &= \frac{C_{Top}(t) - C_{Low}(t)}{z_{Top} - zLow} && (2.20)\\ &= \frac{C_{Top}(t) - C_{Low}(t)}{h} && (2.21) \end{aligned}$$

With h the thickness of the membrane. Therefore the second partial derivative is:

$$\begin{aligned} \frac{\partial^2 C}{\partial z^2} &= \frac{\partial}{\partial z}(\frac{\triangle C(t)}{h}) && (2.22)\\ &= \frac{\triangle C(t)}{h^2} && (2.23) \end{aligned}$$

Our equation finally becomes:

$$\frac{\partial C(t)}{\partial t} - (\frac{D}{h^2}) \ \triangle C(t) = 0$$

This differential equation presents a solution of the following shape:

$$\triangle C(t) = \alpha e^{-\frac{D}{h^2}t} + \beta \text{ with}\{\alpha, \beta\} \in \Re,$$

The boundary conditions are as follows: at the initial time, the top chamber is filled with Lucifer Yellow at a concentration C_{max}, and the lower chamber is filled with buffer, hence its concentration in LY is zero.

$$\begin{cases} \text{at the initial time, t=0, } C_{max} - 0 = \alpha e^0 + \beta \\ \text{at equilibrium, t=}\infty\text{, } \frac{C_{max}}{2} - \frac{C_{max}}{2} = \alpha e^{-\infty} + \beta \end{cases}$$

$$\Rightarrow \begin{cases} C_{max} = \alpha + \beta \\ \frac{C_{max}}{2} - \frac{C_{max}}{2} = \beta \end{cases}$$

$$\Rightarrow \begin{cases} \alpha = C_{max} \\ \beta = 0 \\ \triangle C(t) = C_{max} e^{-\frac{D}{h^2}t} \end{cases}$$

Because of the conservation of matter, at all times, $C_{max} = C_{Top} + C_{Low}$, therefore in the bottom chamber the diffusion profile is as follows:

$$C_{Low}(t) = \frac{C_{max}}{2}(1 - e^{-\frac{D}{h^2}t})$$

We extract from this equation the characteristic time of diffusion: $\tau = \frac{h^2}{D}$. At a time $t = 2\tau$, the system reached 95% of its equilibrium (and 99.3% at $t = 3\tau$).

This can be extended to the model of diffusion through a porous membrane by replacing the diffusion coefficient D with the effective diffusion coefficient D_{eff} computed previously. Therefore, with a patch thickness of about 1 μm and 10 μm for the Transwell inserts, we can compute that, for each system, the equilibrium is reached after:

$$\begin{cases} \text{Transwell : } 2\tau = 2 \times \frac{(10 \times 10^{-6})^2}{2.25 \times 10^{-12}} \\ \text{Patch : } 2\tau = 2 \times \frac{(1 \times 10^{-6})^2}{2.7 \times 10^{-12}} \end{cases}$$

$$\Rightarrow \begin{cases} \text{Transwell : } 2\tau = 88.8 \ s \\ \text{Patch : } 2\tau = 0.74 \ s \end{cases}$$

We demonstrated here that the characteristic time of diffusion through the membranes are not of the same order of magnitude. The time that we have computed here is the time require to cross the membrane: it is not the time required for the complete diffusion. We only compared the crossing of the membranes because they are the limiting element. This explains why, during experiments, we observed that the Lucifer Yellow crossed the patch much faster than the Transwell. Indeed, by eye only, I could see that after one hour, the blank Transwell did not reach equilibrium at all.

In order to have to comparable systems, we considered switching to 3 μm-pore-size Transwell inserts. Indeed, with a pore density of $2 \times 10^{-6} pores/cm2$, these inserts have a characteristic time of diffusion τ such as:

$$2 \times \tau = 3.12\ s$$

This order of magnitude is closer to that of the patches. However, when we tried to use 3 μm-pore-size Transwell inserts we realized that we could not see HUVEC on the basal side of the membrane because the droplet of medium would cross the membrane, leaving cells to dry before they could adhere.

Final tests Finally, we decided that we could not use Transwell inserts to compare the integrity of our cells on regular inserts versus our patch. We just decided to monitor the evolution of Lucifer Yellow on our patches. Because the gelatin nanofibers are very sensitive, we decided not to monitor every other day. Moreover the patches are variable from one to another (due to the electrospinning step), therefore we were not interested in determining a strict value of permeability, but just in observing the formation of a tigh tissue. In the Figure 2.42, we can see the evolution of the permeability of 4 patches as well as a control patch without cells. This permeability is defined in percentage, such as, for a Patch P and a day D:

$$Permeability(PatchP, DayD) = \frac{Fluorescence(PatchP,DayD)-Fluorescence(Buffer,DayD)}{Fluorescence(LYSolution,DayD)-Fluorescence(Buffer,DayD)}$$

This confirms our immunostaining observation that our model starts to form tight junctions after 15 days (low permeability), and that these are widespread after 20 days (with a permeability that continues to diminish). On day 22 the experiment was stopped to perform a nanoparticle translocation assay (see next section).

c. Conclusion

Results Our Lucifer Yellow assays were not very convincing. Due to the fragile nature of the microengineered patch, we could not mount the translocation PDMS chambers every day. However, in working on the Lucifer Yellow assay we have optimized these translocation chambers for future nanoparticle assay. Indeed, the high concentrations of Lucifer Yellow would undoubtedly indicate if there was a leak from the top to the lower chamber.

We could use our technique to estimate the overall integrity of our cells. Each patch is different, therefore we could not perform direct measurements of our barrier permeability. However, we could observe it this permeability was diminishing over time as the cells are growing and as the Dexamethasone treatment induces their maturation. It can also reveal if a patch is defective.

Finally, we were able to demonstrate that our co-culture model gains integrity over time, and reaches an almost stable minimum from 15 days of Dexamethasone treatment. In the future all translocation experiments will be performed after a minimum of 15 days of co-culture with dexamethasone treatment.

Perspectives In order to be able to give a precise value of our patches' permeability, we could try two techniques. Firstly, we could either perform the Lucifer Assay on a great number of patches to normalize the patch-to-patch variation. However, this would require an important amount of time and effort for an improbable result. The other technique would give a permeability value per patch: we could measure each patch's permeability without the cells, and then use it to normalize the data. Therefore we would be able to announce a percentage of reduced permeability.

2.5 Alveolar barrier protection: nanoparticle translocation analysis

Our work here aims at developing a novel *in vitro* model of the alveolar capillary barrier, in order to study the mechanisms of nanoparticle to cell interactions at the cellular level. In order to test our model, we incubated it with silica nanoparticles and observed their influence on our cells. In the following part, we present the interest of studying silica nanoparticles (NPs) and what can be examined when looking at interactions at the cellular level, then detail how our NPs were obtained and characterized, then we will move on to the experiments on the cells.

2.5.1 Nanoparticles translocation studies

a. Description of silica nanoparticles

Encountering silica nanoparticles Silica nanoparticles are generally created as by-products of sand mining, quartz purification or microfabrication processes [2]. When divided into particles below a hundred microns wide, inhaled $Si0_2$ was shown to trigger health hazards. Indeed, these particles do not dissolve in the body

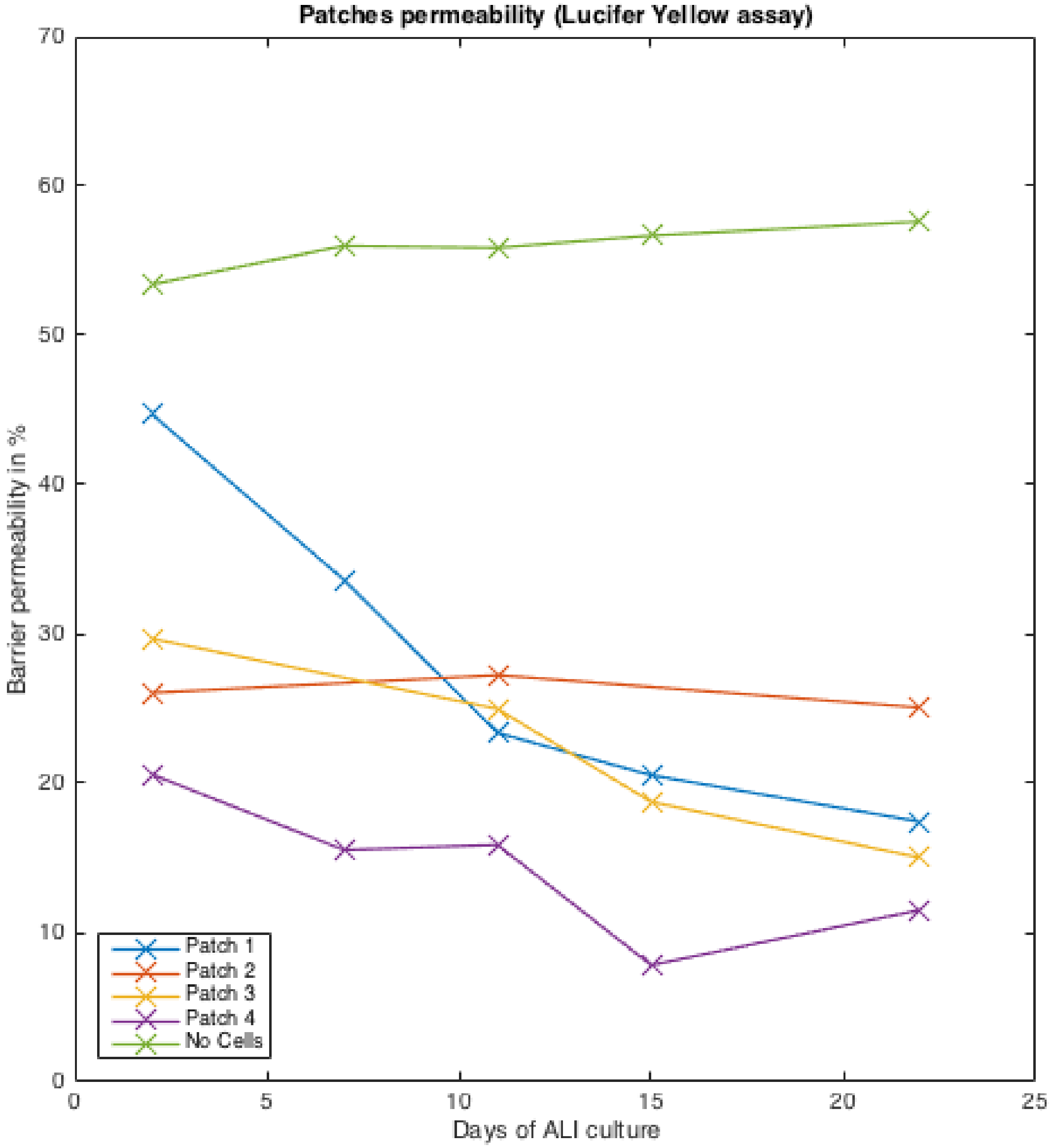

Figure 2.42: Evolution of the transport across the alveolar capillary barrier model cultured on the patch. Measure of the fluorescent intensity of Lucifer Yellow particles incubated on the apical surface for an hour.

and stay inside the lungs, activating inflammatory responses [80]. The effects of these particles on the alveolar barrier are dose-dependent; that is why the same particles are also used for therapeutic reasons.
Indeed, we are starting to use functionalized nanoparticles use as nanovectors for specific targeted therapies. Silica nanoparticles are good candidates for these researchs [81] because they are optically transparent, have a controllable porosity, can be chemically inert, and even biocompatible, depending on the doses used ([82], [83]).

Properties These nanoparticles are made of silicon dioxide ($Si0_2$), forming amorphous or crystalline structures. Its molar mass is 60.08 g/mol and its density reaches 2.196 g/cm^3 for the amorphous form. This means that a nanoparticle 50 nm wide weights 0.0575 ng and contains about 1.05 x10$^($12) moles of silicon dioxyde. The amorphous $Si0_2$ particles have a negative charge, but can be coated with carboxylic (-COOH) or amine (-NH2) groups to change their surface properties.

b. State-of-the art: Methods to assess the impact of inhaled Si02 nanoparticles in the alveoli

When inhaled nanoparticles reach the alveolar space, there are many interactions that can occur with the alveolar elements. Firstly, the alveolar macrophages present can phagocytose the NPs if they are in contact.

The second component of the alveoli encountered by the NPs is the alveolar surfactant, which will impact each type of NPs differently. After this encounter, the NPs will be deposited on the cells [84]. From then on, they can either stay on the surface of the cells and adhere to their membrane, or they can be internalized and/or, finally, they can be exocytosed back in the alveolar space or towards the endothelial cells, through their basal surface ([85], [86]). The same steps can then occur for the interaction with the endothelial cells. This is why is it so complicated to accurately predict the fate of nanoparticles in the lung: it is a cascade of reactions where each step is highly dependent on the physico-chemical properties of the particle.

Interaction with the surfactant For the nanoparticles to enter inside the surfactant, they have to cross the phospholipid bilayer at its surface. This first interaction can result in the formation of different complexes. The NPs can aggregate and be encapsulated by phospholipid vesicles, either a single or multiple vesicles (see Figure 2.43). Another possibility is the formation of big complexes with NP aggregates acting as a glue between several vesicles [5].

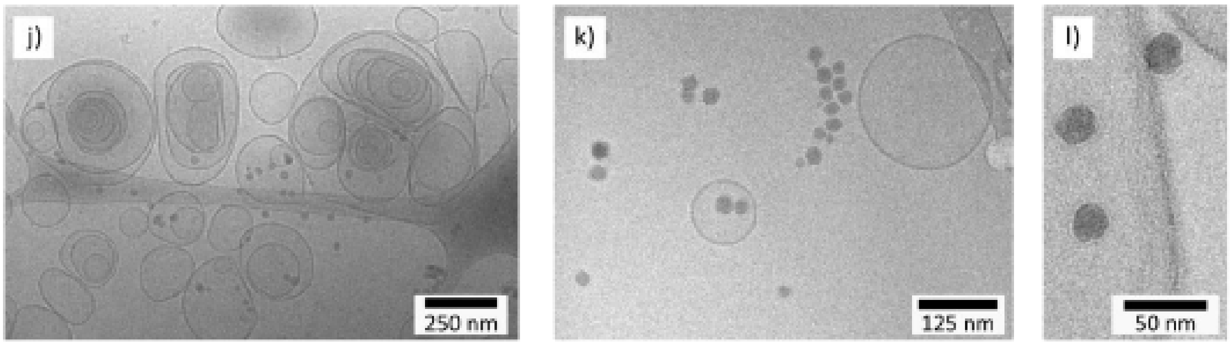

Figure 2.43: Cryo-TEM images Curosurf interacting with 50 nm negatively charged Silica nanoparticles: (i) NPs inside multilamellar vesicles, (j) NPs aggregated in solution and (l) NPs coated with a phospholipid bilayer *Scale bars: 100 nm. Courtesy of Fanny Mousseau*

If the NPs were to cross the phospholipids without interacting with it, once they are bare inside the surfactant they can react with its proteins (SP-A, SP-B, SP-C and SP-D). These can form a corona on the NPs, resulting in a coating that is specific to the NPs ([87], [88], [89]). This corona reduces the free energy of the surface of the nanoparticles, thus resulting in a lower uptake of these NPs compared to the bare NPs.
In order to determine the specific NP-surfactant interaction, researchers tried to put different nanoparticles in contact with alveolar surfactant models (with or without proteins) and observed the complexes formed with Transmission Electron Microscopy [90] or Cryo-TEM ([91], [92], [5], [89]).
Finally, there are many different fates for a nanoparticle entering the alveolar surfactant (see Figure 2.44). These interactions are important because they change the surface of the particles, hence their recognition by the cells. Understanding such processes will help understand the mechanism by which the cells act on the NPs. That is why several *in vitro* models use surfactant models such as AlveoFact (a neonatal surfactant substitution origi- nated from bovine alveolar lavage and composed of surfactant proteins SP-B and SP-C as well as phospholipids) [55] or Curosurf (a commercially available natural porcine lung surfactant that contains the hydrophobic fraction of the complete surfactant) to model these interactions ([93], [94],[95], [86]) as in Figure 2.43. All of these studies found that the addition of surfactant resulted in significant decrease of nanoparticle toxicity.

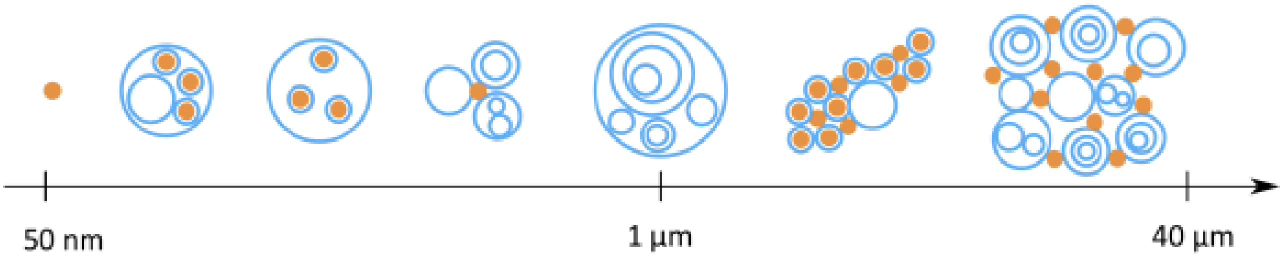

Figure 2.44: Different examples of NP-surfactant complexes of agglomeration and encapsulation (Nanoparticles in red and surfactant vesicles in blue). *Courtesy of Fanny Mousseau*

Impact on the cells When the nanoparticle complex reaches the cells, it can have different impacts on the cells such as toxic effects inducing apoptosis or an inflammatory response, or triggering cell modifications.
The toxicity of the NPs on the cells is often determined either by direct observation of the cells, or with assays such as MTT assay ([96], [97]) or WST-1 assay ([52], [45], [86]).
The inflammatory response can be determined by monitoring the level of inflammatory cytokines (interleukins 1,2, 4, 6, 8 and 10 or TNF-α) or the levels of oxydative stress markers (HO-1 or SOD2) or both ([52], [56], [82]). Most studies found that both the toxic effect of the NPs and the inflammatory response of the cells are dose-dependent.
If the toxicity of the nanoparticle complex has not killed the cells, the inflammatory response may trigger specific cell changes such as the reorganization of its cytoskeleton [45] or the beginning of an internalization process. It would be interesting to perform some live imaging to observe exactly how these modifications take place.

Localization When the nanoparticle complex interacts with the cells, it can either adhere to the cell membrane or be internalized by the cells. The adhesion process is often correlated with the outer surface of the particles, especially the protein corona that may have formed ([88], [89]) . The internalization will then begin or not, depending on the particle physico-chemical properties and size. And finally, for the NP complex to cross the alveolar membrane, it should translocated across the epithelium. This process can either be active or passive.
In order to determine whether the NP complex is internalized, researchers use fluorescent nanoparticles and observe their localization in the cells after an incubation (of 10 minutes up to a few days) using confocal microscopy ([93], [57], [45], [86]).
Once the particles are internalized by the cells, it is interesting to look at where they are localized. Indeed, in the case of models with different types of cells, it was observed that the NP uptake can be mainly inside the macrophages but only if the particles reach a certain size ([57], [98]), whereas it was often observed that they are not taken up by endothelial cells ([96], [49], [57], [55]).

Mechanism In order to determine whether the internalization process in an active or a passive process, a widespread method is to perform NP incubation on the cells at 4 °C. At this temperature, the active mechanisms of the cells are significantly inhibited [99].
The translocation mechanism can also be influenced by external parameters such as flow-induced shear stress or breathing-induced mechanical stretch or which was shown to increase the percentage of translocated particles [12] by reducing barrier permeability [100].

2.5.2 Nanoparticles characterization

a. Size

We work here with nanoparticles obtained from Sigma Aldrich (Ultrastable fluorescent silica nanobeads Ref.797952).They were suspended to 1 mg/mL in sterile PBS and sonicated for 20 minutes before use. Before starting our experiments on our alveolar barrier model, we first characterized these particles in terms of size.

DLS principle We used Dynamic Light Scattering (DLS) to determine the apparent hydrodynamic diameter (Dh) of our particles. We used a Malvern Zetasizer Nano ZS instrument (single angle measurements at 173 °, He-Ne-Laser with l = 633 nm). The particle stock solution was diluted in our **LY buffer** to 100 µg/mL before observation. This buffer, adjusted to pH 7.4 is composed of:

- 500 mL HBSS
- 12.5 mL of 1 M D-Glucose
- 10 mL of 1 M HEPES
- 1 mL of 625 mM $CaCL_2$
- 1 mL of 250 mM $MgCl_2$

Observed results We measured with the DLS method an apparent hydrodynamic diameter of 50 ±6.5 nm (see Figure 2.45). This confirmed that our particles have the designated size and that they did not aggregate in our LY Buffer.

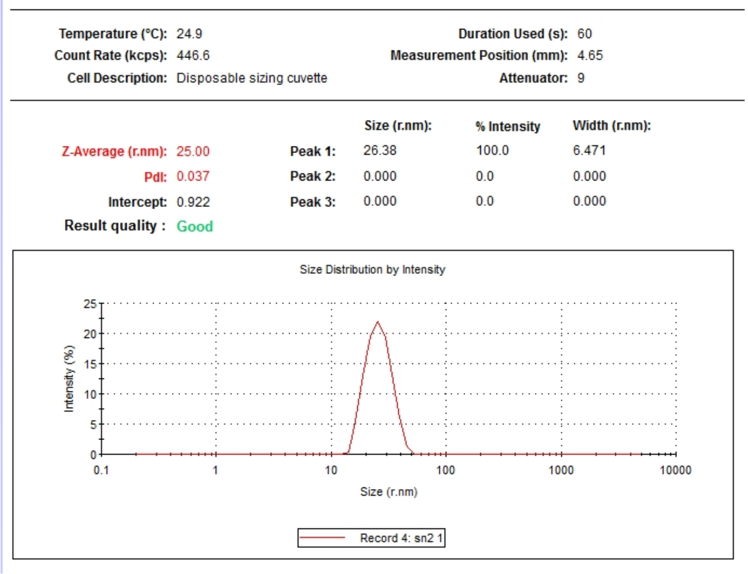

Temperature (°C):	24.9	Duration Used (s):	60
Count Rate (kcps):	446.6	Measurement Position (mm):	4.65
Cell Description:	Disposable sizing cuvette	Attenuator:	9

			Size (r.nm):	% Intensity	Width (r.nm):
Z-Average (r.nm):	25.00	Peak 1:	26.38	100.0	6.471
PdI:	0.037	Peak 2:	0.000	0.0	0.000
Intercept:	0.922	Peak 3:	0.000	0.0	0.000
Result quality :	Good				

Figure 2.45: The hydrodynamic diameter of our $Si0_2$ particles was measured with Dynamic Light Scattering analysis

b. Toxicity

The next step was to assess the cytotoxicity of our particles. Indeed, we are interested in the translocation across the alveolar barrier, but these mechanisms will be biased if the quantity of nanoparticles damages the cells.

Protocol We seeded HUVEC and A549 cells on glass coverslips for 48 hours then incubated them with nanoparticles dilutions from 5 to 100 µg/mL. After 24 hours of incubation at 37 °C, the samples were fixed and stained with sirActin (in green) and Hoechst (blue) in order to observe any changes in the cell morphology.

Results For high concentrations of particles (*i.e.* 100 µg/mL for A549 and 75 µg/mL for HUVEC), the cells were almost all dead and detached (see Figures 2.46f, 2.47e, and 2.47f). At 75 µg/mL, the A549 cells exhibit numerous vacuoles and the cytoskeleton seems to have burst (see Figure 2.46e). At 50 µg/mL, the actin filaments are disorganized compared to the control (see Figure 2.46d). Below this concentrations, the A549 cells did not exhibit a particularly disturbed organization (see Figure 2.46).
Regarding HUVEC, at 50 µg/mL it seems that the cells are less elongated but we do not see vacuoles or an important cell detachment (see Figure 2.47d). Below this concentration, the cells do not exhibit disturbed morphologies (see Figure 2.47).

Conclusion This first toxicity assay enabled us to observe the important cytotoxicity of our Silica nanoparticles on our epithelial and endothelial cells from concentrations from 50 µg/mL and above. Interestingly, the important toxicity of silica nanoparticles at 100 µg/mL had been reported in the literature [97]. However, if they observed a mild toxicity at 10 µg/mL, they did not test it for concentrations in between. Based on our results, in the future, we decided to perform our translocation assays with concentrations ranging from 0 to 50 µg/mL.
These toxicity assays were a first qualitative method to assess the toxicity of our nanoparticles. For more precision, it would be interesting to use more specific techniques like a WST-1 or MTT assays

2.5.3 Translocation tests

a. Material and method

In order to assess the behavior of our static model of the alveolar barrier, we performed nanoparticles translocation tests. We used the PDMS chambers optimized for the Lucifer Yellow assays and the particles previously characterized. Co-cultures with Dexamethasone treatment at day 22 of culture were used for this experiment. We first measured the barrier integrity with a 1 h incubation with Lucifer Yellow in LY Buffer according to the protocol detailed previously. Then the particles were incubated on the patches, at respectively

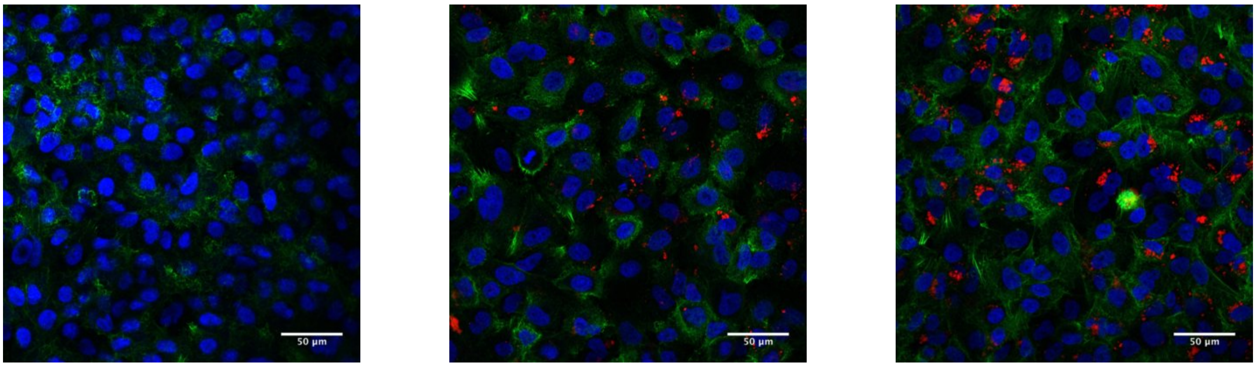

(a) Control (b) 5 µg/mL (c) 25 µg/mL

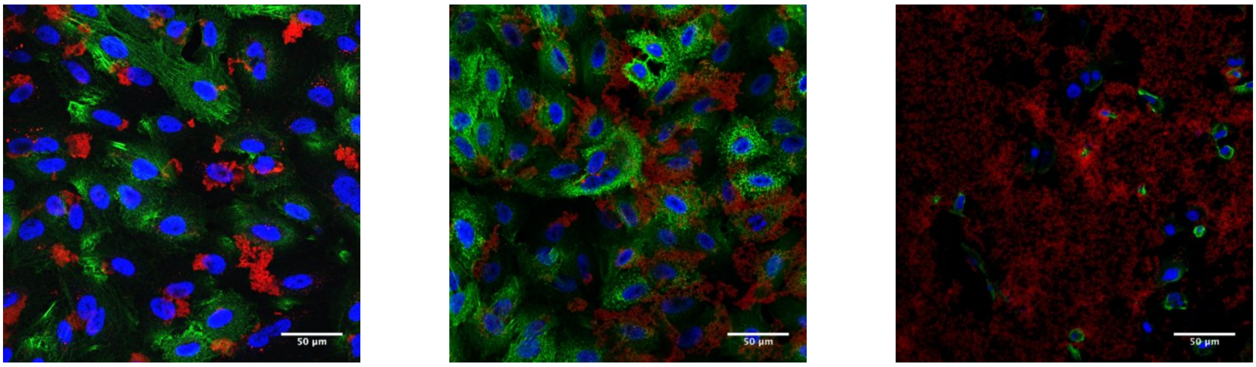

(d) 50 µg/mL (e) 75 µg/mL (f) 100 µg/mL

Figure 2.46: Toxicity of $Si0_2$ nanoparticles on A549 cells cultured on glass coverslips and incubated for 24 hours with the NPs.
Red: $Si0_2$, Green: actin, Blue: Nuclei. *Scale bars: 50* µ*m*

5, 10, 25 and 50 µg/mL, with a duplicate for each condition. After 24 hours of incubation at 37 °C, the NPs were collected in the top and lower chambers and their fluorescence was observed with a plate-reader. Immediately after, the NPs samples from the lower chambers were deposited on A549 cells growing on coverslips for 24 hours. These samples were incubated for 24 hours then fixed. This enabled us to observe the particles post-translocation.

b. Results

Impact of NPs on barrier integrity The Lucifer Yellow assays were performed with exactly the same chamber attributed for each patch from one day to the next to minimize the experimental variability. The paracellular transport of LY accross our barrier seemed slightly different before and after the nanoparticle incubation as we observe an increase of permeability at day 23 (see Figure 2.48). Therefore it seems that, for the concentrations used here, the nanoparticles could have altered the alveolar barrier integrity. Interestingly, the major loss of integrity was observed on the patch incubated at the highest nanoparticle concentration. This could indicate a potential toxicity of the particles.
However, it is important to remind here that these measures were performed with only one sample per condition, therefore we cannot conclude with certainty. It would be interesting to repeat the operation with triplicates, as well as with a control sample not incubated with particles.

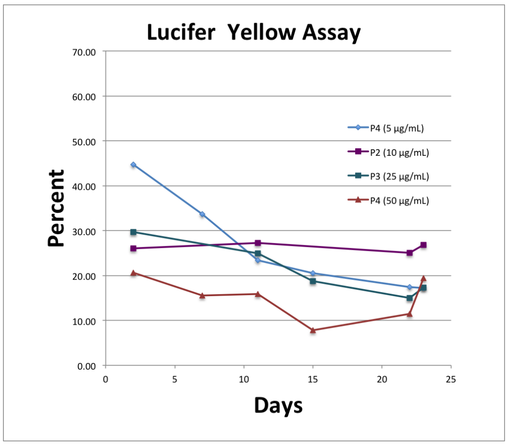

Figure 2.48: Lucifer Yellow assay on the patches

Internalization of the nanoparticles We used confocal imaging and immunofluorescence to assess whether the nanoparticles are internalized and where. The patches were fixed after the 24 hours incubation and they

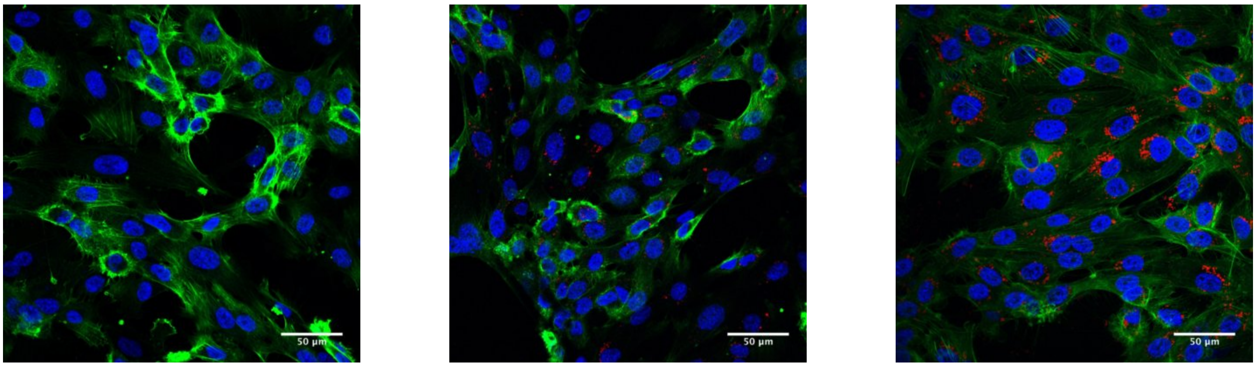

(a) Control (b) 5 $\mu g/mL$ (c) 25 $\mu g/mL$

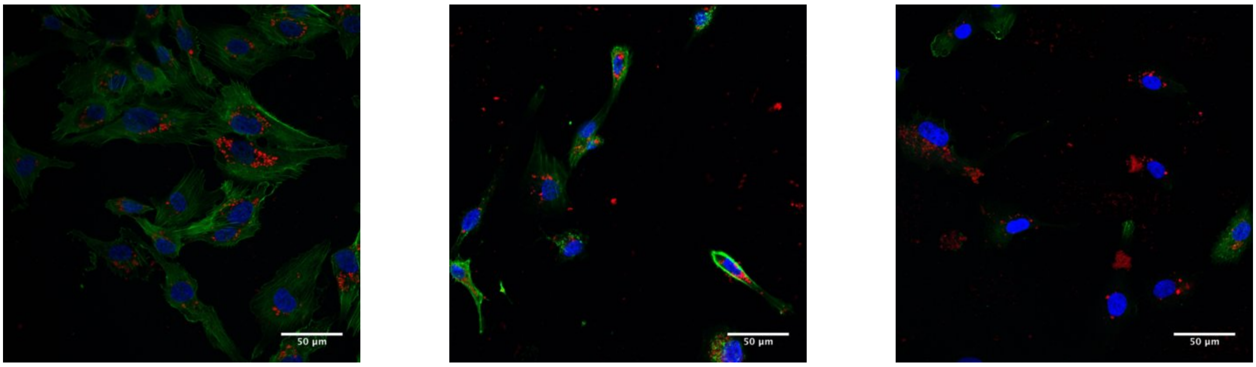

(d) 50 $\mu g/mL$ (e) 75 $\mu g/mL$ (f) 100 $\mu g/mL$

Figure 2.47: Toxicity of $Si0_2$ nanoparticles on HUVEC cells cultured on glass coverslips and incubated 24 hours with the NPs.
Red: $Si0_2$, Green: cytoskeleton, Blue: Nuclei. *Scale bars: 50* µm

were stained for observation.
The results can be seen on the Figure 2.49. These results were obtained from the patch incubated with particles at 25 $\mu g/mL$. The patch was stained with ZO-1 to evaluate the tight junctions (Figure 2.49a in green) and with sirActin to examine the cytoskeleton (Figure 2.49b in magenta).

As we can see in the Figures 2.50 and 2.50a, the nanoparticles are mainly localized on the surface of the A549 cells. We also observed that there are fewer nanoparticles internalized on the patch (see Figure 2.50b) than there were in 2D cultures (see Figure 2.46c). This could be explain by the fact that a part of these particles crossed to the basal chamber via paracellular transport. Moreover, some particles internalized could also be exocytosed to the basal chamber during the 24 hours incubation. It would be interesting to analyze the kinetics of this translocation process to observe how it takes place.

Analysis of the particles post-translocation Using the A549 cells on coverslips to aggregate the particles, we could observe that they were not dissolved by the cells. They were always more particles left in the apical chamber than the basal chamber which indicates that the barrier integrity is important enough, so that the system has not reached a diffusion equilibrium after 24 hours of incubation (for example, see Figures 2.51d, 2.51c and 2.51b).
With the plate-reader, we could assess that for particles incubated at 50 $\mu g/mL$, only 3.9% (±0.7%) of them had crossed the patch and reached the basal chamber. This number reached 4.8% (±0.3%) at 25 $\mu g/mL$, 18.7% (±5.5%) at 10 $\mu g/mL$ and 22.5% (±3.7%) at 5 $\mu g/mL$. It is interesting to see that the more particles, the less they cross the barrier. One hypothesis to explain such result would be that the cells are already engaged with either a small cytotoxicity of the NPs to be performing an active transcellular transport.

2.5.4 Discussion

Discussion We were able to observe the impact of $Si0_2$ nanoparticles on our microengineered alveolar model. This first experiment enabled us to observe that $Si0_2$ nanoparticles deposited onto the patch are partially

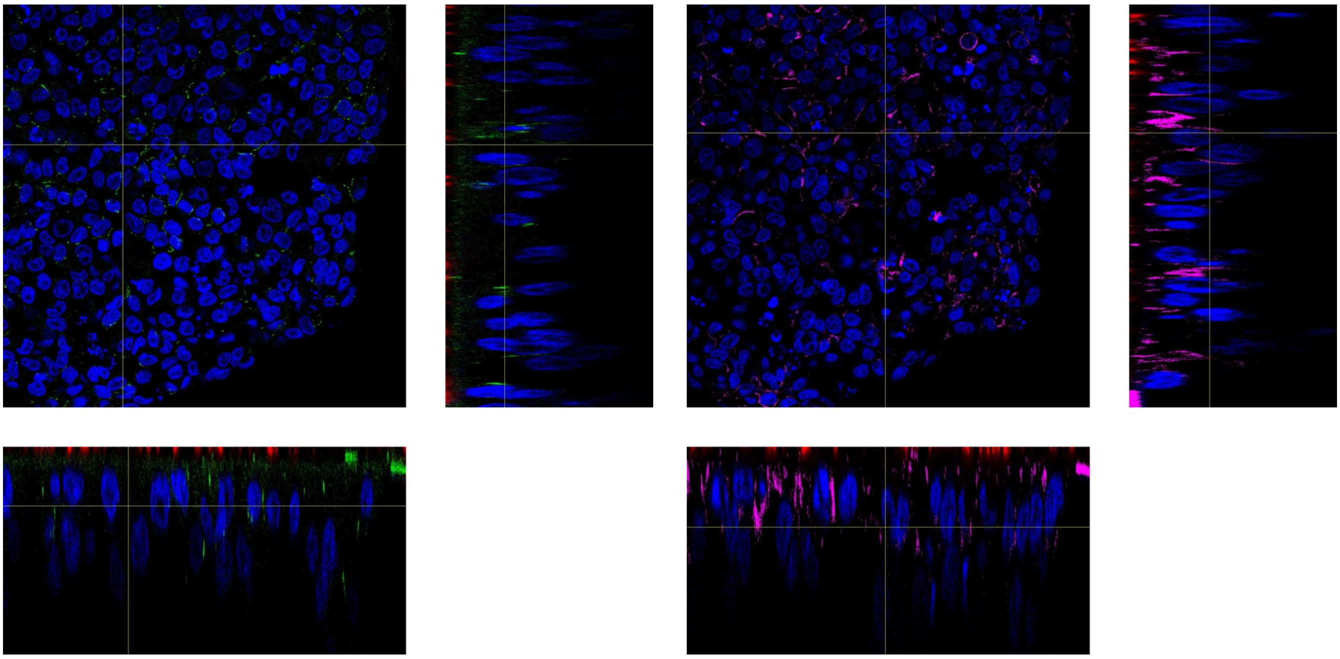

(a) Patch post translocation (Green : ZO-1)

(b) Patch post translocation (Magenta: Actin)

Figure 2.49: Observation of the nanoparticles on the patch after 24 hours of incubation (Day 20). We cannot see here particles internalized in the cell layers.
Red: $Si0_2$ Nanoparticles, Magenta: Actin, Green: Tight junctions, Blue: Nuclei

internalized by the epithelial cells and some reach the basal side of the alveolar barrier.

We could not observe NPs in the layer of endothelial cells (see Figure 2.49a), which confirms the previous observations that endothelial cells do not internalize the nanoparticles in these barrier models [49]. We suppose that this internalization occurs in 2D culture (see Figure 2.47c) but not in these suspended cultures because the HUVEC cells are known to produce weak intercellular junctions. Therefore in 3D the particles deposit at the bottom of the well whereas in 2D they would deposit on the cells, thus forcing an interaction.

Moreover, this experiment did not allow us to understand how the nanoparticles reached the basal chamber: is it an intracellular transport or it is a paracellular transport due to a weakening of the cellular junction ? It would be interesting to perform these experiments at 4 °C because at this temperature the active particle uptake is significantly inhibited ([101], [84]). If the transport is equivalent at 4 °C and 37 °C, this would indicate that the transport is mostly paracellular.

We were also surprised to observe so few nanoparticles internalized on the patch. We wondered if this could be explained by a corona formation on the particles ([88],[45]). Indeed, the cells are grown in Endothelial Cell Growth Media, containing a lot of proteins. If the patches were not rinsed sufficiently, the remaining proteins could coronate the particles thus reducing their internalization. We have also observed that epithelial cells cultured of the patch tend to produce more MUC5AC and surfactant proteins. This seems to indicate that they produce a type of surfactant-like liquid which could interact with the nanoparticles. Indeed, translocation models using surfactant has shown that the surfactant-induced coating of the $Si0_2$ nanoparticles reduces their internalization by A549 cells [86].

Perspectives We wish to repeat this experiment in order to answer the different questions raised here. We wanted to try the nanoparticle incubation for different duration to observe the kinetics of the transport across the cell bilayer. This would enable us to determine whether there is an active endocytosis and which mechanisms are involved.

Another interesting experiment would have been to perform an immunostaining of the patch to be able to distinguish precisely the different types of cells and confirm where the particles are located. Finally, we had planned to used different particles to observe the effect of the size or the charge on the translocation process. This would be interesting to validate our model for different particle conditions.

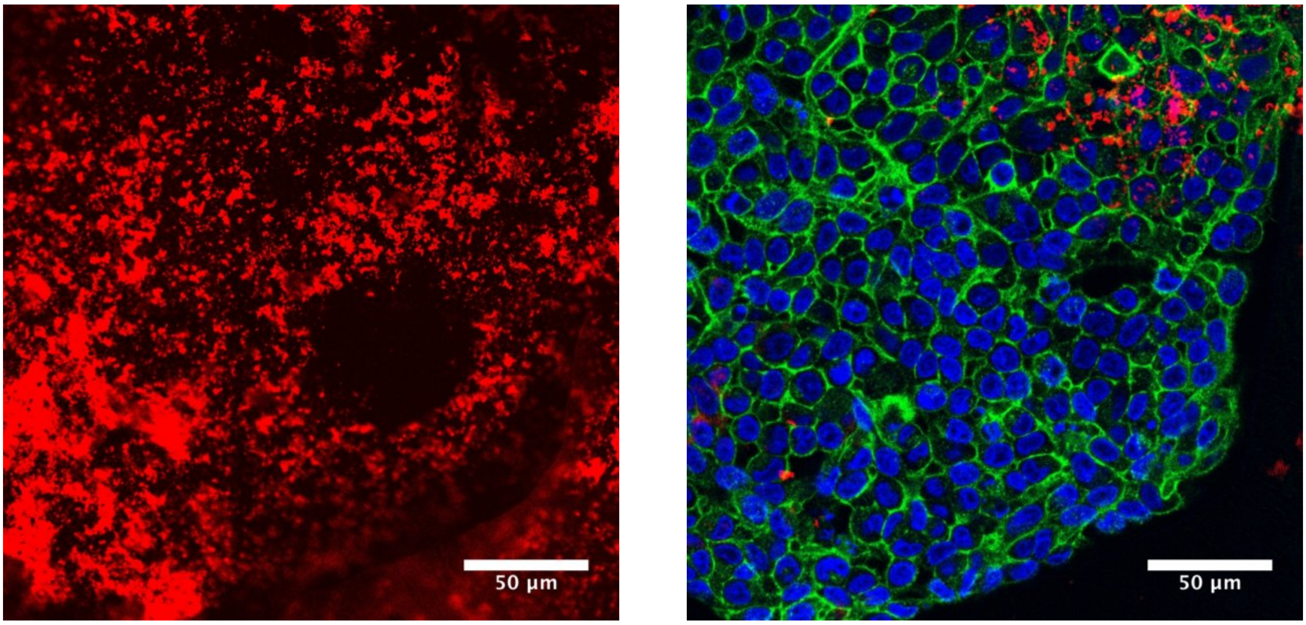

(a) Nanoparticles on top of the patch (b) Internalization of NPs on the patch

Figure 2.50: Observation of the nanoparticles on the patch after 24 hours of incubation (Day 20). There are very few particles internalized and most have deposited on the alveolar epithelium.
Red: $Si0_2$ Nanoparticles, Green: Actin, Blue: Nuclei.

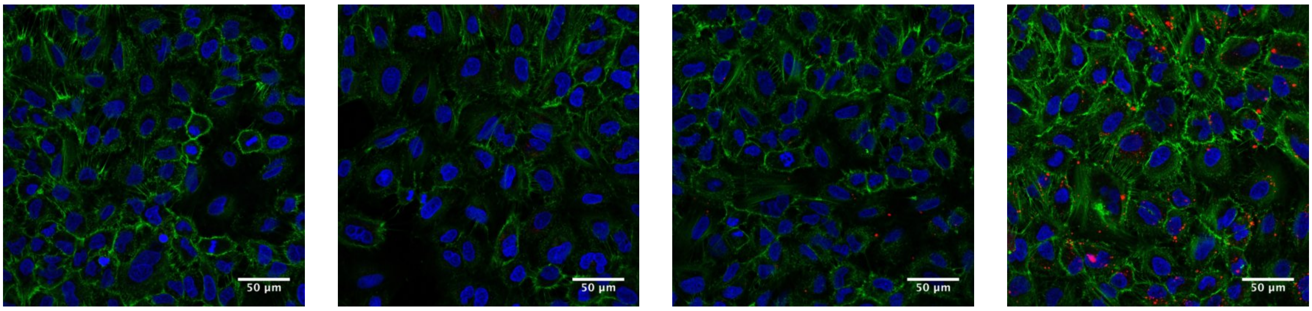

(a) Control: no NPs (b) Without incubation (c) Apical chamber (d) Basal chamber

Figure 2.51: Observation of the particles post-translocation (*i.e.* obtained from the basal chamber of the patch translocation assays), after another 24 h incubation with A549 cells. (Red: $Si0_2$, Green: cytoskeleton, Blue: Nuclei) *Scale bars: 50* µm

2.6 Achievements and perspectives

Method for an alveolar capillary barrier In this chapter, we presented our method to produce a model of the alveolar capillary barrier. This models uses two well characterized cell lines: and HUVEC and A549 cells. The outstanding feature of this model resides in the cell-supporting membrane. Indeed, we offer here a microengineered membrane constituted of a rigid frame supporting a network of gelatin nanofibers. This biocompatible polymer offers a profitable surface for cell growth and intercellular communication through its pores. We achieved a long-term co-culture of both cell types on this patch, with the use of a Dexamethasone treatment to halter cell proliferation and induce the maturation of the tissues.
In the end, we presented an optimized and robust process for the fabrication of this membrane, as well as for the implementation of the co-culture.

Characteristics of our alveolar capillary barrier model In order to characterize our model we observe different specific phenotypes of the alveolar capillary barrier. In our culture conditions *i.e.* at an Air-Liquid Interface (ALI) and with Dexamethasone treatment, we were able to observe consistent production of surfactant proteins SP-A, SP-B and proSP-C, as well as some secretory activity with the presence of MUC5AC. Interestingly, we also observed the presence of Type I markers such as Caveolin1 and NXK2.1.
The A549 cells are known for their variable phenotype, which can vary depending the culture conditions or the different clones generated with time ([72], [44]). With our specific culture conditions, it seems that we obtained

a mixed phenotype, in between Type I and Type II cells, with intracellular transport activity (Caveolin1) as well as surfactant (or surfactant-like) production (SP-A, SP-B, proSP-C and MU5AC). These two cellular activities are all the more important that they all play a major role in particle translocation, which our model is aimed for.

We have also demonstrated the ability of our model to form two cell layers with adherent junctions (E or VE-Cadherin and N-Cadherin). Moreover, with the Dexamethasone treatment, the cells exhibited important tight junctions (Occludin and ZO-1 expression) in both layers.
We later used Lucifer Yellow assays to try and quantify the permeability of our barrier model. We concluded that we were limited by the patch-to-patch variations, and that we could not exhibit one value of permeability for our model in general. However, we used this assay to demonstrate that the Dexamethasone treatment was improving the integrity of the barrier over time, reaching a minimum after 15 days of culture.
Verifying a model's permeability is a crucial step in the development of a translocation model. We could demonstrate here that we generated a barrier with good integrity, as shown by the important cellular tight junction formation but we could not quantify it. It would be interesting to try and implement a TEER measurement of our model to obtain quantitative data on its permeability.

Nanoparticle translocation assay We performed a first test of nanoparticle translocation on our model. We used 50 nm $Si0_2$ nanoparticles incubated for 24 hours on top of our alveolar cells. We have observed a possible incidence of these particles on the permeability of our cell layer. This could be due to a potential toxicity of the nanoparticles. We have also observed that only epithelial cells internalized the nanoparticles.
This first experiment allowed us to demonstrate that we can use our model for particle translocation analysis. However, it would be interesting to do more tests and try and understand whether this mechanism is passive or active. In the future, we also wish to study different incubation duration as well as different sorts of particles.

Chapter 3

The Alveoli-on-a-chip: microfluidic technologies to recapitulate the alveolar capillary barrier functions *in vitro*

3.1 Introduction

We developed a microengineered *in vitro* model of the alveolar capillary barrier. Our objective is to use this model to understand the interactions of inhaled nanoparticles with the alveolar tissues. However, recent research has shown that the dynamics of the alveoli play a role in the translocation mechanisms of the alveolar barrier. Indeed, it seems that strain in the alveoli induces reactive oxygen species generation and increases nanoparticle translocation [12]. Moreover, we have seen that endothelial cells are remarkably responsive to flow induced shear stress. Under mechanical stimulus, endothelial cells change morphologies and align along the flow or perpendicular to the strain exerted [102]. Furthermore, these stimuli are known to regulate the permeability of the cell layer ([10], [11]). All of these results underline the importance of integrating the mechanical cues of the alveolar environment in our model.

In this chapter, we introduce the Organs-on-a-chips: a novel technology that allows to replicate the complex alveolar mechanical stimuli at the cellular level. We will present a review of the literature on current dynamic alveolar models. We will then present our efforts to create an unique design of microfluidic chip that integrates our microengineered patch. Then we will detail the technical choices and fabrication processes optimized to produce the Alveoli-on-a-chip. Finally, we will present our efforts to recapitulate the dynamic strain and shear stress in the chip, as well as their impact on our *in vitro* model.

3.2 Microfluidic modeling of the alveolar barrier: principle and review of current technologies

3.2.1 Organs-on chip: a revolutionary technology

a. Growing interest for dynamic culture

Limitations of 2D culture As we have seen previously, 2D cell cultures in dishes allowed the scientific community to gain insight on cellular pathways and phenotypes. However, it finally became clear that only a 3D microenvironment could recapitulate intricate cell-cell or cell-matrix interactions as well as complex transport dynamics for nutrients and cell, or other characteristics of complex tissues [103]. Indeed, we need to replicate *in vitro* the complex microenvironment of the tissues in order to observe behaviors similar to the *in vivo* observations [104].

Introducing 3D culture These 2D limitations triggered the development of a new technique: **3D culture**, where several types of cells are cultivated together, on 3-dimensional substrates reproducing both the spatial and chemical environment of the tissue [105]. A specific type of 3D culture is organoid culture, which consists of self-assembled clusters of cells. They proved useful in analyzing signaling pathways or drug responsiveness, because they reproduce the spatial gradient encountered by chemicals compounds reaching the tissues [106]. Some 3D cultures are designed with micro-engineered substrates, often based on hydrogels or other polymers (natural or synthetic) that mimick the extra-cellular matrix (ECM). These matrices help the cells to be able

to move within their architecture, similar to the way cells would move in living tissue [107]. These are thus improved models for cell migration, differentiation, survival, and growth. Furthermore, 3D cell cultures provide more accurate depiction of cell polarization, since in 2D, the cells can only be partially polarized [107]. Moreover, cells grown in 3D conditions exhibit different gene expression than those grown in 2D [107].
For the purposes of drug screening, it is much more useful to test gene expression of *in vitro* cells grown in 3D than 2D, since the gene expression of the 3D cultures will more closely resemble gene expression *in vivo*. Lastly, 3D cell cultures have greater stability and longer lifespans than 2D cultures [108]. This means that they are more suitable for long-term studies and for demonstrating long-term effects of the drug. 3D environments also allow the cells to grow undisturbed as they do not need to undergo regular trypsinization [108].

Limitations of static culture 3D cultures present many advantages compared to 2D culture, but still, they lack an important feature of the human body: dynamics. Indeed, most organs are constantly experiencing dynamics forces in the body: mechanical contraction (heart and guts), inflation/deflation (lung or brain) or flow-induced shear stress (blood vessels or oesophagus). However, these forces were shown to greatly influence organ development or functions ([109], [102]), which means that they are crucial features in reproducing tissue environment. This is why the last generation of cell culture evolved towards a 3D culture with integrated chemical environment and dynamic forces: the **Organ-on-chip** technology. This technology uses microfabrication techniques to recreate the spatial environment of a tissue, then actuates it with the help of microfluidic methods.

b. Organs-on-chips: principle and applications

A short history In 2010, the team of Professor Donald Ingber from the *Wyss Institute for Biologically Inspired Engineering at Harvard University* published a revolutionary paper introducing the **Organ-on-a-chip technology** [12]. They developed a biomimetic microsystem reconstituting the critical functional unit of the alveolar capillary interface of the human lung. Later, Ingber described the Organ-on-a-chip technology as "a microfluidic cell culture device created with microchip manufacturing methods that contains continuously perfused chambers inhabited by living cells arranged to simulate tissue- and organ-level physiology" [29]. From then on, numerous research groups throughout the world have started to develop diverse organs-on-chip such as the kidney, gut, liver, brain, heart, skin, etc...([110], [30])

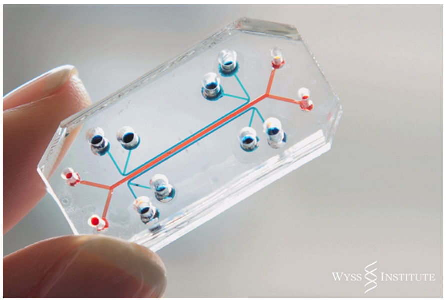

Figure 3.1: An example of an Organ-on-a-Chip. *Wyss Institute*

Organs-on-chip: principle Organs-on-Chips are microfluidic cell culture devices. By recapitulating the multicellular architectures, tissue-tissue interfaces, physicochemical microenvironments and vascular perfusion of the body, these devices produce an accuracy of tissue and organ functionality that was not possible with conventional 2D or 3D culture systems. Altogether, these microchips are highly accurate *in vitro* models of a fonctional organ tissue. Not only do they reproduce the complex features of a functional organ, but they offer practical advantages for laboratory use. Indeed, they enable high-resolution, live imaging and *in vitro* analysis of biochemical, genetic and metabolic activities of living cells in a functional tissue and organ context ([29], [30]). Moreover, while expanding the capabilities of cell culture models, they provide a low-cost alternative to animal and clinical studies for drug screening and toxicology applications.

Applications This technology has great potential to advance the study of tissue development and organ physiology. As an *in vitro* model of a specific tissue, this technology enables scientists to gain insight on the physiology of the tissue. Not only does it replace human or animal testing, but also the Organs-on-Chips permit analyses at the tissue-scale, which was not possible before. Moreover, as we design the microenvironment to grow our cells, we can tune it to observe specific cell response. The influence of the environment's mechanical stimuli such as elasticity modulus, flow shear stress or electric potential can now be directly analysed. Similarly, biochemical gradients can be implemented to observe a dose-response type of cell behavior [111]. These 3D physiological models are especially helpful in translocation analysis [112], [113], [45], [114].
Another application is disease etiology. By tuning the chip's microenvironment we can reproduce and observe the mechanisms at the origin of diverse diseases. For example inflammation factors can be perfused in a chamber to mimic edema [115]. In this way, many diseases have been modeled recently [30]. This allows for

a better understanding of the pathological pathways, in order to design specific drugs. Moreover, once these diseases properly induced into a microchip, these chips could serve as disease models for drug screening. Indeed, in the context of drug discovery and development, these chips can be especially valuable for the study of molecular mechanisms of action, prioritization of lead candidates, toxicity testing and biomarker identification. These chips can determine the toxicity of novel drugs, with better predictability than 2D or spheroid cell culture [115]. At a bigger scale, we can consider the possibility of connecting different Organs-on-Chips to create a sort of "Patient-on-Chip". This would allow for a more global toxicity analysis of certain drugs, as we could test their effects on all organs simultaneously. This could a great way to anticipate potential side effects before even reaching the clinical trial phase.

3.2.2 Developing the lung-on-a-chip

a. Features of the lung-on-a-chip

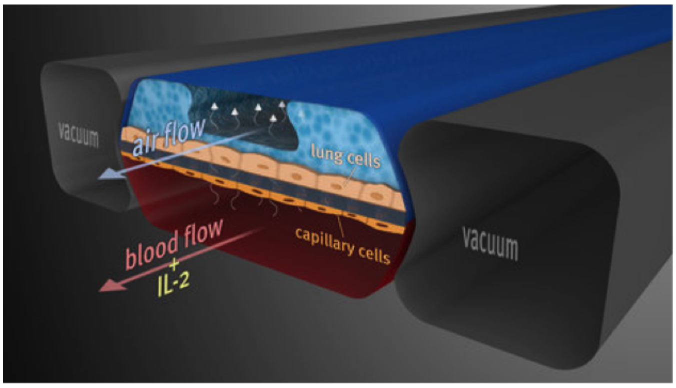

Figure 3.2: Specific features of the Lung-on-a-chip include a co-culture of an alveolar epithelium and an endothelium on a porous membrane. Some chips include microfabricated systems to reproduce the blood flow shear stress and the breathing induced stretching of the cells. *Wyss Institute*

Designing a Lung-on-a-chip represents a technological challenge, in reconstituting all of the several complex features of the functional organ. The generic term Lung-on-a-chip is used to describe any chip that reproduce a part of the lung. Therefore, it can refer to either bronchi-on-a-chip, bronchioles-on-a-chip or alveoli-on-a-chip. These are often associated because they have similar features: a thin **membrane** supporting **both an epithelium and an endothelium**, a vascular **chamber perfused** with nutritive medium mimicking blood flow and an apical **chamber under cyclic strain** mimicking breathing dynamics. Such a sophisticated microsystem can be seen on the Figure 3.2, the *Wyss Institute*'s version of an alveoli-on-a-chip.

In our static microengineered *in vitro* model, we have already reproduced the first two features, *i.e.* a barrier tissue (with an alveolar epithelium and an endothelium) on a thin microengineered membrane.

b. A review of current Lungs-on-Chips

The Lung-on-a-chip was one of the first Organ-on-chip system to be developed. Indeed, the lung is not an easily accessible organ for *in vivo* studies, especially at the microscopic level. Therefore we only have a partial understanding of its functioning and this lack of expertise proves urgent as pollution issues are increasing the number of lung-injury associated deaths.

Different objectives Several groups around the world have worked on recreating a Lung-on-a-chip, with different objectives in mind. However, for reasons that we explained previously, the use of Lung-on-chips as physiological *in vitro* models of the airway barrier for fundamental research is predominant. If many static studies performed tests for the toxicity and the translocation of nanoparticles, most the Organs-on-chip models are still focusing on understanding the physiology of the lung. Indeed, these dynamic models were used to assess the effect of the dynamic cues that were implemented and controlled for the first time *in vitro* ([59], [116], [100], [117], [58]). The second focus seems to be disease modeling, like pulmonary oedema [7], asthma [118], COPD [118] or thrombosis [119].

Flow only systems Flow-induced shear stress plays an important role in endothelial cells: it influences their organization, protein expression and inflammation state ([120], [102]). Moreover it changes their ability to form a tight epithelium. Therefore in our efforts to create a tight barrier, a first step in improving static cultures is to mimick the blood flow. This is usually performed with a peristaltic pump or a syringe pump, with cell culture medium to mimick blood. Some studies even used citrated human blood [119].

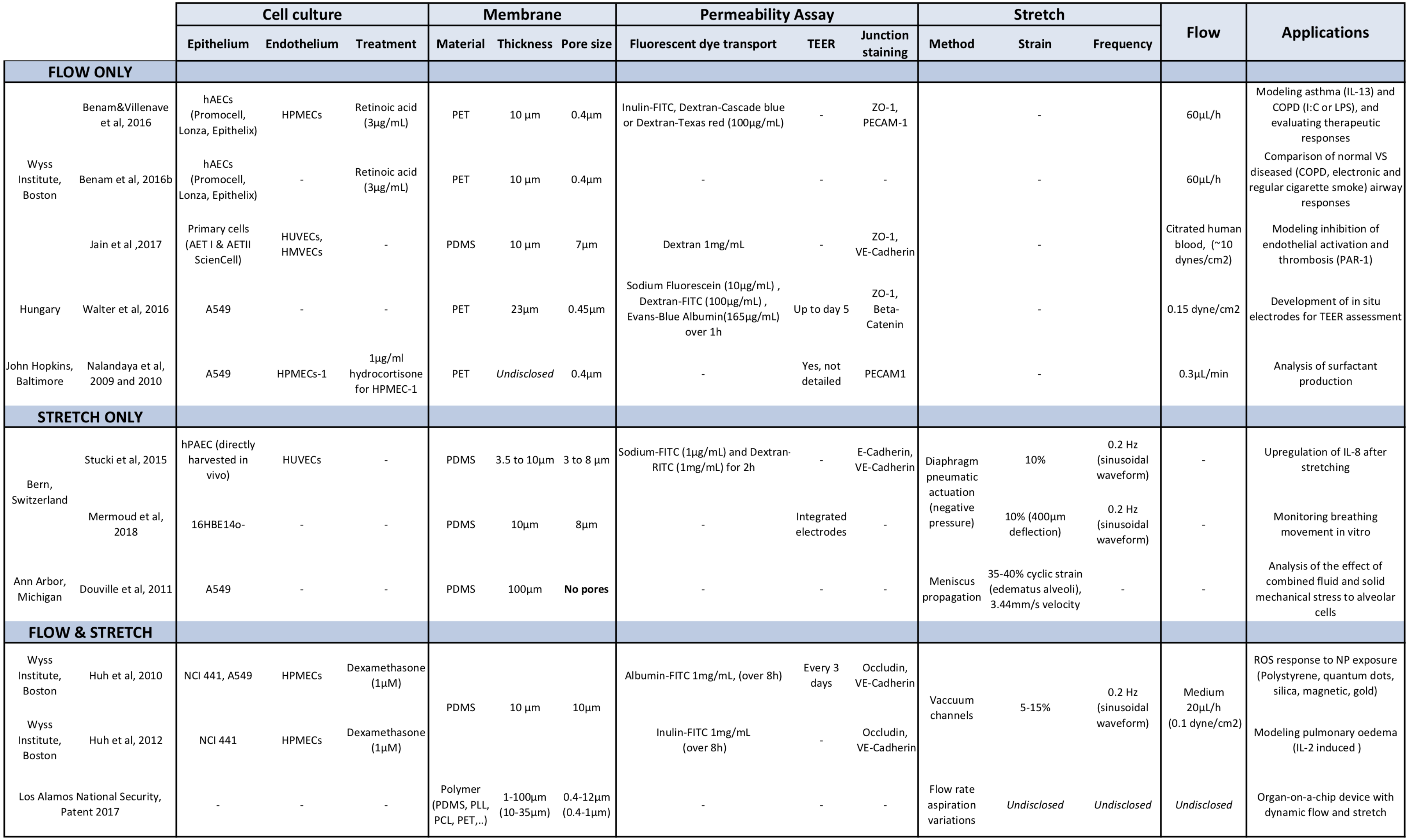

		Cell culture			Membrane			Permeability Assay			Stretch			Flow	Applications
		Epithelium	Endothelium	Treatment	Material	Thickness	Pore size	Fluorescent dye transport	TEER	Junction staining	Method	Strain	Frequency		
FLOW ONLY															
Wyss Institute, Boston	Benam&Villenave et al, 2016	hAECs (Promocell, Lonza, Epithelix)	HPMECs	Retinoic acid (3µg/mL)	PET	10 µm	0.4µm	Inulin-FITC, Dextran-Cascade blue or Dextran-Texas red (100µg/mL)	-	ZO-1, PECAM-1		-		60µL/h	Modeling asthma (IL-13) and COPD (I:C or LPS), and evaluating therapeutic responses
	Benam et al, 2016b	hAECs (Promocell, Lonza, Epithelix)	-	Retinoic acid (3µg/mL)	PET	10 µm	0.4µm	-	-	-		-		60µL/h	Comparison of normal VS diseased (COPD, electronic and regular cigarette smoke) airway responses
	Jain et al ,2017	Primary cells (AET I & AETII ScienCell)	HUVECs, HMVECs	-	PDMS	10 µm	7µm	Dextran 1mg/mL	-	ZO-1, VE-Cadherin		-		Citrated human blood, (~10 dynes/cm2)	Modeling inhibition of endothelial activation and thrombosis (PAR-1)
Hungary	Walter et al, 2016	A549	-	-	PET	23µm	0.45µm	Sodium Fluorescein (10µg/mL) , Dextran-FITC (100µg/mL) , Evans-Blue Albumin(165µg/mL) over 1h	Up to day 5	ZO-1, Beta-Catenin		-		0.15 dyne/cm2	Development of in situ electrodes for TEER assessment
John Hopkins, Baltimore	Nalandaya et al, 2009 and 2010	A549	HPMECs-1	1µg/ml hydrocortisone for HPMEC-1	PET	*Undisclosed*	0.4µm	-	Yes, not detailed	PECAM1		-		0.3µL/min	Analysis of surfactant production
STRETCH ONLY															
Bern, Switzerland	Stucki et al, 2015	hPAEC (directly harvested in vivo)	HUVECs	-	PDMS	3.5 to 10µm	3 to 8 µm	Sodium-FITC (1µg/mL) and Dextran-RITC (1mg/mL) for 2h	-	E-Cadherin, VE-Cadherin	Diaphragm pneumatic actuation (negative pressure)	10%	0.2 Hz (sinusoidal waveform)	-	Upregulation of IL-8 after stretching
	Mermoud et al, 2018	16HBE14o-	-	-	PDMS	10µm	8µm	-	Integrated electrodes	-		10% (400µm deflection)	0.2 Hz (sinusoidal waveform)	-	Monitoring breathing movement in vitro
Ann Arbor, Michigan	Douville et al, 2011	A549	-	-	PDMS	100µm	**No pores**	-	-	-	Meniscus propagation	35-40% cyclic strain (edematus alveoli), 3.44mm/s velocity	-	-	Analysis of the effect of combined fluid and solid mechanical stress to alveolar cells
FLOW & STRETCH															
Wyss Institute, Boston	Huh et al, 2010	NCI 441, A549	HPMECs	Dexamethasone (1µM)	PDMS	10 µm	10µm	Albumin-FITC 1mg/mL, (over 8h)	Every 3 days	Occludin, VE-Cadherin	Vaccuum channels	5-15%	0.2 Hz (sinusoidal waveform)	Medium 20µL/h (0.1 dyne/cm2)	ROS response to NP exposure (Polystyrene, quantum dots, silica, magnetic, gold)
Wyss Institute, Boston	Huh et al, 2012	NCI 441	HPMECs	Dexamethasone (1µM)				Inulin-FITC 1mg/mL (over 8h)	-	Occludin, VE-Cadherin					Modeling pulmonary oedema (IL-2 induced)
Los Alamos National Security, Patent 2017		-	-	-	Polymer (PDMS, PLL, PCL, PET,..)	1-100µm (10-35µm)	0.4-12µm (0.4-1µm)	-	-	-	Flow rate aspiration variations	*Undisclosed*	*Undisclosed*	*Undisclosed*	Organ-on-a-chip device with dynamic flow and stretch

Figure 3.3: Review of current dynamic models of the alveolar capillary barrier

Reproducing breathing movements One of the main challenges of the Lung-on-a-chip is to obtain the specific stretching of the cells that will mimic breathing motions. Four different techniques were developed in the literature:

- Direct mechanical stretching of the membrane, either with vaccuum channels on the sides of the membrane ([7], [7], [121]) as in Figure 3.2. Interestingly, this technology does not directly impact the cells (excepted for the wanted stretch) but it is very complex to implement;
- Indirect mechanical stretching of the membrane, with a pneumatic diaphragm ([100], [117]) as in Figure 3.4. This technology presents the advantage of being similar to the *in vivo* mechanism;
- Meniscus propagation with a compressed fluid ([122], [58]) as in Figure 3.5, easy to implement but does not reproduce the *in vivo* air-liquid interface;
- Micro-aspiration: a difference of input/output flow rate creates a depression in the lower chamber, which deforms the membrane [123] as in Figure 3.6. This negative pressure system reproduces the *in vivo* characteristics of breathing inflation, but perturbs the continuity of the blood flow.

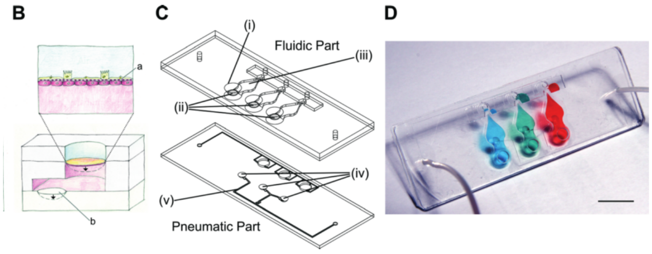

Figure 3.4: Pneumatic diaphragm actuation (Stucki *et al*, 2015 [100])

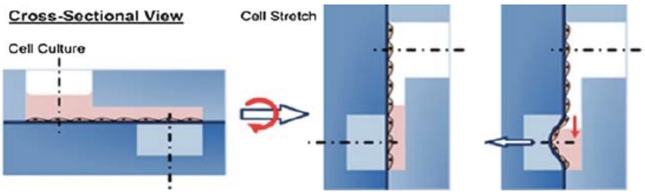

Figure 3.5: Meniscus propagation (Douville *et al*, 2011 [58])

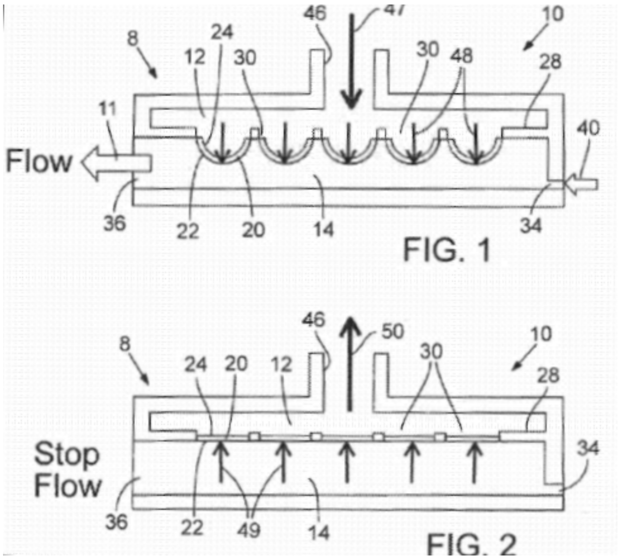

Figure 3.6: Principle of the microfluidic aspirator system (Los Alamos National Security, 2017 Patent [123])

Model validation Similarly to static alveolar capillary models, most of these Lungs-on-a-chip were tested for barrier integrity with immunostaining of junction markers, with TEER (Trans-Epithelial Electric Resistance) measurement or with translocation assays of fluorescent hydrophilic molecules. Endothelial cell alignment was also observed, as well as protein expression correlated to the mechanical stimuli.

c. Current issues and limits

Issuing combined forces It is important to notice that, even though most models presented in the literature have the ability to undergo both cyclic stretch and flow shear stress, a few are actually used with both conditions altogether. Only for some is this intended to analyze the effects of only one of these specific forces [117]. This could be due to the complexity of having cells in culture under stretch without inducing cell death. Indeed, in order to control the stretch effectively applied to the cells, each chip must be extensively characterized to be able to link the energy given to the system (vaccuum negative pressure, pneumatic positive pressure, meniscus positive pressure or micro-aspiration flow rate) to the effective deformation of the membrane. This is not always easy and the negative pressure, for example, is a parameter that can be hard to precisely monitor [7].

Membrane The cell-supporting membrane is also a key parameter in these chips. Indeed, it should be as thin as possible, to reproduce the *in vivo* conditions, with still an notable elasticity to be able to deform under stress, but it should also be robust and reproducible to be used as a standard tool for toxicity analysis. Some groups used standard PET membranes ([118], [124] [125], [59]), whereas some groups developed their own PDMS membranes ([12], [58], [100], [117]). All of these membranes are usually 10 μm thick, which is about 50 times the size of the actual alveolar capillary membrane (0.2 μm). Only Stucki *et al* [100] could propose a thinner membrane, of about 3.5 μm, which is still 17 times higher than the *in vivo* measurements.

A closed environment In addition, these chips have a typical confined microfluidic setting that does not allow for a precise control of injected solutions. Indeed, solutes tend to adhere to the PDMS walls of the channels. This is important because it can compromise precise cell seeding, as well as the dosage of chemical compounds delivered to the cells for disease modeling or drug testing. This closed environment is an important drawback of these Lung-on-a-chip. For some chips, their closed and robust design prevents from performing live-imaging of the cells, and it is extremely complicated to collect the cells for analysis [7].

3.2.3 Conclusion and objectives

a. Conclusion

The Organs-on-chips offer a revolutionary method to accurately reproduce *in vitro* the complex features surrounding a tissue: a specific 3D architecture, a multi-cellular organization, potential flows or gradients of nutrients or chemicals, and even dynamic constraints.

Modeling the Lung-on-a-chip has been particularly looked into because of the current need for a tool to model the lung *in vitro*. These chips aim at becoming a standard for lung testing for biologists, toxicologists and pharmacologists.

However, all of these chips fail to reproduce the close cell-cell contact between the alveolar epithelium and its endothelium. Moreover, they do not allow for an easy access to the cells, either for seeding or for analysis. We will present here our Alveoli-on-a-chip, that proposes technical solutions to tackle these issues.

b. Objectives - specifications of the Alveoli-on-a-chip

After this review of the current models proposed, we highlighted their main faults and advantages. In order to offer a innovative model of the alveolar capillary barrier, we decided to develop an Alveoli-on-a-chip that would meet the following criteria. These were our minimal objectives, and are listed in order of importance.

1. Incorporate our microengineered PEGDA-gelatin patch as a membrane;
2. Comprise a "medium chamber" containing enough medium to allow for cell survival;
3. Comprise an "air chamber" for Air-Liquid interface culture of the alveolar epithelium;
4. Have a watertight separation between these two chambers;
5. Allow cell survival in the confined environment;
6. Be reversible: the patch is to be taken in and out of the chip at any moment;
7. Be available for microscope observation at high magnitude (at least x40);
8. Resist to a continous nutrient perfusion of the endothelium through the "medium chamber";
9. Allow for a controlled deformation of the cell bi-layer through air pressure variation in the "air chamber";
10. Develop a robust and highly reproducible object.

3.3 The Alveoli-on-a-chip: reproducing the specific microenvironment of the alveoli

In developing our Alveoli-on-a-chip, we designed and tested several models of microchip. I will describe here the different versions, list the issues encountered with each, and present the technical solutions investigated, leading to the next version. Because the fabrication techniques employed are similar for each version, I will not detail the fabrication protocols. Only for the final version will I describe the protocols, and how it was optimized for high-throughput manufacturing. The details of the microfabrication techniques are all specified in the Appendix, where you will also find larger pictures of all CAD technical drawings.

3.3.1 Coming up with a working chip

In the following section, the different designs of the microfluidic chip are presented. They were all obtained by Computer-Aided Design (CAD) with a dedicated software, SolidWorks (SolidWorks 2016, Dassault Systems). This software was used to generate the models and their associated technical drawings with quotations.

The models were then exported to KeyShot (Luxion) to generate renderings. A rendering is the process of creating a photorealistic image of our CAD object using the properties of the materials used, as well as light, texture or viewpoint effects.

Using a CAD software was an important decision in making this Alveoli-on-a-chip. Firstly, it allows for a virtual validation of the geometry before having to fabricate a single part. This allows to spot errors of conception and perform interference check (such as verifying that holes and edges are perfectly aligned). This saves a great part of both time and money usually spent in prototyping. Moreover, the parameterization of the model enables rapid changes of one part's design with a fast implementation of these changes in the rest of the parts. Secondly, CAD enables a rapid visualization of the object designed, which is useful for scientific communications. Thirdly, in the objective of robust production, having CAD drawings allows for exporting different designs directly into different machines (3D-printer, cutting plotter or laser-based engraving). Finally, CAD can also serve to generate dynamic models of stresses and strain (deformation or flow-induced shear stress models) such as those encountered in the alveoli.

a. Chip V1: Initial design

Specifications The first version of our Alveoli-on-a-chip consists of two parts of PDMS and a glass slide. The lower part (**L1**) contains the medium input/ouput channels as well as the endothelial chamber, a cylindric chamber of 9 mm of diameter (see Figure 3.7a). The top part (**T1**) also contains input and output channels irrigating the air chamber, which was firstly designed with a diameter of 7 mm (see Figure 3.7b).

Realisation Both parts were obtained by replica-molding of PDMS onto 300 μm-thick patterned substrates obtained by photolithography of SU-8 resin. Both parts were then peeled of the wafer and cut with a razor blade to an approximate rectangle of 45x24 mm. These PDMS molded parts had a thickness varying from 3 to 10 mm, due to the manual manufacturing process.

The chamber of the low part was opened through with a 9 mm metal puncher. It was also pierced with 1 mm punchers at each extremity of the channels. This part was bonded to glass with the channels facing towards the glass slide using a plasma treatment. The top part channels were pierced too.

Assembly Once assembled the patch was placed between the low part and the top part (see Figure 3.7c). The chip was sealed with plasma for testing. Indeed, this first design met the first three criteria of our specifications (see subsection b.), but in order to test the fourth one, I performed the testing with plasma-bonding. This fourth criteria (watertight chambers) was the main focus at first, and I decided that I would make the chip open (reversible closing, criterion 6) after successfully achieving the first 5 criteria.

Testing The first tests quickly revealed that, when I tried to flow medium in the lower chamber the chip would leak from the lower chamber to the top one, contourning the patch. Indeed, as the patch is sandwiched between the two layers, the PDMS deforms to encapsulate it, which generates a small area around the patch where the two parts are not in contact (see black arrow on Figure 3.7d).

Conclusion This first chip comprised two chambers but had important internal leakages. It met the first three criteria (see subsection b.), but not the fourth one: having distinct chambers. Moreover, it was incredibly thick (about 1-1.5 cm total), which prevents high-magnitude microscopic observation.

b. Chip V2: Patch-containing layer

Specifications In the second version, the solution envisaged to solve the "sandwiching issue" was to implement another PDMS layer with an integrated circular hole of the size of the patch. Once placed in this layer, the patch is not protruding, therefore not deforming the PDMS parts, thus solving our previous issue.

For the second version of the chip, I also changed the top (**T2**) and bottom (**L2**) patterns. They still both comprise input/output channels and a central chamber of 9 mm diamter, but their channel geometry was modified. The entry points of the channels are changed so that they are aligned, which will reduce the non-linear movements in the chamber and allow for more homogeneous culture conditions in the chamber. The outward parts of the channels are made symmetrical for aesthetic reasons. They are also longer, which makes it easier to connect the tubing (see Figures 3.8a and 3.8b). All parts are also smaller in width and length (40x20 mm), they are narrower than a glass slide, which makes it easier to position them before bonding.

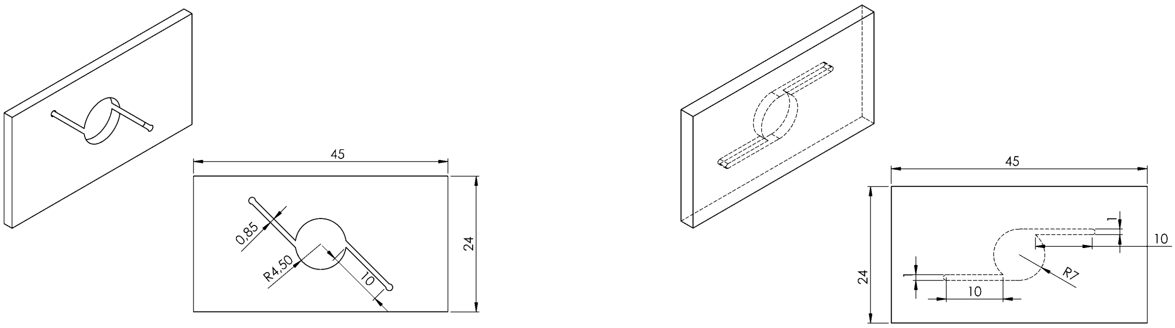

(a) Lower part (**L1**) (b) Top part (**T1**)

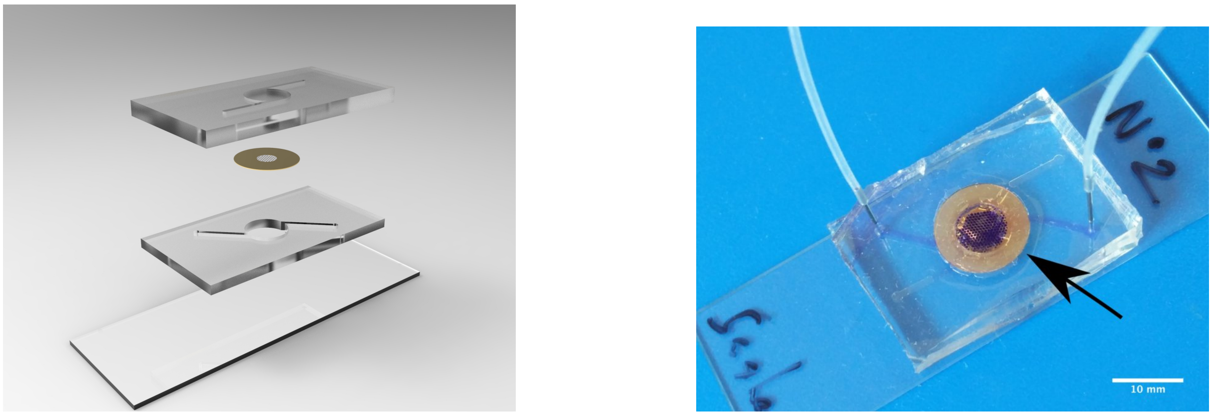

(c) Burst view rendering (d) Photo of the chip

Figure 3.7: First version of the Alveoli-on-a-Chip

Realisation The real improvement is the third PDMS layer. This *patch-containing layer* (**PCL1**) was obtained by cutting a specific pattern in a PDMS sheet with a cutter plotter, (a software controlled metal blade). The PDMS sheet was obtained commercially (Silex, UK), and is 0.2 mm thick, which means that it can completely contain the patch in the 14 mm diameter hole cut in its center (see Figure 3.8c). We intentionally let a 1 mm margin to account for patch manufacturing defects.

Assembly As previously, the two PDMS molded parts are cut to the wanted dimensions, the input/output channels are pierced open, and the lower chamber (**L2**) is punched through. Finally, the patch-containing layer (**PCL1**) is plasma-bonded to the top side of the lower part.

Testing As usual, at these early stages, all three layers where plasma-bonded together for flow testing. In this version, we solved the previous model issue, as all PDMS surfaces were complete contact (see Figure 3.8d). However, we still observed leaks from the bottom to the top chamber around the patch (see the red liquid reaching the top chamber in Figure 3.9). Indeed, it not possible to make a patch-containing layer matching exactly the contour of the patch, as the contours often vary up to 1 mm in diameter from one patch to another. Moreover, I also observed that the patch tends to swell with medium, and its PEGDA grid can round up and touch the ceiling of the air chamber. This induces an important destruction of the gelatin fiber network.

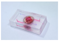

Figure 3.9: Picture of the second version of the microfluidic chip

Conclusion This version solved our previous issue (patch sandwiching), but we still need to solve the leaks of medium flowing around the patch and up to the top chamber (criteria 4), as well as the damages to the fibers.

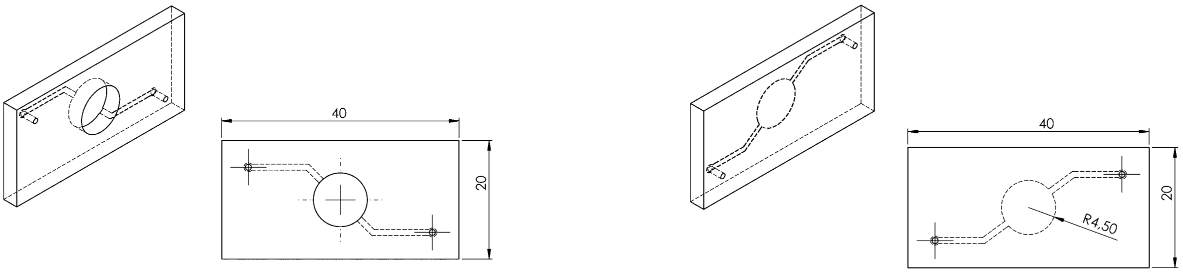

(a) Lower part (**L2**)

(b) Top part (**T2**)

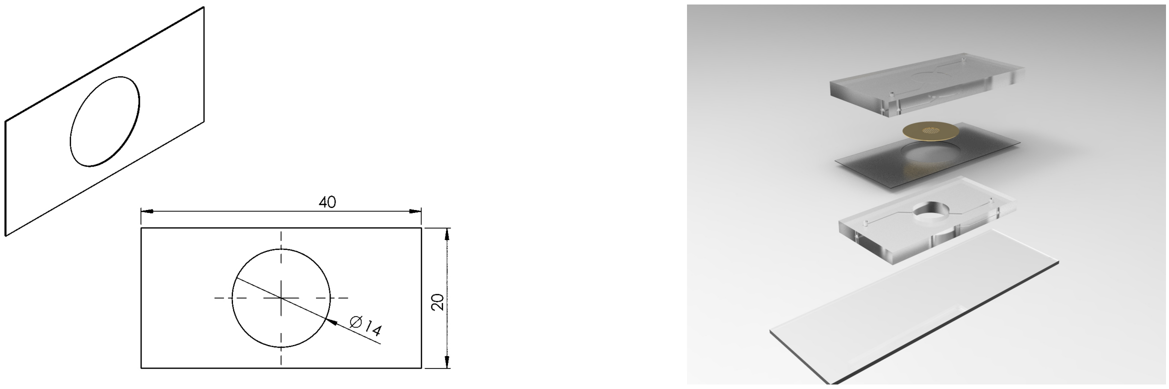

(c) Patch-containing layer (**PCL1**)

(d) Burst view rendering

Figure 3.8: Second version of the Alveoli-on-a-Chip

c. Chip V3: Taller air chamber

New specifications In the third version, the chip was almost unchanged, with only a small modification: the air chamber is designed with a bigger volume (see Figure 3.10a). In order to do so, I simply glued 5 coverslips (diameter 9 mm) on top of the SU-8 resin wafer (see Figure 3.10b). The new top part (**T3**) is just molded on top of this new wafer, and we obtain a final air chamber height of 1 mm.

Testing and conclusion Implementing a larger air chamber solved our issue of damaged fibers. However, we still have to prevent the medium flowing in the lower chamber from reaching the top chamber.

d. Chip V4: Medium layer and pre-bonded patch

Specifications Obtaining watertight chambers separated by a handmade patch was extremely difficult. Indeed, we could not design a tailor-made system, because each patch is handmade. These differences are usually of a few hundred microns, but it is enough to trigger a leakage.
In trying to tackle this issue, I envisaged a fourth version that was completely different from the previous ones. The idea was to 'pre-bond' the patch: it would be plasma-bonded between two PDMS parts, to prevent any leaks. Because we still wanted an open chip (to be able to directly seed the cells), I designed a *middle layer* (**ML1**), to be bonded on top of the patch, with a volume important enough to contain medium for cell seeding and culture (see Figure 3.11a). This way, the patch is sealed into the PDMS layers, but we can still access the fibers for seeding, and close the top chamber with a top part (**T3**).

Realisation This medium layer is a simple flat of PDMS cut to the desired dimensions of the chip (40x20 mm), with a 9 mm hole punched in the center.

Assembly The lower part (**L2**) and the patch-containing layer (**PCL1**) are obtained and assembled as previously described. The patch is placed in the **PCL1** and the medium layer (**ML1**) is plasma-bonded above. I then sterilized this ensemble with UV light and seeded cells on the bottom side of the patch. When the cells were adherent, I flipped the ensemble and placed medium on top of the patch to prevent the cells from drying. I then took a glass slide functionalized with plasma, and then placed the ensemble (**L2**, **PCL1**, patch

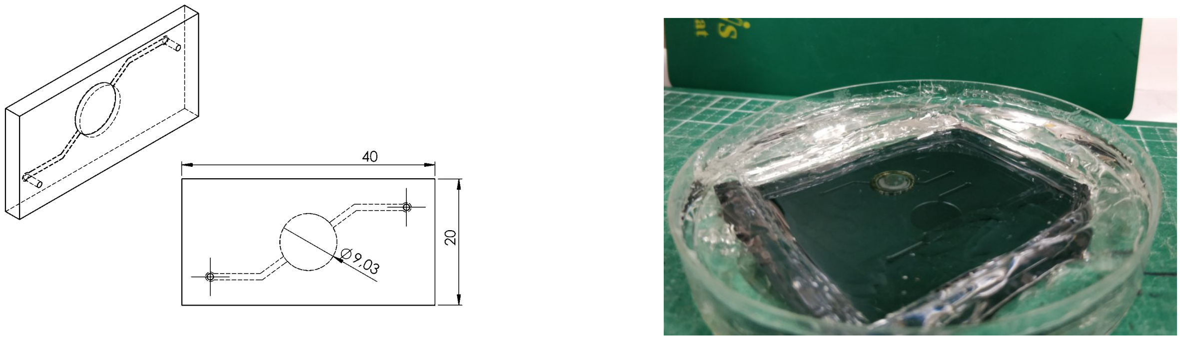

(a) New top channel (**T3**) (b) Microfabrication trick

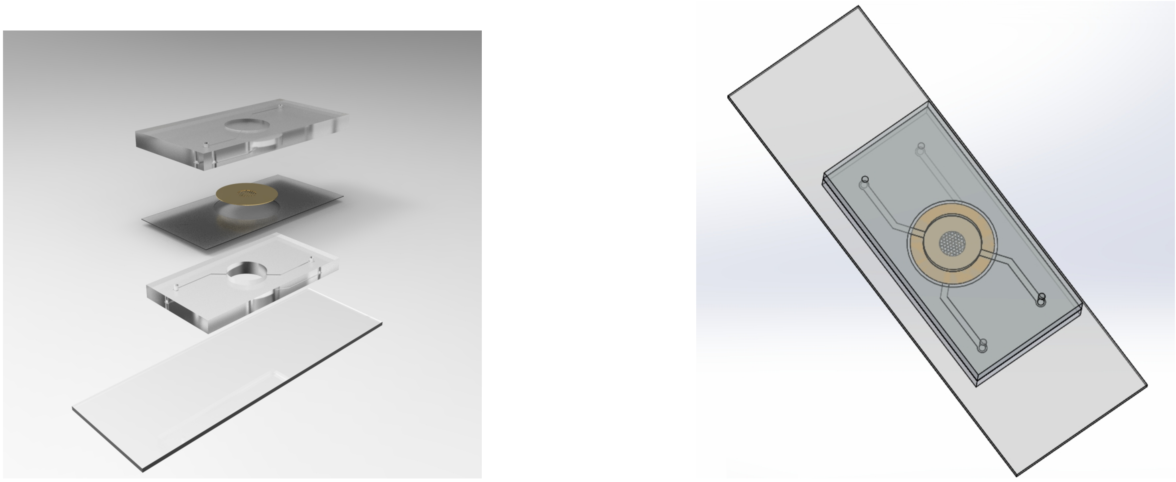

(c) Burst view rendering (d) CAD view of the assembled chip

Figure 3.10: Third version of the Alveoli-on-a-Chip

and **ML1**) on top. This whole assembly was then filled with medium and placed back in the incubator. After a couple hours, I seeded cells on the other side, and closed the chip with a top part **T3** functionalized with plasma (see Figure 3.11b).

Testing This test was repeated for five chips. For each, the next day I observed that the plasma bonds had failed and that the chips were leaking. Indeed, not only these bonds were made with only one of the surfaces being functionalized, but they were made in a humid environment and could (obviously) not be strengthened by the usual 80 °C oven incubation recommended post plasma treatment.
In addition, all parts that were made by direct molding on a wafer (*i.e.* the **L2**, **ML1**, and **T3**) were not flat. Indeed, because of the surface tension of the liquid PDMS poured in the Petri dish, the molded parts are drawn up to their sides.
Another critical issue, that I only discovered now that I had seeded cells was that, the low part being so thick (about 1 cm), I could not observe my cells on the microscope above a 10x magnitude. So not only were my chips leaking, but I had no idea whether my cells were still alive or not.

Conclusion This fourth chip was a failure, but it was interesting to explore another vision of the system, and it unveiled several underlying issues.

e. Chip V5: Observing the cells

Specifications The idea for the fifth chip was to use the PDMS sheets that we were using for the patch-containing layer (**PCL1**) to make the low part. Indeed, the patterns of the lower part (channels and chamber) are large enough (smallest dimension is 1 mm) to be directly cut into the PDMS sheet, and does not require photolithography. The final distance of observation between a microscope objective and the patch would then be the sum of the thickness of the bottom glass slide and the thickness of this PDMS sheet (*i.e.* 0.17 mm + 0.2

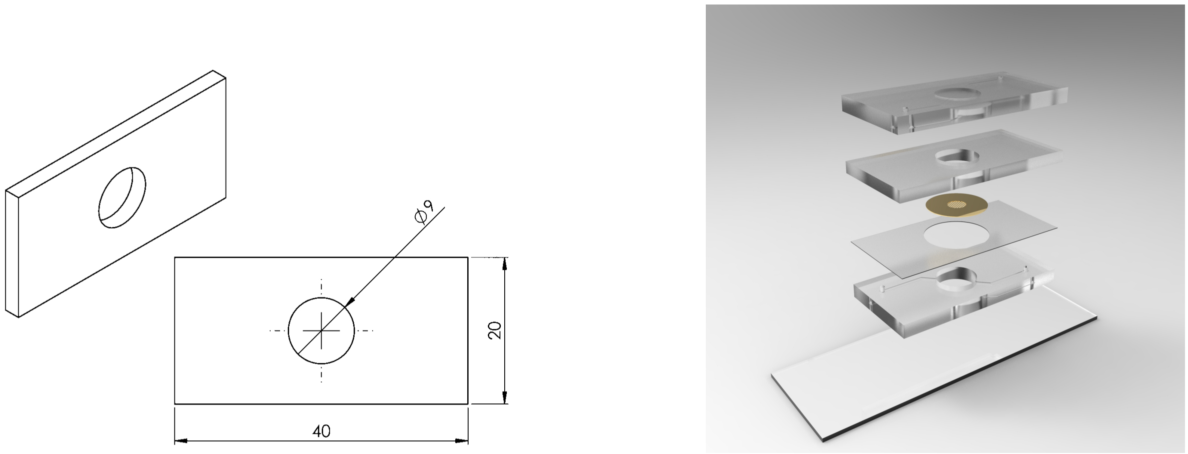

(a) New medium layer (**ML1**) (b) Burst view rendering

Figure 3.11: Fourth version of the Alveoli-on-a-Chip

mm = 0.37 mm). This allow for a good control of the observation distance. The new low part **L4** was therefore cut into a 200 μm thick PDMS sheet (Silex, UK) with a cutter plotter, to the final dimensions specified in Figure 3.12a.

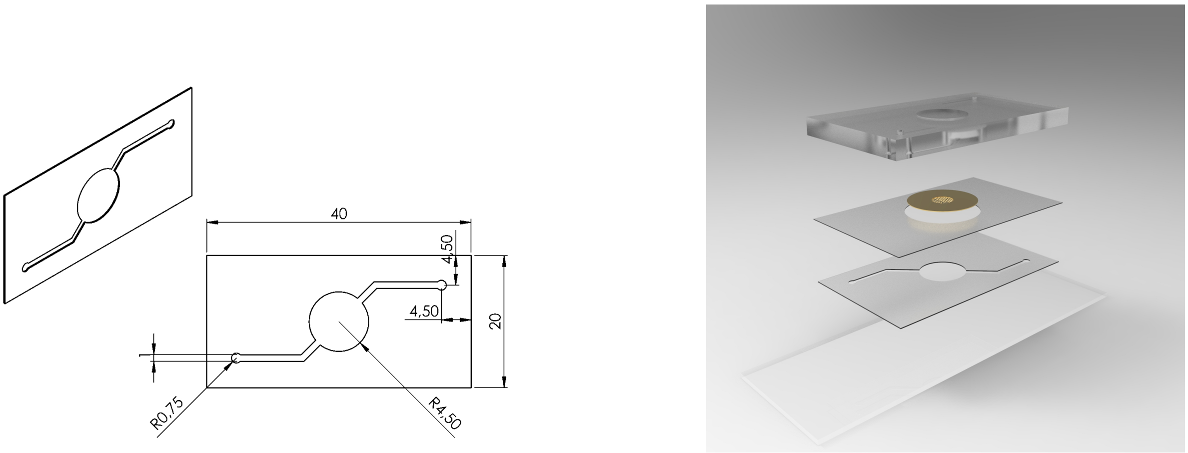

(a) Lower channel (**L4**) (b) Burst view rendering

Figure 3.12: Fifth version of the Alveoli-on-a-Chip

Testing and conclusion This technique enabled microscopic observation up to 20x magnitude if the chip was bonded to a glass slide, and a 40x magnitude if the chip was bonded to a glass coverslip. This allowed us to meet our seventh criteria.(see subsection b.). However, we had not solved our previous problem, meaning that the PDMS molded parts that are not flat.

f. Chip V6: Getting technical

Rationale In working on the sixth version, I tried to tackle the issue of the flatness of the parts. Indeed, it compromised most of the plasma-bonding. Moreover, because in the end we wanted a reversible chip, I had planned on relying only on the surface properties of PDMS for sealing the chip. My plan was to place the lower and top parts in close contact, previously dried and extensively cleaned of dust, and to gently press them to remove the bubbles. I had observed that such ensemble could resist to medium flowing in the lower chamber. However, we had decided to reproduce the breathing motions of the alveoli with a positive pressure system. This meant that, at some point we wanted to be able to increase the pressure in the top chamber to deform the patch. I had tested this "passive bonding" method, and it was leaking when the pressure reached 50 mbar. Finally, the new idea was to create a mold for the top part. This 3D-printed mold would constrain the PDMS poured inside so that the part molded would be flat and have a controlled height. The mold specifications as well as the fabrication process are detailed in the next paragraph.

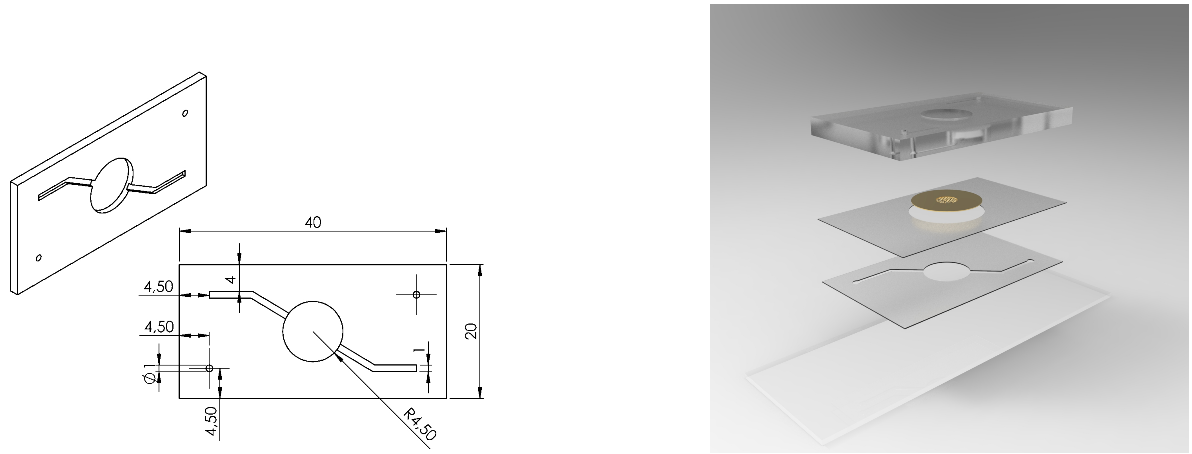

(a) New top part (**T4**)

(b) Rendering of the burst view

Figure 3.13: Sixth version of the Alveoli-on-a-Chip

Assembly As usual, the low part **L4** and the patch containing layer **PCL1** are plasma-bonded together and to the glass coverslip. Finally, the obtained top part (**T4**) (see Figure 3.13a) is placed on top.

Testing This new version was a great improvement regarding the 'passive bonding' method. With absolutely clean and dry PDMS parts, I could reach up to 100 mbar of pressure in the upper chamber before observing leaks.

Conclusion Sadly, further experiments (detailed in the next section) demonstrated that this pressure was not sufficient to induce a deformation of the patch, therefore we needed to come up with a solution to keep the chip closed tight.

3.3.2 PDMS molding implementation

The decision to mold the top part of our chip was an important advance in our project because, from then on, the complete chip has a regulated height, which means it can be included inside more complex objects. Here are more details on the mold and its use.

a. Mold design and fabrication

Design The mold is intended to generate one top part at a time. It is constituted of a rectangle carved 2 mm deep into the resin. At the bottom of this rectangle lies a pattern constituted of two channels (1 mm width and height) and a circular chamber (diameter 9 mm and height 1.5 mm), as can be seen on Figure 3.14a. This generates 2 mm thick parts with a 1.5 mm high chamber. The roof of the chamber is only 0.5 mm thick, which is quite thin in order to allow for an important gas exchange for cell survival.

In order to facilitate the molding process, I used poka-yoke by placing four pins on the top part and four holes in the lower part so that the mold is always centered.
Two overflow channels were created to drain any excess of PDMS. These channels are placed in the top part so that only the PDMS above the rectangle can over. They are accessible with a gradual ramp (see Figure 3.14a).

Fabrication The mold was generated with SolidWorks and printed on a FormLabs 3D printer. The parts were then extensively cleaned with isopropanol and UV-reticulated. They were then bathed in water for 48 h and left to dry for a few days.

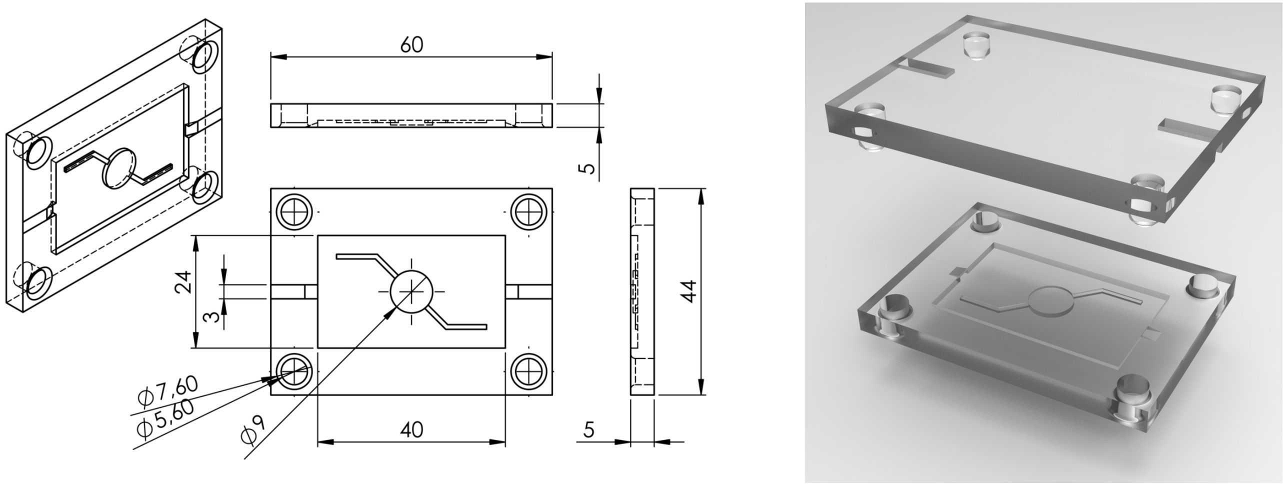

(a) Specifications of the top part mold

(b) Rendering of the mold

Figure 3.14: 3D-printed mold to generate the top part **T4**

b. Molding technique

Process and issues The PDMS part were obtained by pouring 1:10 RTV PDMS on the mold, degassing the ensemble in the dessicator, and curing in the oven at 70 °C for a few hours.
The first attempts produced top parts of controlled height, but they were not transparent. Indeed, the superior surface of these parts was molded on the resin, which has an important roughness due to the precision of the 3D printer (see Figure 3.15a). In order to solve this issue, I decided to place a glass slide on top of the PDMS rectangle before degassing. This produced perfectly transparent parts, but these parts were often full of bubbles (see Figure 3.15b).
By placing the glass slide after the PDMS degassing and deposing it slowly from one of the shorter edges of the engraved rectangle to the other (see Figure 3.15c), we could get rid of bubbles. In this way, the PDMS sticks to the glass slide while it descends onto the mold.

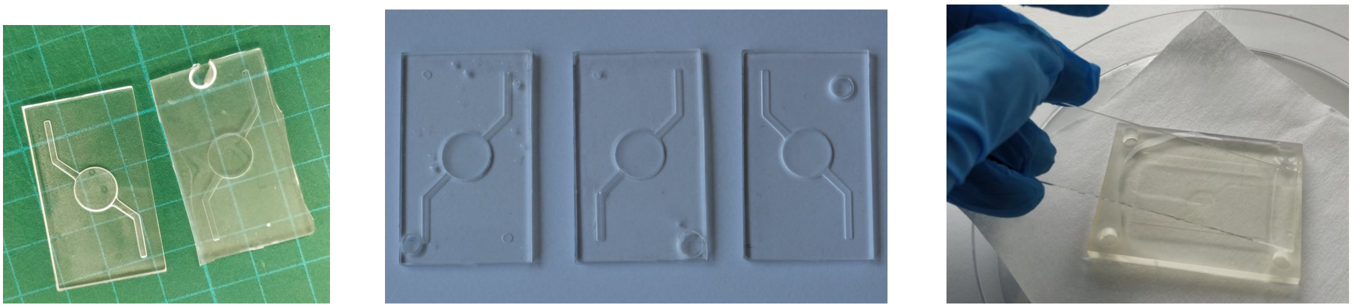

(a) Rough surface

(b) Bubbles in the top part

(c) Glass slide technique

Figure 3.15: Optimization of the manufacturing process for PDMS molded top parts: the use of a glass coverslip allows for the generation of a smooth and transparent surface, whereas the use of a dessicator prevents the formation of bubbles.

3.3.3 Implementing a clamp system

In order to reach our objective of designing a reversible microfluidic chip, we needed to find a reversible method to close the chip. I decided to design a tailored clamp to keep the chip tightly closed. Our first idea was to use a screw-based system but this system does not allow for an equal distribution of the pressure on the surface of the chip. This induces an uneven deformation of the chip, which resulted in important leakage.

a. Magnetic clamp: first version

Specifications In order to solve the pressure distribution question, we decided to use a magnetic closing system. With a symmetric distribution of the magnets, the pressure will be even on the whole surface of the chip. The clamp was designed as can be seen on the Figures 3.16a and 3.16b, with two parts containing symmetrically encrusted magnets. The clamp had two openings, one on the top to be able to see the channels and the cells by eyes (and spot bubbles), and one below to be observable on the microscope. To this last effect, the outer dimensions of the clamp were designed to be exactly those of a glass slide.

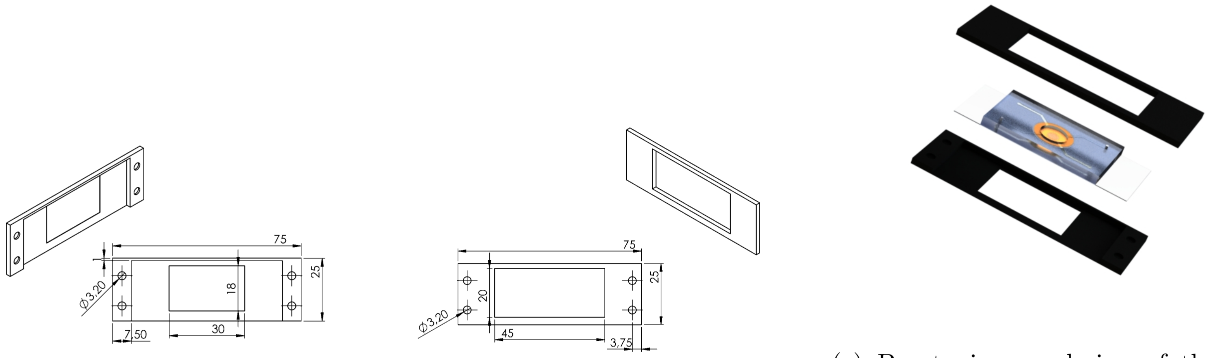

(a) Specifications of the low part (b) Specifications of the top part (c) Burst view rendering of the first clamp

Figure 3.16: Design of the first clamp system developed to exert a homogeneous pressure on the top of the clamp and prevent any leakage.

Realisation This clamp was designed to have internal dimensions exactly of the size of the chip. Because we now have a controlled height of the top part (**T4**), we can compute the exact height of the overall chip, and design the clamp so that it is a little bit smaller. This will assure that pressure is exerted at all times on the superior surface of the chip.

Finally, the clamp was 3D-printed and the magnets were press-fit inside their dedicated holes. The magnets were 3 mm in diameter and 0.5 mm thick, and were N42 Neodymium magnets of 0.08 kg pull strength (from First4magnets).

Testing As it appears, this first clamp was extremely weak. Firstly, because I did not want to elevate the patch too high and loose our ability to observe it at a x40 magnitude, I made the low clamp extremely thin (0.5 mm). Therefore, it was too thin to actively support the closing pressure and was importantly deformed after UV-reticulation. Another issue was that the magnets were too far from the center of the chip, therefore, under high pressure, we still observed leaks around the patch area.

Conclusion This magnetic clamp system is a promising solution but it should be designed to exert precise pressure on specific points, and keep a small and practical shape, while resisting to strong internal pressure.

b. Second clamp: a stronger design

Specifications The second version was much stronger. In order to thicken the lower part, I analyzed our microscope and concluded that we could still place a microscope objective in direct contact with the chip's glass coverslip if the hole designed in the chip was large enough.

The next modifications were to increase the number of magnets, and place them closer to the center of the chip. In the end, both chip parts (see Figures 3.17a and 3.17a) are 5 mm thick.

Testing After flow and pressure testing, I observed that this clamp was strong enough to maintain all the PDMS layers in close contact: for the first time, I did not see any leaks in between these layers. However, some patches having a particularly small outer diameter, I would still observe leaks from the lower to the upper chamber from time to time.

Conclusion This clamp was functioning, but when performing pressure tests, I observed that for pressures of 800 mbar and above, the chip would sometimes leak. Therefore I believed that we could use stronger magnets to hold everything in place.

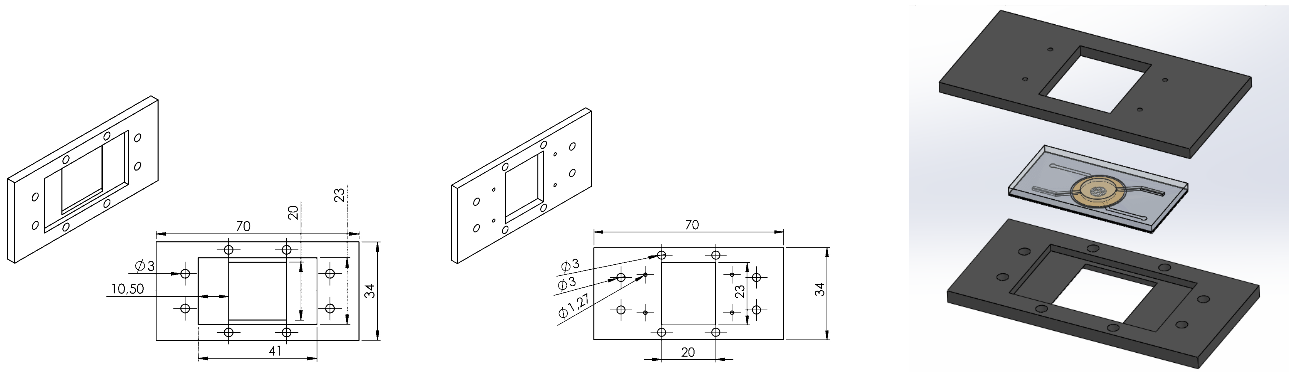

(a) Specifications of the low part (b) Specifications of the top part (c) Burst view

Figure 3.17: Final design of the second 3D-printed closing clamp

c. Final clamp: design and validation

Specifications In the final clamp I used larger magnets at the extremities of the chip (5 mm diameter, 1 mm thickness, Neodymium, 0.3 kg pull strength from *first4magnets*). The luers were removed and pin holes were included.

Realisation As previously, the clamp was 3D-printed, then intensively washed with Isopropanol and reticulated by UV-light. The magnets were press-fit in position.

Testing As the closing properties of the clamp were previously tested, I tested another important parameter: the clamp's toxicity. As the clamp is expected to stay in the incubator for several weeks, we needed to check that it was not releasing toxic chemicals in the atmosphere.
The test was designed as a crash test: if the cells could survive a week in direct contact with the 3D-printed part, we assumed that they could survive a few months in indirect contact (because the clamp only touches the chip, and not the cells). Therefore, the test was simple: I seeded A549 and HUVEC cells in 6-well plates and added small parts of the 3D-printed objects.

Results After 3 days I observed the cell's state and morphology with bright field microscopy. As is shown on Figure 3.19, the cells in contact with the PDMS and the Grey resin parts do not present an important number of vacuoles (compared to the control photo). However the cells in contact with the Clear resin showed an advanced state of apoptosis (see Figure 3.19d).
Because using the Clear resin to print the clamp allows for an easy monitoring of the flow in the chip, I decided to find a way to reduce the toxicity of the printed parts. After several tests I found that putting the parts in water for 48 hours, rinsing them twice (10 min in water each time) and then sterilizing them with UV light allowed for all the remained chemicals to dissolve and disappear. I performed another toxicity test and was not able to see differences in cell state between the control and the cells in contact with the 'cleaned' clear resin.

Conclusion We have designed a strong magnetic clamp that prevents leakages outside of our Alveoli-on-a-chip, and allows for live monitoring at a high magnitude (x40), without compromising the viability of our cells.

3.3.4 Final chip design and fabrication

a. Top part final design

Specifications The final top part is constituted of two layers of PDMS that are plasma-bonded together: the top layer (**T4**) and the closing layer(**CL**). The ensemble is 2.2 mm thick. As shown on Figure 3.20a, the final air chamber has a diameter of 7 mm and a height of 1.5 mm. The channels have a 1 mm square section. The closing layer (**CL**) is a 0.2 mm thick rectangle and consists of a circular hole of 5 mm diameter in its center. It also contains two smaller holes (1.2 mm diameter) that are placed at the extremities of the channels of the lower part.

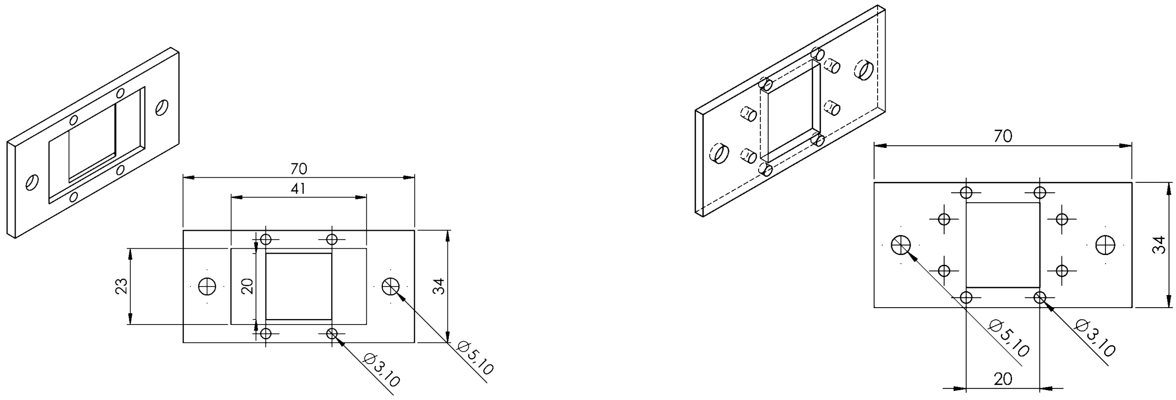

(a) Specifications of the final low part (b) Specifications of the final top part

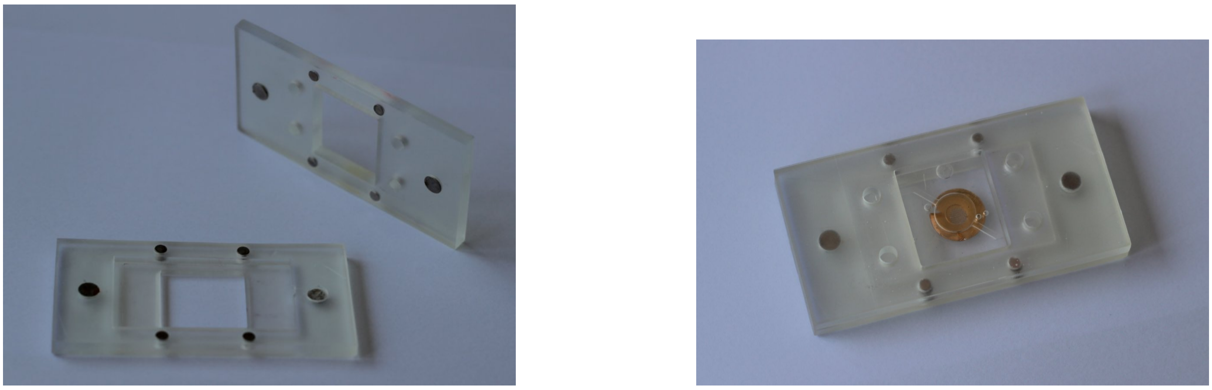

(c) Final clamp parts (d) Chip in the final clamp

Figure 3.18: Final design of the 3D-printed closing clamp

Technical details The technical decisions and advantages of the top part were detailed about. The closing layer **CL**, however, is a new invention. It plays a crucial role for water-tightness: this thin layer is very deformable, and will bend to fit exactly on the patch. This creates a gasket between the patch and the top part, blocking any leakage that could occur from the outer side of the patch.

The closing layer **CL** also contains two small holes that were placed here to facilitate the process of piercing entries in the top part to access the lower part. Indeed, they mark the exact spot that has to be pierced, thus avoiding to localize this spot by placing the top part above the lower part, and risking to break the glass coverslip when piercing. Moreover, they are wider than the pins used to flow medium in the lower chamber, which leaves us a margin for errors if the multiple layers are not perfectly aligned.

b. Low part final design

Specifications The final lower part is constituted of two layers of PDMS (a lower layer and a patch-containing layer) that are plasma-bonded together and to a glass coverslip. The specifications of the lower layer **L4** are already detailed above. The patch-containing layer **PCL2** is similar to the **PCL1**, with the addition of two small holes (diameter 1.2 mm).

Technical details Similarly to the closing-layer **CL2**, these small holes are used for the flow input and output pins. However, if they were a convenience for the closing layer, here they are absolutely necessary. Indeed, as explained in the following section detailing the fabrication steps, the **PCL2** cannot be pierced after it is bonded to the lower layer and glass coverslips. Therefore, the input and output holes must be anticipated and cut out before, otherwise we could not access the lower chamber. Their diameter was chosen to give a margin of error for the alignment process.

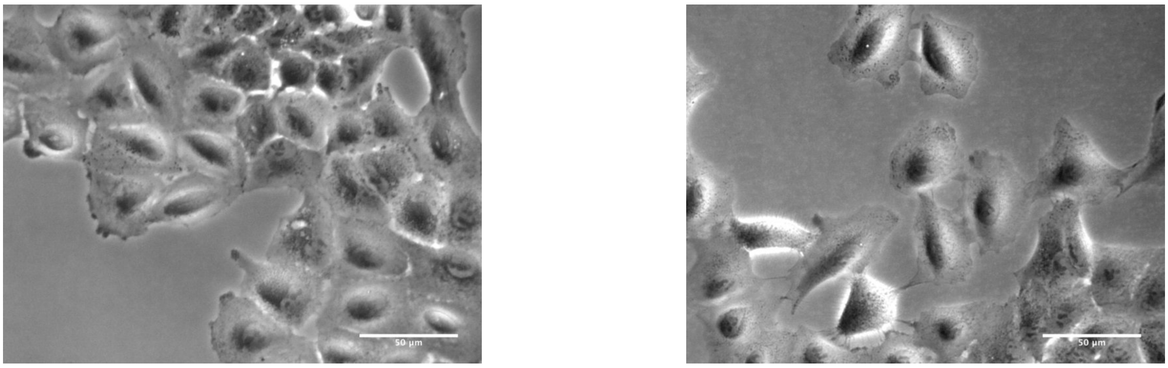

(a) Control: A549 cells

(b) Cells in contact with PDMS

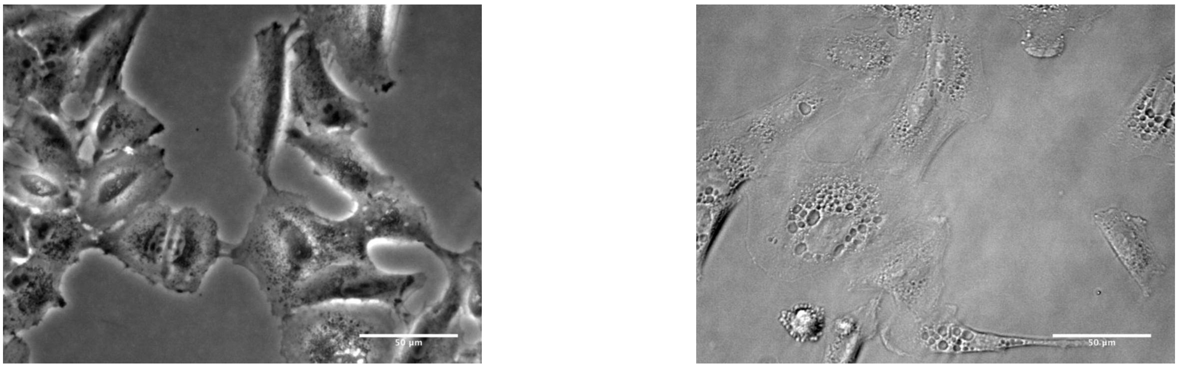

(c) Cells in contact with Grey resin

(d) Cells in contact with Clear resin

Figure 3.19: Toxicity of the microfabrication material on A549 cells (cultured on glass coverslips for a day and incubated for 3 days with specific parts). (All resins were obtained from FormLabs) *Scale bars: 50 µm*

c. Fabrication and assembly protocol

PDMS sheets and cutter plotter The lower layer **L4**, patch-containing layer **PCL2** and closing layer **CL** are obtained from 0.2 mm thick PDMS sheets. The patterns are cut out with the help of a cutting plotter (GraphTec). The cutting parameters must be tested and optimized to the two types of plastics used to support and protect the PDMS sheet. Care should be taken that the parts are cut so that the protective layer of the PDMS sheet should be on top of the faces that will be plasma-functionalized. Indeed, the PDMS cut parts will not keep flat if they rest on the protective layer instead of the supportive layer. Otherwise, it impossible to bond the parts without bubbles in between layers.

Lower part assembly The lower part should be assembled in the following manner, respecting the order of the steps. The protocol is detailed in the Appendix but here is a short resume:

1. Clean the lower layer **L4** and the patch-containing layer **PCL2** with adhesive tape and make sure that all holes are empty and that there is no residue of PDMS or plastic
2. Functionalize a clean 40x20 mm glass coverslip and the lower layer (**L4**) with plasma.
3. Flip **L4** on top of the coverslip and align it. Gently press them together and remove any air trapped in between
4. Place the ensemble in the oven at 90 °C for 8-10 minutes
5. After, take this lower ensemble from the oven, remove the thick plastic supporting layer, and place it in the plasma with the patch-containing layer for functionalization
6. Assemble the two parts with the same technique as above and place the ensemble in the oven at 90 °C for 8-10 minutes
7. Take the lower part in the oven and remove the thick plastic supporting layer. Cover the channels with adhesive tape until use.

Top part assembly The top part should be assembled in the following manner, respecting the order of the steps. The protocol is detailed in the Appendix but here is a short resume:

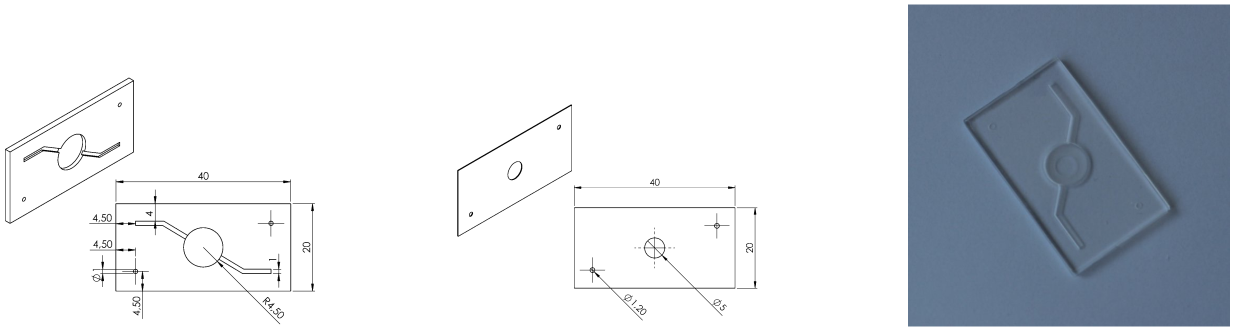

(a) Final top layer **T4** (b) Final closing layer **CL** (c) Photo the final top part

Figure 3.20: Specifications of the top part of our **Alveoli-on-a-chip**.

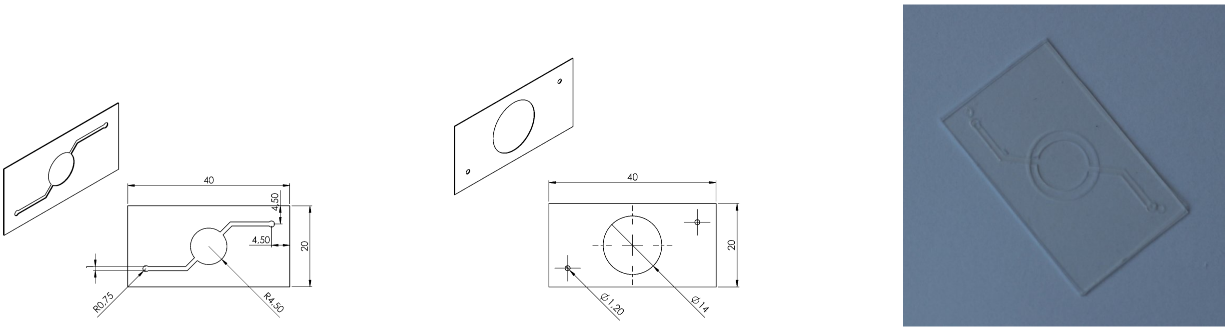

(a) Final lower layer **L4** (b) Final patch-containing layer **PCL2** (c) Picture of the final lower part

Figure 3.21: Specifications of the lower part of our **Alveoli-on-a-chip**.

1. Clean the closing layer **CL** w ith adhesive tape and make sure that all holes are empty and that there is no residue of PDMS or plastic
2. Clean a molded top part **T4** and pierce 0.75 mm holes in the two extremities of the channels
3. Functionalize both parts with plasma, then flip the closing layer on top of the PDMS top part, align them and gently press them together with a razor blade to remove air in between
4. Place the ensemble in the oven at 90 °C for 8-10 minutes.
5. Then peel off the thick plastic supporting layer and cover the channels with adhesive tape until use.

3.3.5 Conclusion

After a long research and development process, we are able to present an innovative microfluidic chip: our Alveoli-on-a-chip. This chip was custom-made to integrate our microengineered patch in a dual environment. We managed to create two water-tight chambers that would both integrate our patch, and be strong enough to resist to actuation.

This chip displays several technological innovations. Firstly, it is a reversible chip, which greatly facilitates the *in chip* culture, one of the main drawbacks of conventional Organ-on-chips. This also allows to take the cells out of the chip momentarily for analysis. This is very useful for long-term observation because you do not need to destroy the chip to access to the cells. Secondly, this chip allows for live observation at an important magnitude (40x). We developed a chip that met the criteria that we aimed for. It now has to be tested for long-term precise actuation as well as cell survival.

3.4 Dynamics of the Alveoli-on-a-chip

In terms of mechanical design, the Alveoli-on-a-chip offers interesting features: its extremely thin alveolar membrane (less than a micron), its air-liquid interface environment, and the possibility for reversible cell culture and live-imaging. We have simulated the mechanical environment of the alveolar capillary barrier. Now our next objective is to integrate the patch in this chip and to reproduce the different mechanical forces exerted

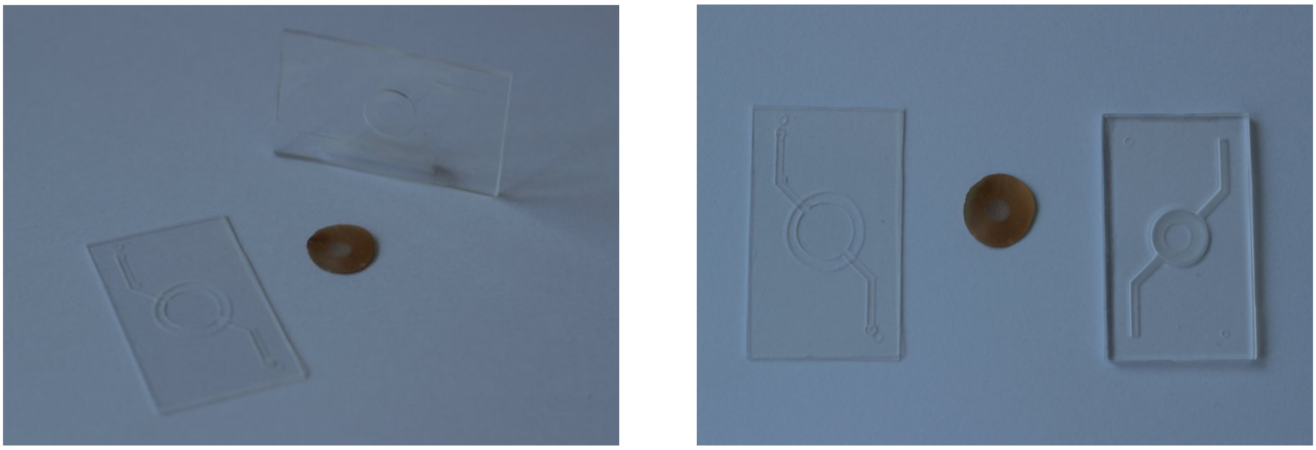

(a) Final chip: two parts (b) Final chip: assembled

Figure 3.22: Specifications of the lower part of our **Alveoli-on-a-chip**.

on the alveolar capillary barrier: the breathing-induced deformation and the blood flow-induced shear stress. We will present here the physical characteristics of these two motions using what is known from the literature, as well as introduce mathematical models describing the forces in our chip. We will then move on to the technical setup we developed and validated to implement these forces in our chip. Finally we will analyze the effect of such forces on our cell model and discuss the obtain results.

3.4.1 Reproducing blood flow dynamics

a. *In vivo* conditions of blood flow shear stress

Every organ is fed by a continuous perfusion of nutrients coming from the blood flow. In the lung, the contact between the capillaries and the alveoli is not only design for nutritive purposes, but also to enable gas exchange. Therefore, the alveolar capillaries present features that are unique in the human body. We will overview these features in order to understand the specificities that need to be accounted for in our effort to mimic alveolar blood flow in our chip.

Adaptation to pressure The pulmonar micro-capillaries have a diameter of about 5-10 μm. The diameter of the cross section of a capillary is function of the transmural pressure, and, according to the work of Huang *et al* [126], this diameter can vary from about 8 μm at 18 cmH2O to 5 μm at 2 cmH2O. This adaptation mechanism allows the pulmonary capillaries to absorb cardiac blood flow rate variations without significant pressure variation. It is made possible by the elasticity of the capillaries, which have very few structural elements in their ECM. Pulmonary capillaries flow with about 15 mmHg internal pressure (about 20 mbar), a pressure 6 to 10 times lower than arterial blood pressure. This low pressure is a necessity to temper possible cardiac perturbations as lung capillaries is a series circulation.

Shear stress The capillar network represents an important volume of the interstitium: about 50%. As blood is not compressible, the continuous flow filling this network generates an almost rigid structure that stabilizes the alveolar walls. Moreover, the capillaries follow quite a flexuous route, reaching alternatively into neighboring alveoli. It obliges for a slower flow, and red blood cells stay for longer in the functional exchange zone: up to 1 second at rest. This is much more than the estimated time necessary for equilibrium (0.25 s). The blood flow is variable along the bronchial tree, but in the apex region, close to the alveoli, it is estimated to be around 1.29 mm^3/s [127], which corresponds to 77.4 $\mu L/min$. The physiological blood flow induced shear stress is around 1 to 10 $dynes/cm^2$ (*i.e.* 0.1 to 1 Pa) on the endothelial cells [13]. As seen previously, this shear stress induces the production of key proteins for immune functions regulation, as well as an enhanced integrity of the endothelial layer [102].

b. Mathematical analysis of the flowing motions in the Alveoli-on-a-chip

Flow analysis In order to reproduce the dynamics of the alveoli *in vitro* we will analyze our Alveoli-on-a-chip and characterize the mechanical properties of its flow with a mathematical model.

The Capillary number **Ca** is representative of the importance of the viscous forces versus the surface tension forces in our system. **Ca** can be computed as follows:

$$Ca = \frac{\mu\ U}{\delta} \tag{3.1}$$

i.e:

$$Ca = \frac{\mu\ Q}{\delta\ D\ h} \tag{3.2}$$

$$\text{with} \begin{cases} \mu = 6.922 \times 10^{-4}\ Pa.s,\ \text{the viscosity of water at 37 °C} \\ \delta = 7.28\ Pa,\ \text{the surface tension of an air-water interface} \\ Q,\ \text{the input flow rate} \\ D = 9 \times 10^{-3}\ m,\ \text{the width of the chamber} \\ h = 0.2 \times 10^{-3}\ m,\ \text{the height of the chamber} \end{cases}$$

The Reynolds number **Re** is representative of the type of flow in the chamber: a low Reynolds number indicates a laminar flow whereas a switch towards an important Reynolds number indicates a more turbulent flow. **Re** is defined as follows:

$$Re = \frac{\rho\ U\ D}{\mu} \tag{3.3}$$

i.e:

$$Re = \frac{\rho\ Q}{\mu\ h} \tag{3.4}$$

$$\text{with} \begin{cases} \rho = 993.37\ kg/m^3,\ \text{the density of water at 37 °C} \\ \mu = 6.922 \times 10^{-4}\ Pa.s,\ \text{the viscosity of water at 37 °C} \\ Q,\ \text{the input flow rate} \\ h = 0.2 \times 10^{-3}\ m,\ \text{the height of the chamber} \end{cases}$$

With these assumptions we were able to characterize our flow in the channels and in the chamber of the Alveoli-on-a-chip and compare them with expected *in vivo* values from the literature [58]. The results are presented in Table 3.1. As we can see. we have laminar flows in our channels but this flow is more turbulent in the chamber, but within reason. The capillary numbers are low for each parts which means that the viscous forces are negligible compared to the capillary forces.

	Alveolar ducts	**Channel**	**Alveolar Sacs**	**Chamber**
Re	0.68	0.01	0.43	11.9
Ca	8.37e-5	7.92e-7	6.64e-5	8.80e-8

Table 3.1: Flow dynamics in our Alveoli-on-a-chip (for a flow rate of 100 $\mu L/min$)

We assess the validity of our model in terms of reproducing the physical forces of the alveoli. Our regime is a bit turbulent in the basal chamber of our chip, but we could optimize this by reducing the height of this chamber. This would require finding a manufacturer for PDMS sheets below 0.2 mm thick, but this could also help in increasing the magnitude at which we could observe our cells.

Shear stress Another important parameter to monitor in our model is the flow-induced shear stress that will be exerted on the cells in the chip. A precise control of this parameters is of prime importance in the alveolar capillary barrier model, as we have seen previously that shear stress can activate certain phenotypes of the cells such as immune functions.

We assimilate our chamber to a Hele-Shaw cell because its horizontal dimensions are larger than its height. With this assumption, the wall shear stress on the top and bottom surfaces of the chamber can be computed as follows ([128], [129]):

$$\tau_w = \frac{6\ \mu\ Q}{w\ h^2} \tag{3.5}$$

Therefore, for an input flow rate of 100 $\mu L/min$, the shear stress exerted on the cells is 0.385 $dynes/cm^2$. This is too low to observe any incidence on the cells. For a minimal shear stress of 0.55 Pa (*i.e.* 5.5 $dynes/cm^2$), we would need to flow 1.5 mL per minute. This would induce a consumption of about 2 liter per day. At a price of 200 euros per 500 mL of medium, this cannot be considered. The possible options to reach such an important shear stress are: reducing the size of the basal chamber of the chip, using an additive (such as Dextran or Alginate) in the medium to increase its viscosity or build a close circuit that would flow the medium in a loop.

c. Actuation system design and implementation

Even though we already knew that it would be hard to obtain a significant shear stress on the cells, we tried to establishing a continuous flow in the Alveoli-on-a-chip, in order to validate its use for long-term cell culture.

In order to establish the flow in the Alveoli-on-a-chip, we had to solve numerous technical difficulties. Indeed, when inserting the patch, because the chip is reversible, anything from dust to drops that stands in between the top and the lower part would induce an important leakage. And connecting the chip to the flow actuators was also complex because if a bubble gets trapped in the system it could starve the cells. Finally, there were a few maneuvers that proved necessary to maintain the cells in culture for a long time.

Placing the patch in the chip When inserting the patch in the chip, there are a multiple details that should be taken care of. That is why we developed an extremely detailed protocol, that may seem a bit tedious, but is actually the necessary to ensure perfect integration of the patch in the chip. I will not detail how we came up to this protocol but it was essentially by trying and failing. In order to avoid contamination, all the materials used are sterile. Microfabricated parts are also cleaned from dust using adhesive tape. The protocol is detailed in the Appendix but here is a short resume:

1. Fill the channels and the basal chamber of the lower part (**E**) with medium
2. Take a patch outside of its culture plate (**G**) and gently touch a sterile gauze (**H**) to remove any excess of medium
3. Place the patch carefully in the basal chamber and take the top PDMS part and place it above the patch. Smoothly remove any bubble between the two PDMS parts
4. Prepare two Tygon tubes with metallic pins and place them in the lower channel input and output. Place the ensemble in the lower clamp and thread the tubes in the top clamp (see Figure 6.6) to close the system
5. Connect one tube (input) to a syringe containing some medium (equipped with a $0.22\ \mu m$ filter) (**B**), and plug the other tube (output) to an empty syringe with a filter (**C**)
6. Hold the clamp vertical, with the exit channel upwards, then use the two syringes to push medium in (**B**) or aspirate (**C**) until all bubbles are removed
7. Place the chip and its clamp (**D+E**) in a big Petri dish (**F**) to prevent leakages, and place the ensemble in the incubator for static culture, or move on to the actuation protocol

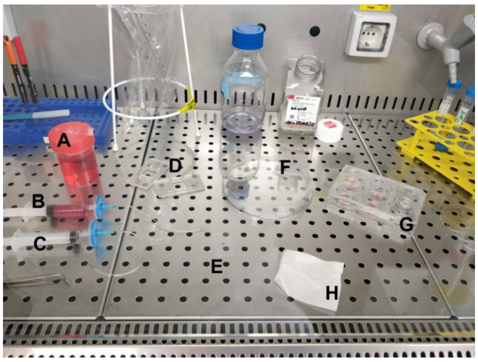

Figure 3.23: Integration of the patch in the chip

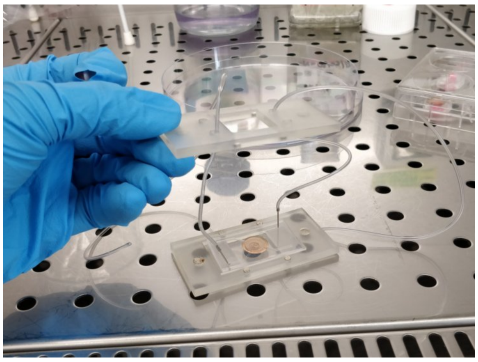

Figure 3.24: Integration of the chip in the clamp

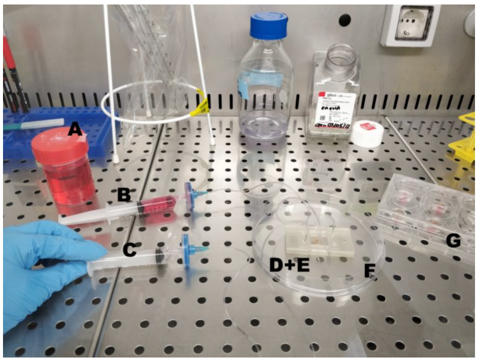

Figure 3.25: Removing the bubbles in the lower part of the chip

Connecting the chip to the actuation system Before we can connect the chip to the flow actuator, we need to carefully prepare the whole setup. Here we detail the protocol to connect 4 chips in parallel. Firstly we

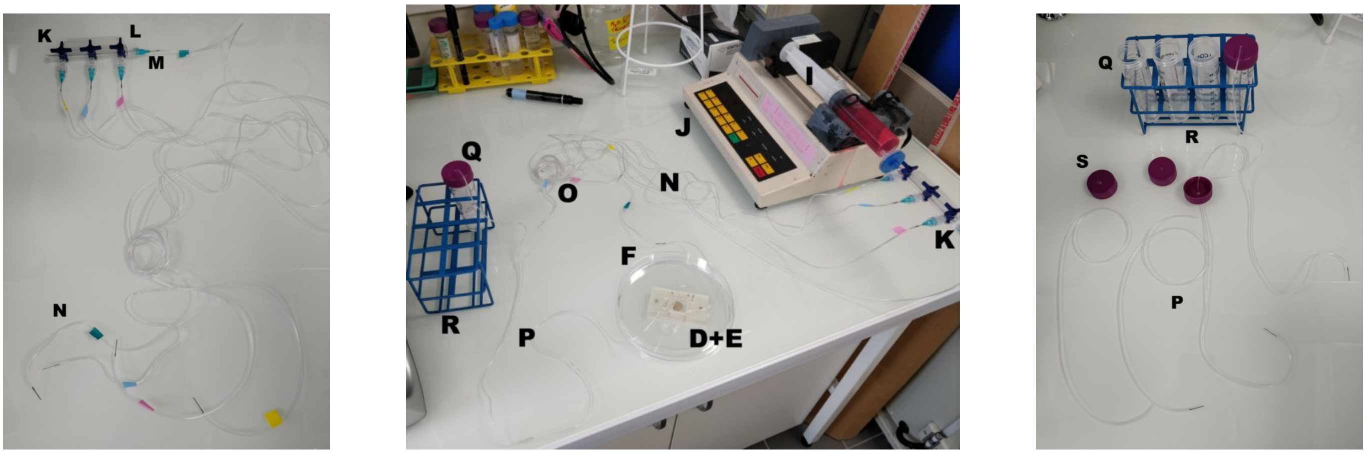

(a) Medium input (b) Connecting a chip (c) Medium ouput

Figure 3.27: Implemented system to achieve continuous medium perfusion in the Alveoli-on-a-chip

need to prepare the medium input: a 50 mL syringe (see **I** on Figure 6.10) filled with medium (usually ECGM with Dexamethasone) and place a 0.22 μm filter at its tip. We then use a microfluidic distributor (see **K** on Figure 6.8) flowing into a sterile connector (**L**) (female-female), a syringe tip (**M**) and then Tygon tubes (**N**). These four sterile Tygon tubes should be about 1 meter long, with metallic pins at one of their extremities (see **N** on Figure 6.8). These tubes should reach the inside of the incubator, where they should be rolled into coils (**O**), leaving about 15 cm of length after the coil, where the metal pin is, to connect to the chips.
The medium ouput is composed of four sterile 50 mL Falcon tubes (see (**Q**) on Figure 6.9) placed in a sterile tube holder (**R**). Four 30 cm long Tygon tubes (**P**) reach into these Falcon tubes through 1 mm wide holes in their caps (**S**).
Finally, we connect the chip in its clamp to the system using metal pins (see Figure 6.10). An important detail is that, in order to avoid introducing bubbles in the circuit, we should always push medium into the tubes, and once both tubes are dripping, they can be connected together.

Long-term flow maintenance Once the chip in place and fully connected, there are a few things to take care of. Firstly, the 50 mL syringe should be protected with aluminum foil to protect it from the light. The medium is not pre-warmed but it will heat gradually as it flows inside the coil that is placed in the incubator. Moreover, as the syringe pump heats up when used, the medium is not extremely cold in the first place.
It is important to monitor the flow rate to know when the Falcon tubes in the incubator will be full (and therefore change them). Similarly, the 50 mL syringe should be changed regularly. Each time, we used new tubes and new syringes to avoid contaminations.

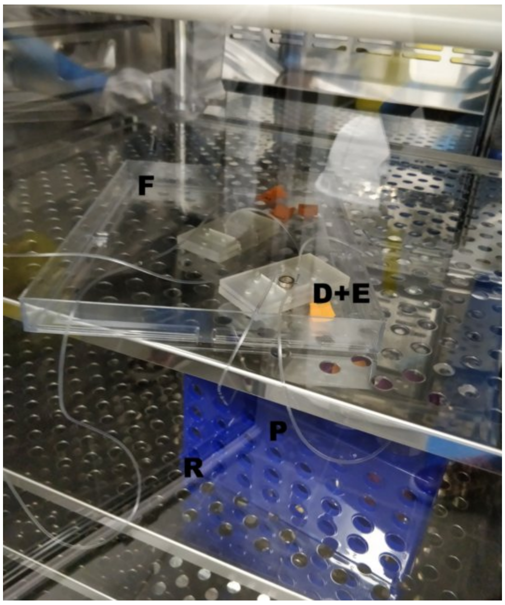

Figure 3.28: Two Alveoli-on-a-chip and their reservoirs in the incubator

Protocol discussion This protocol seems very complicated at first hand. It does indeed have numerous steps, but these are mostly very simple steps. Great care should be taken at all times to avoid bubbles. Moreover, this protocol should be performed quickly because the ventilation inside the biological hood tends to dry the cells very fast. Once the chip closed, the rest of the connecting should be done quickly so that the cells are not too cold. In the end, it just takes a little practice to correctly connect the chips.

d. Cell culture under flow conditions

Using the protocol detailed above, we put several patches under flow culture conditions and observed the effects on the cells.

Leaks and bubbles The two main concerns when cultivating cells in a microfluidic chip are leaks and bubbles. Our Alveoli-on-a-chip was designed specifically to prevent leaks, either to the outside of the chip, or from the lower to the top chamber. Indeed, we were able to culture cells (a co-culture with Dexamethasone) in the chip for a maximum of 18 days without observing any leaks.
Regarding the bubbles, in our first tests, we had bubbles forming under the patch in the chip. After a few days, the cells would starve and die where the bubble was. I decided to perform several actions: firstly, I noticed that autoclaved Tygon tubes were more rigid, and less permeable, therefore I always autoclaved my tubes before using them. Secondly, I centrifuged the cell culture medium before aspirating in the 50 mL syringe(s), and made sure to remove all the extra air in the syringe by flicking it and pressing out any bubbles. We also took care to always place the syringe so that the medium pushed out was taken from the bottom of the laid syringe (therefore any bubbles forming would be trapped on its ceiling). Finally, the whole medium circuit was completely filled with medium (all bubbles) removed before being connected to the chip. With such measures, we did not observe bubbles in the lower chamber of the chip anymore.

Survival We were able to culture cells for a maximum of 18 days without any leaks. On Day 18 the chip was moved for microscope observation and a sudden movement displaced one of the pins, causing the medium to flow in between the chambers. We could have placed the patch in another chip to pursue the culture but we decided to fix it and observe the cell layer integrity. We stained the cells with Phalloidin in order to observe the cytoskeleton of the cells (see Figure 3.29). We were able to maintain cells alive under flow conditions for 18 days and the cells presented normal cytoskeleton morphology. It would be interesting to try again and to perform immunostaining of the two types of cells to see if one cell type sustained more damage than the other.

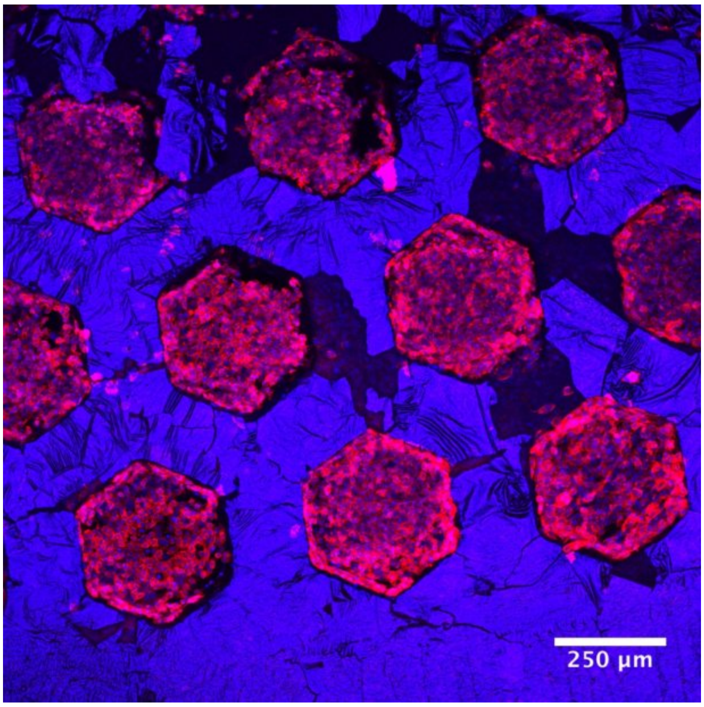

Figure 3.29: Immunofluorescence staining of the endothelial cells in the chip after 18 days under a flow rate of 100 µL/min (Total of 32 days of culture).
Red: Actin, Blue: Hoechst. *Scale bar: 250* µ*m*

e. Conclusion

Discussion The dimensions of our Alveoli-on-a-chip are relevant to the generation of a continuous flow in the basal chamber of our Alveoli-on-a-chip that retains the same characteristics as the *in vivo* alveolar capillaries. Indeed, we have demonstrated that we have a laminar flow, with a low Capillary number. We have also

established a relation between the input flow rate that we control and the shear stress exerted on our cells. We were able to implement long-term culture under flow conditions without leaks or contamination. This achievement was the accomplishment of a long series of attempts. Finally, we optimized a protocol to put the patch in the chip with flow, quickly enough to protect the cells, while making sure to keep everything sterile and prevent the formation of any bubble anywhere in the circuit.
We observed the survival of cells cultured under a flow rate of 100 $\mu L/min$ for 18 days. If the patch's gold layer was damaged by the flow, the alveolar structures were still intact. However, we could not observe endothelial cell alignment due to our low shear stress.

Perspectives If we had more time to continue the experiments, it would have been interesting to try and reduce the dimensions of our basal chamber as well as increase the viscosity of our medium until we could obtain endothelial cell alignment. Moreover, we could perform immunostaining to observe whether the protein expression of both cell layers was changed. Finally, we could have performed a Lucifer Yellow assay and a translocation test with nanoparticles to see if the flow in the basal chamber would change the behavior of our model.

3.4.2 Reproducing breathing dynamics

In order to mimic the microenvironment of the alveolar barrier, we need to generate a cyclic deformation of the cell layer. We have already mentioned our intention to deform the patch using positive pressure in the upper chamber of the microfluidic chip. However, since the mechanical properties of our patch are different from that of the alveolar barrier, we need to determine the pressure level to reach to induce the wanted (*i.e.* the physiological) deformation. In order to do that, we performed a review of the literature to understand the physiological mechanism and levels of the alveolar stretching. We then implemented a technical setup to mechanically deform the patch in the chip, and finally we determined the optimal pressure fluctuations required.

a. *In vivo* conditions

Dynamics As previously described, during inhalation, our diaphragm contracts, entraining the deployment of the inner pleura. Because of its elasticity, the interstitium expands and the alveoli inflate. At this moment, the internal pressure of the alveoli varies to a depression of about -1 cmH20 (i.e. about 100 Pa) [130]. This negative pressure aspirates the air in, resulting in inflation of the alveolar sacs.
During breathing, the total lung volume capacity evolve with the pressure and this cycle shows some hysteresis. This phenomenon can be explained by both the successive recruitment of the deflated alveoli, and the following stretching of these alveoli beyond their initial volume [131].

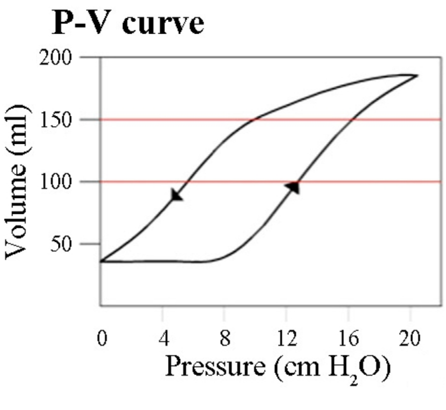

Figure 3.30: Hysteresis loop: lung volume evolution with the transpulmonary pressure. *Roan & Water, 2011 [132]*

Alveolar dynamics The alveolar capillary barrier is submitted to a cyclic stretching motion due to breathing. At a frequency of 0.2 Hz, each alveolus stretches, distending the epithelium and endothelium up to 8 to 12% linear strain in physiological conditions [6]. Higher linear strain values (17 up to 22%) correspond to a pathophysiologic ventilation state, leading to cell death ([6], [133]) In the alveoli, the surface tension forces are governed by Laplace's Law, according to which surface tension is inversely proportional to the radius of the alveoli. Therefore, the surface tension of the walls of small alveoli is greater than that of the walls of large alveoli [131]. Here, the surfactant plays a crucial role, as it diminishes the alveolar wall's total surface tension, thus increasing its overall compliance. This was confirmed by the observation that premature newborns, whose lungs lack complete differentiation and do not produce enough surfactant, exhibit breathing difficulties [134]. This phenomenon was also observed in patients undergoing acute lung injuries [135].
Finally, when it comes to a deeper understanding of the micro-mechanics of the alveolar space inflation, we have to admit that most questions remain unanswered. Indeed, the lungs are complex and fragile organs, with great inter-subject differences of morphology. Clinical, animal, mathematical and numerical studies have

shown interesting data, but there is no clear consensus on how these results could be unified under a single theory [132].

b. In chip implementation

Generating a breathing-like pressure variation Using a home-made MatLab script, I was able to generate a code that controls a Fluigent Controller (MFCS-EZ). The MatLab script creates an interface (see Figure 3.31a) that generates a script (a .au3 file) commanding for a sinusoidal curve reaching a maximum pressure input of 200 mbar (for example), with a frequency of 0.2 Hz (see Figure 3.31b). The MatLab interface allows to change the maximal pressure reached, as well as the frequency of the .au3 script.

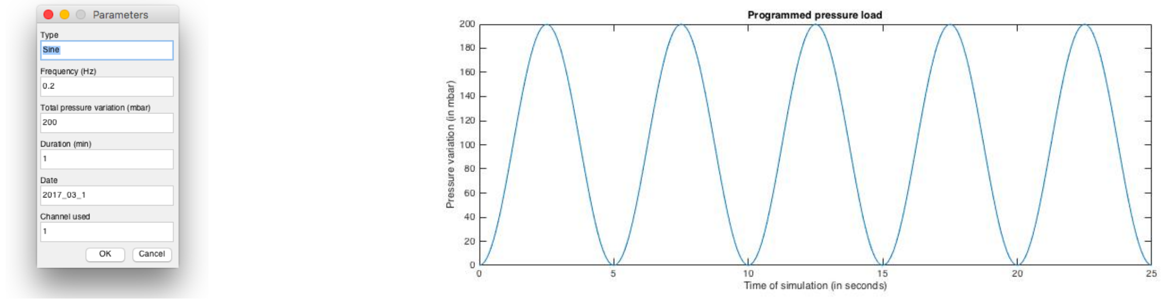
Parameters
Type: Sine
Frequency (Hz): 0.2
Total pressure variation (mbar): 200
Duration (min): 1
Date: 2017_03_1
Channel used: 1

(a) MatLab command window (b) Sinusoidal shape of the pressure implementation

Figure 3.31: Generating sinusoidal pressure control in the Alveoli-on-a-chip

Experimental setup We used the MFCS-EZ Fluigent controller because it has a fast and stable response to command, which allows for generating a smooth sinus function. This controller was connected to an entry of the top part of the Alveoli-on-a-chip using Tygon tubes. The output channel of the air chamber is connected to a sterile filter with another Tygon tube.
The Alveoli-on-a-chip is then placed on the confocal microscope. For the preliminary tests we used fixed cells (co-culture of A549 and HUVEC with Dex, 20 days old), and we put sterile PBS in the lower chamber (see Figure 3.32).

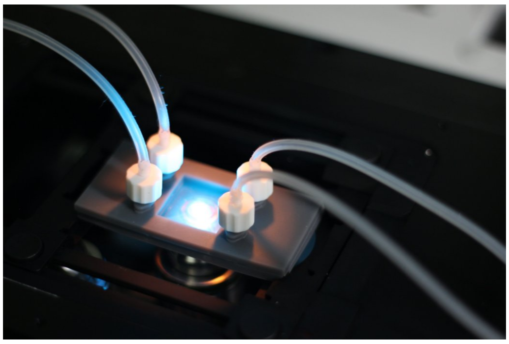

Figure 3.32: Experimental setup to measure the deformation of the patch according to pressure variations

Air pressure was then gradually increased in the upper chamber with the Fluigent Controller, and the subsequent deflection of the cells was observed. The deflection could be measured by focusing on the patch, then deforming it, finding the new focus and observing the traveled distance. A confocal microscope was used for this experiment because it possesses a piezoelectric stage, allowing for extremely precise vertical displacements (up to 1 µm).

c. Results

Using the setup described above, we tested several patches, several times. For each patch, we applied increasing then decreasing pressure, up to a point were we could not deform the patch anymore.

Preliminary results In the first tests, we made the focus on the PEGDA frame because it is a well-defined surface, and it is easy to make sure that we are perfectly focused on it. We observed that we could deform the patch to a maximal deflection of 100 to 140 µm with only 40 to 100 mbar of applied pressure (depending on the patch). We could see the deformation occurring on the microscope, as can be seen with the successive pictures taken during pressure variations (see Figure 3.33).

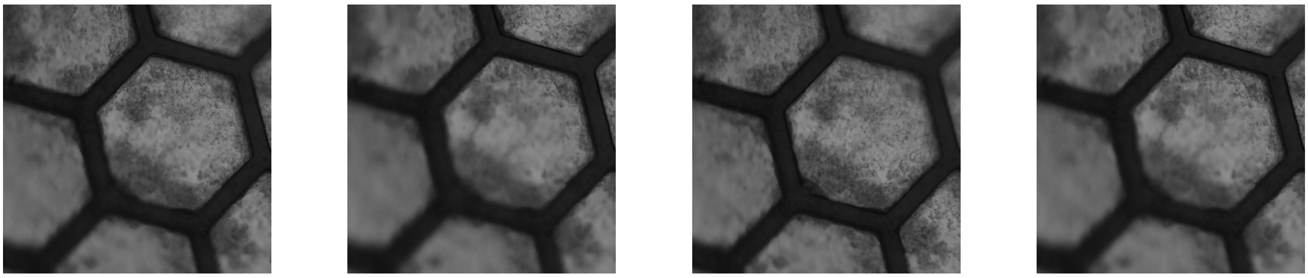

(a) Low pressure (b) High pressure (c) Low pressure (d) High pressure

Figure 3.33: Proof of concept: positive pressure induced patch deformation

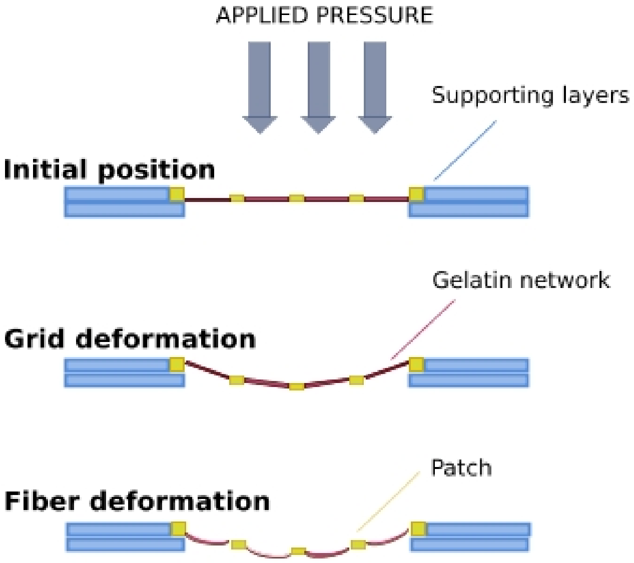

Figure 3.34: Patch positionning and deformation under pressure

However, I observed that the deflection that I was measuring was not due to a deformation of the nanofibers (as we would expect), but to a displacement of the global PEGDA frame. Indeed, immersed in liquid, the center frame is less rigid than when it is dry. Therefore the pressure applied does first pushes the honeycomb grid into a meniscus-like shape (see **Grid deformation** on Figure 3.34). Subsequently, and when the grid reaches the lowest position, the pressure builds up in the top chamber until it is important enough to deform the cell layer (see **Fiber deformation** on Figure 3.34). Finally, this means that we did not measure the deflection of the cell layer but that of the whole patch. These preliminary results are interesting because they prove that we can use positive pressure to deform the patch.

Measurement method optimization In order to measure only the deformation of the cellular tissue, we stained the cells with Hoechst and we focused on their nuclei. This method is a little less precise because making the focus by eye on the same level of a 3D shape (a cell's nuclei) is harder than with a 2D shape (the lower surface of the PEGDA frame). However, I tested and concluded that I could lose focus and come back to the same focus several times with an overall precision of 10 μm. Therefore, in the following experiments, we will record the vertical displacement down to the hundredth of millimeter only.
The protocol was optimized as follows:

- Establish the focus on the PEGDA frame
- Gently increase the pressure
- Adjust the focus until the PEGDA frame is in-focus again
- Repeat the operation until the PEGDA frame does not go out of focus: we reached the maximal **Grid deformation**.
- Establish the focus on the cell layer. This will be our zero for the deflection measures
- Gently increase the pressure
- Adjust the focus until the cells are in-focus again
- Note the travelled distance d_z
- Repeat the operation until the cells do not go out of focus: this will be the maximal **Cell layer deformation**.

The hereby measured deflection can converted to linear strain by assuming that the cell layer behaves like a thin membrane. In such case, according to the book *Introduction to Microsystem Design* by Werner Karl Schomburg [136], because we can assume here that the thickness of the cell layer does not change importantly comparatively to the the overall deformation, we have the following relation:

$$\epsilon = \frac{2}{3}\,\frac{d_z^2}{R^2} \tag{3.6}$$

$$\text{with} \begin{cases} \epsilon, \text{ the linear strain in the honeycomb} \\ d_z, \text{ the measured deflection} \\ R = 200\ \mu m, \text{ the radius of the honeycombs} \end{cases}$$

This relation allows us to estimate the linear strain induced in the cell layer by the applied pressure, just by monitoring the deflection of this layer.

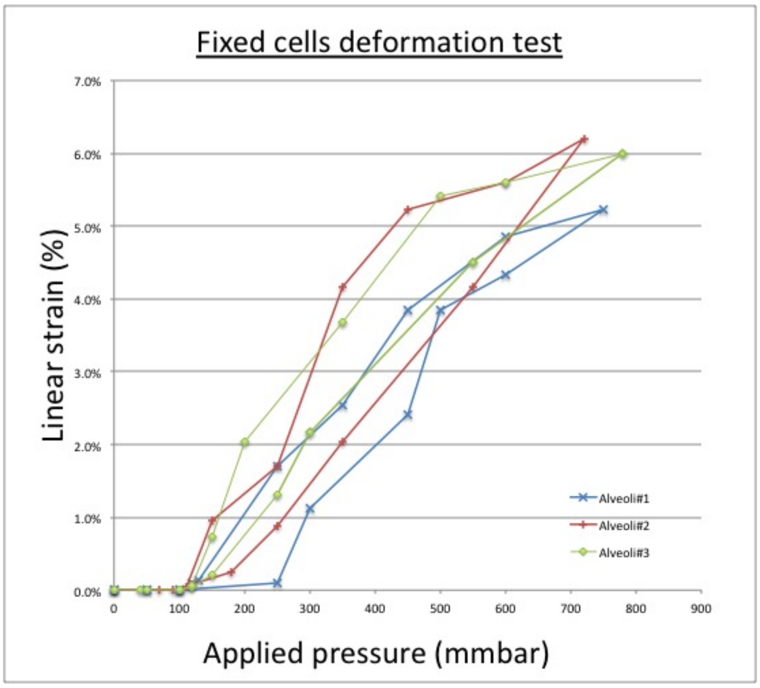

Figure 3.35: Cell layer deformation under pressure (fixed co-culture)

Results Finally, we performed this test on 4 patches, and in different alveoli (honeycombs) each time, and several times in each alveoli. We could observe that there is less than 2% difference when measuring the deformation twice on the same alveoli, which indicates that there is no residual deformation in the cells after stretching. Therefore we moved on to measuring the one deformation trend per alveoli.
In the Figure 3.35 is presented the results obtained for 3 alveoli of the same patch. In this experiment, we start. We reached a maximal pressure of 780 mbar, leading to a maximal strain of 6.2%. Above this pressure, the cell layer was not deforming anymore.

Stretch on live cells We have demonstrated that an increase of pressure of about 800 mbar is sufficient to induce a 6.2 % deformation. However, we now need to make sure that the cells can survive when repeatedly undergoing such pressure. This is why we wanted to test this deformation actuation on live cells. However, we did not have enough time to reach this milestone of the project.

d. Conclusion

Results We have implemented a system to produce precisely controlled positive pressure variations inside the upper chamber of our Alveoli-on-a-chip. We were able to demonstrate that the chip in its clamp resisted to up to 780 mbar without leaking.
The maximal deformation of our cell bi-layer that we could obtain was 6.2%, which is close to the minimal physiological linear strain 8%, but still too low. This means that our system is too rigid to accurately reproduce the *in vivo* dynamics of the alveolar barrier.
Another worrying point is that 780 mbar is a very high pressure: we fear that live cells might not survive to such pressure.

Perspectives Our system is not optimized: it is too rigid. However, when we will switch to live cells, we can expect to observe a greater flexibility of the cell layer (because the PFA fixation rigidifies the cellular membranes). This could lower the required pressure to deform the cells up to 12% linear strain. Testing on live cells will also enable us to check that the cells can survive these positive pressure cycles at the long term. Sadly, we did not have time to pursue these experiments.
However, if switching to live cells was not enough to reach physiological conditions (*i.e.* a higher deformation for a lower pressure) in our system, we have already thought of backup strategies. Indeed, we could see about increasing the honeycomb diameter to have bigger (thus more flexible) cell bi-layers. This would also mean increasing the honeycomb inter-distance to make sure that the patch is rigid enough and stays flat. Another

strategy would be changing the mechanical properties of the nanofiber network. This could be done either by changing the electrospinning parameters to reduce the diameter of the fibers, or by testing materials more flexible than gelatin, like elastin for example. These methods would be interesting to test, but they would require an important amount of time.

3.5 Conclusion

3.5.1 Results

In this chapter, we have imagined and realized an novel microfluidic object that can recapitulate the dynamic stimuli present in the alveoli: the Alveoli-on-a-chip. We offer a unique microfluidic chip that incorporates our microengineered PEGDA-gelatin patch as a membrane between a "medium chamber" containing enough medium to allow for cell survival and an "air chamber" for Air-Liquid interface culture of our alveolar capillary model. After numerous iterations and testing, we obtained a design that allows for a watertight separation between these two chambers, which was crucial for us, as we intend to use this model for translocation studies. Moreover, the fabrication processes were optimized and perfected and we can now offer a robust and highly reproducible object.

The main novelty in this chip, and to our knowledge, we are the first ones who achieved this, is its reversibility: the patch can be taken in and out of the chip at any moment for cell culture or for analysis. Moreover, our chip is so thin that it allows for *in situ* monitoring with a microscope at high magnitude (at least x40).

The Alveoli-on-a-chip was put under flow for continuous nutrient perfusion of the endothelium for up to 18 days. We could observe that the cells survived in the confined environment. We were also able to obtain a controlled deformation of the cell bi-layer through air pressure variation in the apical chamber.

3.5.2 Discussion and perspectives

If the fabrication processes were extensively characterized and optimized, our Alveoli-on-a-chip stands as a proof of concept rather than a ready-to-use tool. Indeed, we lacked of time to complete its validation and there are several points that need further investigation.

Our reproduction of the flow did not induce enough shear stress to model the physiological conditions *in vivo*. This means that our 3D model lacks important features that can only be induced by this mechanical stimuli, such as the formation of tighter junctions or the expression of certain proteins that play a role in the immune defense of the endothelium [102]. In order to improve this aspect of the chip, we could increase the viscosity of our medium with specific biocompatible compounds, in order to induce a higher shear stress.

Similarly, we have not obtained a satisfying deformation of our cellular bilayer. This does also prevent our model from mimicking the *in vivo* cellular behavior as cyclic stretch is known to enhance surfactant secretion and release by AET II cells [132]. Without this feature, our model lacks an important part of the translocation process: the interaction between the surfactant and the particles, which influences greatly the fate of these particles ([55], [86]). There is still important work that needs to be done to obtain the perfect deformation of the cell bilayer. Indeed, this parameter depends on the cell's rigidity (which is time-dependent) and the patch's mechanical properties, which can vary from lot to lot.

Finally, we offer a microfluidic chip that models the alveolar capillary barrier under flow conditions, and that could also include a cyclic strain in the upcoming future. The Alveoli-on-a-chip has two outstanding features: its 1 μm thin membrane, and its reversibility.

Chapter 4

iPSC differentiation into endothelial and alveolar epithelial cells

4.1 Introduction

In the process of recapitulating the functions of the alveolar barrier on a chip, the first step of our project was to design a biocompatible, mechanically active microfluidic chip, seeded with cells epitomizing specific tissue functions. Pursuing the long-term objective of developing an accomplished model, we believed that it was meaningful to enhance the accuracy of our chip's expression of cellular functions. The recent advancements in stem cell sourcing and differentiation provided a valuable alternative to the cancerous cell lines or high-maintenance primary cells currently adopted. Indeed, as previously described, the immortalized A549 cell line presents cell phenotypes that are not associated with typical alveolar epithelium behavior. Even though these cells can be used to accurately estimate the toxicity of some chemical compounds, they are not reliable enough to design highly-specific and targeted drugs as they can have unpredictable behaviors [43]. As for HUVEC cells, they can only survive a few passages before losing most of their specific functions, thus they are a poor model for long-term observations required for disease modeling or drug screening.

In this part we introduce the avant-garde technology of induced pluripotent stem cells (iPSC) and explain how we started to implement this technology in our chip. All experiments that were performed in this direction are detailed below. Our first objective was to characterize the behavior of the iPSC on our microfabricated scaffold to ensure that these cells kept their extraordinary properties, before moving on and optimizing two differentiation protocols to obtain both vascular endothelial and alveolar epithelial cells. These protocols were tested and adapted to our iPSC cell line in order to maximize the differentiation efficiency, before trying to differentiate the cells directly on the patch.

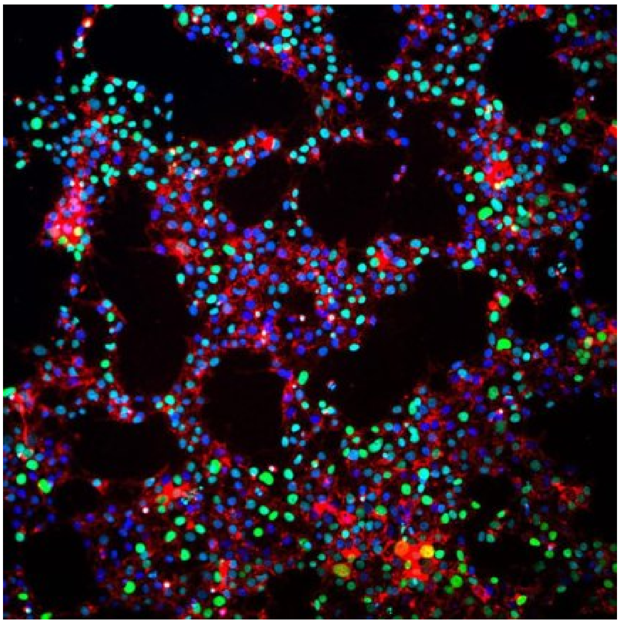

Figure 4.1: Immunofluorescent staining of pluripotency markers of iPSC. *Matt Spindler, Gladstone Institutes*

The interest of this work was not only to improve our model of the Alveoli-on-a-chip, but also to adapt two differentiation protocols to a commercialized iPS cell line. Indeed, if we were to test and implemented a differentiation protocol tailored to this cell line, this would be extremely interesting in terms of reproducibility for any lab wishing to use such protocols. Moreover, success in validating these protocols on our microfabricated patch has applications not only in organ-on-chip or other models, but also for tissue repair implants.

4.2 General introduction: the iPSC revolution

4.2.1 From iPSC discovery to their multiple applications

a. Scientific discovery

iPSC discovery: the scientific method In their paper published in 2006[137], Yamanaka (Figure 4.2) and Takahashi (Kyoto University) reported the generation of pluripotent stem cells from fibroblast cultures in mice. The original and straightforward method that they used for this discovery is fascinating (and is more detailed in the Appendix).
They selected 24 genes as candidates for factors inducing pluripotency in somatic cells (based on the hypothesis that they also play pivotal roles in the maintenance of embryonic stem cell (ESC) identity) and tried to activate successively each one of those genes until they obtained ESC. Single gene activation did not produce ESC, but the activation of the 24 genes did. Therefore they worked their way down by removing a single gene, then two, and so on until they found four genes that were sufficient and necessary to produce ESC. These newly generated cells (with 4 factors) were then introduced in a mouse and they observed teratoma formation with all three germ layers. These four factors (*Oct3/4*, *c-Myc* *Klf4* and *Sox2*) were concluded to be the minimum essential for induced pluripotent stem cell generations.

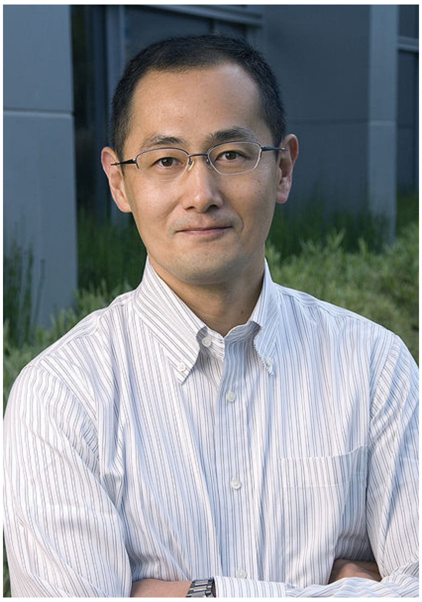

Figure 4.2: Pr. Shinya Yamanaka

Reprogramming human cells Within a year, Yamanaka and Takahashi demonstrated reprogramming of human cells into iPSC, using the same four pivotal genes: *OCT3/4*, *SOX2*, *KLF4*, and *C-MYC* with a retroviral system [137]. Shortly after, another independent research team reported the reprogramming of human cells: James Thomson and colleagues [138] used the following transcription factors OCT4, SOX2, NANOG, and LIN28 in a lentiviral system to generate iPSC.

b. Generating iPSC: current state-of-the-art

In order to generate an iPS cell line, the fabrication steps are: choosing the donor and the cell type to be sampled for reprogramming, choosing the reprogramming method, cultivating the cells hereby obtained, and finally selecting the clones to culture, expand, freeze and store. The choice of different methods for each of these steps will influence the final behavior of the produced iPSC line. That is why it is important to be aware of the origins and fabrication process of the iPSC that you are working with.

Donor origin Anyone can be an iPSC donor. This means that we can constitute large banks with a wide variety of genomes. For specific tests, however, donors with a specific condition can be required. Once the donor is chosen, it is crucial to choose the cell type to be sampled. iPSC are mostly obtained from four different types of cells, usually easily accessible, each presenting different advantages and drawbacks:

- Fibroblasts from the skin, which have an excellent reprogramming efficiency at early passages (3 to 5) but often show numerous gene mutations due to sun exposure [137];
- Keratinocytes from hair follicules, which are easy to sample but are difficult to reprogram [139];
- Peripheral blood mononuclear cells, can be obtained from a simple blood draw, but these are highly sensitive samples [140];
- Urine-derived cells, which exhibit stem cell characteristics and can be obtained from urine samples without the need of a biopsy or needles[141].

Reprogramming methods In order to obtain pluripotent cells, we need to reprogram adult cells to a stem cell state. To this day, there are three different methods to reprogram somatic cells:

- Somatic Cell Nuclear Transfer: manual technique that consists in removing the DNA of an oocyte and injecting the DNA of a zygote instead ([142] , [143]). It produces cells that are identical to ESCs, but this complex technique requires expensive and ethically problematic source material;

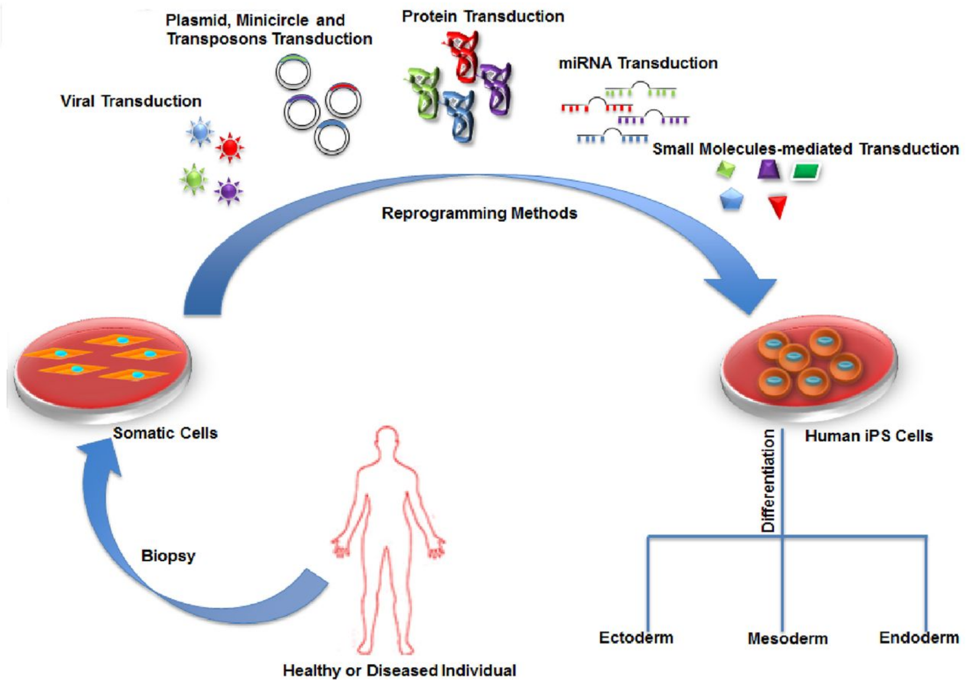

Figure 4.3: Different reprogramming processes are possible to obtain iPSC from a patient's somatic cells. *Biochemical Journal*

- Cell fusion: fusing a fibroblast and an ESC in order to obtain an ESC-like cell [144]. This easy technique produces tetraploid cells, which cannot be used for clinical purposes.;
- Direct reprogramming: transformation of somatic cells into stem cells by direct modification of the cell's genome through genetic material encoding for an pluripotent stem cell state. This genetic materials can be: reprogramming protein factors [104], recombinant proteins [145], microRNA [146].

Interest of direct reprogramming Direct reprogramming methods are high-efficiency techniques that do not raise ethical concerns and are therefore used for generating large banks of reprogrammed cells. Briefly (the details can be found in the Appendix), the reprogramming can be performed with:

- Lentiviruses: we randomly insert the reprogramming genes in the host's genome, forcing the expression of the Yamanaka factors. It is very reproducible and is effective but integrates DNA into the host cell's genome, which can interfere in subsequent experiments (especially clinical research because inserted genes are oncogenes).
- Episomal DNA: we deliver episomal DNA,*i.e.* DNA that will not be inserted in the genome. This is a nearly integration-free method: the replication is stable, and takes place outside the nuclei. These DNA plasmids are virus-free. However, these reprogramming plasmids have a low efficiency.
- Sendai Virus: This respiratory virus is a single-stranded RNA virus, non-integrating and replication-deficient. It is easy to use, has a high efficiency and is free of genetic perturbation as the virus cannot enter the nucleus. Sendai viral vectors also reprogram cells with relatively high efficiency, which helps diminish its important cost.
- mRNA delivery: we deliver mRNA to the cells and wait for their automatic replication. This method is highly efficient (with 1 to 2% of cells reprogrammed), non-integrative and non-viral method. However, it is not universal and takes 17 days of reprogramming with a constant supply of expensive mRNA . It is mostly used for therapeutic applications.

c. iPSC to revolutionize life sciences

iPSC can be easily sourced, from any donor, and can be subsequently differentiated into any kind of tissue. These incredible properties open the way for numerous applications.

Research applications Firstly, iPSC can be used for fundamental research. Indeed, they can replace the primary or immortalized cell lines that have been used by researchers for so many years. They can provide multiple origins for a same tissue, allowing to experiment on more than just one person's cells. In the same way that microfabrication enabled the development of complex engineered cellular micro-environments, iPSC will improve the biological fidelity of such tissue models.

Pharmaceutical applications iPSC-improved organ models (such as Organs-on-Chips) developed for fundamental research could also be used for drug screening in the pharmaceutical industry. Furthermore, as wide banks of iPSC are constituted all over the world, the industry has the possibility to screen on several thousands of "*in vitro* patients" at a time. Thus they increase the variability of genomes tested, therefore the trustworthiness of their medicine. This would also enable to observe whether the efficiency of a drug or its possible adverse effects are only restricted to a certain subgroup of the population due to specific differences (age, biological sex, origin, pregnancy, etc.).
Moreover, because iPSC can be obtained easily, it is now possible to choose the donors and constitute specific banks, for example with a specific genetic mutation. This means that we could constitute sub-populations for specific drug testing. Moreover, we could develop disease models with specific disease affected cells. For example we could collect patient cells that possess the *CFTR* mutation to study cystic fibrosis. Those could be either obtained from a sick donor, or genetically modified in the lab (for example with the CRISPR tool).

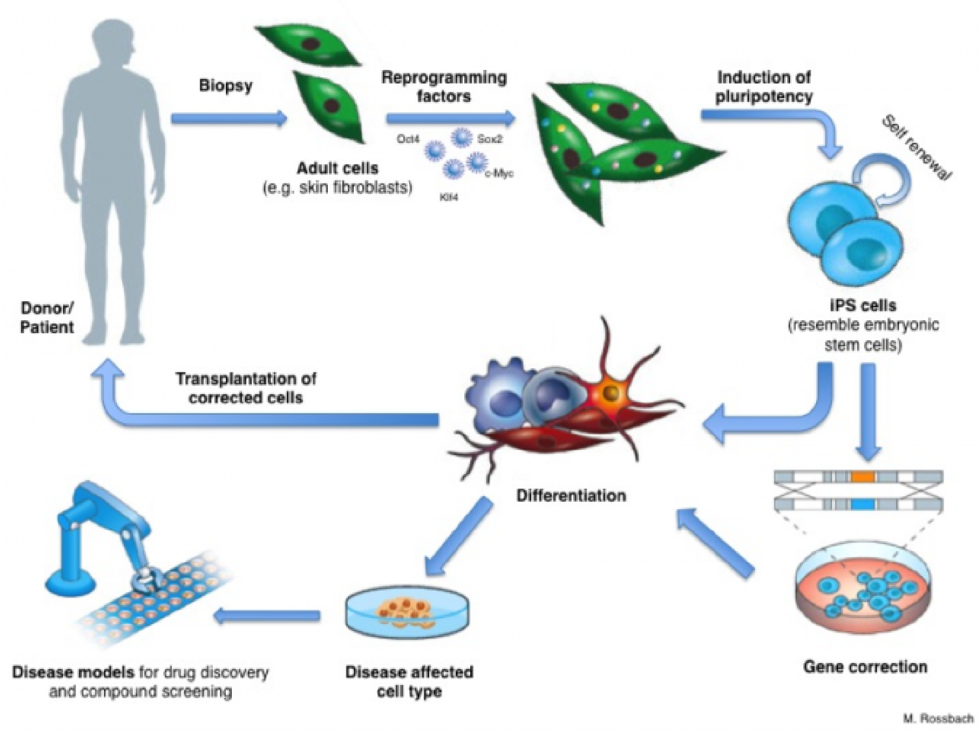

Figure 4.4: iPSC have multiple applications, either for research such as disease modeling or for therapeutic uses such as tissue regeneration.
www.eurostemcell.org

Therapeutic applications Finally, iPSC can be used for therapeutic purposes such as tissue regeneration or implants. Indeed, cells can be engineered from any patient's sample, thus reducing the risk of an immune rejection.
And on a deeper level, we could imagine building patient-specific models to test complex drug cocktails before administering them. For example for certain cancers, there are more than one treatment possible, and the choice depends on tumor specific parameters and the patient's response. The choice is often left to the doctor's expertise. Being able to test *a priori* those different courses of treatment could help making such a decision, and give preliminary indicators on how the patient would react to a certain treatment. Of course, this kind of personalized medicine is extremely expensive, and the price of iPSC technology will have to be reduced before it can become a widespread therapy.

Limitations Currently, these applications are hindered by the gradual progress of research. Indeed, iPSC differentiation has a very low efficiency and can be very time-consuming. Moreover, as these cells were encouraged to stay pluripotent and keep their very high proliferation rate, they have the tendency to evolve into

multipotent tumors (or teratomas), a risk that currently discourages implantation. Indeed gene instability, cell heterogeneity and cell purity are major drawbacks of therapeutic uses of iPSC.
To this day, there are very few projects that reached clinical trial phase, the first one being the macular degeneration project by Takahashi (Kyoto) in 2013. This project was stopped early as regular DNA sequencing of post-implanted cells revealed possible cancerous markers. The trial was halted for safety reasons even though no teratoma was observed. However progress has been made since, and to date, the incidence of teratomas seems to be well controlled in all of the major clinical trials, and few, if any, adverse events owing to the use of iPSC derivatives have been reported [147].
Considering the possible complications, the cost of any study becomes very high as it reaches clinical phases of testing, and only those showing robust clinical benefits will lead to therapies. The main challenge now will be to obtain such funding to continue to explore the potential therapeutic applications of these cells.

4.2.2 Developmental pathway

In this chapter, we will try to recapitulate alveolar functions by using directed differentiation of induced pluripotent stem cells to form our alveolar capillary barrier model. Therefore, it is important to give the reader a short introduction on lung developmental biology. It will give a more precise idea of what happens in a developing foetus that we will try to reproduce in a cell culture dish. Only with this knowledge of the complex multi-cellular evolving environment of the developing lung can we understand the chenical and mechanical cues it receives over time.

a. At the beginning: pluripotent state

Assessing pluripotency There are many different proteins that have been identified as markers of the pluripotent and self-renewing status of stem cells. Currently we still don't know their exact role of each, but they are frequently observed in ESC or they were proven indispensable for pluripotency or self-renewal in knock-out mice. I will present here some of the markers that we looked into in our experiments.

- NANOG is a transcription factor involved in embryonic stem cell proliferation, renewal, and pluripotency. The encoded protein can block ESC differentiation and can also autorepress its own expression in differentiating cells.
- SSEA-4 is synthesized during oogenesis and is present on oocyte, zygote, and early stage embryo membranes.
- OCT-4 (octamer-binding transcription factor 4) is critically involved in the self-renewal of undifferentiated embryonic stem cells. OCT-4 expression must be closely regulated, as too much or too little will cause differentiation of the cells. OCT-4 is initially active as a maternal factor in the oocyte but remains active in embryos throughout the preimplantation period. Its expression is associated with an undifferentiated phenotype and tumors.
- SOX2 (sex determining region Y-box 2), is a transcription factor that is essential for maintaining self-renewal, or pluripotency, of undifferentiated embryonic stem cells. SOX2 has a critical role in maintenance of embryonic and neural stem cells.
- TRA-1-60 is a pluripotent stem cell-specific protein expressed on the surface of undifferentiated human ESCs, iPSC, embryonal carcinoma and embryonic germ cells.

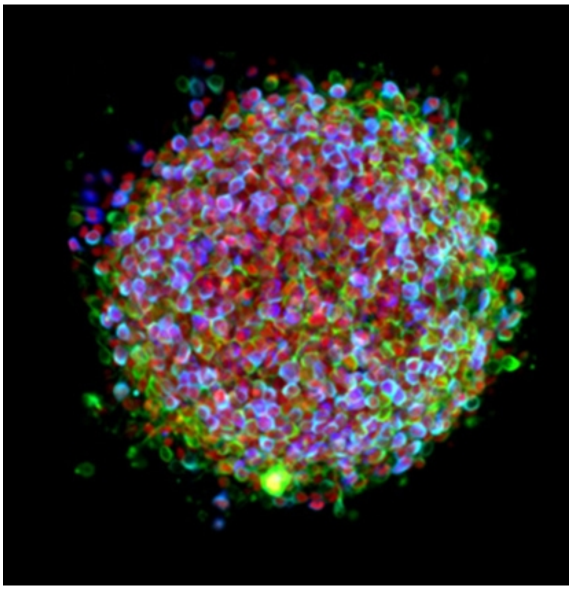

Figure 4.5: Observation of pluripotency markers on an Emrbyoid Body
McLean Hospital and Harvard Medical School/NINDS

The importance of embryoid bodies In the foetus, the pluripotent stem cells of the zygote grows into an embryo and proceeds to the different stages of its development (blastula, gastrula and organogenesis). At the blastular stage, the embryo is still round-shaped and homogeneous. Then a structure will appear: the primitive streak. This structure will begin the orientation of the embryo (left–right and cranial–caudal body axes) and guide its development towards the three germ layers: ectoderm, mesoderm and endoderm.

In directed differentiation protocols the primitive streak induction is achieved by forming embryoid bodies (EBs), which are non-adherent aggregates of stem cells in three dimensions. Additionally, the inductive effects resulting from signaling between cell populations in EBs results in spatially and temporally defined changes, which promotes complex morphogenesis. Tissue-like structures are often exhibited within EBs, including the appearance of blood islands reminiscent of early blood vessel structures in the developing embryo.

In contrast to the differentiation of iPSC in monolayer cultures, where the addition of soluble morphogens and the extracellular micro-environment can both be precisely and homogeneously controlled, the 3D structure of EBs poses challenges to directed differentiation. Indeed, due to great variations in EB size, transport limitations occur within EBs, creating gradients of morphogens, metabolites, and nutrients. Therefore, the delivery of morphogens to EBs results in increased heterogeneity and decreased efficiency of differentiated cell populations compared to monolayer cultures, which can result in a population of cells at heterogeneous state of differentiation.

Finally, although the complexity resulting from the three-dimensional cellular adhesions and signaling may recapitulate more native tissue structures, it also creates challenges for understanding the relative contributions of mechanical, chemical, and physical signals to the resulting cell phenotypes and morphogenesis. Therefore, the use of EBs is often used as a first step, in order to induce the primitive streak. Afterwards, the cells are dissociated to pursue the differentiation protocol in dishes.

b. Development of the alveolar capillary barrier

After the primitive streak induction, the embryo continues to develop to its gastrular phase, and finally starts its organogenesis. We will present here the genesis of the lung and its surrounding capillaries [148].

Embryonic development Organs develop in the foetus during the first 5-7 weeks post fertilization. The lung appears at the end of the fourth week, as a ventral bud of the future esophagus, just after the formation of the primitive gut (see Figure 4.6). The epithelial components of the lung are derived from the endoderm, and the enveloping connective tissue from the mesodermal germ layer. The hemangioblast, a progenitor of endothelial cells also derives from the mesoderm [148].

Lung bud development The lung bud then separates from the gut and grows into tubes of high columnar epithelium (after six to seven weeks). The future branching pattern of the conductive airways is already observable (see Figure 4.6). At the end of seven weeks the lung resembles a small tubulo-acinar gland (*i.e.* a tube-shape cluster of cells), giving the ensuing pseudoglandular stage its name.

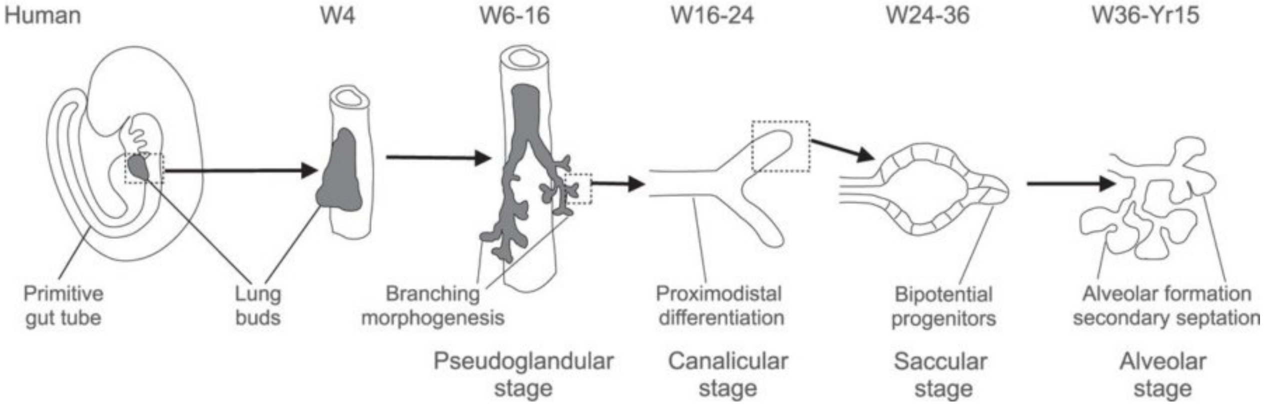

Figure 4.6: Different steps of the foetal development of the alveolar capillary barrier in the human. After Hans Snoeck *et al*, 2015 [149]

Pseudoglandular stage During this stage, we observe the formation of all prospective conductive airways as well as the appearance of the acinar outlines. This is achieved by a continuous growth and branching process of the peripheral epithelial tubes, an expansion that is highly regulated by epithelio-mesenchymal interactions. Indeed the close contact between the epithelium and the mesenchymal cells is crucial in this regulation. Moreover, the observation made by Schneeberger [150] that the epithelial cells in sheet are interconnected with each other by gap junctions indicates that electrical coupling may be responsible for the regulation of cellular differentiation. Nexus-like junctions are present from the early stages of development until the differentiation

into type I and type II alveolar cells has occurred in the periphery. Interestingly, the epithelium was also found to form a functionally tight barrier from the very beginning.
During the pseudoglandular stage, the airway tubes are lined proximally by a high columnar and distally by a cuboidal epithelium. Differentiation of the airway wall occurs in a centrifugal direction, so that typical ciliated, nonciliated, goblet, and basal cells appear first in the proximal airways. Cartilage and smooth muscle cells are found in the trachea early in this stage. After 14 weeks, there is already some secretory activity with the presence of mucous glands.

Canalicular stage The canalicular stage encompasses the early development of the pulmonary paren-chyma. At the end of week 17 we find the newly delineated acinus composed of a stem tubule, the prospective terminal bronchiole, 2-4 future respiratory bronchioles, and some small clusters of short tubules and buds. In the subsequent weeks the originally compact clusters grow by further peripheral branching, by lengthening of each tubular branch, and, last but not least, by a marked widening of the distal airspaces at the expense of the intervening mesenchyme.

Lung vascularization process Simultaneously with the organogenesis, vascular connections develop all around the growing lung tissue.The pulmonary arteries originate from the aortic arches, and develops in the mesenchyme, around the lung early tubules. They form a vascular plexus (*i.e.* network), irrigated by systemic veins from the proximal gut and trachea at first. Then this plexus will connect to the pulmonary veins, originating from the atrial portion of the heart.
As may be expected by the close relationship between the airways and the arterial pathways, the accompanying arterial branches are laid down during the pseudoglandular phase. Because there is only minimal blood flow through these vessels, however, they all remain small and rather inconspicuous. Lung peripheral growth of the canalicular stage is accompanied by an increase in capillarization.

Fusion and maturation of the barrier During the canalicular stage, the capillaries, which previously formed a loose network within the mesenchyme, begin to arrange themselves around the airspaces, subsequently establishing in many places a close contact with the overlying cuboidal epithelium. These contact points are the sites where the epithelial cells decrease in height, develop attenuated cytoplasmic processes, and become invisible (except for the perinuclear region) in the light microscope: we witness the formation of the first thin air-blood barrier portions. The close apposition of capillaries to the epithelium and the epithelial flattening are intimately related phenomena. It is still unclear which of the two processes induces the other. Depending on their location on the vascular tree, endothelial cells will differ in phenotype, hence express different markers or respond differently to similar stimulus [40].The formation of thin air-blood barriers starts peripherally but does not involve the terminal segment of the last tubule branch, because the undifferentiated or cuboidal epithelium is needed for further growth and branching.
Finally, in the terminal branches the alveolar sacs are formed as the cuboidal epithelium differentiates into AET II cells, which in turn differentiate into the AET I cells. Electron microscopic investigations of serially sectioned epithelial cells demonstrated that the reliable criterion to ascertain the forthcoming differentiation into type I pneumocytes was the formation of a cytoplasmic attenuation and not the lack of lamellar bodies (see Figure 4.7).

Indeed, it seems that before differentiation most cells contain lamellar bodies independently of their destiny. Type II cells can incorporate tritiated thymidine, divide, loose their granules, and transform to type I cells. The same sequence was observed in adult lungs after damaging the alveolar epithelium. The secretory Type II cells of the alveolar wall are hence known as the stem cells of the alveolar epithelium. Interestingly, it appears that the secretory cell type of the bronchioles (Clara cells) also represents the progenitor cells of the bronchiolar epithelium.

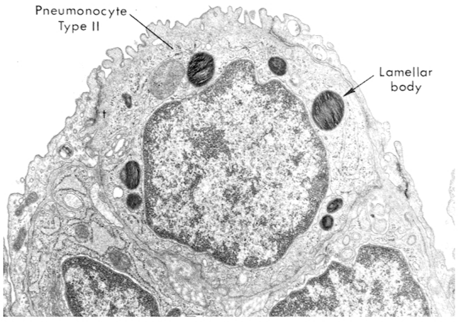

Figure 4.7: Transmission Electron Microscopy of a lamellar bodies in a Type II alveolar cell.
Delaware University, 1998

4.2.3 Conclusion

Induced pluripotent stem cells are only a decade old, and they are already revolutionizing life sciences. Even though the reprogramming process is not fully understood yet, some generation and differentiation techniques have already been implemented, and iPSC already have numerous world-changing applications.
iPSC are widely used in research, to replace embryonic stem cells or mature primary cells (after differentiation). They allow for wide-range testing on different patients, rather than using a single cell line for drug screening. iPSC also have tremendous applications in the therapeutic field, whether it is by direct implantation of cells to replace damaged or diseased tissue, or by the generation of personalized patient models (organs-on-a-chip) for specific drug screening.
Currently, researchers are working on reprogramming methods to obtain an efficient and low-cost method that would not leave any residues in transformed cells. Others work on developing high-efficiency, reliable and low-cost differentiation protocols to be able to obtain any somatic cell from iPSC. Both need to systematically verify cell lines' identity and safety, by checking their genomes, gene-expression patterns and more. One such effort, the European Bank for Induced Pluripotent Stem Cells, based in Cambridge, UK, publicly launched its catalogue of standardized iPSC for use in disease modeling. Yamanaka is also involved in banking iPSC for future therapies, collecting varieties that would be immunologically compatible across a broad population.
However, the greatest challenge to come is not scientific. Researchers are going to need strong support from the pharmaceutical industry and governments to move forward with cell therapies; for drug discovery and disease modeling, researchers must be determined and patient. iPSC can only shorten the discovery process, not skip it. As Yamanaka says, "There's no magic. With iPSC or any new technology, it still takes a long time."

4.3 IPSC behavior on the patch

4.3.1 Assessing iPSC pluripotency

When working with iPSC, before commencing any experiment it is customary to verify that the cells have not lost their properties of pluripotency and self-renewal. The common procedure is to check for the expression of pluripotency markers by immunostaining. Before launching a differentiation protocol, we first ensured that our cells were pluripotent and that such property was maintained after seeding and growing cells on our microfabricated gelatin patch.

a. Pluripotency characterization assays

Cell line The cells used during this work are from the Human Episomal iPSC Line (Gibco, Ref. A18945). These cells were derived from CD34+ cord blood using a three-plasmid, seven-factor episomal system. It is considered as a reference line as it bears no genome alteration from the reprogramming process (this means that they are clinincal grade). According to the iPSC culture methods optimized by Thomson and colleagues [151], cells were cultured feeder-free on Geltrex (ThermoFisher, Ref. A1413202), a soluble basement membrane composed of laminin, collagen IV, entactin, and heparin sulfate proteoglycans. Cells were fed daily with supplemented Essential 8 medium (ThermoFisher, Ref. A1517001) and passaged with a 0.5 mM solution of EDTA (for the detailed maintenance protocol, see the Appendix section).

Evaluation of iPSC pluripotent behavior Prior to seeding the cells on the patch, we stained them for NANOG (see Figure 4.9a), SSEA-4 (see Figure 4.9b) and OCT4 (see Figure 4.9c). The strong staining of all markers in all cells confirms that our culture protocol does not induce any differentiation as the cells keep expressing pluripotency markers (see Figure 4.9). Therefore we can move on to seeding them on the patch.

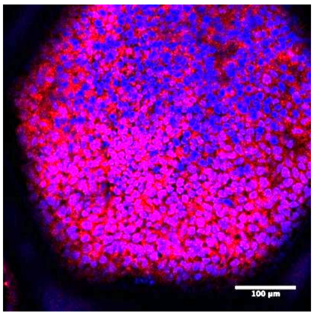

Figure 4.8: NANOG expression on the patch

b. Evolution of the pluripotent behavior on our patch

In order to assess whether culturing iPSC on our micro-engineered patch has any effect on the pluripotent behavior of the cells, we observed the evolution of the pluripotency markers expression after 7 days of culture

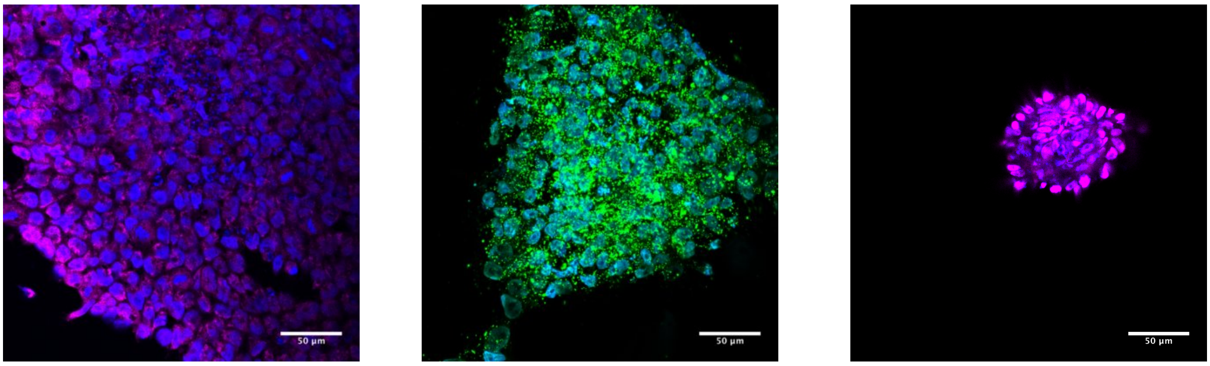

(a) NANOG (b) SSEA-4 (c) OCT4

Figure 4.9: Validation of the pluripotent state of our iPSC colonies after two weeks of culture.
Scale bars: 50 µm

on the patch.
All the markers tested were highly and consistently expressed after 7 days of culture on the patch: NANOG (Figure 4.8), SOX2 (Figure 4.10b), TRA-1-60 (Figure 4.10c) and SSEA-4 (Figure 4.10b).

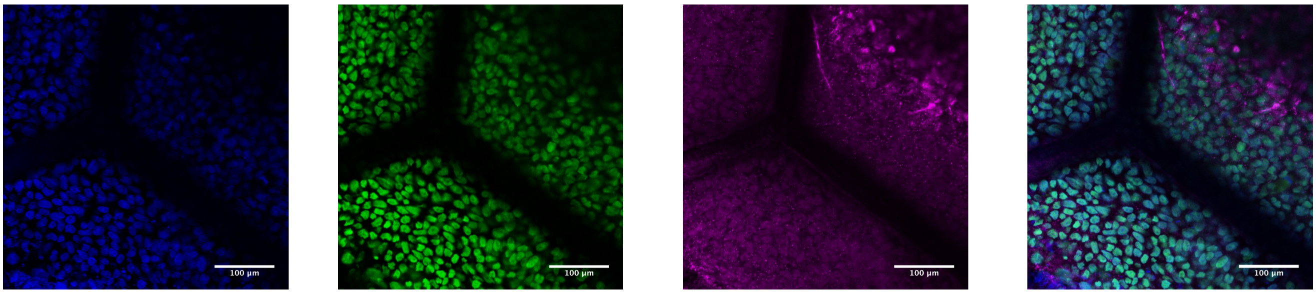

(a) Hoechst (b) SOX2 (c) TRA-1-60 (d) Merge

Figure 4.10: Observation of the pluripotent state of our iPS cell line after 7 days of culture on the patch.
Scale bars: 100 µm

c. Conclusion

Prior to starting any differentiation experiment, we used immunostaining to demonstrate that, with the cell culture methods used, our cells do not start to spontaneously differentiate after some time in culture. Indeed, it was important to ensure that switching cells from Geltrex dishes to our gelatin nanofiber network would generate mechanotransduction signals leading to spontaneous differentiation. This verification is the mandatory preliminary step for all differentiation experiments, because it guarantees that we start the differentiation protocol in good cell state conditions.

We were able to demonstrate here that the iPSC cell line that we used kept its pluripotent and self-renewal properties under our culture conditions, as well as on our patch.

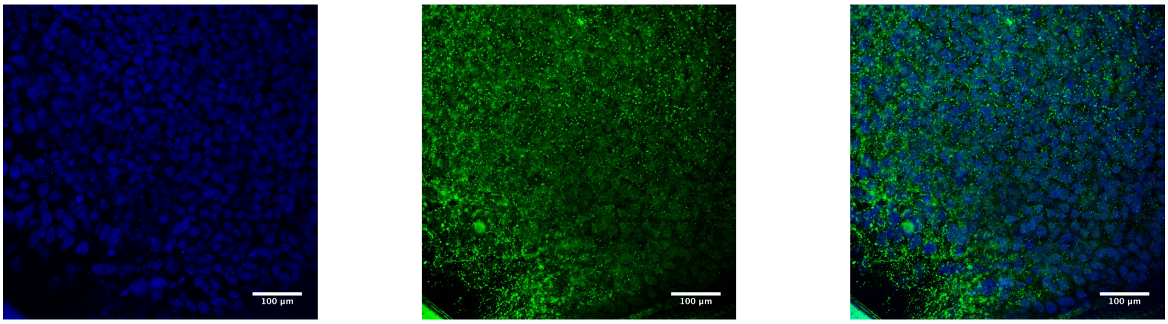

(a) Hoechst (b) SSEA4 (c) Merge

Figure 4.11: Observation of the pluripotent state of our iPS cell line after 7 days of culture on the patch.
Scale bars: 100 µm

4.3.2 Embryoid bodies formation

a. On patch formation

Principle To start our differentiation by inducing the primitive streak, we used EBs. In order to form EBs on our patch, we had to lessen the strong adherence of cells to our gelatin fibers network because otherwise the cells were spreading and we did not observe 3D structures. In order to do so, we first coated each patch with a high dilution Vitronectin solution. Secondly, the cells were treated with ROCK-inhibitor for a few hours. Indeed, Y-27632 is a selective inhibitor of the Rho-associated kinase (a serine-threonine kinase involved mainly in regulating the shape and movement of cells by acting on the cytoskeleton) and it is widely used to prevent the dissociation-induced apoptosis and improve the survival rate of embryonic stem cells and induced pluripotent stem cells.
However, ROCK is also a key regulator of cell migration and cell-cell adhesion. Short ROCK inhibitor treatment time will promote cell migration and cell-cell adhesion, which will lead iPSC to form spheroid morphology. On the contrary, increasing Y-27632 treatment time will inhibit cell migration and cell-cell interaction, which will make the migration of cells more difficult, leading to a weaker cell-cell adhesion power and resulting a flat cluster morphology.

Procedure Each patch was coated with 1:500 Vitronectin (ThermoFisher, Ref. A14700). *i.e.* a final concentration of 1 µ g/mL. Then we seeded 200 000 cells in a 100 µL droplet of E8 medium completed with ROCK-inhibitor to a final concentration of 1 µM. After 1 h, one patch was switched to E8 medium. Three other patches were switched after respectively 2, 3 and 4 hours of ROCK inhibitor treatment.

b. Results

On the day of seeding, after 4 hours, we could already observe a difference between the cells treated for 1 h and those treated for 4 h. Indeed, as can be seen on Figure 4.12, the longer the treatment, the more flat are the cell clusters. After 48 h in E8 medium, we observed that only the samples with 1 and 2 h treatment time exhibited three-dimensional clusters (see Figures 4.13a and 4.13b), whereas both other samples had flat layers of cells (see Figures 4.13c and 4.13d).

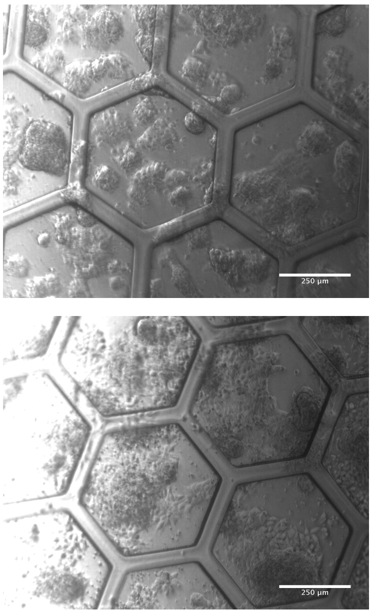

Figure 4.12: iPSC 4 hours post-seeding. Top: 1 h of Y-27632 treatement; Bottom: 4 h of treatment. *Scale bars: 250µm*

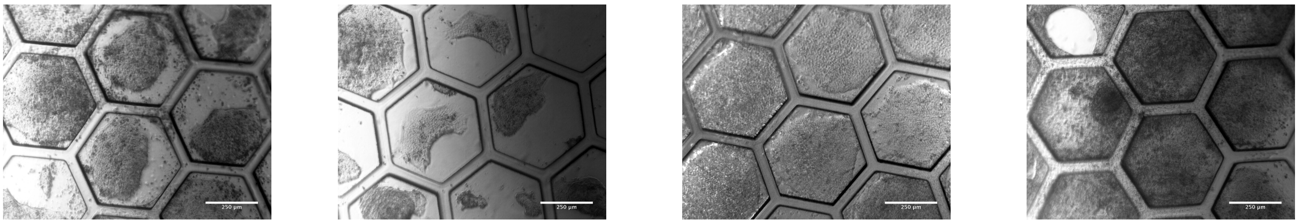

(a) 1h treatment (b) 2h treatment (c) 3h treatment (d) 4h treatment

Figure 4.13: Embryoid bodies formed after 48 h in culture for different lengths of ROCK-Inhibitor treatment at Day 0. *Scale bars: 250 µm*

c. Conclusion and perspectives

Conclusion We were able to observe that differences in duration of ROCK inhibitor treatment can induce important differences in colony shape when seeding EBs. Indeed, over 2 hours of treatment resulted in flat colonies after 48 h in culture, whereas shorter treatment resulted in 3D-shaped colonies.

Perspectives In order to obtain a precise and more reproducible protocol, we could optimize the homogeneity of cell seeding (by using a stencil) and test more conditions between 1 h and 3 h of ROCK inhibitor treatment to determine the optimal duration. Scanning Electron Microscopy could be used to precisely evaluate the height of the EBs formed in culture.

4.3.3 Conclusion: maintained pluripotency on the patch

In this part, we analyzed and confirmed that the iPSC line used for our differentiation experiments remains pluripotent in a feeder-free and E8 feeding condition. Moreover, this pluripotency does not disappear when the cells are seeded on our micro-engineered gelatin nanofiber network. This was a crucial primary step to be able to differentiate the cells directly from our patch in further experiments.
Moreover, we started to analyze the generation of embryoid bodies on the patch. We did not finish to optimize this protocol as cell differentiation *in situ* was postponed (experiments duration exceeded the 3-year time allowed for this work). Therefore, the EB formation experiments were to resume after achieving a proper differentiation in a dish first.

4.4 From iPSC to an endothelium

4.4.1 Differentiation protocols: state-of-the-art

a. Endothelial differentiation: overview of the developmental pathway

Being able to differentiate iPSC into endothelial cells is of growing interest, as these cells interact with all tissues of the human body. Therefore, whether it is for research on human vascular tissue, or for disease modeling on tissue models, a need for endothelial cells in culture arises. That is why multiple protocols to differentiate pluripotent stem cells into endothelial cells were developed in the past decade.
We will present here a quick summary of the method used to produce iPSC-derived endothelial cells. We will focus here on the biochemical signaling occurring in the cells throughout differentiation. We will then present an overview of the different existing protocols. For each, the specific compounds will be presented and I will give references to publications that further detail how these compounds act (and interact) in the differentiation process.

Mesoderm induction During the process of vasculogenesis, preliminary vascular endothelial progenitor cells are believed to originate from angioblasts generated from the cardiac mesoderm [152]. Thus, generation of pure mesodermal cells is the first step for derivation of endothelial progenitor cells. Mesoderm induction can be achieved via Wnt signaling, which directs differentiation of hPSCs into mesoderm, or via GSK3β inhibition which activates this pathway ([153], [154]).

Obtention of endothelial progenitors A pathway to direct mesodermal cells into endothelial progenitors is the activation of protein kinase A, for example via a rise of cyclic AMP levels, which is known to increase vascular development [155].

Endothelial cells specification Once this progenitor stage is obtained, these cells can still differentiate into several endothelial lineages, such as endothelial cells, vascular smooth muscle cells or pericytes. Therefore, specific vascular commitment is required to obtain mostly endothelial cells. This commitment can be obtained by culturing cells with VEGF.

Maturation After specific differentiation cells are cultured in specific medium for several additional days until they reach their mature state.

Purification The obtention of complete endothelial commitment from mesodermal cells has yet to be achieved, that is why most protocols use a purification step. Cells expressing endothelial-like markers such as VE-Cadherin (CD144) or PECAM1 (CD31) are sorted out (either by fluorescence- or magnetic-activated cell sorting: FACS or MACS) after reaching the progenitors phase, and are then replated for further maturation.

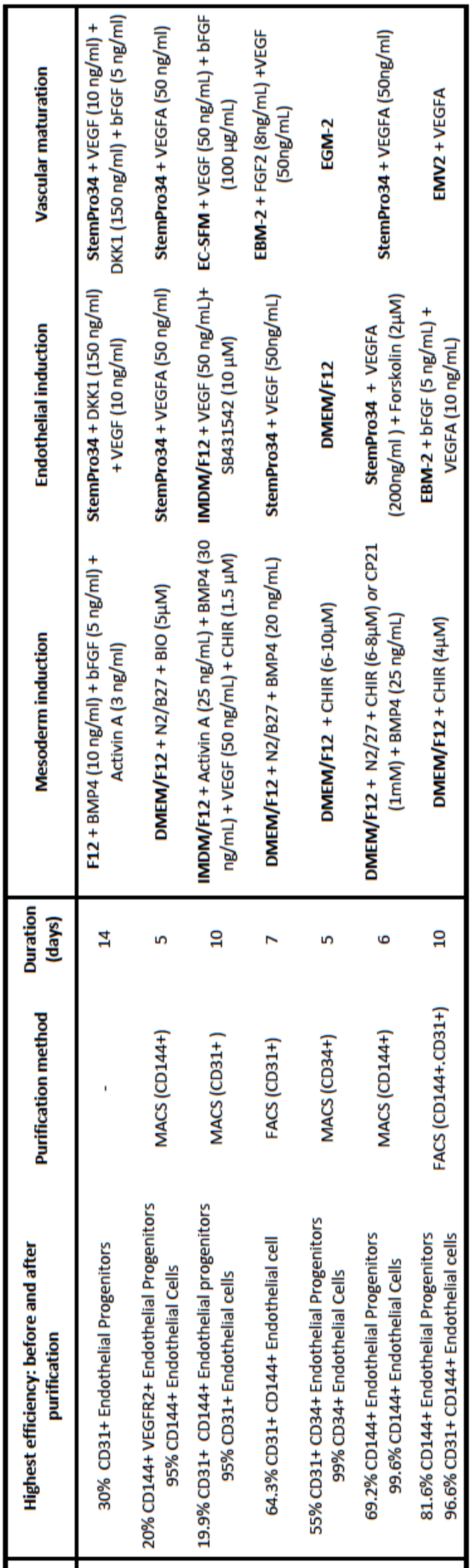

Publication	Highest efficiency: before and after purification	Purification method	Duration (days)	Mesoderm induction	Endothelial induction	Vascular maturation
Yang et al. (2008)	30% CD31+ Endothelial Progenitors	-	14	**F12** + BMP4 (10 ng/ml) + bFGF (5 ng/ml) + Activin A (3 ng/ml)	**StemPro34** + DKK1 (150 ng/ml) + VEGF (10 ng/ml)	**StemPro34** + VEGF (10 ng/ml) + DKK1 (150 ng/ml) + bFGF (5 ng/ml)
Tatsumi et al. (2011)	20% CD144+ VEGFR2+ Endothelial Progenitors 95% CD144+ Endothelial Cells	MACS (CD144+)	5	**DMEM/F12** + N2/B27 + BIO (5µM)	**StemPro34** + VEGFA (50 ng/ml)	**StemPro34** + VEGFA (50 ng/ml)
Orlova et al. (2014)	19.9% CD31+ CD144+ Endothelial progenitors 95% CD31+ Endothelial cells	MACS (CD31+)	10	**IMDM/F12** + Activin A (25 ng/mL) + BMP4 (30 ng/mL) + VEGF (50 ng/mL) + CHIR (1.5 µM)	**IMDM/F12** + VEGF (50 ng/mL)+ SB431542 (10 µM)	**EC-SFM** + VEGF (50 ng/mL) + bFGF (100 µg/mL)
Sahara et al. (2014)	64.3% CD31+ CD144+ Endothelial cell	FACS (CD31+)	7	**DMEM/F12** + N2/B27 + BMP4 (20 ng/mL)	**StemPro34** + VEGF (50ng/mL)	**EBM-2** + FGF2 (8ng/mL) +VEGF (50ng/mL)
Lian et al. (2014)	55% CD31+ CD34+ Endothelial Progenitors 99% CD34+ Endothelial Cells	MACS (CD34+)	5	**DMEM/F12** + CHIR (6-10µM)	**DMEM/F12**	**EGM-2**
Patsch et al. (2015)	69.2% CD144+ Endothelial Progenitors 99.6% CD144+ Endothelial Cells	MACS (CD144+)	6	**DMEM/F12** + N2/27 + CHIR (6-8µM) *or* CP21 (1mM) + BMP4 (25 ng/mL)	**StemPro34** + VEGFA (200ng/ml) + Forskolin (2µM)	**StemPro34** + VEGFA (50ng/ml)
Liu et al. (2016)	81.6% CD144+ Endothelial Progenitors 96.6% CD31+ CD144+ Endothelial cells	FACS (CD144+.CD31+)	10	**DMEM/F12** + CHIR (4µM)	**EBM-2** + bFGF (5 ng/mL) + VEGFA (10 ng/mL)	**EMV2** + VEGFA

Figure 4.14: Literature review of current protocols for endothelial cell differentiation

b. Mains protocols to generate iPSC-derived endothelial cells

In order to choose the protocol which is best for our model, I reviewed the different endothelial differentiation protocols (see Figure 4.14). These protocols were optimized either with embryonic stem cells [152], [156], or iPSC [157], [158], [159] or both [160], [14]. Acronyms used to refer to cell culture mediums and differentiation factors listed in the Figure 4.14 are explained below.

Differentiation factors:

- Activin A: is a member of the transforming growth factor beta (TGF-β) family inducing cardiomyogenesis together with BMP4 ([161], [162]);
- BMP4: the Bone Morphogenetic Protein 4 promotes mesoderm induction ([163]);
- BIO: 6-bromoindirubin-3-oxime is a GSK-3β inhibitor [164];
- bFGF (or FGF2): the basic Fibroblast Growth Factor promotes mesoderm induction [165];
- CHIR: CHIR99021 is a GSK-3β inhibitor ([166], [167]);
- CP21: CP 21R7 is a GSK-3β inhibitor produced by the company Roche;
- DKK1: the dickkopf-related protein 1 is an antagonist of the WNT signaling pathway [168];
- Forskolin: activates the enzyme adenylyl cyclase and increases intracellular levels of cAMP [155];
- SB: SB 431542 is a GSK-3β inhibitor [169];
- VEGF(A): Vascular Endothelial Growth Factor exerts an angiogenic function and induces endothelial specification [170].

Cell culture media:

- DMEM: Dulbecco's Modified Eagle Medium
- EC-SFM: Human Endothelial Serum-Free Medium (ThermoFisher)
- EBM-2: Endothelial Growth Basal Medium (Lonza)
- EGM-2: Endothelial Cell Growth Medium (Lonza)
- EMV2: Endothelial Cell Growth Medium MV2 (PromoCell)
- F12: Ham's F12 Nutrient Mixture
- IMDM: Iscove's Modified Dulbecco's Medium
- StemPro34: serum-free medium for human hematopoietic cells (ThermoFisher)
- N2 and B27 are cell culture supplements

Analysis Mesoderm can be induced with Activin A and nodal (both members of the TGF-β superfamily ([152], [157]), and it is maintained with FGF factors ([152], [159]) or WNT signaling such as DDK1 [152] , while BMP is responsible for its patterning ([152], [157], [160], [14]).

Yang *et al.* [152] and Sahara *et al.* [160], did not use GSK3-β inhibitors for mesoderm induction, which could explain their low efficiency before purification.

Conclusion In all of these protocols, the efficiency of the endothelial progenitors differentiation is variable but has increased over the years. The purification method is a crucial step, as mixed cell types cannot be used for experiments. Furthermore, we notice that all protocols require an important amount of VEGF for maturation and further cell culture, which is extremely costly.

Finally, we must underline that endothelial differentiation is a rapid process (less than 15 days), but requires financial investment and technical skills for the purification process. This is all the more pertinent when we account for the fact that endothelial cells hereby produced can usually only be propagated through passage 5, and lose their proliferation properties at this point. Performing multiple experiments with iPSC-derived endothelial cells also means optimizing a just-in-time production line.

Bearing all these considerations in mind, I hesitated between the protocols developed by Patsch and colleagues [14] or Liu *et al.* [159], for they offered the most promising results in terms of efficiency, both prior and after the purification step. Finally, because of the shorter duration of the differentiation and because we had better access to MACS than FACS, we decided to continue and use Patsch *et al.*'s protocol.

4.4.2 Patsch *et al.* : protocol rationale

a. Mesoderm induction

As explained previously, the first step towards endothelial differentiation is the direction towards mesodermal fate. This is achieved through the Wnt signaling pathway, which can be activated via GSK3-β inhibition. Patsch and colleagues examined the effect of several GSK3-β inhibitors, including BIO (6-bromoindirubin-3-oxime), CP21 (CP21R7), SB (SB216763) and CHIR (CHIR09921). CP21 and and CHIR proved to be able to potently and selectively inhibit GSK3 to activate canonical Wnt signaling. They added the BMP4 protein for it is known to be a potent inducer of mesoderm. Activation of WNT signaling (via GSK3 inhibition with CP21 or CHIR) combined with BMP4 induced strong commitment of hPSCs towards mesoderm.

b. Endothelial cells differentiation

Mesodermal cells are then cultured with VEGF to induce endothelial fate. The highest levels of CD144 expression were obtained with the combination of BMP4 + CHIR or BMP4 + CP21. This indicates that coupling BMP4 with a GSK3-β inhibitor does not only increase mesoderm differentiation efficiency, but that it is also beneficial in the long-term objective of generating endothelial differentiation.

In order to increase the rate of endothelial progenitors obtained, one technique is to use protein kinase A activation, which leads to vascular development [155], and can be activated via an increase in cyclic AMP levels. Therefore, forskolin (a cAMP activator) was added and nearly doubled endothelial differentiation efficiency (see Figure 4.15).

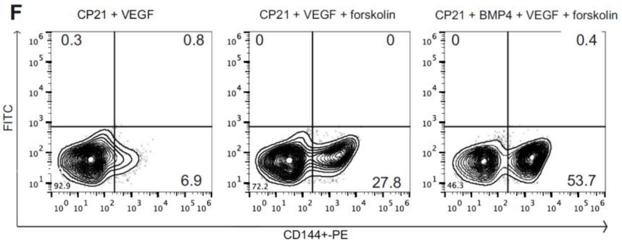

Figure 4.15: Interest of using BMP4 and forskolin for endothelial commitment (FACS Analysis of VE-Cadherin positive cells). *Patsch et al. [14]*

c. Purification and expansion

In order to obtain a pure cell line, the endothelial cells must be sorted out. This was performed by magnet-activated cell sorting (MACS) based on CD144+ cells. The cells were then replated and expanded in culture with VEGF treatment. The protocol was overall validated as it offered a purity of over 95.9% CD144+ cells, and they strongly expressed specific endothelial markers such as VE-Cadherin (CD144), vWf or PECAM1 (CD31), as can be seen on Figure 4.16.

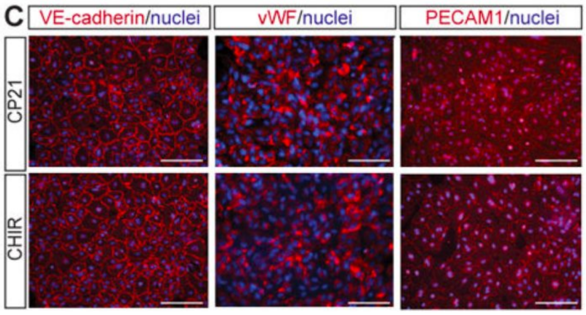

Figure 4.16: Expected results with Patsch *et al*'s protocol. All cells (100%) were expressing VECAdherin and PECAM1 for both GSK3 inhibitors. 73.48% of the hPSC-ECs differentiated with CHIR and 74.52% of the cells differentiated with CP21 express vWF.*Scale bars: 50 µm*

4.4.3 Differentiation experiments: adapting the protocol to our iPSC line

The four steps of the protocol that we just detailed are summarized in Figure 4.17. For each stage, the differentiation factors used and the specific genes expressed are listed, as well as a bright field picture of the cell morphology along the differentiation. For each of these steps, I will detail the protocol followed and present the results obtained. All protocols are detailed in the Appendix at the end of the manuscript.

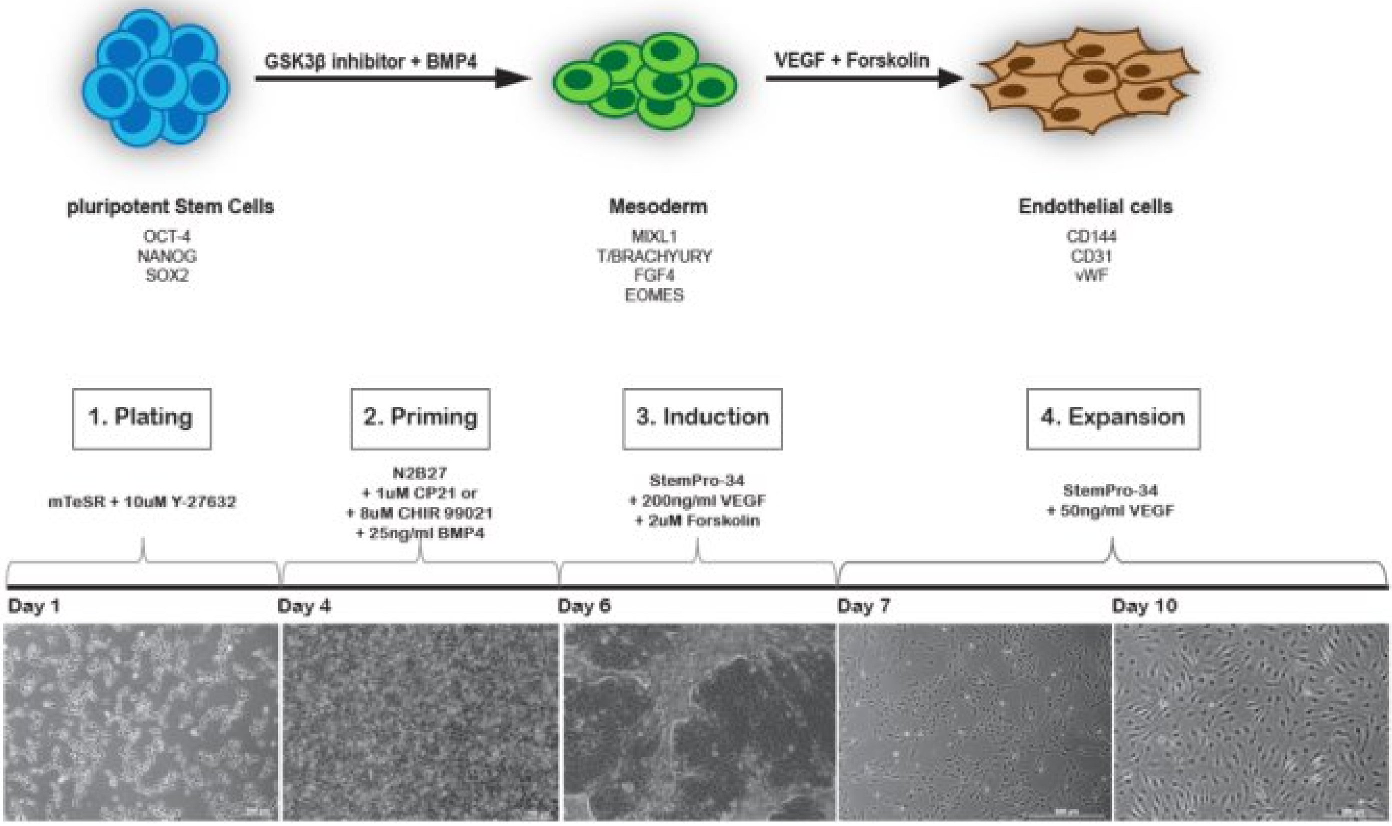

Figure 4.17: The differentiation protocol of Patsch *et al*, 2015 [14] consists of 3 steps of differentiation, a separation step and a maturation step.

a. Mediums and cytokines preparation

The two media for mesoderm and endothelial induction can be prepared in advance, filtered and stored at -20 °C for one month.

Lateral mesoderm induction base medium composition:

- 500 mL DMEM/F12 medium
- 500 mL Neurobasal medium
- 20 mL B27 supplement (1.94% vol)
- 10 mL N2 supplement (0.97% vol)
- 1 mL of **50mM** β-mercaptoethanol (0.097% vol)

Endothelial induction base medium composition:

- 100% StemPro 34 medium + StemPro34 Supplement (500mL)
- 5 mL Pen/Strep (1% vol)
- 5 mL Glutamax (1% vol)

Differentiation factors dilution and aliquoting:

- CHIR99021: Resuspend 10 mg of CHIR99021 in 5 mL DMSO. Store at -80 °C or -20 °C for a year. Final concentration: 4.3 µM.
- BMP4: Resuspend 10 µg of BMP4 in 4 mL of 510 mM citric acid pH 3. Store at -80 °C or -20 °C for a year. Final concentration: 5 µg/mL.
- VEGF165: Dissolve 100 µg of VEGF165 in 1 mL sterile water. Store at -80 °C or -20 °C for a year. Final concentration: 100 µg/mL.
- Forskolin: Dissolve 10 mg of forskolin in 2.436 mL DMSO. Store at -20 °C for a month. Final concentration: 10 mM.

b. Differentiation protocol

Step 1: Plating The Gibco's Human Episomal iPSC line was cultured on 1:100 Geltrex-coated Petri dishes and fed with E8 medium. Cells were passaged with 0.5 mM EDTA in PBS every 4 days and replated on fresh Geltrex. For the following experiments, cells were used at passages between 15 and 20.

- **Step 1: Detachment** The following protocol is detailed for differentiation into a 60 mm dish. Cells are rinsed from an 80% confluent 3.5 mm dish twice with 2 mL of warm PBS for about 2 minutes, then digested with 1 mL warm Accutase for 3-5 minutes at 37 °C, counted and centrifuged in an excess of E8 medium at 1000 rpm for 5 minutes.
- **Step 2: Seeding** We added 4 mL of warm E8 medium with 1 µM Y27632 in a 6 mm Geltrex-coated plate (Dilution ratio 1:30). Cells are resuspended in E8 medium supplemented with ROCK-inhibitor (Y27632 dihydrochloride) and seeded to a final density of 37 000-47 000 cells per cm^2 (*i.e.* 1-1.3 million cells total). Cells are then incubated overnight at 37 °C, 5% CO_2.

  Cells clusters must be broken by pipetting in order to seed single-cells. Cells stretched on the Geltrex-coating, and the ROCK-inhibitor compound enabled single cell survival, as can be seen on Figure 4.18a.
- **Step 2: Priming** After 24h, we prepared the complete lateral mesoderm inducing medium by adding CHIR99021 to a final concentration of 6 µM, and BMP4 to a final concentration of 25 ng/mL. The old medium is discarded and replaced with 20 mL of the new medium. Cells are incubated for 3 days.

  Some colonies grew. The cells lost their circular shape and their small size as they differentiated towards mesoderm, as can be seen on picture 4.18b.
- **Step 3: Induction** At day 4, we replaced the medium with 3 mL of pre-warmed endothelial induction base medium supplemented with VEGF (final concentration 200 ng/mL) and Forskolin (final concentration 2 µM). Medium is renewed the next day.
- **Step 4: Separation** At day 5, as can be seen on Figure 4.18c, the cells were highly confluent. We prepared fibronectin-coated (2 $\mu g/cm^2$) plates. Endothelial cells were sorted with the MACS method, that is detailed in the section c. below.

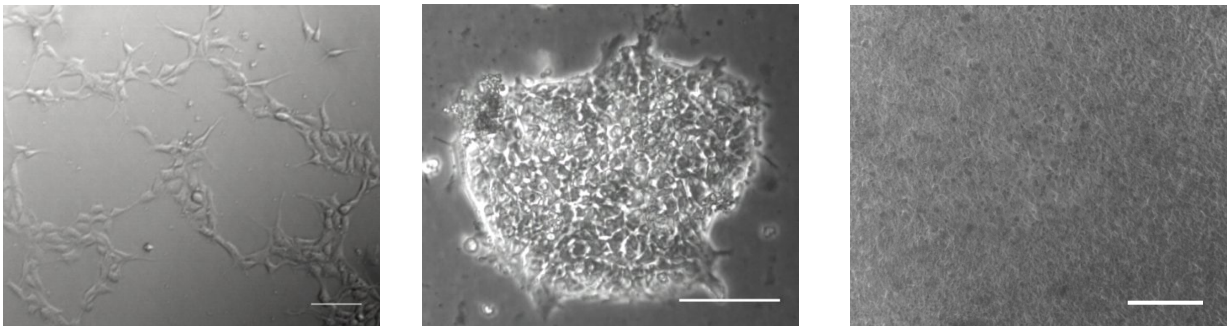
(a) (b) (c)

Figure 4.18: Evolution of the differentiation of induced pluripotent stem cells to endothelial cells according to the protocol of Patsch *et al.*[14]. (a) Day 1: Single-cell plating, (b) Day 2: Zoom on a mesodermal colony, (c) Day 5: Endothelial progenitors. *Scale bars: 100* µ*m*

Observed results We managed to obtain cells exhibiting expected morphologies all along the differentiation process. The first step was determinant in the success of this protocol. Indeed, if there were too little cells they would die not being able to form colonies. If there were too many, however, the cells would be overconfluent at day 5 and were detaching.

After a few attempts, we finally observed cells with the typical elongated morphology of endothelial cells, as we can see in Figure 4.19.

c. Magnet-activated cell sorting

After inducing the differentiation of iPSC into endothelial progenitors, we sorted the cells according to their CD144 (VE-Cadherin) expression.

MACS Principle In order to select only the CD144+ cells, we used MACS (Magnetic-Activated Cell Sorting) a technique that can isolate live (or dead) cells with magnetic microbeads. The beads are attached to the cells via a complex Steptavidin - Biotin - CD144 Antibody chain that I will detail below.

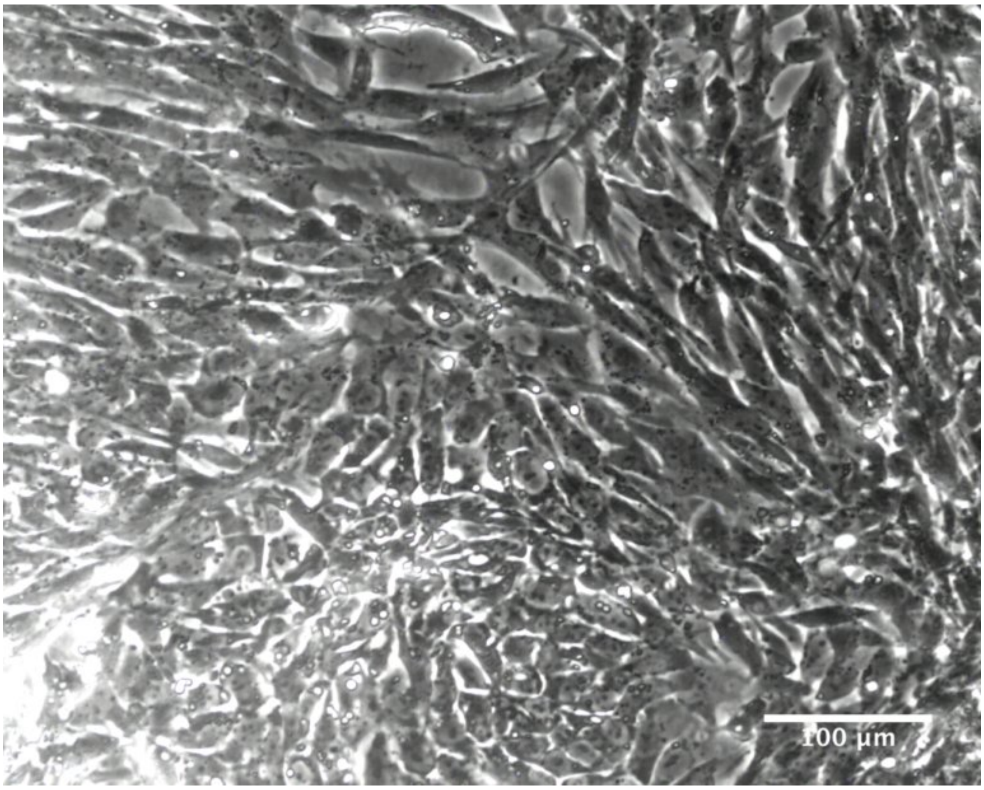

Figure 4.19: Elongated morphology of our endothelial progenitors at Day 5. *Scale bars: 100* µ*m*

Firstly, the antibody of interest, here CD144 (VE-Cadherin) is conjugated to DSB-X Biotin. This derivative of desthiobiotin has the ability to bind to streptavidin and avidin, just like regular biotin. However, with DSB-X Biotin, the chemical bond can be reversed quite easily. Indeed, if harsh chaotropic agents (6.0 M guanidine) and low pH (1.5) are required to break the biotin-streptavidin bond, a simple excess of D-biotin or D-desthiobiotin at room temperature and neutral pH is sufficient to break the DSB-X-streptavidin bond.
After marking the cells with the specific antibodies, the streptavidin- conjugated magnetic beads are introduced to the cells. The two chemicals (biotin-streptavidin) bond, and the beads are attached to the cells. A magnet helps collecting the cells, and after a few washing steps, the beads are released from the cells via the reversible process mentioned in the previous paragraph.

MACS experiments The Magnetic-Activated Cell Sorting was performed on our cells as follows:

1. Conjugating antibodies with DSB-X Biotin: The CD144 antibody was labeled with DSB-X biotin using the **DSB-X Biotin Protein Labeling Kit** from Molecular Probes (Ref.D-20655);
2. Preparing the beads: the magnetic beads (obtained from the **Dynabeads FlowComp Flexi kit**, Invitrogen, Ref.11060D) were washed and resuspended in MACS buffer (PBS with 0.1% wt/vol BSA and 2 mM EDTA);
3. The cells were digested with Accutase, mechanically detached and collected. They were resuspended in MACS buffer with 25%vol DSB-X biotinylated antibody and incubated at 4 °C on a shaking platform for 25 min for **antibody labeling**;
4. The cells were rinsed and resuspended in a solution of 75 µL/mL of magnetic beads and placed at 4 °C on a shaking platform for 32 min for **beads attachment**;
5. The cells were rinsed and collected with a magnet on one side of the tube. The cells and debris remaining at the bottom of the tube were discarded. This operation was repeated three times for cell selection;
6. The CD144+ cells were resuspended in the release buffer (from the kit) and placed at 4 °C on a shaking platform for 12 min for **beads release**;
7. The solution was intensively pipetted to break the bonds and the beads were collected with a magnet (see Figure 4.20);
8. The remaining cells were rinsed, counted and resuspended in endothelial induction base medium supplemented with 50 ng/mL VEGF for seeding.

Separation results After performing the magnetic sorting process, we counted 3 million CD144- cells for a total of about 6 million cells before the separation, which means that with this protocol, we obtained a **differentiation efficiency of 50%**, which is much lower than the 81.6% expected in the protocol.
The MACS technique requires multiple washing steps as well as several incubations at 4 °C. These actions importantly reduce the number of selected cells, either by washing them off, or by apoptosis. Indeed, even though we counted 3 millions of CD144- cells (about half of our initial cell number), after all the washing steps we only counted 320 000 remaining cells. This means that about 2.7 million cells have been lost in the MACS process.

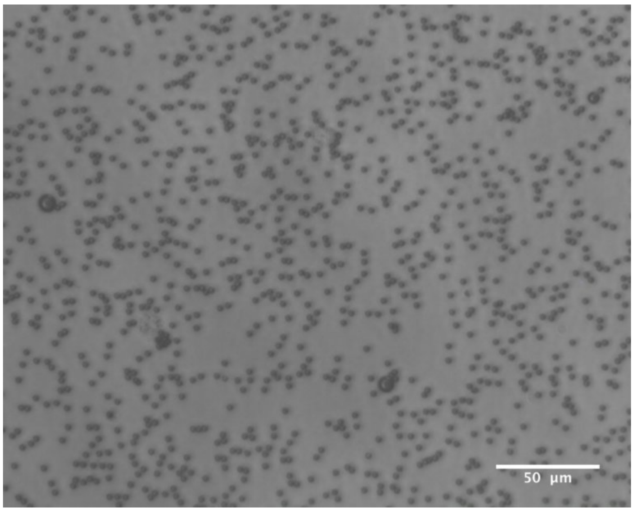

Figure 4.20: Picture of the magnetic beads (2.8 µm in diameter) after cell release: we can see that there are no cells still attached: the releasing procedure was successful.

Final step: Expansion We planned on culturing the stem cell-derived endothelial cells until they reach confluency (usually 3-5 days), changing the medium every other day. These cells can be cryopreserved for further use (1.5 million cells/vial) or expanded for functional assays.
However, after the multiple washing steps required for magnetic beads release, only few cells were left. We observed that, 24 h after seeding, no cells had attached. We waited for another 4 days but the cells never attached.

Discussion and perspectives Using Patsch *et al.*'s protocol [14], we managed to obtain a good induction of iPSC into endothelial progenitors, reaching an efficiency of **50%** CD144 positive cells. However, when it came to the sorting procedure, we lost about 90% of the positive cells in the process. Finally, the remaining cells never attached, probably because they had died in the process.
Obviously, this experiment should be repeated and optimized. There are two directions: first, we should focus on increasing the differentiation efficiency. This could be done by testing several Geltrex dilutions for plate-coating or by testing and optimizing the initial seeding density. Induction could also be enhanced by testing and finding the optimal CHIR99021 concentration (said to be between 6 and 8 µM), which is cell-line dependent. The second direction to work on is the improvement of the MACS procedure. Indeed, the protocol of the kit gives wide ranges of duration for each incubation step (see Table 4.1). This is something we could tune to optimize the separation and increase cell survival. For each of those steps, I looked into duration usually used by other researchers and I was able to determine a narrower window for our next tests.

STEPS	Used duration	Protocol Range	Literature Range
Antibody Labeling	25 min	5 - 30 min	10 min
Beads Attachment	25 min	5 - 35 min	10 - 20 min
Beads Release	12 min	2- 30 min	2 - 10 min

Table 4.1: Main steps of the Magnetic-Activated Cell Separation protocol

Because we could only perform the experiment once, I had decided to ensure a good performance by maximizing all the incubation periods. However this was a bad move as it resulted in extremely high cell death. As we can see in Table 4.1, data from other groups suggests that shorter incubations are recommended. Finally, in order to improve this last step of the differentiation protocol, we would need to do this experiment again and test shorter incubation periods until we obtained consistent cell survival.

4.4.4 Conclusion and perspectives

Discussion Obviously both the induction efficiency and the purification step need to be optimized, but the results are promising. I have presented the perspectives for improvement here if I were to do this experiment again..

Conclusion Overall, because both the differentiation cytokines and the MACS products are extremely expensive, we reconsidered the relative cost between using iPSC-differentiated endothelial cells and the HUVEC line. Indeed, both cannot be used after passage 5, but HUVEC can grow faster. Moreover we do not need 15 days to prepared the HUVEC. Finally, because we decided to continue using HUVEC for the rest of this project.
Because of this decision, and because of the limited time we had left, it was decided to put a hold to this differentiation experiment.

4.5 Directed differentiation of iPSC to an alveolar epithelium

Recapitulating the lung foetal development *in vitro* is the scientific objective of our directed differentiation. We will review these developmental stages and how they might be reproduced *in vitro*. As the general mechanism of pulmonary development was detailed previously, we will here focus on the biological pathways that are activated throughout the differentiation. This will give an overview of the mechanisms that we want to epitomize here, as well as the chemical cues that might be used to induce directed differentiation.

4.5.1 Developmental pathway and current differentiation protocols

As presented in the general introduction, the lung develops according to the following pathway: a region of the definitive endoderm (DE) specifies into the anterior foregut endoderm (AFE), then into the ventral AFE, and finally differentiates into lung progenitors. From these progenitors, the alveolar epithelium arises with the induction of distal lung differentiation. The evolution of each developmental stage and the corresponding cell signaling will be thoroughly explained below, with an insight on existing protocols, thanks to the very well documented review of Hans-Willem Snoeck (Professor at Columbia Center for Translational Immunology, Columbia University Medical Center) [149].

a. Differentiation of iPSC into definitive endoderm

The use of non-adherent cell culture conditions leads to the spontaneous formation of embryoid bodies (EBs). These clusters of cells form spheres where gastrulation takes place spontaneously. The primitive streak is then induced with BMP4 and canonical WNT signaling for 24 h. Traditionnaly, using a Rho kinase inhibitor (such as Y-27632) helps increase the DE yield at the beginning of the differentiation as it increases cell viability ([171], [172]). Some protocols estimate that endogenous WNT signaling is sufficient to induce DE with the subsequent Activin A treatment ([173], [174]).
Indeed, high concentrations of Activin A, which mimicks nodal signaling in the embryo, is known to induce DE formation ([175], [176], [177]). After 4 days of exposure to Activin A, the DE surface markers EPCAM [178], c-KIT [175], and CXCR4 [176] as well as the transcription factors SOX17 and FOXA2 arise. Inducing DE from EBs can be improved by adding low concentrations of BMP4 and FGF2 [179]. Importantly, forgetting FGF2 would induce ectodermal differentiation [176]. Moreover, the BMP4 signaling must be stopped after DE induction as it will then promote a hepatic fate [175]. All these factors are used in concentrations that can vary depending on the cell line or the lot number of the products used ([173], [174], [172]) and need to be determined empirically.
The DE specification method can determine the final fate of the differentiated cells. Indeed, Huang *et al.*[180] observed that lung potential arises relatively early in DE induction (d4-4.5), and is lost later on, despite continued expression of DE markers. Finally, up to 95 % pure DE can be achieved in iPSC, although significant variability exists among cell lines in their capacity to generate DE.

b. Anteroposterior patterning and induction of anterior foregut endoderm

As mentioned before, the specification of DE into AFE is extremely sensitive, as it has an tremendous influence on the ability to consequently generate lung progenitors. DE generated using the optimized strategy described above will adopt a more posterior fate [173], likely explaining why the generation of lung and airway epithelial cells has lagged behind the success in the generation of pancreatic, hepatic, and intestinal cells ([175], [177]).
Obtaining anterior endoderm commitment was a great challenge. Green *et al.* [173] performed a precise

screening of possible morphogen combinations and searched for an expression of the foregut marker SOX2, the suppression of the posterior marker CDX2, and the maintenance of the endoderm marker FOXA2. This was achieved best when inhibiting BMP4 signaling (with the physiological antagonist NOGGIN) and TGF-β (with the pharmaceutical antagonist SB-431542). The timing was crucial as prolonged inhibition (over 48 h) of both signals made the cells unresponsive to the following lung progenitor induction [173].

This underlines the complexity of elaborating such protocols. Indeed, we need to find the perfect combination of morphogens to find the appropriate signaling, to which the cells are only receptive for a narrow window of time. This strategy to generate AFE has been reproduced in several reports ([181], [182], [183], [33]). A variation on this protocol was reported by Firth *et al.* [181], where after initial inhibition of BMP4/TGF for 2 days, TGF inhibition in the presence of BMP4 was applied for an additional 3 days. Indeed, during its anterior migration, the cells fated to become AFE also pass through a zone where the BMP4 inhibitor Noggin is expressed. This variation obtained similar AFE commitment efficiency.

In order to improve the efficiency of cell differentiation to lung field progenitors, Huang *et al.* [180] developed a protocol with sequential inhibition of BMP and TGF-β followed by inhibition of TGF-β and Wnt signaling over the course of 48 h. It corresponds to what was observed in mouse embryos, as the DE cells destined to become AFE are crossing a region where Nodal/Activin inhibitor Lefty and the BMP4 inhibitor Noggin are expressed, followed by expression of the Wnt inhibitor, Dkk1 [184]. Wong *et al.* [185] generated AFE from iPSC by exposing DE to SHH (Sonic HedgeHog) and FGF2. Huang *et al.* however found that AFE induction using SHH and FGF2 was less efficient than using sequential BMP4/TGF inhibition and WNT/TGF inhibition [180].

c. Specification into ventral anterior foregut and lung field

Induction of ventral AFE and lung field is achieved by adding specific factors essential for lung field specification in the mouse: Wnt (or the small molecule CHIR), BMP4, FGF7, FGF10, and Retinoic Acid ([186], [187], [188]). With this method Green *et al.*[173] and Huang *et al.* [180] obtained up to 90% of FOXA2+.NKX2.1+ expressing cells between days 15 and 25 of differentiation. This efficiency is cell line dependent, which is a well known fact in lineage-specific differentiation experiments ([189], [190]). Moreover, timing and morphogen concentrations are to be optimized at each stage for each cell line to maximize differentiation efficiency [180].

Removing Retinoic Acid (RA), or blocking Wnt or BMP signaling entirely abolished the generation of NKX2.1+ cells, while FGF signaling appeared dispensable in this model [180].

In vivo transplantation under the kidney capsule of immunodeficient mice was used to assess the potential of differentiated cells. They formed cystic and tubular structures lined by a uniformly FOXA2+NKX2.1+ epithelium that ranged from pseudostratified containing cells consistent with basal, ciliated, club, and goblet cells to a monolayer consisting of flatter cells expressing markers of AET I and AET II cells. Glandular structures resembling submucosal glands were also present. No other endodermal elements were observed. However, the growths also contained smooth muscle, cartilage, and areas containing looser connective tissue, which were of human origin. This confirms that this protocol successfully generated lung progenitor cells. It is an extremely promising result regarding the potential of these cells to ultimately form an alveolar epithelium.

Using a ventralization strategy similar to Huang *et al.* [180], Gotoh *et al.* [182] generated human lung progenitors with similar efficiency and identified a surface marker specific for NKX2.1+ lung cells, carboxypeptidase M (CPM), which allows for a further flow cytometric purification.

d. Differentiation into mature cell types

Lung progenitors can be fated towards either proximal or distal differentiation depending on the conditions used for culture and expansion. The method developed by Green *et al.* was to remove BMP4 from the ventralization cocktail (Wnt, BMP4, FGF10, FG7, RA), which induced expression of SP-C, the AET II cells marker [173]. Wong *et al.* observed that low concentrations of BMP4 induced proximal markers [185]. Finally, Huang *et al.* [180], also found that BMP4 addition during the terminal stages reduced expression of distal markers such as surfactant proteins and AET I markers PDPN and AQP5.

Interestingly, culture at an air-liquid interface is thought to promote proximal airway epithelium. Wong *et al.* applied ALI conditions to AFE cells further differentiated in the presence of FGF7, 10 and 18, and it yielded CFTR expressing cells [185]. However, they also observed expression of NKX2.1 in these presumed proximal airway epithelia, a marker that is only expressed by AET II and Club cells in the mature lung.

Longmire *et al.* [183] differentiated NKX2.1+ mouse cells in the presence of FGF2 and FGF10, obtained the expression of a variety of airway and alveolar markers. Furthermore, addition of maturation components

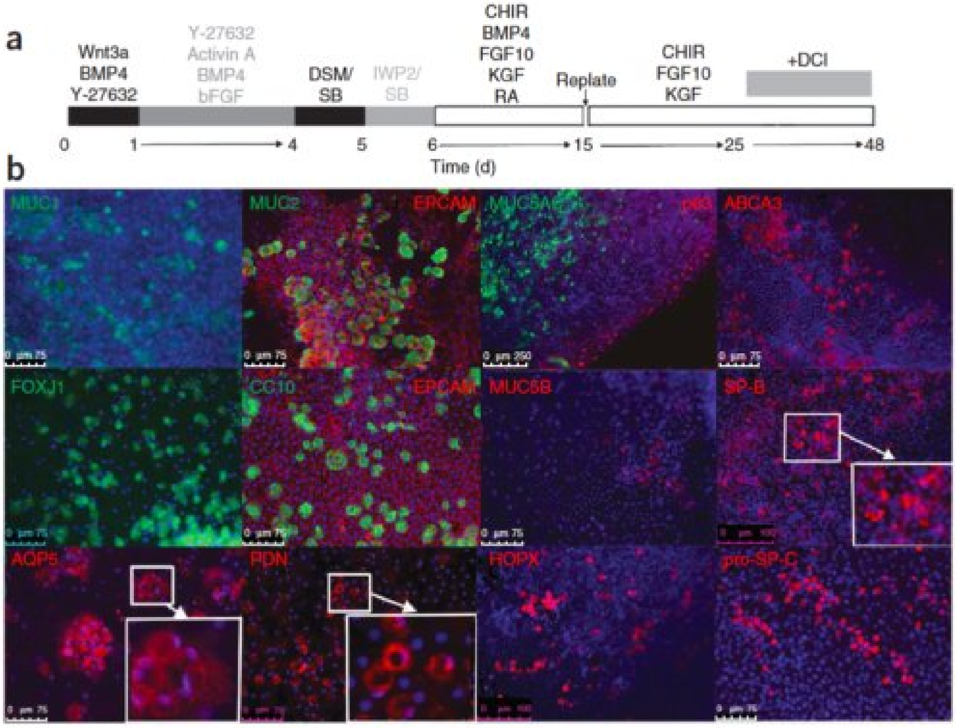

Figure 4.21: Terminal differentiation of iPSC-derived lung and airway progenitors. (a) Culture protocol of RUES2 cells shown in panels. (b) Representative examples of the expression of markers of mature lung and airway epithelial cells after culturing RUES2 cells according to the protocol shown in a. Immunofluorescence images represent reproducible results from four independent experiments.*Huang et al. [15]*

consisting of dexamethasone, butyrylcAMP or 8-Bromoadenosine 3'-5'-cyclic monophosphate, and isobutylmethylxanthine (DCI conditions) [46] further upregulated the expression of SP-C, SP-B, and CC-10 [183]. Reliable distal differentiation was achieved by Huang *et al.* ([180], [15]). By continued culture in the presence of FGF7, FGF10, and Wnt agonism in addition to DCI, they achieved cultures where over 50 % of the cells expressed the AET II marker, SP-B. Furthermore, after seeding onto human decellularized lung matrix, ample expression of SP-C was observed. Functionality of the cells was verified by their capacity to take up and release fluorescent SP-B, which demonstrates an active role in surfactant recycling. Further examination of the cultures in the long term (over 50 days) revealed areas of proliferation, where cells express the AET II marker, SP-B or co-express SP-B and the AET I marker, podoplanin (PDPN) [15], suggestive of bipotential alveolar progenitors [191] (see Figure 4.21).

4.5.2 Differentiation experiments: adapting the protocol to our cell line

As we have just seeen, there are very few differences between the protocols published for lung epithelial cells differentiation. Huang *et al.* [15], however, proposed a protocol specifically optimized for distal lung epithelium, successfully generating alveolar epithelium. Moreover, they developed a technique that is clinical grade, which could add potential applications to our project if we manage to differentiate the cells on our patch.
Therefore we decided to follow their experimental protocol (Nature Protocols, 2015) [15]. The general differentiation pathway was presented above, and all the reagents commercial reference and stock preparation procedures are thoroughly detailed in the paper. In this part, I will detail how we started to adapt this protocol to our iPSC cell line, explaining the issues encountered and the measures taken to solve them. Finally, we will present our attempt at performing *in situ* differentiation directly on our microengineered patch.

a. Differentiation medium composition

The medium used throughout the differentiation is refered to as the Serum-Free Differentiation medium (SFD), and is composed of:

- 750 mL IMDM (with Bicarbonate)
- 250 mL F-12
- 7.5 mL of 7.5% wt/vol BSA
- 10 mL GlutaMAX

- 5 mL N2 supplement
- 10 mL B27 supplement
- 10 mL Penicillin-Streptomycin

Each day, this SFD medium is freshly completed with: L-ascorbic acid (final concentration: 50 µg/mL) and Mono-Thioglycerol (MTG, final concentration: 0.04 µL/mL). This medium will then be referred to as the *complete SFD.*

b. Primitive streak formation

Reagents The Day 0 medium (primitive streak formation) is composed of complete SFD (serum-free differentiation medium) with: ROCK inhibitor (10 µM), Wnt3a (10 ng/mL) and BMP4 (3 ng/mL).

Experimental steps Cells used are Gibco's Human Episomal iPSC line, maintained feeder-free on Geltrex-coated (1:100) plates in E8 medium. Cells were always used between passages 15 and 25. On Day 0, a 75–90% confluent 35 mm plate is digested with warm 0.05 % (wt/vol) trypsin, resuspended in d0 medium and plated into Ultra-Low attachment 6-well plates with a seeding ratio of 1:3.

Observed results After 24 h, we could observe perfectly formed spherical embryoid bodies (see Figures 4.22 and 4.24), of sizes ranging from 100 µm at Day 1 to nearly a 1 mm at Day 3. This step is made extremely easy by the use of ultra-low attachment plates. The only technical difficulty was detaching the cells in small homogeneous clusters (3-10 cells) while avoiding single-cells in suspension, which only required a bit of practice and was perfected at each new seed.

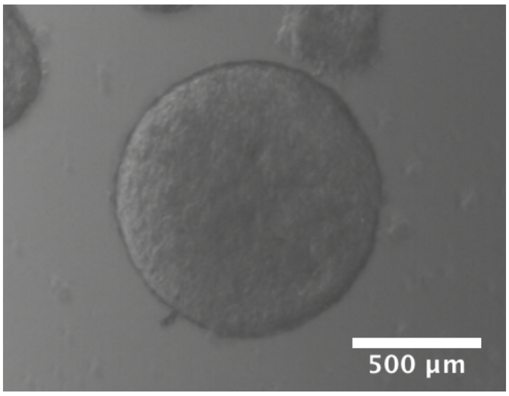

Figure 4.22: Embryoid body formed by iPSC in Ultra-Low Attachment plates (Day 3)

c. Definitive Endoderm induction

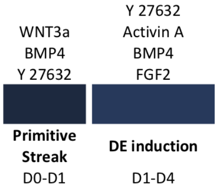

Reagents DE induction medium (d1-d3) is composed of complete SFD with: 10 µM ROCK inhibitor, 100 ng/mL Activin A, 0.5 ng/mL BMP4 and 2.5 ng/mL FGF-2, respectively.

Experimental steps After 24h of primitive streak induction, embryoid bodies are directed towards definitive endoderm by collecting them in a Falcon, and replating them in DE medium for the next 3 days.

Results We observed consistent EB formation after 3 days, with very few floating single cells. However, the EBs were heterogeneous in size, as can be see on Figure 4.23. This is problematic because differences in EB size might result in different induction timing as morphogens may take a longer time to diffuse through larger EBs. Moreover, depending on the experiments, after a few days I could observe completely different densities in the wells. This was an important concern because wells with a high density of EBs required feeding at Day 2, which can change the differentiation kinetics. Therefore it was important that each well had similar densities for each experiment, and the number of wells to use can be adjusted if necessary.

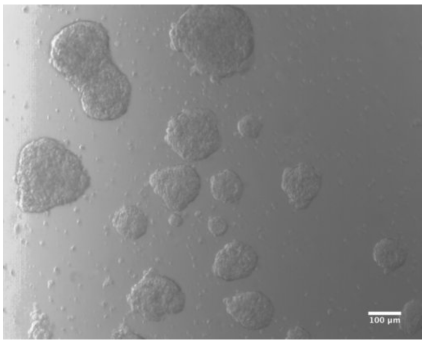

Figure 4.23: Example of poorly seeded embryoid bodies: the EB are very heterogeneous and we observe a lot of single cells (Day 3). *Scale bar: 100 µm*

Optimization of the density of the EB population In order to obtain similar densities in each well it was important to seed the exact same number of cells. However it is impossible to count iPSC cells with the regular method (counting cell) because cells cannot be trypsinized into single cells otherwise they die within a few hours.

In order to solve this issue, I trained myself to collect almost the same number of cells each time for EB seeding. In order to do so, I always used the same method: taking a third of a 80% confluent 35mm Petri dish. I trypsinized the other two thirds and counted the number of cells left. I repeated the experiment until I was able to assess by eye a precise estimation of always the same 80%, which corresponded to 1 to 1.2 million cells. In the end I was able to estimate and collect about 350 to 400 000 cells to fill a 6-well ultra-low attachment well plate.

Optimization of EB size We also noted that it is crucial to have reproducible results in term of embryoid bodies size, as it will impact the timing of the differentiation that we are trying to optimize.

I perfected the trypsinization process: exacly 1 mL of warm trypsin per 35 mm dish for 45 seconds to obtain homogeneous clusters at Day 0 (see Figure 4.24a). In the end, along Days 1, 2 and 3 the size of the EB obtained are quite homogeneous (see Figure 4.24), which enables for reproducible experiments up to Day 3 of differentiation.

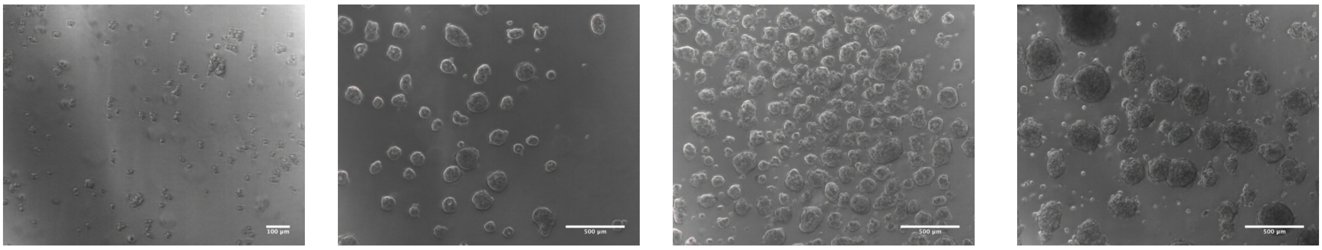

(a) Day 0 seeding (b) Day 1 (c) Day 2 (d) Day 3

Figure 4.24: Definitive endoderm induction: optimization of embryoid bodies size and density. *Scale bars: (a) 100 µm; (b), (c) and (d): 500 µm*

d. Assessing the DE differentiation kinetics

		Day 3	**Day 3.5**	**Day 4**
CXCR4+	Exp1	*NA*	71.78%	75.08%
	Exp2	41.70%	56.60%	51.74%
	Exp3	51.08%	73.63%	78.56%
	Average	**46.39%**	**67.34%**	**68.46%**
c-Kit+	Exp1	*NA*	65.96%	68.61%
	Exp2	15.20%	38.96%	18.03%
	Exp3	8.79%	44.04%	55.63%
	Average	**12.0%**	**49.65%**	**47.42%**
CXCR4+. c-Kit+	Exp1	*NA*	18.8%	28.7%
	Exp2	10.2%	18.4%	27.4%
	Exp3	13.5%	31.8%	35.4%
	Average	**11.85%**	**23%**	**30.5%**

Table 4.2: Expression of definitive endoderm specific proteins over Days 3 to 5 of differentiation, assessed by flow cytometry (% of cell population)

Importance of DE induction kinetics Before proceeding to the patterning of the definitive endoderm, we need to assess the exact kinetics of the DE induction. Indeed, the AFE induction efficiency is much higher if the AFE patterning starts in within 6 to 9 h after the DE yield maximizes. This yield can be measured by observing maximum DE gene expression (CXCR4, c-KIT and EpCAM). Determining the optimal AFE patterning time is essential to pursue our differentiation. Afterwards, this timing will be a constant in our protocol as for a given cell line maintained appropriately in defined conditions, the DE induction kinetics should remain stable throughout passages.

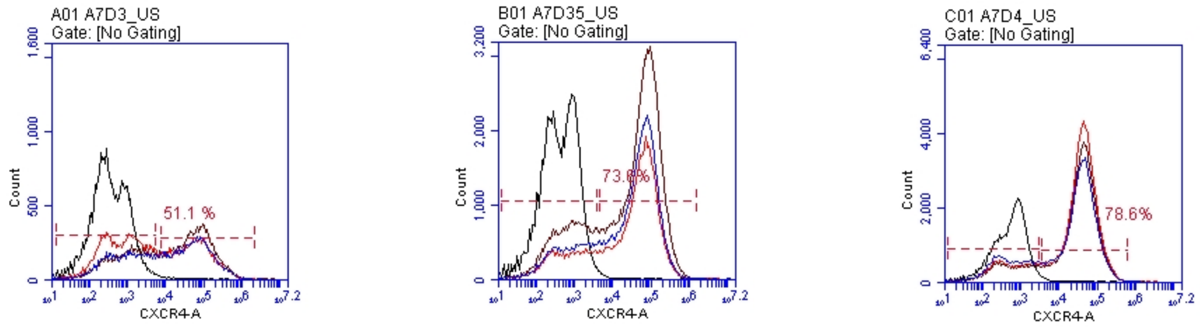

(a) CXCR4: Day 3 (b) CXCR4: Day 3.5 (c) CXCR4: Day 4

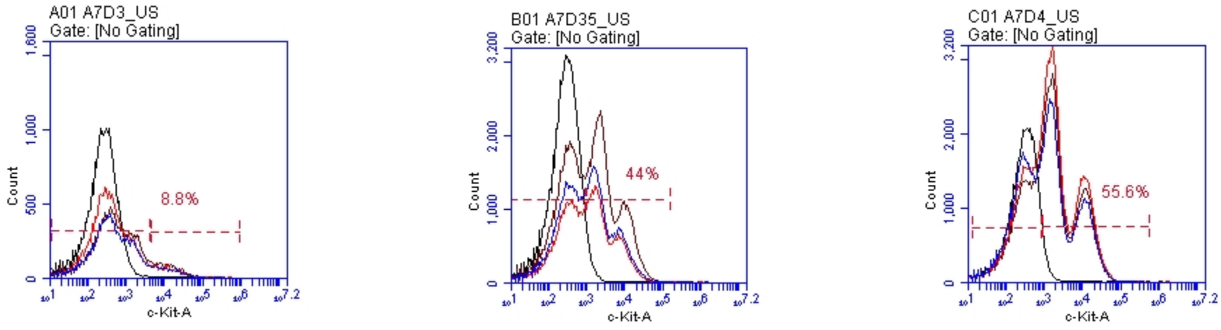

(d) c-KIT: Day 3 (e) c-KIT: Day 3.5 (f) c-KIT: Day 4

Figure 4.25: Flow cytometry analysis of CXCR4 and c-KIT expressions at Day 3, Day 3.5 and Day 4 of differentiation (Data from Exp 3)

Flow cytometry analysis In order to determine the time of the maximum DE yield, we performed a flow cytometry analysis to assess CXCR4 and c-Kit protein levels at several timepoints: days 3, 3.5, and 4. Three samples were collected for each timepoint, and the whole experiment was repeated three times with iPSC at different passages. The protocol for flow cytometry is detailed in the Appendix. All cells were differentiated according to the exact same optimized protocol up to Day 3. Unfortunately, data at D3 for the first experiment could not be recorded.

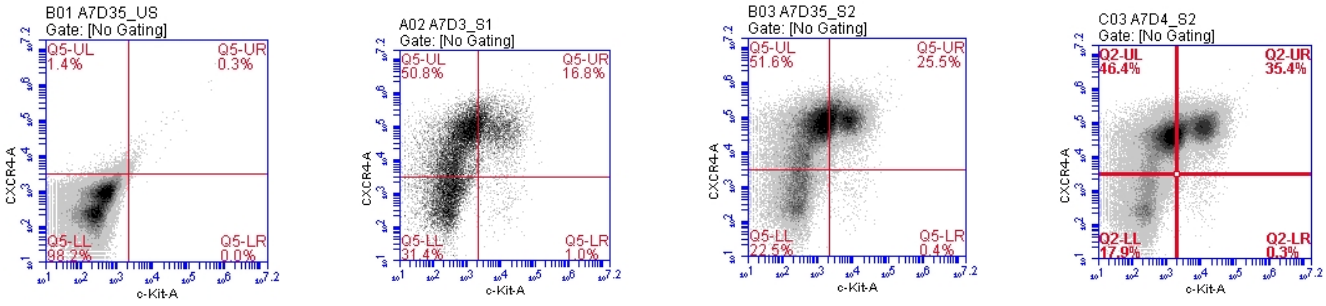

(a) Unstained cells (b) Exp 3 Day 3 (c) Exp 3 Day 3.5 (d) Exp 3 Day 4

Figure 4.26: Assessing the CXCR4+.c-Kit+ population (Data from Exp 3)

Flow cytometry results Data recorded during the third experiment can be observed in Figures 4.25 and 4.26. We can see that the levels obtained on Day 3.5 and Day 4 are very close compared to Day 3. The c-Kit marker was almost not expressed at Day 3. On Days 3.5 and 4 however, we observe two levels of fluorescence. A hypothesis could explain these 2 separated peaks observed on Figures 4.25e and 4.25f: the low fluorescence peak could be due to partially stained cells, either because they express very few c-Kit proteins,

or because these could be dead cells.
On average over three samples, we obtained variable protein expression levels that are reported in Table 4.2. It seems that the maximum DE yield is reached around Day 4 for CXCR4+-c-Kit+ cells, even though the maximum of c-Kit expression seems to be at Day 3.5. For both markers, the expression levels were very close at Days 3.5 and 4. During the 3rd experiment we observed that protein expression was diminishing during Day 4.5 and Day 5, and we could confirm that the peak of DE yield is around Day 3.5 and Day 4. During the 2nd experiment, the expression levels of both markers were much lower than the two other experiments, however, the trend is the same over the three days. This could be due to an excessive pipetting during the staining process, which damages the membrane proteins by shear stress.

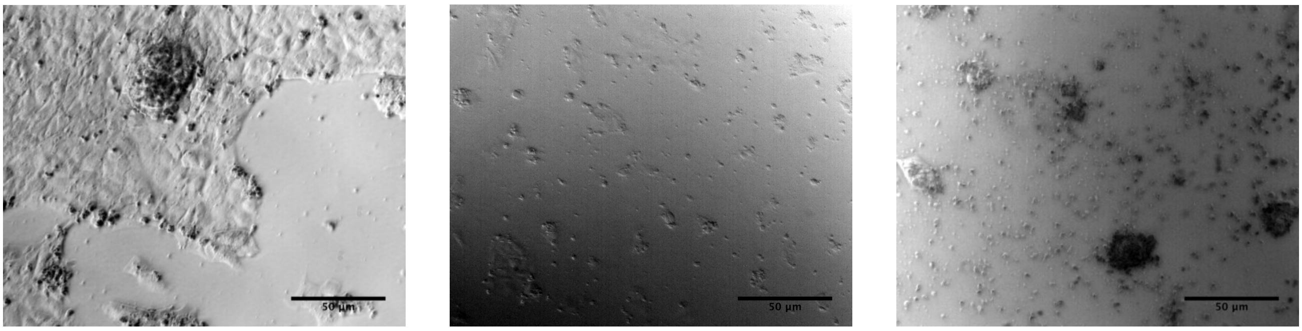

(a) Cells replated at Day 4 (b) Cells replated at Day 4.5 (c) Cells replated at Day 5

Figure 4.27: Anterior Foregut Endoderm replating day: observation of cells at Day 8. *Scale bars: 50* µm

Conclusion The results did not permit to obtain a clear peak of DE yield, as both markers do not peak on the same Day. However it was clear that the maximum reached should be between Days 3.5 and 4. Therefore, we decided to repeat the experiments to obtain more precise data. In the meantime, we decided to switch to AFE induction at Day 4, in the morning (hence 9-12 h after Day 3.5), because the protocol recommended to switch 6-9 h after the maximum DE yield. In this way we are acting as if the maximal DE yield was in between Day 3.5 and Day 4, which is not a very precise method but will allow us to pursue testing with the cells in culture. Indeed, because launching a differentiation is so expensive in reagents, we tried to pursue each launch as long as possible in order to anticipate the future problems we will encounter.
Our decision to proceed to AFE patterning at Day 4 was confirmed by the observation that cells replated at Day 4 exhibited a more flat and elongated morphology at day 8 than the other cells from the two other conditions we had tried (Day 4.5 and Day 5 replating), as can be seen on Figure 4.27.

e. Anterior foregut patterning of DE

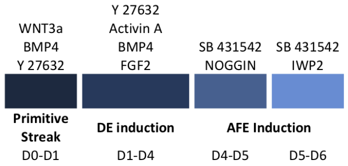

Procedure: replating At Day 4, the EBs are digested with trypsin before replating. This step is extremely sensitive as we need to digest them enough to be able to estimate the number of cells and replate them, but over-trypsinization results in an intensive cell death. Cells are replated on 0.2% (vol/vol) fibronectin-coated plates prepared the day before. At this time, it is recommended to try several seeding densities to see which fits best your cell line. We tried to seed at both 50 000 and 75 000 cells per cm^2.

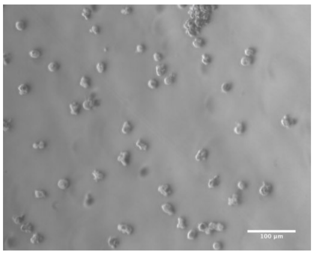

Figure 4.28: Cell clusters resulting from mild trypsinization of embryoid bodies at Day 4. *Scale bar: 100* µm

After several tests, my optimized **Embryoid Body dissociation protocol** is the following:
- Collect EBs in a 15 mL tube (one well at a time!)
- Centrifuge for 5 min at 300 g

- Discard medium and resuspend in 1.5 mL warm TryplE
- Wait about 1 min and flick the tube for 3 more minutes
- Wait for all the EBs left to settle down. Transfer the cloudy supernatant into 4 mL STOP medium
- Add 0.5 mL TryplE to the EBs and flick for 3 more minutes until all EBs are dissociated
- Transfer to STOP Medium. Add 4 mL of SFD
- Centrifuge for 5 min at 300 g
- Resuspend cells in 4 mL PBS to rinse the STOP Medium
- Centrifuge for 5 min at 300 g
- Either fix the cells for flow cytometry analyis, or resuspend them in d4/4.5/5 medium and seed on Fibronectin-coated plates

Experimental steps: medium change Regarding the rest of the AFE patterning, the steps are pretty simple: medium is changed to d5/5.5/6 medium after 24 hours.

Reagents The d4/4.5/5 medium (AFE induction medium 1) is composed of complete SFD with: 100 ng/mL of NOGGIN and 10 µM SB431542.
The d5/5.5/6 medium (AFE induction medium 2) is composed of complete SFD with: 1 µM IWP2 and 10 µM SB431542, respectively.

Observed results After replating between days 4 and 15, the cells exhibit a novel morphology: they grow in colonies, with extended cytoplasms (see Figure 4.29). We also observe important cell-cell junctions in the colonies: this is typical of epitheliums.
Flow cytometry experiments revealed that about 15% of the cells stained positively for SOX2 (an AFE marker) at Day 6 (see Figure 4.30a). This measurement was performed on 3 data points but out of only one experiment. The peak for positively stained cells is poorly defined: we have a lot of parasitic cells with a semi-fluorescence comprised between the positive or the negative peak.

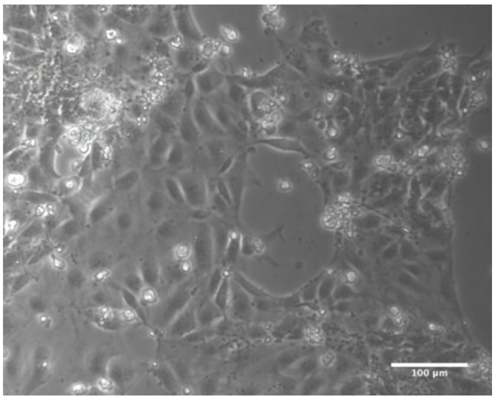

Figure 4.29: iPSC differentiating into Anterior Foregut Endoderm, Day 5.5

Immunostaining observations showed that not all cells at Day 6 stained positively for SOX2 (see Figure 4.30d), but some were partially stained. We observed that the differentiated cells are localized in the more densely packed regions (see Figures 4.30b and 4.30e).

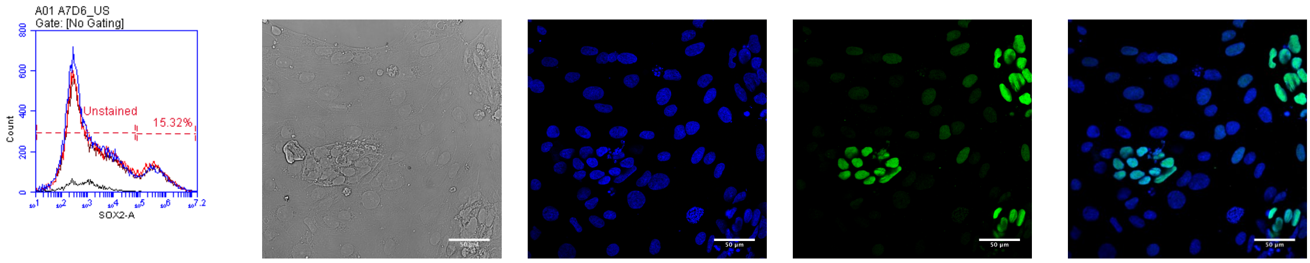

(a) Flow cytometry (b) Bright Field (c) Hoechst (d) SOX2 staining (e) Merge

Figure 4.30: Anterior Foregut Endoderm induction analysis: flow cytometry and immunostaining of cells at Day 6 of differentiation *Scale bars: 50 µm*

Conclusion Even though the differentiation kinetic was thoroughly optimized, it seems that we only have a limited success in AFE differentiation. This could be explained by our imprecise timing to start AFE patterning because the expression of CXCR4 and C-Kit markers did not peak at the same moment, and were not extremely high (respectively less than 70 and 50 % at peak). Indeed, the protocol recommends to pursue with over 80% CXCR4.c-Kit+ cells. We also observed that, regarding the AFE induction, denser regions showed better differentiation. It is possible that an important cell-cell contact could help in the induction of AFE. Therefore, it could be interesting to try again with a higher seeding density at Day 4.

f. Lung progenitor induction

Procedure On day 6 of differentiation, the medium must be replaced with specific medium to induce lung differentiation. This medium must then be replaced every other day until day 15.

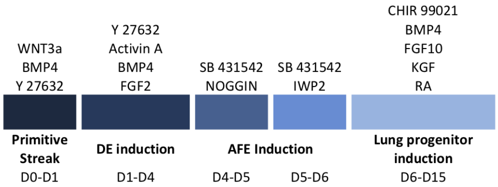

The d6/6.5/7–d15 medium is composed of complete SFD with: 3 µM CHIR99021, 10 ng/mL KGF, 10 ng/mL FGF10, 10 ng/mL BMP4, 20 ng/mL EGF and 50 nM retinoic acid.

Optimization Lung field induction is achieved by using Wnt, FGF, BMP and RA signaling. At this point, the concentration in Retinoic Acid must be optimized because it is highly cell-line dependent. We tested 0.05, 0.0625 and 0.1 µM of RA and observed the evolution of cell growth.

Observed cell growth and morphology From Day 6 to Day 12, we could observe important cell growth. Cells are growing in dense colonies, with sometimes circular 3D structures that can be observed (see Figure 4.31b). These might be the development of first lung buds.
With a concentration of Retinoic Acid of 0.1 µM, the cell survival was much less important than for the two other conditions. However, as can be seen on Figure 4.31, the cells fed with 0.0625 µM RA exhibit a more important cell growth and survival over the following days than with 0.05 µM of RA.

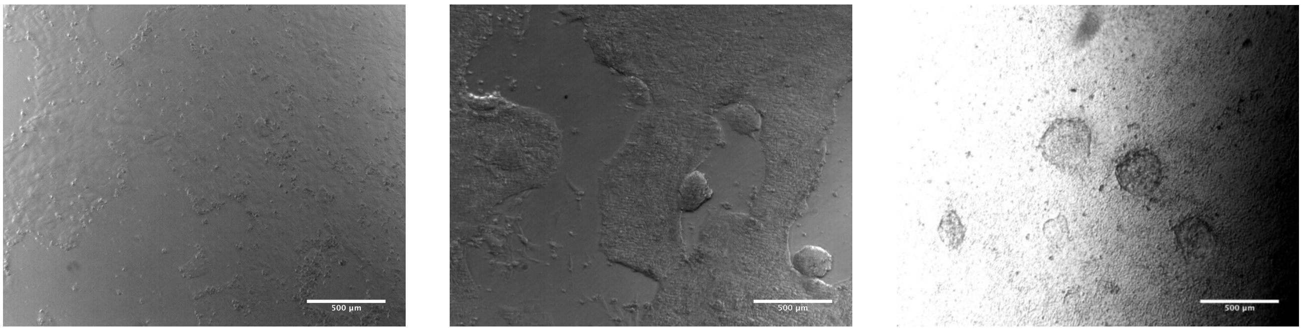

(a) 0.0625 µM Day 8 (b) 0.0625 µM Day 10 (c) 0.0625 µM Day 12

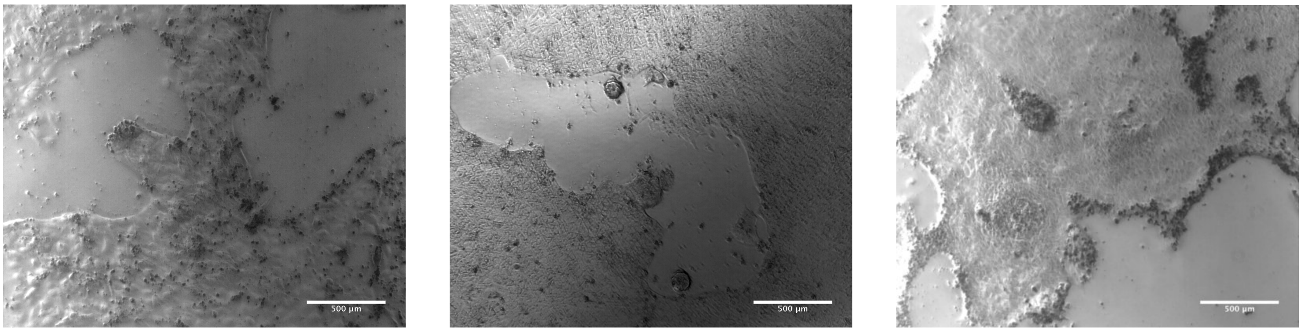

(d) 0.05 µM Day 8 (e) 0.05 µM Day 10 (f) 0.05 µM Day 12

Figure 4.31: Influence of Retinoic Acid concentration on cell growth and survival over the Days 8, 10 and 12. *Scale bars: 500 µm*

Evidence of endoderm commitment In order to characterize the commitment to the endoderm layer, and to obtain clues on which seeding density and which RA concentration were optimal over the long term, we observed evidence of germ-layer specific protein expression at Day 15 of differentiation.
The cells were fixed at Day 15 and stained with widely accepted germ layer markers: beta-III tubulin (TUJ1)

in red for ectoderm, alpha-fetoprotein (AFP) in green for endoderm, and smooth muscle actin (SMA) in yellow for mesoderm. The pictures presented here are representative of what was observed on each well, but were obtained from a single experiment.
As can be observed on Figure 4.32, cells are widely stained in green, evidence of Endoderm commitment. There is no trace of Mesodermal cells, but there is a slight contamination of TUJ1+ neuronal cells (in red), as can be expected at this time of differentiation. The upcoming replating step at Day 15, if performed correctly, is supposed to reduce the neuronal cell outgrowth. Moreover, it seems that these neuronal cells are less developed in the 0.0625 µM RA wells, another argument in favor of using such Retinoic Acid concentration. The seeding density, however, does not seem to have any impact. Of course, for a reliable conclusion, we would need to repeat the experiment. A quantification could also be performed with flow cytometry. We would be limited because we would only be able to detect the red and green cells simultaneously, but these are precisely the markers that we are interested in.

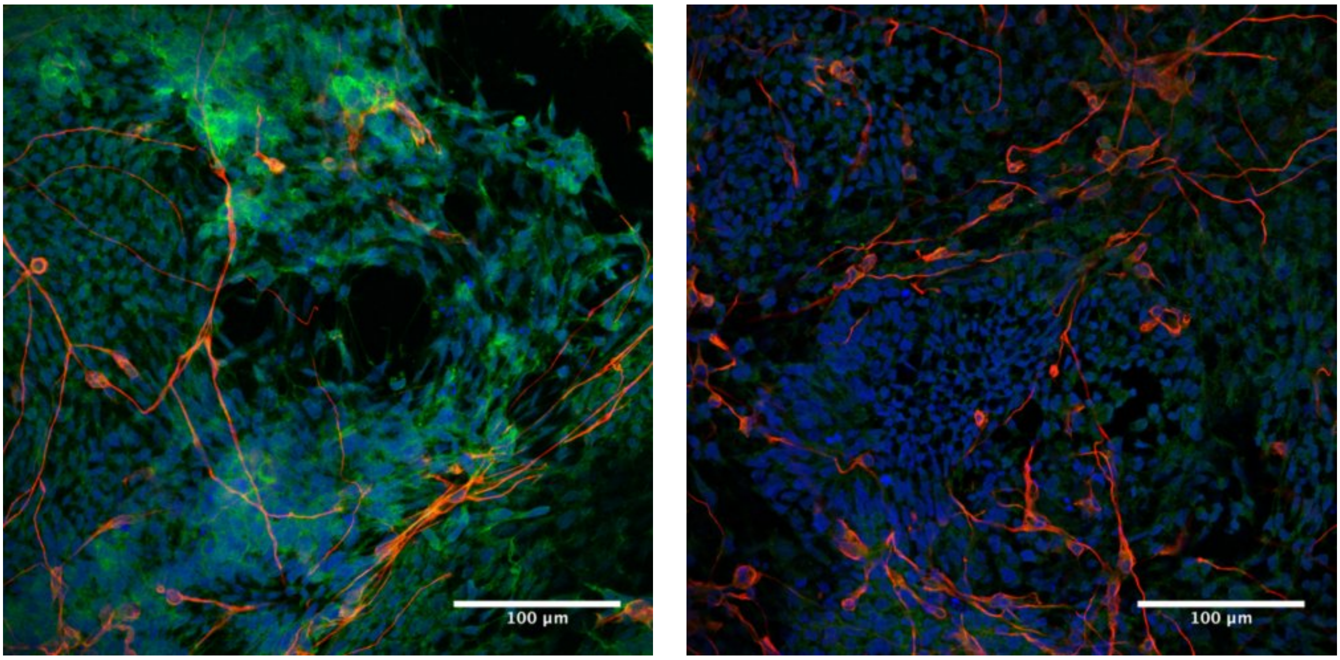

(a) 0.0625 µM - Seeding 50 000 cells/cm^2 (b) 0.0625 µM - Seeding 75 000 cells/cm^2

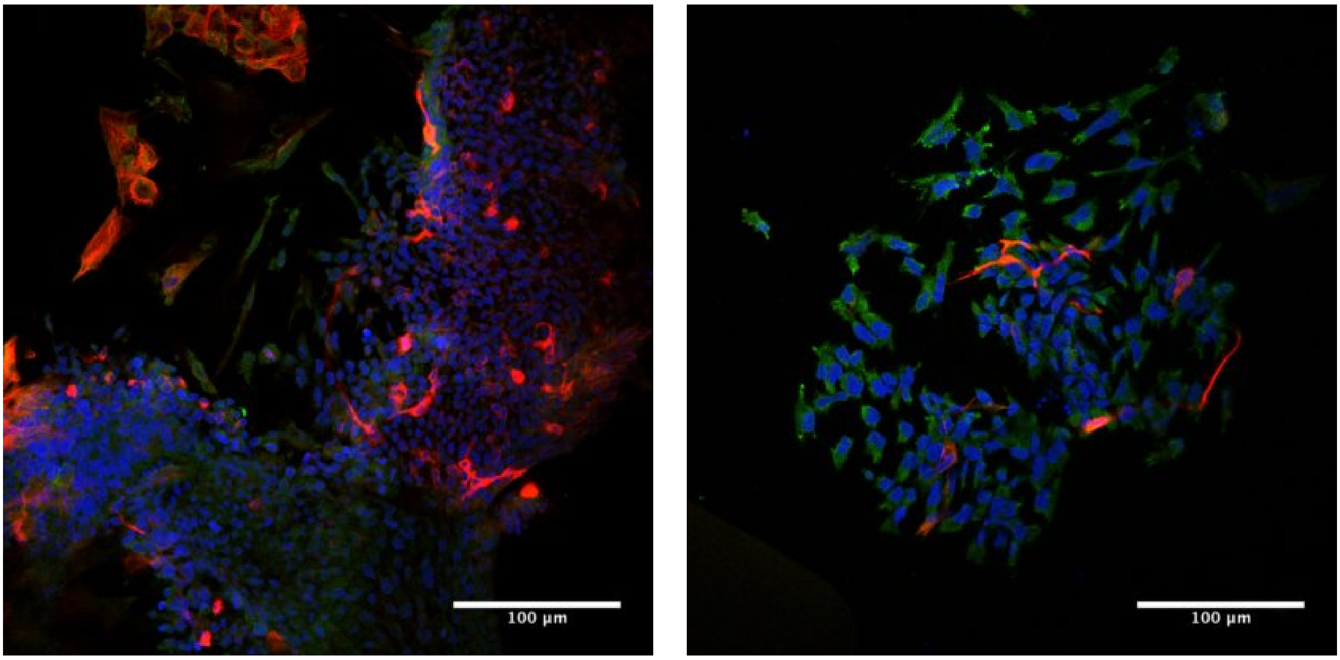

(c) 0.05 µM - Seeding 50 000 cells/cm^2 (d) 0.05 µM - Seeding 75 000 cells/cm^2

Figure 4.32: Anterior Foregut Endoderm induction analysis: 3-germ layers immunostaining of cells at Day 15 of differentiation. AFP (Green), TUJ1 (Red) and SMA (Yellow). *Scale bars: 100 µm*

Assessing NKX2.1 expression The anterior foregut endoderm cells obtained could be partially specified towards a putative lung bud fate, as suggested by the 3D structures observed in the dishes (see Figures 4.31b and 4.31c). We verified this assumption by performing an immunostaining of the cells at day 15 and observed important expression of lung marker NKX2.1 (see Figure 4.33). This marker is extremely important as it is thought to be a decisive marker of lung progenitor cells [67].

Moreover, the protocol recommends to assess the expression of NKX2.1 and FOXA2 cells to choose the optimal concentration of retinoic acid. From what we could observe at day 15, the expression of NKX2.1 was higher in cells treated with 0.0625 µM RA (Figure 4.33a) than in cells treated with 0.05 µM RA (Figure 4.33b).

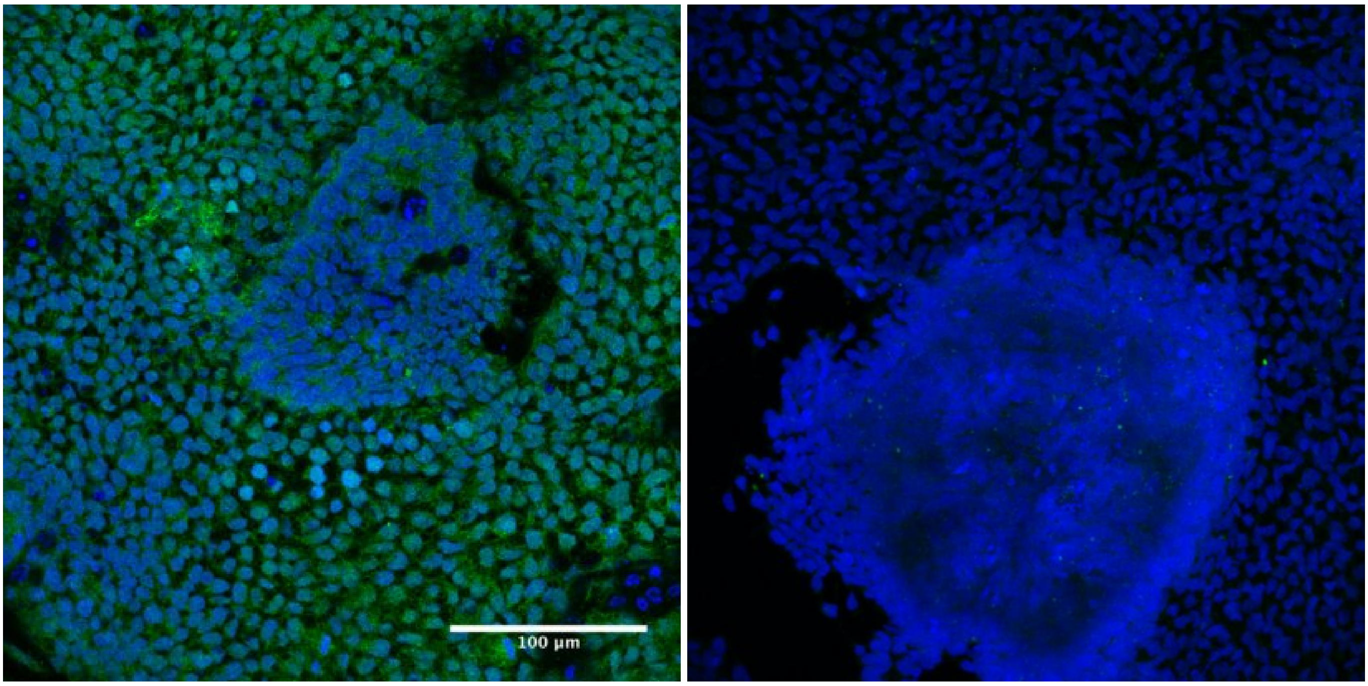

(a) 0.0625 µM - Seeding 50 000 cells/cm^2 (b) 0.05 µM - Seeding 50 000 cells/cm^2

Figure 4.33: NKX2.1 staining (green) of cells at Day 15 of differentiation. *Scale bar: 100* µm

Conclusion We performed a first analysis of the effects of some of the variable parameters: timing of AFE patterning, EB plating density and Retinoic Acid concentration, either through flow cytometry, or immunostaining, or both. Even though in this preliminary work we have not optimized the timing of AFE patterning, we could already observe that it had an influence on cell morphology at day 7. For all we could observe up to this point, the plating densities tested had no important effect on cellular development. The Retinoic Acid concentration, however, seemed to have an effect on the outgrowth of TUJ1+ neuronal cells, as well as on the cell growth and survival up to day 15.

g. Lung progenitors expansion

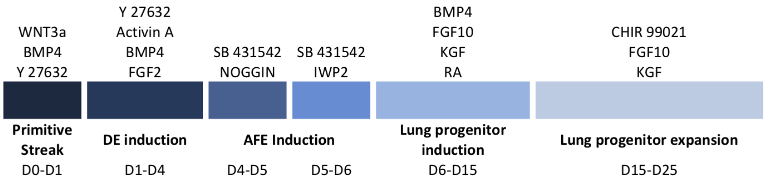

We have successfully obtained lung progenitor cells, that we will now differentiation towards a more distal lung cells, aiming at obtaining distal bronchi epithelial cells or even alveolar epithelial cells.

Procedure The d16-d25 medium is composed of complete SFD with: 3 µM CHIR99021, 10 ng/mL KGF and 10 ng/mL FGF10.

New plates are coated the day before with 0.33% (vol/vol) fibronectin. The d16 cells are briefly digested with trypsin, then this trypsin is aspirated. The remaining cells are then mechanically detached from the plate, with care taken to keep the cells in clusters before seeding them again on the new plates (in a 1:3 to 1:5 ratio).

This step is crucial as it is essential for lung specification, but also because it allows removing non-endodermal cells in the culture. According to the protocol, these cells are either neurectodermal cells or FOXA2–. P63+. NKX2.1–. SOX2–. EpCAM+. PAX6–. PAX8– cells whose identity is unclear [15]. As it happens, trypsin preferentially digests these into single cells or small cell clusters that stay in the supernatant and are removed by aspiration.

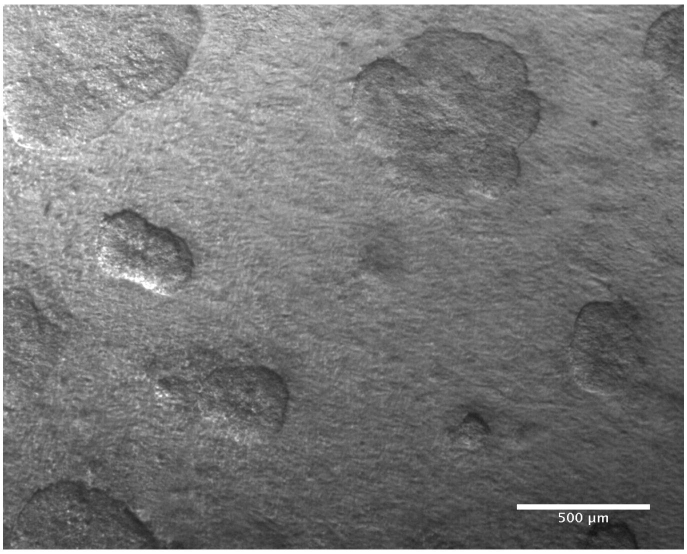

Figure 4.34: Lung progenitor cells (Day 15 of differentiation).
Scale bar: 500 µm

It is crucial to pay attention to the fact that dissociation into single cells compromises viability compared with clump passaging, that is why it is required to be extremely delicate when replating. According to the protocol, viability can be improved by plating at confluent or overconfluent density, suggesting that the lung progenitors require close cell contact for survival, which is something that we had already observed in the previous phases during AFE induction. Furthermore, single-cell re-plating promotes the outgrowth of TUJ1+ neuronal cells.

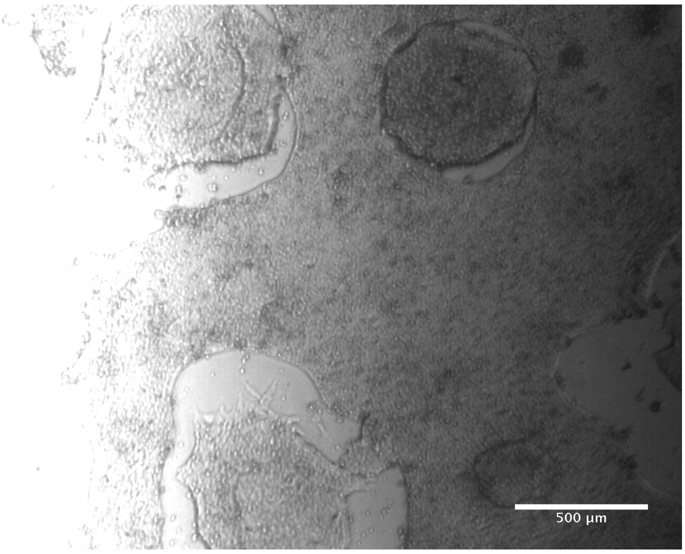

Figure 4.35: Lung progenitor cells (Day 15 of differentiation).
Scale bar: 500 µm

Preliminary results During the first attempts, I had a hard time obtaining adherent cells after this d15 replating step. According to the protocol, this is a common occurrence and the clumps can take up to 6 days to completely attach. The first time I performed this experiment, I observed that less than 5% cells had attached after 48 hours. I tried several techniques:

- Collecting all the old medium (with a 1 mL tip), waiting for the clumps to sink down, aspirating most of the supernatant (leave 2 mL) and add the new medium before distributing back to the wells;
- Collecting half of the old medium (with a 1 mL tip), waiting for the clumps to sink down, aspirating most of the supernatant (leave 2 mL) and add the new medium before distributing back to the wells;
- Removing half the old medium in each well (with a 1 mL tip), and adding directly 1 mL of the new medium

At day 26, I could observe that the third technique was the one which resulted with the most adherent cells. However, it was not normal that I had such a hard time obtaining adherent cells after the replating at day 15. Therefore I experimented different detachment techniques and trained to improve cell survival.

Optimization After multiple attempts, a protocol for a mild trypsinization with high cell survival and few single cells was optimized as follows (for 24-well plates):

- Collect d15 medium in a 15mL tube. Work with a maximum of 2 wells at a time !
- Wash with 300 µL per well of PBS for about 1 min
- Discard and add 200 µL of TryplE for 1 min

- Aspirate the TryplE and splash back the 1 mL d15 medium in each well
- Pipet up and down with medium force about 5 times to detach the cells
- Put cells in 1.5 mL tubes and wait about 2 min for the clumps to settle
- Discard d15 medium and add d16 medium (depending on the replating ratio)
- Replate on fibronectin coated plates (0.33%)

With this protocol we obtained 60 to 80% adherent cells at day 17.

Final results At Day 15, the cells exhibits complex tissue-like organisation. Some 3D structures are forming, as well as circular holes, as can be seen on Figures 4.34 and 4.35.
When replating the cells, we observe that they form tightly joined structures: they detach in films rather than in clusters or single-cells.

h. Distal lung maturation

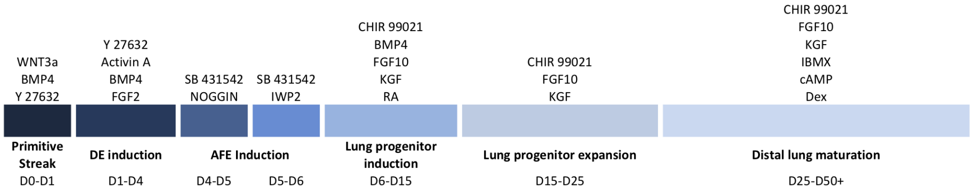

Procedure The d26 medium is composed of complete SFD with: 3 µM CHIR99021, 10 ng/mL KGF and 10 ng/mL FGF10, 25 ng/mL Dexamethasone, 0.1 mM IBMX and 0.1 mM cAMP.
At this stage, if non-endodermal cells are growing again, it is recommended to replate the cells on new plates coated with 0.33% (vol/vol) fibronectin the day before. I never got to reach this stage for we lacked some differentiation products, and we had already decided to put a hold to iPSC experiments because we were running out of time. Therefore, the differentiation was stopped at Day 32, without medium change at Day 26.

Observed results After 26 and 32 days of differentiation, the cells continued to grow in flat colonies, and they still exhibited those 3D structures that could be possible lung buds (see Figures 4.36a and 4.36b).

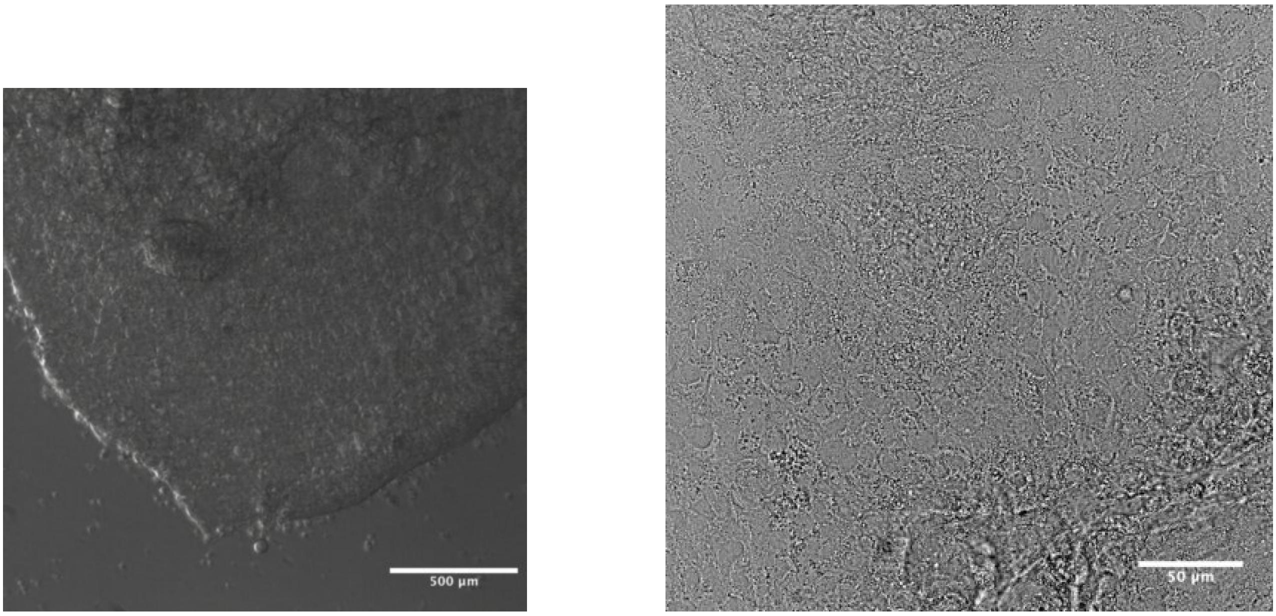

(a) Lung progenitors cells at Day 26.
Scale bar 500 µm

(b) Lung progenitors cells at Day 32.
Scale bar 50 µm

i. Assessing cellular phenotype after 25+ days of differentiation

Procedure The protocol developed by Huang *et al.* [15] was tested on Gibco's Episomal iPSC line. The differentiation was pursued until Day 26, thus generating mature lung progenitors. Unfortunately, we could not perform the last stage: distal lung maturation. However, we decided to examine the phenotype of the progenitors that were obtained, in order to assess the efficiency of the protocol up to day 26.

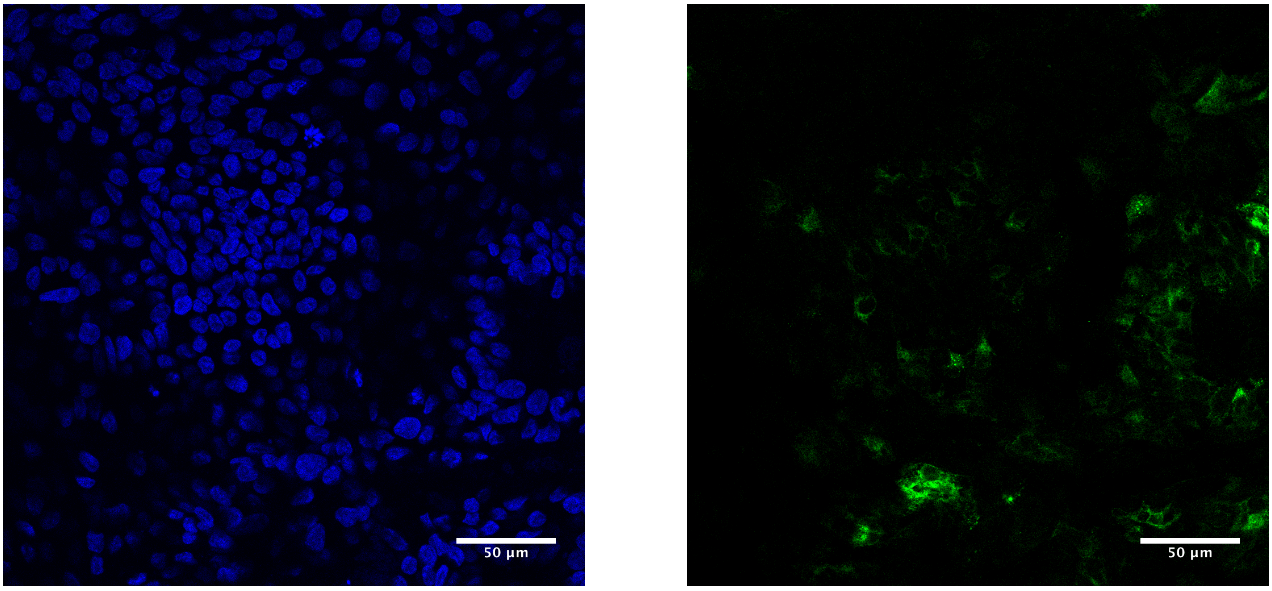

(a) Hoechst (b) AFP : Alpha-Fetoprotein

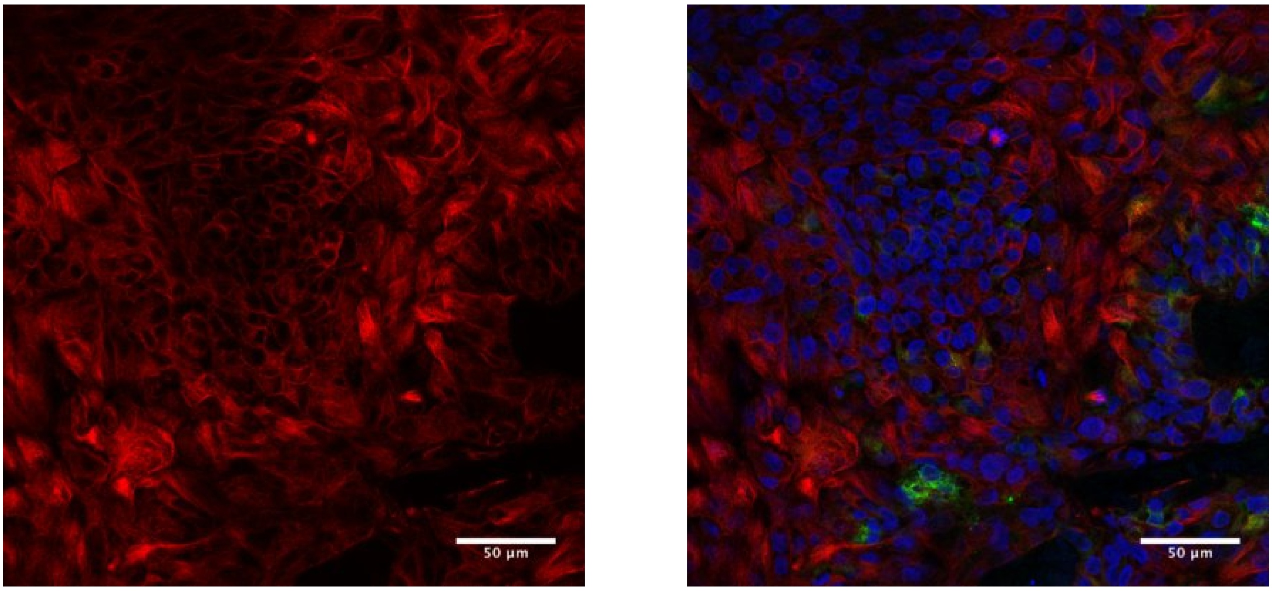

(c) TUJ1: beta-III tubulin (d) Merge

Figure 4.37: Characterization of differentiated cells at Day 32: the 3-Germ layer assay demonstrates that there are no remaining neuronal cells. The absence of SMA staining indicates that there are no thyroidal cells. AFP (Green), TUJ1 (Red) and SMA (Yellow). *Scale bars: 50* µm

3 Germ Layers After 32 days of differentiation, we examined the evolution of the three germ-layer specific markers, as can be seen in Figure 4.37. We observe sporadic expression of AFP (Figure 4.37b), a protein mostly expressed in undifferentiated endoderm or in the yolk sac and the liver during fetal development. This could be either undifferentiated endodermal cells, or cells that differentiated towards an hepatic fate, which is one of the possible endoderm derivative. Happily, this contamination is very limited, and might have been overcome with the Day 25 replating technique.

The mesoderm marker SMA (smooth muscle actin) was not expressed in our cells (data not shown), which indicates that cells are not expressing airway phenotypes. This could be either because the cells are not mature enough, or because Huang's protocol directs cells towards a distal fate, where there are no smooth muscle cells [180].

Finally, the TUJ1 marker (beta-III-tubulin) is highly expressed in differentiated cells at Day 32, as can be seen on Figure 4.37c. From the pictures we can see that this marker is no longer specific to neural cells. Indeed in mature cells, the beta-III-tubulin is a protein used to form the microtubules. Therefore, the TUJ1 staining shows an overview of our lung progenitors cells' cytoskeleton.

Interestingly enough, when we had proceeded with the cells testing for a low concentration of Retinoic Acid (0.05 μM from day 8), not only did these cells form very small colonies, with high cell death, but they also exhibited a non-mature cell state, with an important contamination of neuronal cells (see Figure 4.38). This confirms our observations that low concentrations of Retinoic Acid do not promote cell proliferation and maturation.

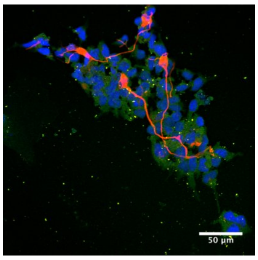

Figure 4.38: Characterization of differentiated cells at Day 32: 3-Germ layer assay. *Scale bars: 50* µm

Lung cell-type differentiation marker: NKX2.1 The differentiation was further assessed by immunostaining of a lung progenitor marker, NKX2.1 [67], as well as of ZO-1, a tight junction protein. We could observe a consistent formation of tight junctions as can be seen on Figure 4.39c, thus confirming the differentiation towards an epithelium with a strong tissue integrity. Such important intercellular junctions might have been hinted at on Day 15 during the replating step, as trypsinized cells were only detaching in sheets, and not as single cells.

The NKX2.1 marker was also expressed at Day 32 but weaker than at Day 15, suggesting that we might have contamination of non lung progenitor cells or that the cells are not mature enough.

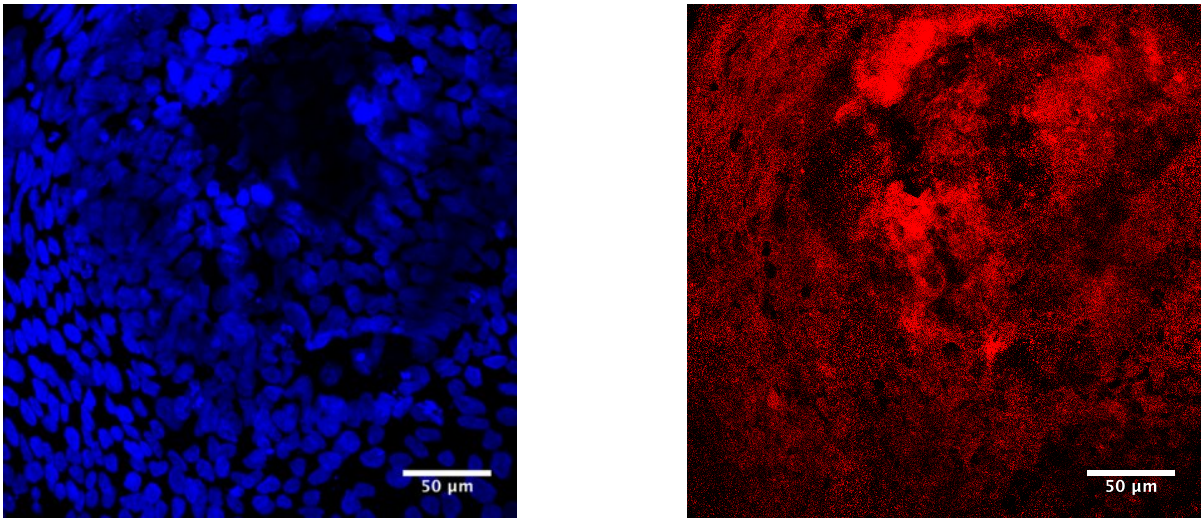

(a) Nuclei staining (b) NKX2.1 staining

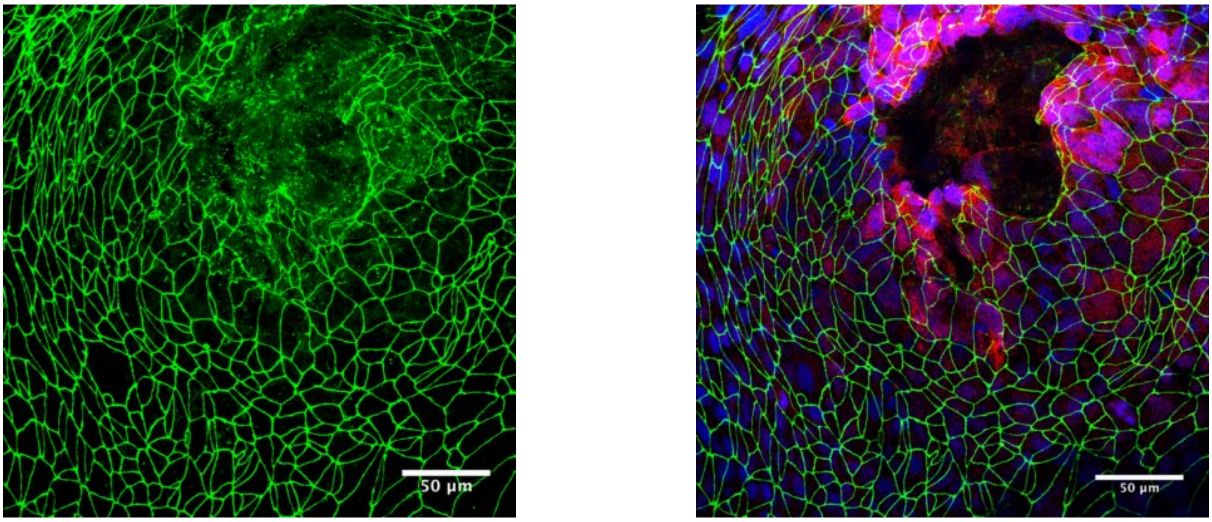

(c) Tight junctions staining (ZO-1) (d) Merge

Figure 4.39: Characterization of differentiated cells at Day 32. The strong NKX2.1 staining indicates a commitment to the lung lineage. The tissue formed exhibits important tight junction formation. *Scale bars: 50* µm

Lung functions specific marker Most mature lung functions cannot be observed at this stage of the differentiation, however in the protocol, it had been observed that few cells already express the MUC5AC marker ([180], [15]). This was confirmed in our experiment, as we observed some expression of MUC5AC at Day 32 (see Figure 4.40a). This marker is typical mucus secretory cells of the small aiway epithelial cells. Observing the expression of MUC5AC confirms the commitment of our differentiated cells to lung or airway epithelial cells.

Two other lung markers were observed at Day 32: Podoplanin (see Figure 4.40b) and Caveolin 1 (see Figure 4.40c), both AET I cell markers. This result is quite encouraging, as these markers are observed quite early. Indeed, Huang *et al.* [15] did not report observing PDPN before day 50. However, these markers are commonly found in epithelial cells (excepted AET II), therefore they could be expressed here because we have bronchial epithelial cells.

We also stained for AQP5 and SP-B, Type I and Type II specific markers, respectively. Both observations were negative, suggesting that alveolar lung commitment cannot be obtained without the next 25 days of maturation with the specific differentiation factors.

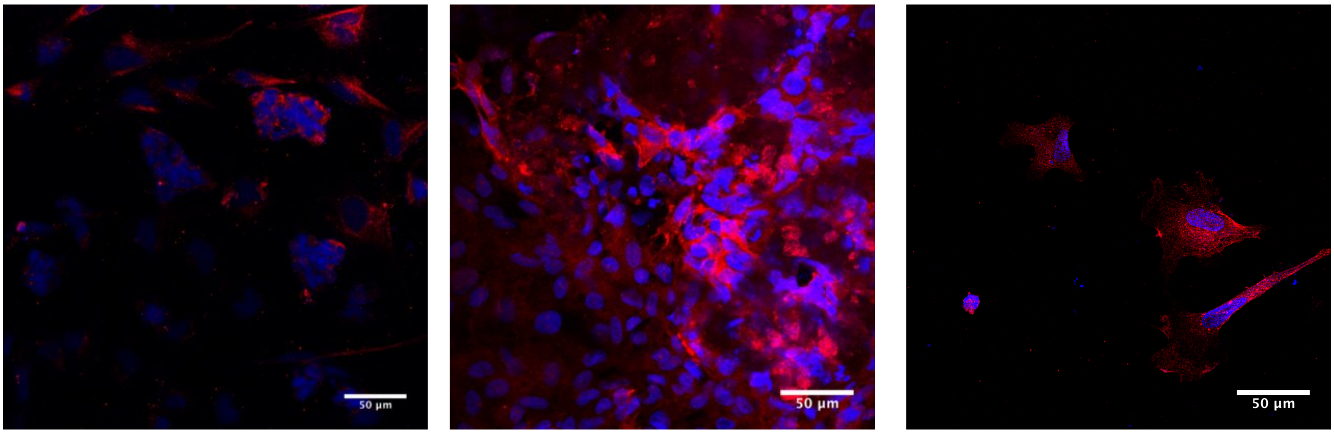

(a) MUC5AC staining at Day 32 (b) PDPN staining at Day 32 (c) Caveolin 1 staining at Day 32

Figure 4.40: Characterization of differentiated cells at Day 32. *Scale bars: 50* µm

Conclusion The characterization of the cells obtained at Day 32 (without performing the last medium change of the protocol) suggested that we have indeed lung progenitor cells, expressing NKX2.1, PDPN, Cavolin1 and MUC5AC specific markers. The differentiation efficiency seems good, as the contamination of liver-like cells (AFP expressing cells) is quite minimal. However, the differentiation towards alveolar fate is not complete yet, as the cells are not mature, and do not exhibiting distal lung specific markers (such as SP-B or AQP5), which indicates that the following maturation state is a requirement to obtain a commitment to a distal alveolar fate..

j. Conclusion

We have performed the differentiation of iPSC into lung progenitor cells. We used the protocol developed by Huang *et al.*, [15], a 50-day differentiation method, with multiple steps and several parameters that should be tested and tailored to the iPSC line used. Such optimization is the key to building a reproducible, high-efficiency protocol designed for a specific cell line.

One of the main challenges was to assess the best time to switch from Definitive Endoderm induction to Anterior Foregut Endoderm induction. This time is optimal 6 to 9 hours after the maximum yield of DE [15], therefore we tried to assess maximum DE induction by monitoring the expression of CXCR4+ and c-KIT+ cells. We used flow cytometry to observe the expression of CXCR4 and c-Kit markers but, even with a triplicate and multiple time-points, we obtained a very low DE yield (less than 40%). Indeed, this yield is not only cell-line specific, but it is dependent on the previous steps of the differentiation: the size and plating density of embryoid bodies and the frequency at which they were fed. That is why we had to go back and firstly focus on obtaining reproducible EB size and plating density, by implementing an extremely detailed protocol for EB plating.

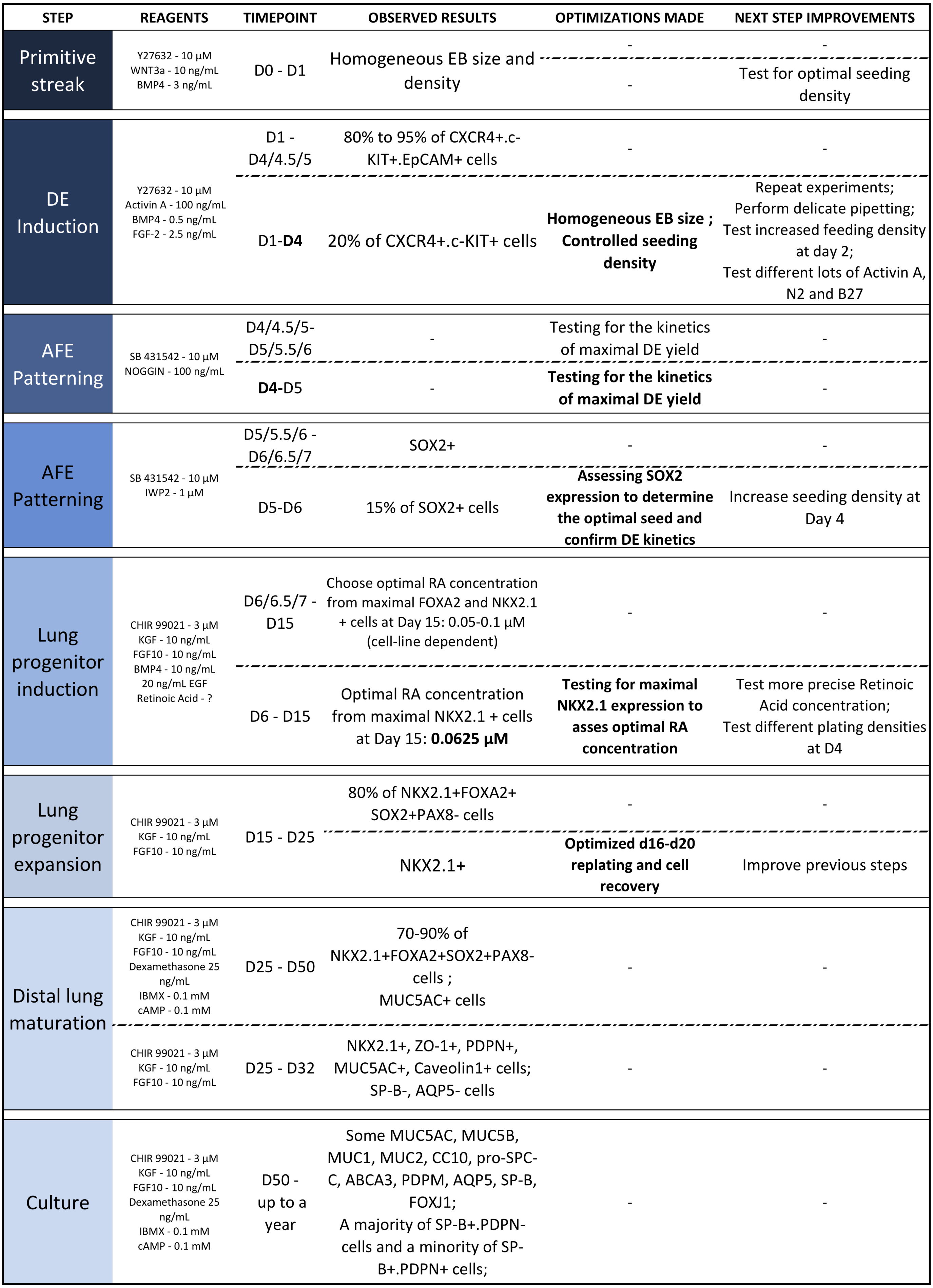

STEP	REAGENTS	TIMEPOINT	OBSERVED RESULTS	OPTIMIZATIONS MADE	NEXT STEP IMPROVEMENTS
Primitive streak	Y27632 - 10 µM WNT3a - 10 ng/mL BMP4 - 3 ng/mL	D0 - D1	Homogeneous EB size and density	-	-
				-	Test for optimal seeding density
DE Induction	Y27632 - 10 µM Activin A - 100 ng/mL BMP4 - 0.5 ng/mL FGF-2 - 2.5 ng/mL	D1 - D4/4.5/5	80% to 95% of CXCR4+.c-KIT+.EpCAM+ cells	-	-
		D1-**D4**	20% of CXCR4+.c-KIT+ cells	**Homogeneous EB size ; Controlled seeding density**	Repeat experiments; Perform delicate pipetting; Test increased feeding density at day 2; Test different lots of Activin A, N2 and B27
AFE Patterning	SB 431542 - 10 µM NOGGIN - 100 ng/mL	D4/4.5/5-D5/5.5/6	-	Testing for the kinetics of maximal DE yield	-
		D4-D5	-	**Testing for the kinetics of maximal DE yield**	-
AFE Patterning	SB 431542 - 10 µM IWP2 - 1 µM	D5/5.5/6 - D6/6.5/7	SOX2+	-	-
		D5-D6	15% of SOX2+ cells	**Assessing SOX2 expression to determine the optimal seed and confirm DE kinetics**	Increase seeding density at Day 4
Lung progenitor induction	CHIR 99021 - 3 µM KGF - 10 ng/mL FGF10 - 10 ng/mL BMP4 - 10 ng/mL 20 ng/mL EGF Retinoic Acid - ?	D6/6.5/7 - D15	Choose optimal RA concentration from maximal FOXA2 and NKX2.1 + cells at Day 15: 0.05-0.1 µM (cell-line dependent)	-	-
		D6 - D15	Optimal RA concentration from maximal NKX2.1 + cells at Day 15: **0.0625 µM**	**Testing for maximal NKX2.1 expression to asses optimal RA concentration**	Test more precise Retinoic Acid concentration; Test different plating densities at D4
Lung progenitor expansion	CHIR 99021 - 3 µM KGF - 10 ng/mL FGF10 - 10 ng/mL	D15 - D25	80% of NKX2.1+FOXA2+ SOX2+PAX8- cells	-	-
			NKX2.1+	**Optimized d16-d20 replating and cell recovery**	Improve previous steps
Distal lung maturation	CHIR 99021 - 3 µM KGF - 10 ng/mL FGF10 - 10 ng/mL Dexamethasone 25 ng/mL IBMX - 0.1 mM cAMP - 0.1 mM	D25 - D50	70-90% of NKX2.1+FOXA2+SOX2+PAX8- cells ; MUC5AC+ cells	-	-
	CHIR 99021 - 3 µM KGF - 10 ng/mL FGF10 - 10 ng/mL	D25 - D32	NKX2.1+, ZO-1+, PDPN+, MUC5AC+, Caveolin1+ cells; SP-B-, AQP5- cells	-	-
Culture	CHIR 99021 - 3 µM KGF - 10 ng/mL FGF10 - 10 ng/mL Dexamethasone 25 ng/mL IBMX - 0.1 mM cAMP - 0.1 mM	D50 - up to a year	Some MUC5AC, MUC5B, MUC1, MUC2, CC10, pro-SPC-C, ABCA3, PDPM, AQP5, SP-B, FOXJ1; A majority of SP-B+.PDPN- cells and a minority of SP-B+.PDPN+ cells;	-	-

Figure 4.41: Results obtained at different steps of the alveolar epithelium differentiation protocol: protein expression levels, protocol optimization and future perspectives

The next challenge was finding the replating density that was best for Day 4 replating. Immunostaining observations of SOX2, an AFE marker, indicated that high density regions showed more important AFE commitment. It would be interesting to repeat the experiment at several densities and to quantify the AFE induction efficiency with flow cytometry. Therefore, we would observe whether a higher density is indeed required for improved AFE commitment, as well as determine the optimal seeding density for our cell line.
The following step was to find the optimal Retinoic Acid concentration for AFE induction. We tested several concentrations and several seeding densities and assessed the germ layer commitment of cells at Day 15. We could also observe here that high density replating prevented the contamination of TUJ1+ neuronal cells. Moreover, the 0.0625 µM concentration of Retinoic Acid seemed to enhanced cell growth and survival, whereas using a 0.05 µM concentration resulted in non-differentiated cells with important neural contamination.
Further optimization lied on the replating density at Day 15. Unfortunately, its influence on the differentiation can only be completely apprehended at Day 50, a time point we never attained. However, an important part of our work was to find a technique that would allow cell survival after the replating steps. We tested several methods and could validate one with great success.
In the end, we characterized the phenotype of the cells obtained at Day 32 of differentiation, and could conclude that they were indeed lung progenitor cells, with very small contamination of other types of cells (such as hepatocytes or similar cells). An encouraging result was the observation of widespread expression of the lung progenitor marker NKX2.1, as well as sporadic expression of distal lung markers such as PDPN, Caveolin1 and MUC5AC. Moreove intense intercellular junctions (ZO-1 proteins) was observed, underlining the formation of an impermeable epithelium. Finally, we tested for the expression of alveolar-specific markers (AQP5 and SP-B), but observed negative results. I wish we could have pursued the experiment up to day 50, in order to assess whether the cells would have indeed committed to an alveolar fate.
Finally, we have worked on optimizing the protocol developed by Huang *et al.* [15] for the Human Episomal iPSC Line (Gibco, Ref. A18945). It required a long and meticulous process, testing different parameters such as compound concentrations, plating density, timing, manual cell detachment speed or even pipetting force at each step. After several runs, I was able to optimize a few of those parameters at each step. All of my work and improvements are summarized in the Table 4.41, which, for each step, compares the results and recommendations of the protocol (top line) with mine (line below). I am now convinced that, in order to produce a reliable protocol adapted to our cell line, we would need to continue this extensive testing, with continuous back and forth validations, which will require a very long time (over a year) and an important budget (the total cost for one run from day 0 to day 50 is about 2000 euros). Unfortunately we could not continue this experiment because of the aforementioned reasons.

4.5.3 In situ differentiation experiments

Our desire was to optimized Huang *et al.*'s protocol on the commercial Episomal iPS Cell Line from Gibco (Ref. A18945), bearing in mind the final objective to use the alveolar epithelium hereby obtained to enhance our *in vitro* model of the alveolar capillary barrier. Our first attempts at the directed differentiation in a dish highlighted numerous parameters that will require testing and optimization. We wondered if we could optimize these parameters directly for a patch *in situ* differentiation, and if we would obtain even better differentiation efficiency. Therefore, our attempt at differentiating the iPSC directly from the patch is detailed and reported in the following section.

a. Formation of embryoid bodies

Protocol As detailed in section 4.3.2, EBs can be formed on the patch by performing a specific low-adherence coating (Vitronectin diluted 1:500) and adding ROCK inhibitor for a few hours of treatment. However, since the D0 medium of the alveolar differentiation protocol already contains ROCK inhibitor, we needed to test different methods. The differentiation was therefore performed with two different starting conditions: either complete D0 medium was used from the beginning (Condition D0), or EBs underwent a 1 h ROCK inhibitor treatment and then, a new medium was used: the d0 medium, deprived of ROCK inhibitor (Condition 1 hY).

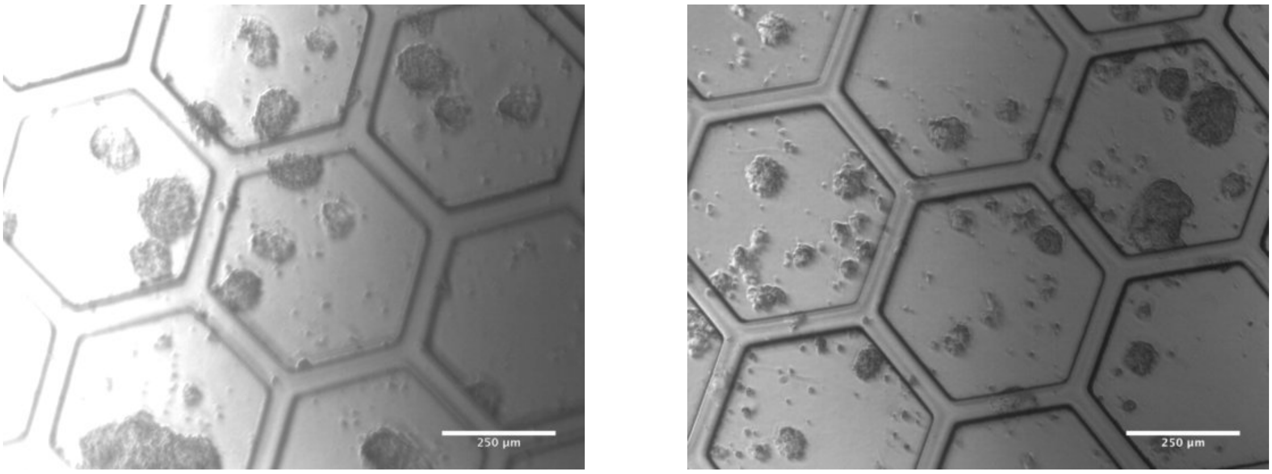

(a) Day 0 + 2 hours - D0 condition (b) Day 0 + 2 hours - 1hY condition

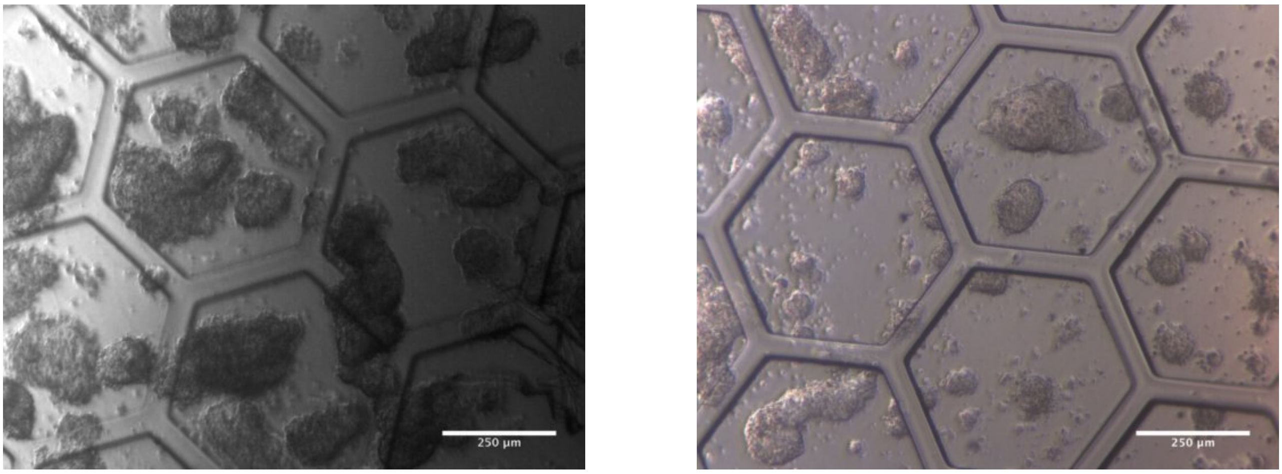

(c) Day 0 + 3 hours - D0 condition (d) Day 0 + 3 hours - 1hY condition

Figure 4.42: Testing ROCK inhibitor treatment duration to form embryoid bodies on the patch. *Scale bars: 250* µm

Results We observed embryoid body formation on Day 0 after 2 and 3 hours post-seeding (see Figure 4.42). As expected, after 2 h we could already observe the incidence of the long-term ROCK treatment: cell colonies seeded with complete D0 medium (D0 condition) were flat and spread across the patch (see Figures 4.42a and 4.42c), whereas a limited ROCK inhibitor exposure (1hY condition) generated 3D colonies: the embryoid bodies (see Figures 4.42b and 4.42d).

EB evolution After 24 hours, for both the D0 and the 1hY condition the cells had grown all over the patches. For the D0 condition we observed agglomerates of cells in 3D, (see dark spots on Figure 4.43 left). Regarding the 1hY condition, there are also 3D structures, but these present a precisely defined contour (see Figure 4.43 right), which is a good indicator of undifferentiated colonies.

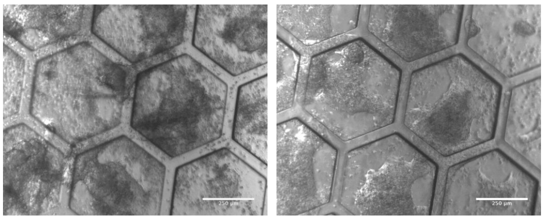

Figure 4.43: After 24 h for D0 (Left) and 1hY (Right). *Scale bar: 250* µm

b. DE induction

DE induction evolution At Day 1 the medium was changed to DE induction medium. The cells were then cultured up to Day 4 in this medium without medium renewal.

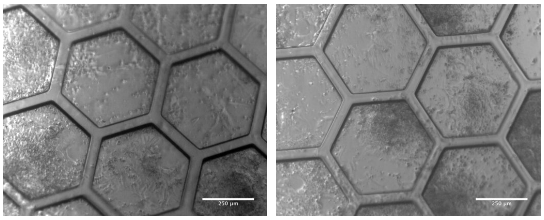

Figure 4.44: After 24 h for D0 (Left) and 1hY (Right). *Scale bar: 250* µm

Observed results After 48 hours, both conditions have evolved into a flat layer of cells covering the patch. (see Figure 4.44). Over the Days 2 to 4, we could observe cells growing on the patch. As the EB seeding is heterogeneous by definition, there were areas of the patch with very different cell densities.

c. AFE induction

At day 4 the medium was changed to d4/4.5/5 medium to induce AFE patterning. On day 4, before changing the medium, we could observe extremely dense areas (see Figures 4.45a and 4.45b).
Finally, after 24h of AFE patterning, some cells started to show an elongated morphology (see Figure 4.45c).

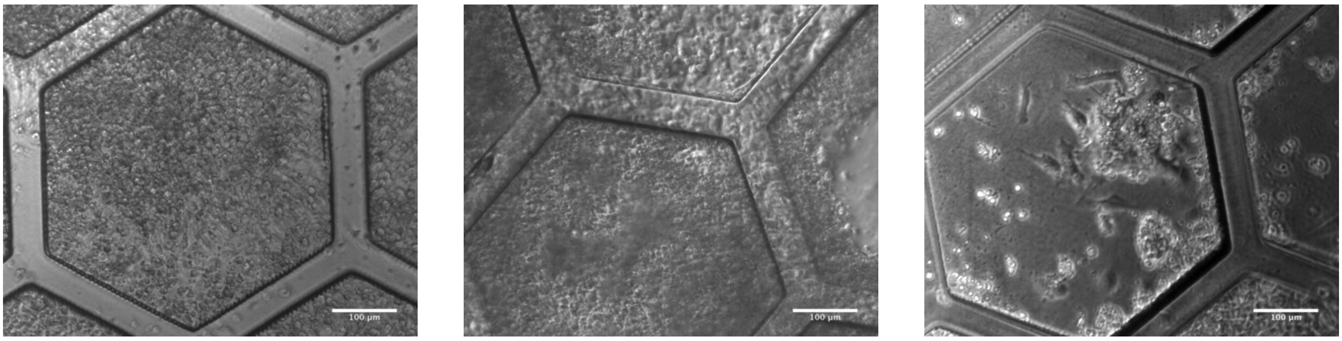

(a) Day 4 - D0 condition (b) Day 4 - 1hY condition (c) Day 5 - D0 condition

Figure 4.45: Day 4: cells before and after starting AFE patterning. *Scale bars: 100* µm

d. Lung progenitor induction and expansion

Following the AFE induction, the medium was changed to d6/6.5/7 medium and renewed every other day until day 15. Similarly to what was observed on a petri dish, the cells formed colonies with somewhat 3D structures similar to early lung buds (see Day 12 Figure 4.46 left and Day 15 Figure 4.46 right).

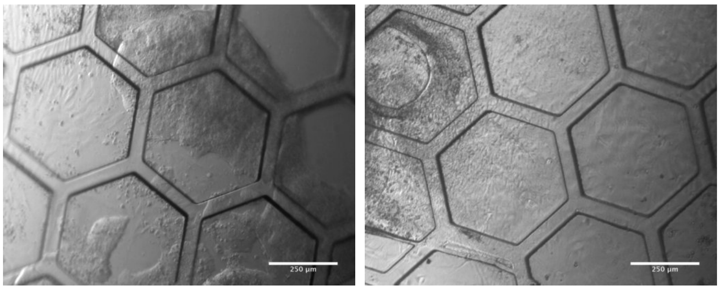

Figure 4.46: Lung progenitor induction: Day 12 (left) and Day 15 (right). *Scale bar: 250* µm

Day 15 replating At day 15, the cells were trypsinized and seeded on new patches. This step however was highly variable as the trypsinization time depends on the patch and its cell density. Moreover, as cells adhere strongly on gelatin, a trypsinization of about 9 minutes was necessary to detach all cells, and this resulted in the death of almost all cells.

Results Finally, after a few attempts, I decided to trypsinize for only 4 minutes, leaving cells behind (see Figure 4.47a) but increasing cell survival. This means that in order to seed the cells at the right density at day 15, we might need more than one patch to seed a new one. This raises severe cost concerns. Moreover, such method of trypsinization means that we are selecting cells, which will change the outcome of our experiment. This is all the more an issue that Huang *et al.* [15] precised that the cells that are preferentially digested are the neuronal progenitors. This means that we would need to implement a two-step trypsinization that could separated these two kinds of cells. This would be take a long time to optimize.
Another issue was that, between day 15 and day 20, I observed holes in the gelatin network. This was a great concern because newly divided cells grew on top of each other, forming extremely dense areas among holes (see Day 20, Figure 4.47b). As we know that 3D structure and cellular density influence cellular differentiation, it was not possible to pursue the differentiation.

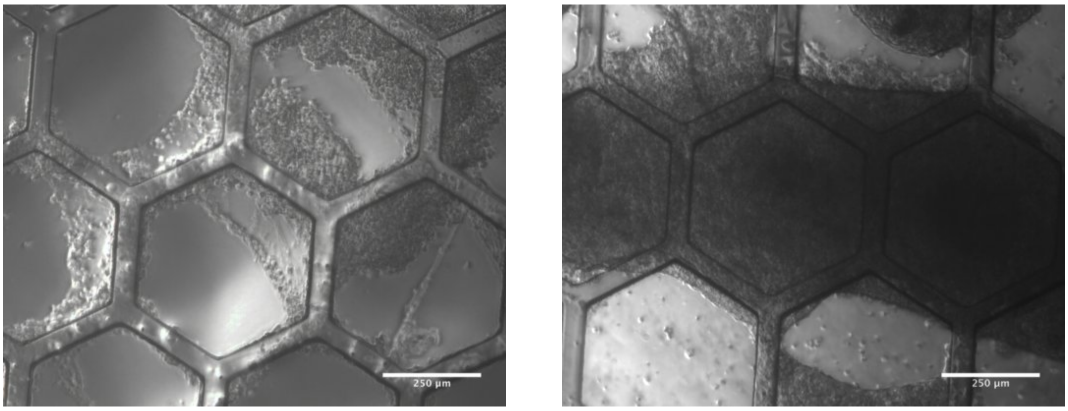

(a) Day 15 (b) Day 20

Figure 4.47: Evolution of lung progenitor induction and expansion. *Scale bars: 250 µm*

Conclusion The appearance of holes in the gelatin network put a hold to our attempts at *in situ* differentiation. I wondered whether the fibers were destroyed by a chemical reaction or by the cells. I tried to place a patch in d15 medium for a week but I did not observe any holes, which means that it was not a chemical reaction with a compound of the d15 medium that destroyed the cells.
As we have mentioned in a previous chapter, some cells like endothelial cells are known to produce gelatinase, an enzyme that can digest gelatin. After some research, I learned that other cells produce gelatinase: airway cells [192], brain cells [193], liver cells [194], fibroblasts [195] as well as most cancerous cells [196] (especially sarcomas). Interestingly, all of these cells could be present in our culture at day 15. Indeed, there could be brain and liver cells obtained from missed differentiation from the endodermal state. The airway cells or lung fibroblasts would be more expected at this stage of the differentiation because we expect lung progenitor cells.

e. Conclusion

Discussion The *in situ* differentiation is more complex than the direct differentiation as the patches present a high variability from one to another, due to the random deposition of the fibers during the electrospinning process. Another concern is the poorly controlled embryoid body formation. Indeed, the EBs are different in size and their seeding is heterogeneous because we cannot control where they attach. Moreover, EBs adhere on patches and start spreading, therefore they do not keep the spherical shape that they have for 3 days in the Ultra-Low Attachment plates recommended in Huang's protocol. The effective shape of the colonies, as well as the removal of ROCK inhibitor from the d0 medium are two factors that might induce changes in the differentiation process, and this could take a long time to assess.
Another limitation of performing *in situ* differentiation from the beginning is that the replating steps are more fluctuating because of the strong adherence of cells to gelatin fibers. As we know that overtrypsinization can kill the cells, and a low trypsinization would not allow for the removal of neuronal cells, therefore it is a critical drawback.
Finally, the destruction of the gelatin nanofibers by the cells is terminal: if the cells hydrolyse the fibers before producing their own extracellular matrix, we cannot pursue the differentiation *in situ*.

Decision In my opinion, because the differentiation protocol is already extremely complex and variable in a dish, I believe that working directly on *in situ* differentiation is not a good idea. I believe that we should first characterize and optimize our protocol in a dish so that it is perfectly tailored to the Episomal iPSC line, then we should see about differentiation on the patch.
We could imagine further experiments where we seed our lung progenitors on patches at Day 25 of differentiation, so that we could induce distal lung maturation *in situ*. Indeed, as the gelatin nanofiber network of our patch has mechanical properties extremely similar to that of the alveolar interstitium tissue, it could induce cues to improve alveolar commitment. Also, culturing the cells in an Air-Liquid Interface condition was shown to enhance alveolar commitment and cellular maturation [185].
Furthermore, if we were to observe an improvement of the alveolar commitment after seeding cells on the patch at Day 25, we could consider seeding the cells from day 15. If this improves again the differentiation efficiency we could seed the cells earlier, and so on. I do believe that testing patch effects in this backward manner would

be the most efficient method to determine when we can introduce the cells on the patch without observing radical changes in the differentiation kinetics or fate.

4.6 Achievements and perspectives

4.6.1 Endothelial differentiation

Obtained results We tried to adapt the method of Patsch *et al.* [14] to our iPSC line, and managed to obtain endothelial progenitors from iPSC in 6 days, judging by the cell morphology. We measured CD144+ cells to confirm that we obtained a 50% efficiency.
When using MACS to sort out the CD144+ cells for purification, most of the cells were lost in the process. In the end, we observed that the remaining cells (less than 6% of the CD144+ cells) never attached to the culture substrate and died.

Discussion These results demonstrate that the protocol can be adapted to our iPSC line. We obtained a differentiation efficiency of 50% against 69.2%, which is not so distant. This is all the more encouraging that we can still test to optimize the seeding density as well as the CHIR concentration to improve our efficiency. Similarly, our failure at performing the magnetic separation is not final, as there are numerous parameters to optimize, therefore numerous possibilities of improvement.

Perspectives In the end, the endothelial differentiation was put to a hold because of the important cost of the differentiation products, as well as the important time required to optimize the Magnet-Activated Cell Sorting process. Moreover, as endothelial cells can accurately be modeled by HUVEC primary cells in our Alveoli-on-a-chip, there was no urgent need for a replacement. As both HUVEC and iPSC-derived endothelial cells are quite expensive and have a short life-span (below 6 passages), in the end, buying HUVEC appears as time-saving. We believe that it would be interesting to work on endothelial differentiation again if we work on differentiating iPSC towards specific alveolar-like endothelial cells.

Just in: latest techniques Recently published papers offer a novel approach: they add Matrigel to the induction medium in an effort to facilitate signaling cues for epithelial-to-mesenchymal transition, which occurs during gastrulation [197]. Combined with a two-step approach: Matrigel and Activin A followed by CHIR and BMP4 treatment, this technique greatly improves the mesodermal differentiation efficiency. Indeed, with this technique, Palpant and colleagues [198] reported over 90% CD31+.CD144+ cells by day 14 of differentiation, without the need of a sorting step. This novel and high-efficiency protocol seems very promising.
Our interest for iPSC-derived endothelial cells could rise again as a recent conference proceeding of the Canadian Cardiac Society (Ho & Stewart, September 2017) [199] announced that the culture of iPSC-derived endothelial cells with iPSC-derived lung progenitors helps promoting their differentiation to a distal epithelial state.

4.6.2 Alveolar differentiation

Original objectives In this experiment, we tried to reproduce and optimize the techniques developed by Huang *et al.* [15] to differentiate iPSC into alveolar epithelial cells. Our objective was to obtain a better model for alveolar cells, compared to the expensive and short-lifed primary cells or the cancerous A549 cell line. Moreover, such cells were expected to show more intense alveolar epithelium phenotypes such as widespread tight junctions and intense surfactant production.

Obtained results After 6 months of repeated differentiation experiments, we were able to master some handling techniques, to optimize some technical steps (such as Embryoid Bodies plating and dissociation, or the re-plating technique at Day 15), and to start to optimize given variable parameters (such as AFE patterning launch day, seeding densities or Retinoic Acid concentration) depending on our cell line. The protocol was optimized until Day 15, and tested until Day 26. In the end, we demonstrated our ability to obtain lung progenitor cells, with few contaminating cells.

Discussion This work is a proof of concept that the protocol developed by Huang *et al.* [15] can be used on Gibco's Episomal iPSC line. A fully optimized protocol should be obtained by successive testing of all variable parameters, but this will require some more time. Unfortunately, we did not have time to pursue the differentiation to its term. Still, we proved that the differentiation is possible and generates cells with crucial barrier phenotypes such as intercellular tight junctions. This confirms that using iPSC for our Alveoli-on-a-Chip would be an important improvement on the existing model.

4.6.3 *In situ* differentiation

The *in situ* differentiation was not a success for both cell types, however I believe that it could be an interesting improvement on our differentiation protocol. Indeed, after optimizing the differentiation protocol for our cell line in a dish, switching to a culture on the patch should help in inducing the maturation of the cells.

Indeed, for lung progenitor cells, the air-liquid interface culture was shown to improve the maturation into alveolar cells [185]. Moreover, as we have seen that during foetal development, the lungs and its associated capillary network grow in close contact, it could be interesting to observe if the maturation (or even the differentiation) *in situ* of both cell types together would help improving the differentiation delays or efficiency.

4.6.4 Conclusion

What we achieved here was the essential preliminary work required for our iPSC differentiation.

What came out of this work with iPSC, outside of the technical skills and the important knowledge in developmental biology, is an estimation of the amount of work and the time required to lead both differentiation experiments to a success. After over two years working on these protocols, we could estimate that optimizing each for culture on our patch is at least a 2 to 3-year work. And then we would have to start implementing the co-culture of both cell types and long-term survival in the microfluidic chip.

In conclusion, even though replacing our cells by differentiated iPSC should be a great improvement on our chip, it remains an tremendous challenge. Now that we have experienced the technical difficulties that come with iPSC culture and differentiation, we can rescale this project. Along with more time allowed for this research, I would also recommend an up-scaling in materials. Indeed, being able to verify our cell state with RT-pCR along the differentiation process seems a crucial tool to validate our work and save time.

Chapter 5

Conclusion

5.1 Achievements

This dissertation detailed our efforts in developing an innovative *in vitro* model of the alveolar capillary barrier, combining several state-of-the-art technologies: microfabrication, microfluidics and the direct differentiation of induced pluripotent stem cells.

We have developed a static *in vitro* model of the alveolar capillary barrier with a microengineered membrane and two cell lines (Chapter 2). This membrane reproduces the extra-cellular matrix of the alveoli by mimicking its dimensions (about 1 to 1.5 the *in vivo* alveolar diameter and 5 times its thickness) and its material properties (using gelatin as our biopolymer). To our knowledge, this membrane is the thinnest ever published for tissue modeling. We also achieved the long-term (over two months) culture of our mature alveolar capillary barrier, and were able to observe its accuracy in epitomizing specific barrier functions such as its selective permeability or the production of alveolar surfactant. Finally, a first experiment demonstrated its potential as a research tool for nanoparticle translocation.

Mechanical cues generated by the alveolar capillary barrier's microenvironment can play a role in nanoparticle translocation, therefore we believed that is was important to upgrade our model by reproducing these mechanical stimuli. We developed a specific microfluidic chip for this purpose. The **Alveoli-on-a-chip** is a reversible watertight chip that enables live microscopic observation at high magnitude (40x). We also demonstrated its capacity to support the dual stimuli, *i.e.* the continuous nutrient flow and the cyclic pressure variations.

Finally, we considered improving our cell models by using induced pluripotent stem cells instead of our immortalized cell lines. In order to do so, we started by working on the optimization of two protocols for the direct differentiation of iPSC into both an endothelium and an alveolar epithelium from a commercially available iPSC line. We also observed the behavior of iPSC on our microengineered patch.

5.2 Perspectives

The different elements of discussion of this manuscript have underlined different axes for research:

- **Endothelial functions** We had a hard time observing endothelial-specific functions such as a mature expression of PECAM1 and VE-Cadherin. This could be explained by culture conditions that not fit the endothelial cells. It might be improved by testing different Dexamethasone concentrations or by adding consistent shear stress on the endothelial cells.
- **Nanoparticle assays** Our translocation experiment was a preliminary work, but already showed interesting results. However, it would be interesting to repeat the experiment and analyze different parameters such as: the localization of nanoparticle internalization, the difference of translocation at 4 and 37 °C (passive or active transport), or the effect of the size, charge or coating of the nanoparticles.
- **Mechanical stretch** The Alveoli-on-a-chip enables cyclic stretching of our cell bilayer, but we still have to perform the test on live cells to observe their survival. Moreover, considering the pressure actually required to obtain physiological stretch levels, it will be crucial to increase the elasticity of the patch. This means testing different polymers or polymer compositions and assessing their deformation in the chip.

- **Shear stress** In order to obtain physiological levels of shear stress without using tantamount quantities of cell culture medium, tests should be performed with biocompatible compounds that could increase the viscosity of our medium.
- **iPSC differentiation** The protocols for direct differentiation of iPSC were not fully optimized. These experiments should be pursued with a systematic improvement of each step of the differentiation. When each protocol is optimized, we could start the *in situ* differentiation, moving in steps backwards from the maturation on the patch. This would allow to demonstrate whether our patch enhances the differentiation efficiency. It would also be interesting to study the effects of a co-differentiation with both cell types on the patch.

Bibliography

1. Lozano, R. *et al.* Global and regional mortality from 235 causes of death for 20 age groups in 1990 and 2010: A systematic analysis for the Global Burden of Disease Study 2010. *The Lancet* **380,** 2095–2128 (2012).
2. Ortiz, E. E.A.A. G. *Air quality in Europe — 2015 report* **5,** 1–64 (2015).
3. Ariyananda, P. L., Agnew, J. E. & Clarke, S. W. New techniques Aerosol delivery systems for bronchial asthma, 151–156 (1996).
4. Tsuda, A., Henry, F. S. & Butler, J. P. Particle Transport and Deposition : Basic Physics of Particle Kinetics. **3** (2013).
5. Mousseau, F., Le Borgne, R., Seyrek, E. & Berret, J. F. Biophysicochemical Interaction of a Clinical Pulmonary Surfactant with Nanoalumina. *Langmuir* **31,** 7346–7354 (2015).
6. Birukov, K. G. *et al.* Magnitude-dependent regulation of pulmonary endothelial cell barrier function by cyclic stretch. *American journal of physiology. Lung cellular and molecular physiology* **285,** L785–L797 (2003).
7. Huh, D. *et al.* BIOENGINEERING A Human Disease Model of Drug Toxicity – Induced Pulmonary Edema in a Lung-on-a-Chip Microdevice. **4** (2012).
8. Liu, L. *et al.* Nanofibrous gelatin substrates for long-term expansion of human pluripotent stem cells. *Biomaterials* **35,** 6259–6267 (2014).
9. Tang, Y., Liu, J. & Chen, Y. Agarose multi-wells for tumour spheroid formation and anti-cancer drug test. *Microelectronic Engineering* **158,** 41–45 (2016).
10. Collins, N. T. *et al.* Cyclic strain-mediated regulation of vascular endothelial occludin and ZO-1: Influence on intercellular tight junction assembly and function. *Arteriosclerosis, Thrombosis, and Vascular Biology* **26,** 62–68 (2006).
11. Tarbell, J. M. Shear stress and the endothelial transport barrier. *Cardiovascular Research* **87,** 320–330 (2010).
12. Huh, D., Matthews, B. D., Mammoto, A., Hsin, H. Y. & Ingber, D. E. Reconstituting Organ-Level Lung Functions on a Chip. **328,** 1662–1668 (2010).
13. Fredberg, J. J. & Kamm, R. D. Sress Transmission in the Lung: pathways from organ to molecule. *Annual Review of Physiology* **68,** 507–541 (2006).
14. Patsch, C. *et al.* Generation of vascular endothelial and smooth muscle cells from human pluripotent stem cells. *Nature Cell Biology* **17,** 994–1003 (2015).
15. Huang, S. X. L. *et al.* The in vitro generation of lung and airway progenitor cells from human pluripotent stem cells. *Nature Protocols* **10,** 413–425 (2015).
16. Lim, S. S. *et al.* A comparative risk assessment of burden of disease and injury attributable to 67 risk factors and risk factor clusters in 21 regions, 1990-2010: A systematic analysis for the Global Burden of Disease Study 2010. *The Lancet* **380,** 2224–2260 (2012).
17. Yang, W., Peters, J. I. & Williams, R. O. Inhaled nanoparticles-A current review. *International Journal of Pharmaceutics* **356,** 239–247 (2008).
18. Ali, I. & Jun, Y. J. Mathematical models for in-plane moduli of honeycomb structures - A review. *Research Journal of Applied Sciences, Engineering and Technology* **7,** 581–592 (2014).
19. Richard Drake, Wayne Vogl, A & Mitchell, A. W. M. *Gray's Anatomy* (2015).
20. Guyton, A. C. Measurement of the respiratory volumes of laboratory animals. *American Journal of Physiology* **150(1),** 70–77 (1947).
21. Douglas, C. G. & Haldane, J. S. The regulation of normal breathing. *The Journal of Physiology* **38,** 420–440 (1909).
22. Pelosi, P., Rocco, P. R. M., Negrini, D. & Passi, A. The extracellular matrix of the lung and its role in edema formation. *Anais da Academia Brasileira de Ciencias* **79,** 285–297 (2007).

23. Stone, V. *et al.* The role of oxidative stress in the prolonged inhibitory effect of ultrafine carbon black on epithelial cell function. *Toxicology in Vitro* **12,** 649–659 (1998).
24. Brown, D. M., Wilson, M. R., MacNee, W., Stone, V. & Donaldson, K. Size-dependent proinflammatory effects of ultrafine polystyrene particles: A role for surface area and oxidative stress in the enhanced activity of ultrafines. *Toxicology and Applied Pharmacology* **175,** 191–199 (2001).
25. Brown, D. M. Calcium and ROS-mediated activation of transcription factors and TNF- cytokine gene expression in macrophages exposed to ultrafine particles. *AJP: Lung Cellular and Molecular Physiology* **286,** 344L–353 (2004).
26. Vos, T, Allen, C, Arora, M & Zuhlke, L. J. Global, regional, and national incidence, prevalence, and years lived with disability for 310 diseases and injuries, 1990–2015: a systematic analysis for the Global Burden of Disease Study 2015. *The Lancet* **388,** 1545–1602 (2016).
27. Springmann, M., Godfray, H. C. J., Rayner, M. & Scarborough, P. Analysis and valuation of the health and climate change cobenefits of dietary change. *Proceedings of the National Academy of Sciences* **113,** 4146–4151 (2016).
28. DiMasi, J. A., Grabowski, H. G. & Hansen, R. W. Innovation in the pharmaceutical industry: New estimates of R&D costs. *Journal of Health Economics* **47,** 20–33 (2016).
29. Bhatia, S. N. & Ingber, D. E. Microfluidic organs-on-chips. *Nature biotechnology* **32,** 760–772 (2014).
30. Benam, K. H. *et al.* Engineered In Vitro Disease Models. *Annual Review of Pathology: Mechanisms of Disease* **10,** 195–262 (2015).
31. Ward, H. E. & Nicholas, T. E. Alveolar type I and type II cells. *Internal Journal of Medicine* **14,** 731–734 (1984).
32. Fehrenbach, H. Alveolar epithelial type II cell: defender of the alveolus revisited. *Respiratory research* **2,** 33–46 (2001).
33. Ghaedi, M. *et al.* Technical advance Human iPS cell – derived alveolar epithelium repopulates lung extracellular matrix. *Journal of Clinical . . .* **123,** 4950 (2013).
34. Hermanns, M. I., Unger, R. E., Kehe, K., Peters, K. & Kirkpatrick, C. J. Lung epithelial cell lines in coculture with human pulmonary microvascular endothelial cells: development of an alveolo-capillary barrier in vitro. *Laboratory Investigation* **84,** 736–752 (2004).
35. Chang, M. M. J., Shih, L. & Wu, R. Pulmonary Epithelium: Cell Types and Functions. *The Pulmonary Epithelium in Health and Disease,* 1–26 (2008).
36. Caminiti, S. P. & Young, S. L. The pulmonary surfactant system. *Hospital practice (Office ed.)* **26,** 87–90,94–100 (1991).
37. Kuroki, K & Voelker, D. R. Pulmonary Surfactant Proteins. *Journal of biological chemistry* **269,** 25943–25946 (1994).
38. Hermans, C. & Bernard, A. State of the Art Lung Epithelium – specific Proteins Characteristics and Potential Applications as Markers. *Am J Respir Crit Care Med* **159,** 646–78 (1999).
39. McLennan, G & DeYoung, N. The pulmonary alveolar macrophage. *Internal Journal of Medicine* **14,** 721–730 (1984).
40. Sumpio, B. E., Timothy Riley, J. & Dardik, A. Cells in focus: Endothelial cell. *International Journal of Biochemistry and Cell Biology* **34,** 1508–1512 (2002).
41. Lieber, M, Smith, B, Szakal, a, Nelson-Rees, W & Todaro, G. A continuous tumor-cell line from a human lung carcinoma with properties of type II alveolar epithelial cells. *International journal of cancer. Journal international du cancer* **17,** 62–70 (1976).
42. Salomon, J. J. *et al.* The Cell Line NCl-H441 Is a Useful in Vitro Model for Transport Studies of Human Distal Lung Epithelial Barrier (2014).
43. Swain, R. J., Kemp, S. J., Goldstraw, P., Tetley, T. D. & Stevens, M. M. Assessment of Cell Line Models of Primary Human Cells by Raman Spectral Phenotyping. *Biophysical Journal* **98,** 1703–1711 (2010).
44. Kondo, H., Miyoshi, K., Sakiyama, S., Tangoku, A. & Noma, T. Differential Regulation of Gene Expression of Alveolar Epithelial Cell Markers in Human Lung Adenocarcinoma-Derived A549 Clones. *Stem Cells International* **2015** (2015).
45. George, I., Vranic, S., Boland, S., Courtois, A. & Baeza-Squiban, A. Development of an in vitro model of human bronchial epithelial barrier to study nanoparticle translocation. *Toxicology in Vitro* **29,** 51–58 (2015).

46. Gonzales, L. W., Guttentag, S. H., Wade, K. C., Postle, A. D. & Ballard, P. L. Differentiation of human pulmonary type II cells in vitro by glucocorticoid plus cAMP. *American Journal of Physiology. Lung Cellular and Molecular Physiology* **283,** L940–L951 (2002).
47. Wang, J. *et al.* Differentiated human alveolar epithelial cells and reversibility of their phenotype in vitro. *American Journal of Respiratory Cell and Molecular Biology* **36,** 661–668 (2007).
48. Rothen-Rutishauser, B. M., Kiama, S. G. & Gehr, P. A Three-Dimensional Cellular Model of the Human Respiratory Tract to Study the Interaction with Particles. *American Journal of Respiratory Cell and Molecular Biology* **32,** 281–289 (2005).
49. Klein, S. G., Serchi, T., Hoffmann, L., Blömeke, B. & Gutleb, A. C. An improved 3D tetraculture system mimicking the cellular organisation at the alveolar barrier to study the potential toxic effects of particles on the lung. *Particle and Fibre Toxicology* **10** (2013).
50. Alfaro-Moreno, E. *et al.* Co-cultures of multiple cell types mimic pulmonary cell communication in response to urban PM10. *European Respiratory Journal* **32,** 1184–1194 (2008).
51. Foster, K. A., Oster, C. G., Mayer, M. M., Avery, M. L. & Audus, K. L. Characterization of the A549 Cell Line as a Type II Pulmonary Epithelial Cell Model for Drug Metabolism. *Exp Cell Res* **243,** 359–366 (1998).
52. Bitterle, E. *et al.* Dose-controlled exposure of A549 epithelial cells at the air-liquid interface to airborne ultrafine carbonaceous particles. *Chemosphere* **65,** 1784–1790 (2006).
53. Hermanns, M. I. *et al.* Primary human coculture model of alveolo-capillary unit to study mechanisms of injury to peripheral lung. *Cell and Tissue Research* **336,** 91–105 (2009).
54. Kasper, J. *et al.* Inflammatory and cytotoxic responses of an alveolar-capillary coculture model to silica nanoparticles: Comparison with conventional monocultures. *Particle and Fibre Toxicology* **8,** 1–16 (2011).
55. Kasper, J. Y. *et al.* Pulmonary surfactant augments cytotoxicity of silica nanoparticles: Studies on an in vitro air-blood barrier model. *Beilstein Journal of Nanotechnology* **6,** 517–528 (2015).
56. Brandenberger, C. *et al.* Effects and uptake of gold nanoparticles deposited at the air-liquid interface of a human epithelial airway model. *Toxicology and Applied Pharmacology* **242,** 56–65 (2010).
57. Dekali, S. *et al.* Assessment of an in vitro model of pulmonary barrier to study the translocation of nanoparticles. *Toxicology Reports* **1,** 157–171 (2014).
58. Douville, N. J. Alveolar Microfluidic Systems for the Study of Barrier Function, Cell Damage, and Migration at the Air-Blood Barrier by Nicholas J. Douville (2011).
59. Nalayanda, D. D. *et al.* An open-access microfluidic model for lung-specific functional studies at an air-liquid interface. *Biomedical Microdevices* **11,** 1081–1089 (2009).
60. Higuita-Castro, N. *et al.* Using a Novel Microfabricated Model of the Alveolar-Capillary Barrier to Investigate the Effect of Matrix Structure on Atelectrauma. *Scientific Reports* **7,** 1–13 (2017).
61. Yang, X. *et al.* Nanofiber Membrane supported lung-on-a-chip Microdevice for Anti-cancer Drug Testing. *Lab on a Chip* (2018).
62. Srinivasan, B. *et al.* TEER Measurement Techniques for In Vitro Barrier Model Systems. *Journal of Laboratory Automation* **20,** 107–126 (2015).
63. Tang, Y. *Design and fabrication of advanced microdevices for stem cell and cancer cell studies (Doctoral dissertation, Université Pierre et Marie Curie-Paris VI).* PhD thesis (University Pierre et Marie Curie, 2016).
64. Nguyen, M., Arkell, J. & Jackson, C. J. Human endothelial gelatinases and angiogenesis. *International Journal of Biochemistry and Cell Biology* **33,** 960–970 (2001).
65. Belot, N *et al.* Molecular characterization of cell substratum attachments in human glial tumors related to prognostic features. *Glia* **36,** 375–390 (2001).
66. Lu, P., Weaver, V. M. & Werb, Z. The extracellular matrix: A dynamic niche in cancer progression. *Journal of Cell Biology* **196,** 395–406 (2012).
67. Hawkins, F. *et al.* Prospective isolation of NKX2-1–expressing human lung progenitors derived from pluripotent stem cells. *Journal of Clinical Investigation* **258,** 169–184 (2017).
68. Uchida, T. *et al.* Receptor for advanced glycation end-products is a marker of type I cell injury in acute lung injury. *American Journal of Respiratory and Critical Care Medicine* **173,** 1008–1015 (2006).
69. McElroy, M. C. & Kasper, M. The use of alveolar epithelial type I cell-selective markers to investigate lung injury and repair. *European Respiratory Journal* **24,** 664–673 (2004).
70. Sun, S. W. *et al.* Caveolae and caveolin-1 mediate endocytosis and transcytosis of oxidized low density lipoprotein in endothelial cells. *Acta Pharmacologica Sinica* **31,** 1336–1342 (2010).

71. Ren, H., Birch, N. P. & Suresh, V. An optimised human cell culture model for alveolar epithelial transport. *PLoS ONE* **11,** 1–22 (2016).
72. Croce, M. V., Colussi, A. G., Price, M. R. & Segal-Eiras, A. Identification and characterization of different subpopulations in a human lung adenocarcinoma cell line (A549). *Pathology oncology research : POR* **5,** 197–204 (1999).
73. Wallez, Y. & Huber, P. Endothelial adherens and tight junctions in vascular homeostasis, inflammation and angiogenesis. *Biochimica et Biophysica Acta - Biomembranes* **1778,** 794–809 (2008).
74. Müller, A. M. *et al.* Expression of the Endothelial Markers PECAM-1, vWf, and CD34 in Vivo and in Vitro. *Experimental and Molecular Pathology* **72,** 221–229 (2002).
75. Pummi, K. *et al.* Epidermal tight junctions: ZO-1 and occludin are expressed in mature, developing, and affected skin and in vitro differentiating keratinocytes. *Journal of Investigative Dermatology* **117,** 1050–1058 (2001).
76. Anderson, J. M. & Vanitallie, C. M. Tight junctions and the molecular basis for regulation of paracellular permeability. *American Journal of Physiology - Gastrointestinal & Liver Physiology* **32,** G 467–G 475 (1995).
77. Hu, Y. J., Wang, Y. D., Tan, F. Q. & Yang, W. X. Regulation of paracellular permeability: Factors and mechanisms. *Molecular Biology Reports* **40,** 6123–6142 (2013).
78. Grathwohl, P. *Diffusion in Natural Porous Media: Contaminant transport, sorption/desorption and dissolution kinetics* Kluwer Aca (1998).
79. Van Brakel, J. & Heertjes, P. M. Analysis of diffusion in macroporous media in terms of a porosity, a tortuosity and a constrictivity factor. *International Journal of Heat and Mass Transfer* **17,** 1093–1103 (1974).
80. Hornung, V. *et al.* Silica crystals and aluminum salts activate the NALP3 inflammasome through phagosomal destabilization. *Nature Immunology* **9,** 847–856 (2008).
81. Kim, S, Ohulchanskyy, T. Y., Pudavar, H. E., Pandey, R. K. & Prasad, P. N. Organically mod silica nanoparticle co-encapsulating photosensitizing drug & aggregation-enhanced 2-photon absorbing fluorescent dye aggregate for TPA two-photon photodynamic therapy. *Journal of the American Chemical Society* **129,** 2669–2675 (2007).
82. Alessandrini, F. *et al.* Pro-Inflammatory versus Immunomodulatory Effects of Silver Nanoparticles in the Lung: The Critical Role of Dose, Size and Surface Modification. *Nanomaterials* (2017).
83. Murugadoss, S. *et al.* Toxicology of silica nanoparticles: an update. *Archives of Toxicology* **91,** 2967–3010 (2017).
84. Shapero, K. *et al.* Time and space resolved uptake study of silica nanoparticles by human cells. *Molecular BioSystems* **7,** 371–378 (2011).
85. Tsuda, Akira, P. G. *Nanoparticles in the Lung* **c,** 29–32 (2015).
86. Mousseau, F. *et al.* Supported pulmonary surfactant bilayers on silica nanoparticles: Formulation, stability and impact on lung epithelial cells. *Nanoscale* **9,** 14967–14978 (2017).
87. A., L. & A., S. Effects of the Presence or Absence of a Protein Corona on Silica Nanoparticle Uptake and Impact on Cells. *ACS Nano* **6,** 5845 (2012).
88. Lesniak, A. *et al.* Nanoparticle adhesion to the cell membrane and its effect on nanoparticle uptake efficiency. *Journal of the American Chemical Society* **135,** 1438–1444 (2013).
89. Kumar, A. *et al.* Enrichment of immunoregulatory proteins in the biomolecular corona of nanoparticles within human respiratory tract lining fluid. *Nanomedicine: Nanotechnology, Biology, and Medicine* **12,** 1033–1043 (2016).
90. Gasser, M. *et al.* Pulmonary surfactant coating of multi-walled carbon nanotubes (MWCNTs) influences their oxidative and pro-inflammatory potential in vitro. *Particle and Fibre Toxicology* **9,** 1–13 (2012).
91. Gross, T, Zmora, E, Regev, O & Berman, A. Lung-Surfactant - Meconium Interaction : In Vitro Study in Bulk and at the Air - Solution Interface, 3243–3250 (2006).
92. Le Bihan, O. *et al.* Cryo-electron tomography of nanoparticle transmigration into liposome. *Journal of Structural Biology* **168,** 419–425 (2009).
93. Vranic, S. *et al.* Internalization of SiO2 nanoparticles by alveolar macrophages and lung epithelial cells and its modulation by the lung surfactant substitute Curosurf®. *Environmental Science and Pollution Research* **20,** 2761–2770 (2013).
94. Wohlleben, W. *et al.* Influence of agglomeration and specific lung lining lipid/protein interaction on short-term inhalation toxicity. *Nanotoxicology* **10,** 970–980 (2016).

95. Sanchez, A. *et al.* Silica nanoparticles inhibit the cation channel TRPV4 in airway epithelial cells. *Particle and Fibre Toxicology* **14,** 11–19 (2017).
96. Napierska, D. *et al.* Size-Dependent Cytotoxicity of Monodisperse Silica Nanoparticles in Human Endothelial Cells. *Small* **5,** 846–853 (2009).
97. Mu, Q. *et al.* Mechanism of cellular uptake of genotoxic silica nanoparticles. *Particle and Fibre Toxicology* **9,** 29 (2012).
98. Kletting, S. *et al.* Co-culture of human alveolar epithelial (hAELVi) and macrophage (THP-1) cell lines. *ALTEX Online* **35,** 1–11 (2017).
99. Wilhelm, C., Gazeau, F., Roger, J., Pons, J. N. & Bacri, J. C. Interaction of anionic superparamagnetic nanoparticles with cells: Kinetic analyses of membrane adsorption and subsequent internalization. *Langmuir* **18,** 8148–8155 (2002).
100. Stucki, A. O. *et al.* A lung-on-a-chip array with an integrated bio-inspired respiration mechanism. *Lab Chip* **15,** 1302–1310 (2015).
101. Salvati, A. *et al.* Experimental and theoretical comparison of intracellular import of polymeric nanoparticles and small molecules: Toward models of uptake kinetics. *Nanomedicine: Nanotechnology, Biology, and Medicine* **7,** 818–826 (2011).
102. Sinha, R. *et al.* Endothelial cell alignment as a result of anisotropic strain and flow induced shear stress combinations. *Scientific Reports* **6,** 29510 (2016).
103. Greek, R. & Menache, A. Systematic reviews of animal models: Methodology versus epistemology. *International Journal of Medical Sciences* **10,** 206–221 (2013).
104. Yamada, K. M. & Cukierman, E. Modeling Tissue Morphogenesis and Cancer in 3D. *Cell* **130,** 601–610 (2007).
105. Ehrmann, R.L. & Gey, G. The growth of cells on a transparent gel of reconstituted rat-tail collagen. *J. Natl. Cancer Inst.* **16,** 1375–1403 (1956).
106. Sato, T. & Clevers, H. Growing self-organizing mini-guts from a single intestinal stem cell: mechanisms and applications. *Science* **340,** 1190–1194 (2013).
107. Pampaloni, F., Reynaud, E. G. & Stelzer, E. H. K. The third dimension bridges the gap between cell culture and live tissue. *Nature reviews. Molecular cell biology* **8,** 839–845 (2007).
108. Wrzesinski, K. *et al.* HepG2/C3A 3D spheroids exhibit stable physiological functionality for at least 24 days after recovering from trypsinisation. *Toxicology Research* **2,** 163 (2013).
109. Mammoto, T., Mammoto, A. & Ingber, D. Mechanobiology and developmental control. . *Annu. Rev. Cell Dev. Biol* **29,** 27–61 (2013).
110. Bhise, N. S. *et al.* Organ-on-a-chip platforms for studying drug delivery systems. *Journal of Controlled Release* **190,** 82–93 (2014).
111. Kim, S.-H., Lee, G.-H., Park, J. Y. & Lee, S.-H. Microplatforms for Gradient Field Generation of Various Properties and Biological Applications. *Journal of Laboratory Automation* **20,** 82–95 (2014).
112. Braakhuis, H. M. *et al.* Progress and future of in vitro models to study translocation of nanoparticles. *Archives of Toxicology* **89,** 1469–1495 (2015).
113. Nemmar, A., Holme, J. A., Rosas, I., Schwarze, P. E. & Alfaro-Moreno, E. Recent advances in particulate matter and nanoparticle toxicology: A review of the in vivo and in vitro studies. *BioMed Research International* **2013** (2013).
114. Wick, P. *et al.* In vitro-ex vivo model systems for nanosafety assessment. *European Journal of Nanomedicine* **7,** 169–179 (2015).
115. Huh, D. *et al.* A Human Disease Model of Drug Toxicity-Induced Pulmonary Edema in a Lung-on-a-Chip Microdevice. *Science Translational Medicine* **4,** 159ra147–159ra147 (2012).
116. Nalayanda, D. D., Wang, Q., Fulton, W. B., Wang, T.-H. & Abdullah, F. Engineering an artificial alveolar-capillary membrane: a novel continuously perfused model within microchannels. *Journal of Pediatric Surgery* **45,** 45–51 (2010).
117. Mermoud, Y., Felder, M., Stucki, J. D., Stucki, A. O. & Guenat, O. T. Microimpedance tomography system to monitor cell activity and membrane movements in a breathing lung-on-chip. *Sensors and Actuators, B: Chemical* **255,** 3647–3653 (2018).
118. Benam, K. H. *et al.* Matched-Comparative Modeling of Normal and Diseased Human Airway Responses Using a Microengineered Breathing Lung Chip. *Cell Systems* **3,** 456–466.e4 (2016).
119. Jain, A. *et al.* A primary human lung alveolus-on-a-chip model of intravascular thrombosis for assessment of therapeutics. *Clinical Pharmacology & Therapeutics* **(in press)** (2017).

120. Tsou, J. K. *et al.* Spatial Regulation of Inflammation by Human Aortic Endothelial Cells in a Linear Gradient of Shear Stress. *Microcirculation* **15,** 311–323 (2008).
121. Hassell, B. A. *et al.* Human Organ Chip Models Recapitulate Orthotopic Lung Cancer Growth, Therapeutic Responses, and Tumor Dormancy In Vitro. *Cell Reports* **21,** 508–516 (2017).
122. Huh, D. *et al.* Acoustically detectable cellular-level lung injury induced by fluid mechanical stresses in microfluidic airway systems. *Proceedings of the National Academy of Sciences* **104,** 18886–18891 (2007).
123. Nath, P. & Huang, J.-H. *Microfluidic aspirator and methods of making and using the same* 2017.
124. Benam, K. H. *et al.* Small airway-on-a-chip enables analysis of human lung inflammation and drug responses in vitro. *Nature Methods* **13,** 151–157 (2016).
125. Walter, F. R. *et al.* A versatile lab-on-a-chip tool for modeling biological barriers. *Sensors and Actuators, B: Chemical* **222,** 1209–1219 (2016).
126. Huang, Y., Doerschuk, C. M. & Kamm, R. D. Computational modeling of RBC and neutrophil transit through the pulmonary capillaries. *Journal of Applied Physiology* **90,** 545–564 (2001).
127. Burrowes, K. S. & Tawhai, M. H. Computational predictions of pulmonary blood flow gradients: Gravity versus structure. *Respiratory Physiology and Neurobiology* **154,** 515–523 (2006).
128. Usami, S., Chen, H. H., Zhao, Y., Chien, S. & Skalak, R. Design and construction of a linear shear stress flow chamber. *Annals of Biomedical Engineering* **21,** 77–83 (1993).
129. Avari, H., Rogers, K. A. & Savory, E. Wall Shear Stress Determination in a Small-Scale Parallel Plate Flow Chamber Using Laser Doppler Velocimetry Under Laminar, Pulsatile and Low-Reynolds Number Turbulent Flows. *Journal of Fluids Engineering* **140,** 61404 (2018).
130. Sondergaard, S. *et al.* The dynostatic algorithm accurately calculates alveolar pressure on-line during ventilator treatment in children. *Paediatric Anaesthesia* **13,** 294–303 (2003).
131. Escolar, J. & Escolar, A. Lung hysteresis: a morphological view. *Histology and histopathology* **19,** 159–166 (2004).
132. Roan, E. & Waters, C. M. What do we know about mechanical strain in lung alveoli? *American journal of physiology. Lung cellular and molecular physiology* **301,** L625–35 (2011).
133. Tschumperlin, D. J., Oswari, J. & Margulies, S. S. Deformation-Induced Injury of Alveolar Epithelial Cells Effect of Frequency , Duration , and Amplitude. *Am J Physiol Lung Cell Mol Physiol* **162,** 357–362 (2000).
134. Hermansen, C. & Lorah, K. Respiratory distress in the newborn. *Am Fam Physician* **76,** 987–994 (2007).
135. Westaby, S. Mechanisms of membrane damage and surfactant depletion in acute lung injury. *Intensive Care Med* **12,** 2–5 (1986).
136. Schomburg, W. K. Introduction to Microsystem Design. **1** (2011).
137. Takahashi, K. *et al.* Induction of Pluripotent Stem Cells from Adult Human Fibroblasts by Defined Factors. *Cell* **131,** 861–872 (2007).
138. Yu, J, Vodyanik, M. & Smuga-Otto, K. Induced pluripotent stem cell lines derived from human somatic cells. *Science* **318,** 1917–1920 (2007).
139. Nakayama, C., Fujita, Y., Matsumura, W., Ujiie, I. & Shimizu, H. The development of induced pluripotent stem cell-derived mesenchymal stem / stromal cells from normal human and RDEB epidermal keratinocytes. *Journal of Dermatological Science* (2018).
140. Hokayem, J. E., Cukier, H. N. & Dykxhoorn, D. M. Blood Derived Induced Pluripotent Stem Cells (iPSCs): Benefits, Challenges and the Road Ahead. *Journal of Alzheimer's Disease & Parkinsonism* **6** (2016).
141. Shi, L., Cui, Y., Luan, J., Zhou, X. & Han, J. Urine-derived induced pluripotent stem cells as a modeling tool to study rare human diseases. *Intractable & Rare Diseases Research* **5,** 192–201 (2016).
142. Noggle, S. *et al.* Human oocytes reprogram somatic cells to a pluripotent state. *Nature* **478,** 70–5 (2011).
143. Tachibana, M. *et al.* Human embryonic stem cells derived by somatic cell nuclear transfer. *Cell* **153,** 1228–1238 (2013).
144. Do, J. T. *et al.* Erasure of cellular memory by fusion with pluripotent cells. *Stem cells (Dayton, Ohio)* **25,** 1013–20 (2007).
145. Zhou, H. *et al.* Generation of Induced Pluripotent Stem Cells Using Recombinant Proteins. *Cell Stem Cell* **4,** 381–384 (2009).
146. Miyoshi, N. *et al.* Reprogramming of mouse and human cells to pluripotency using mature microRNAs. *Cell Stem Cell* **8,** 633–638 (2011).

147. Trounson, A. & DeWitt, N. D. Pluripotent stem cells progressing to the clinic. *Nature Reviews Molecular Cell Biology* **17,** 194–200 (2016).
148. Burri, P. H. Fetal and postnatal development of the lung. *Annual review of physiology* **46,** 617–628 (1984).
149. Snoeck, H.-W. in *Stem Cells in the Lung: Development, Repair and Regeneration* 268–285 (2015).
150. Schneeberger, E. E., Walters, D. V. & Olver, R. E. Development of intercellular junctions in the pulmonary epithelium of the foetal lamb. *Journal of cell science* **32,** 307–24 (1978).
151. Chen, G. *et al.* Chemically defined conditions for human iPS cell derivation and culture. *Nature Methods* **8,** 424–429 (2011).
152. Yang, L. *et al.* Human cardiovascular progenitor cells develop from a KDR+ embryonic-stem-cell-derived population. *Nature* **453,** 524–528 (2008).
153. Sumi, T., Tsuneyoshi, N., Nakatsuji, N. & Suemori, H. Defining early lineage specification of human embryonic stem cells by the orchestrated balance of canonical Wnt/ -catenin, Activin/Nodal and BMP signaling. *Development* **135,** 2969–2979 (2008).
154. Woll, P. S. *et al.* Wnt signaling promotes hematoendothelial cell development from human embryonic stem cells. *Differentiation* **111,** 122–131 (2008).
155. Yamamizu, K., Kawasaki, K., Katayama, S., Watabe, T. & Yamashita, J. K. Enhancement of vascular progenitor potential by protein kinase a through dual induction of Flk-1 and Neuropilin-1. *Blood* **114,** 3707–3716 (2009).
156. Tatsumi, R., Suzuki, Y., Sumi, T. & Sone, M. Simple and Highly Efficient Method for Production of Endothelial Cells From Human Embryonic Stem Cells. **20,** 1423–1430 (2011).
157. Orlova, V. V. *et al.* Generation, expansion and functional analysis of endothelial cells and pericytes derived from human pluripotent stem cells. *Nature Protocols* **9,** 1514–1531 (2014).
158. Lian, X. *et al.* Efficient differentiation of human pluripotent stem cells to endothelial progenitors via small-molecule activation of WNT signaling. *Stem Cell Reports* **3,** 804–816 (2014).
159. Liu, X. *et al.* Differentiation of functional endothelial cells from human induced pluripotent stem cells: A novel, highly efficient and cost effective method. *Differentiation* **92,** 225–236 (2016).
160. Sahara, M. *et al.* Manipulation of a VEGF-Notch signaling circuit drives formation of functional vascular endothelial progenitors from human pluripotent stem cells. *Cell Research* **24,** 820–841 (2014).
161. Teo, A. K. K. *et al.* Activin and BMP4 synergistically promote formation of definitive endoderm in human embryonic stem cells. *Stem Cells* **30,** 631–642 (2012).
162. Kim, M. S. *et al.* Activin-A and Bmp4 levels modulate cell type specification during CHIR-induced cardiomyogenesis. *PLoS ONE* **10,** 1–16 (2015).
163. Winnier G, Blessing M, Labosky P, H. B. Bone morphogenetic protein-4 is required for mesoderm formation and patterning in the mouse. *Genes & Development,* 2105–2116 (1995).
164. Meijer, L., Skaltsounis, A.-L., Magiatis, P., Polychronopoulos, P. & Knockaert, M. GSK-3-Selective Inhibitors Derived from Tyrian Purple Indirubins. *Cutis* **93,** 43–46 (2014).
165. Mima, T, Ueno, H, Fischman, D. A., Williams, L. T. & Mikawa, T. Fibroblast growth factor receptor is required for in vivo cardiac myocyte proliferation at early embryonic stages of heart development. *Proceedings of the National Academy of Sciences of the United States of America* **92,** 467–471 (1995).
166. Fabian, M. A. *et al.* A small molecule-kinase interaction map for clinical kinase inhibitors. *Nature Biotechnology* **23,** 329–336 (2005).
167. Lian, X. *et al.* Cozzarelli Prize Winner: Robust cardiomyocyte differentiation from human pluripotent stem cells via temporal modulation of canonical Wnt signaling. *Proceedings of the National Academy of Sciences* **109,** E1848–E1857 (2012).
168. Fedi, P. *et al.* Cell biology and metabolism : Isolation and Biochemical Characterization of the Human Dkk-1 Homologue , a Novel Inhibitor of Mammalian Wnt Signaling Isolation and Biochemical Characterization of the Human Dkk-1 Homologue , a Novel Inhibitor of Mammalian W. **274,** 19465–19472 (1999).
169. Soker, S. *et al.* Neuropilin-1 Is Expressed by Endothelial and Tumor Cells as an Isoform-Specific Receptor for Vascular Endothelial Growth Factor. *Cell* **92,** 735–745 (1998).
170. Wang, J. *et al.* Bone marrow mononuclear cell transplantation promotes therapeutic angiogenesis via upregulation of the VEGF-VEGFR2 signaling pathway in a rat model of vascular dementia. *Behavioural Brain Research* **265,** 171–180 (2014).

171. Watanabe, K. *et al.* A ROCK inhibitor permits survival of dissociated human embryonic stem cells. *Nature Biotechnology* **25,** 681–686 (2007).

172. Ungrin, M. D. *et al.* Rational bioprocess design for human pluripotent stem cell expansion and endoderm differentiation based on cellular dynamics. *Biotechnology and Bioengineering* **109,** 853–866 (2012).

173. Green, M. D. *et al.* Generation of anterior foregut endoderm from human embryonic and induced pluripotent stem cells. *Nature Biotechnology* **29,** 267–272 (2011).

174. Nostro, M. C. *et al.* Stage-specific signaling through TGF family members and WNT regulates patterning and pancreatic specification of human pluripotent stem cells. *Development* **138,** 861–871 (2011).

175. Gouon-Evans, V. *et al.* BMP-4 is required for hepatic specification of mouse embryonic stem cell-derived definitive endoderm. *Nature biotechnology* **24,** 1402–1411 (2006).

176. D'Amour, K. A. *et al.* Efficient differentiation of human embryonic stem cells to definitive endoderm. *Nature Biotechnology* **23,** 1534–1541 (2005).

177. Gadue, P., Huber, T. L., Paddison, P. J. & Keller, G. M. Wnt and TGF-beta signaling are required for the induction of an in vitro model of primitive streak formation using embryonic stem cells. *Proceedings of the National Academy of Sciences* **103,** 16806–16811 (2006).

178. Sherwood, R. I., Chen, T. Y. A. & Melton, D. A. Transcriptional dynamics of endodermal organ formation. *Developmental Dynamics* **238,** 29–42 (2009).

179. Xu, X., Browning, V. L. & Odorico, J. S. Activin, BMP and FGF pathways cooperate to promote endoderm and pancreatic lineage cell differentiation from human embryonic stem cells. *Mechanisms of Development* **128,** 412–427 (2011).

180. Huang, S. X. L. *et al.* Efficient generation of lung and airway epithelial cells from human pluripotent stem cells. *Nature Biotechnology* **32,** 84–91 (2013).

181. Firth, A. L. *et al.* Generation of multiciliated cells in functional airway epithelia from human induced pluripotent stem cells. *Proceedings of the National Academy of Sciences* **111,** E1723–E1730 (2014).

182. Gotoh, S. *et al.* Generation of alveolar epithelial spheroids via isolated progenitor cells from human pluripotent stem cells. *Stem Cell Reports* **3,** 394–403 (2014).

183. Longmire, T. A. *et al.* Efficient derivation of purified lung and thyroid progenitors from embryonic stem cells. *Cell Stem Cell* **10,** 398–411 (2012).

184. Perea-Gomez, A. *et al.* Nodal antaginists in the anterior visceral endoderm prevent the formation of multiple primitive streaks. *Developmental Cell* **3,** 745–756 (2002).

185. Wong, A. P. *et al.* Directed differentiation of human pluripotent stem cells into mature airway epithelia expressing functional CFTR protein. *Nature Biotechnology* **30,** 876–882 (2012).

186. Domyan, E. T. *et al.* Signaling through BMP receptors promotes respiratory identity in the foregut via repression of Sox2. *Development* **138,** 971–981 (2011).

187. Weaver, M, Dunn, N. R. & Hogan, B. L. M. Bmp4 and Fgf10 play opposing roles during lung bud morphogenesis. *Development* **127,** 2695–2704 (2000).

188. Malpel, S, Mendelsohn, C & Cardoso, W. V. Regulation of retinoic acid signaling during lung morphogenesis. *Development (Cambridge, England)* **127,** 3057–67 (2000).

189. Bock, C. *et al.* Reference maps of human es and ips cell variation enable high-throughput characterization of pluripotent cell lines. *Cell* **144,** 439–452 (2011).

190. Boulting, G. L. *et al.* A functionally characterized test set of human induced pluripotent stem cells. *Nat Biotechnol* **29,** 279–286 (2011).

191. Desai, T. J., Brownfield, D. G. & Krasnow, M. A. Alveolar progenitor and stem cells in lung development, renewal and cancer. *Nature* **507,** 190–194 (2014).

192. Buisson, A., Zahm, J. & Polette, M. Gelatinase B is involved in the in vitro wound repair of human respiratory epithelium. *J Cell Physiol.* **166,** 413–426 (1996).

193. Amantea, D., Corasaniti, M. T., Mercuri, N. B., Bernardi, G. & Bagetta, G. Brain regional and cellular localization of gelatinase activity in rat that have undergone transient middle cerebral artery occlusion. *Neuroscience* **152,** 8–17 (2008).

194. Watanabe, Y., Haruyama, T. & Akaike, T. Liver-derived matrix metalloproteinase-9 (gelatinase B) recruits progenitor cells from bone marrow into the blood circulation. *Biological & pharmaceutical bulletin* **26,** 564–8 (2003).

195. Silva, E. J.N. L. *et al.* Evaluation of cytotoxicity and up-regulation of gelatinases in human fibroblast cells by four root canal sealers. *International Endodontic Journal* **45,** 49–56 (2012).

196. Meade-Tollin, L. C., Way, D. & Witte, M. H. Expression of multiple matrix metalloproteinases and urokinase type plasminogen activator in cultured Kaposi sarcoma cells. *Acta Histochemica* **101,** 305–316 (1999).
197. Zhang, F. *et al.* Optimizing mesoderm progenitor selection and three-dimensional microniche culture allows highly efficient endothelial differentiation and ischemic tissue repair from human pluripotent stem cells. *Stem Cell Research & Therapy* **8,** 6 (2017).
198. Palpant, N. J. *et al.* Generating high-purity cardiac and endothelial derivatives from patterned mesoderm using human pluripotent stem cells. *Nature Protocols* **12,** 15–31 (2016).
199. Ho, M. & Stewart, D. *Endothelial Cells Promote Distal Airway Patterning of Human Ipsc-Derived Lung Progenitors* in *Canadian Journal of Cardiology* **33** (2017), S51.
200. Yoshioka, N. *et al.* Efficient Generation of Human iPS Cells by a Synthetic Self- Replicative RNA. *Cell Stem Cell* **13,** 1–21 (2013).
201. Hou, P. *et al.* Pluripotent Stem Cells Induced from Mouse Somatic Cells by Small-Molecule Compounds. *Science* **341,** 651–654 (2013).

Chapter 6

Appendix

6.1 Protocols

6.1.1 Cell culture

a. A549

Cell origin The **A549** cells used are Human caucasian lung adenocarcinoma obtained from Sigma-Aldrich (Ref. 86012804) and were received at passage 91. After proliferation, the cells were frozen at passages 93, 94 and 96 for further use. These cells were used in experiments below passage 100.

Cell culture The A549 culture medium is prepared as follows:

- **500 mL of DMEM** (Dulbecco's Modified Eagle Medium,low glucose (1g/L D-Glucose), GlutaMAX Supplement, pyruvate. Ref. Thermofisher 21885025)
- **50 mL (10%) of FBS** (Fetal Bovine Serum, qualified, heat inactivated, E.U.-approved, South America Origin, Ref. Thermofisher 10500-056)
- **5 mL (1%) of P-S**(Penicillin-Streptomycin, 10,000 U/mL, Ref. Thermofisher15140122)

The solution is then filtered and stored at 4 °C for up to one month. 50 mL aliquots are made for everyday use to avoid contamination and reduce heating/cooling cycles.
A549 cells are fed every three days, and passaged approximately every four to six days.

Passage The following protocol is detailed for a T25 cell culture flask. Preferably, cells should be passaged before they reach 80% confluence.

1. Prewarm some PBS and A549 medium
2. Rinse the flask with 3 mL PBS for 2 minutes
3. Aspirate PBS and add 3 mL TryplE
4. Put in the incubator for 3 minutes
5. In the meantime, prepare the new flask(s) with 4 mL of warm medium (write Name, Cell line, Passage number, Passage ratio and Date)
6. Take ou the flask and check cell detachment under the microscope. Wait until over 90% of the cells are detached
7. Add 4 mL of medium in the flask to stop the trypsinization
8. Optionally, centrifuge the solution for 5 minutes at 1200 rpm and count the cells
9. Split the cells into the new flask in a 1:4 to 1:16 ratio
10. Place the flask(s) back in the incubator

NB: Never dilute A549 more than 1:16, otherwise the cells have a very hard time proliferating again

b. HUVEC

Cell origin The **HUVEC** cells used are Human umbilical vein endothelial cell obtained from Sigma-Aldrich (Ref. 200P-05N. After proliferation, the cells were frozen at passages 3 and 4 for further use. These cells were used in experiments at passage 5 or below.

Cell culture The HUVEC culture medium is prepared as follows:

- **500 mL of ECGM** (Endothelial Cell Growth Medium, Ref. Sigma 211-500)
- **5 mL (1%) of P-S**(Penicillin-Streptomycin, 10,000 U/mL, Ref. Thermofisher15140122)

The solution is then filtered and stored at 4 °C for up to one month. 50 mL aliquots are made to avoid contamination and reduce heating/cooling cycles.
The culture medium is renewed after 2 days in culture, and cells are passaged approximately twice a week.

Passage The following protocol is detailed for a T25 cell culture flask. Preferably, cells should be passaged before they reach 60% confluence. HUVEC cells prefer HBSS to PBS, but both can be used in the following protocol. Similarly, it is recommended to halt the trypsinization with Trypsin inhibitor (Ref. Sigma T6414), but FBS can serve as a replacement.

1. Prewarm some PBS (or HBSS), Trypsin inhibitor (or FBS) and HUVEC medium
2. Fill in the wanted number of T25 flasks with 5 mL of HUVEC medium (write Name, Cell line, Passage number, Passage ratio and Date). Place them in the incubator for at least 20 minutes to coat the surface
3. Rinse the cell-containing flask with 3 mL PBS for 2 minutes
4. Aspirate PBS and add 4 mL TryplE. Wait 1 minute
5. Remove 1 mL of TryplE
6. Place the flask under the microscope and wait for cell detachment. Gently tap the flask on the side to help
7. Add 4 mL of trypsin inhibitor (or FBS) to the flask to stop the reaction. Transfer to a 15 mL tube
8. Centrifuge the solution for 5 minutes at 1000 rpm
9. Dilute the cells into the new flask(s) in a 1:4 to 1:6 ratio
10. Place the flask(s) back in the incubator

NB: Never dilute HUVEC more than 1:10, otherwise the cells have a very hard time proliferating again

c. Freezing and thawing protocols

Cell freezing The protocol starts exactly as a passaging step (PBS washing, trypsinization and inhibition), then goes on as follows:

1. Collect the suspended cells in a 15 mL tube
2. Count the total number of cells
3. Centrifuge the cells (at their respective speed)
4. Prepare a solution of **90% FBS and 10% DMSO**, counting 1 mL per million of cells
5. Aspirate the medium and resuspend the cells in the prepared solution. From that moment on, move at a fast pace
6. Put 1 mL of cell solution in each cryopreservation vial
7. Place all the vials in the Isopropanol box
8. Put the box at -80 °C for 48 h
9. Only after 48 h, transfer the vials in liquid nitrogen (-195 °C) for up to 20 years

Cell thawing Thawing is an operation that necessitates a fast pace of action, because DMSO at room temperature is toxic for the cells.

1. Beforehand, warm up the appropriate cell culture medium
2. Prepare the appropriate number of T75 flasks (two for HUVEC, three for A549, one for iPSC for vial of a million cells) with 18 mL warm medium (NB: do not forget to coat it for iPSC or HUVEC thawing)
3. Go pick up the vial
4. Clean it with Ethanol, and quickly open it under the hood to evaporate all liquid nitrogen residue
5. Close the vial and put it 30 seconds in the water bath (37 °C)
6. Go back under the hood and add 1 mL of warm medium
7. Gently pipet up and down until all the cell solution is thawed
8. Divide the 2 mL into the flasks, gently rock them and place them back in the incubator
9. After 4-6 h (*i.e.* when cell have attached), replace the medium to remove all traces of DMSO (NB: this can wait until the next morning if necessary)
10. Leave the cells to grow for 3 to 4 days before starting passaging.

d. iPSC

Cell origin The Gibco Human Episomal iPSC Line was derived from CD34+ cord blood using a three-plasmid, seven-factor (SOKMNLT; SOX2, OCT4 (POU5F1), KLF4, MYC, NANOG, LIN28, and SV40L T antigen) EBNA-based episomal system. This iPSC line is considered to be zero foot-print as there was no integration into the genome from the reprogramming event.It has been shown to be free of all reprogramming genes and will provide researchers with a control line to compare and study a multitude of aspects of stem cell research.

The Gibco Human Episomal iPSC Line has a normal karyotype and endogenous expression of pluripotent markers like Oct4, Sox2, and Nanog (as shown by RT-PCR) and Oct4, SSEA4, TRA-1-60 and TRA-1-81 (as shown by ICC). Whole genome expression and epigenetic profiling analyses demonstrated that this episomal hiPSC line is molecularly indistinguishable from human embryonic stem cell lines

Cell culture Induced pluripotent stem cells are cultured in E8 Medium (Ref. Thermofisher A1517001), a xeno-free and feeder-free medium specially formulated for the growth and expansion of human pluripotent stem cells (PSCs). Originally developed by Guokai Chen *et al.* in the laboratory of James Thomson (published as "E8") and validated by Cellular Dynamics International, Essential 8 Medium has been extensively tested and proved to maintain pluripotency in multiple iPSC lines. In addition, Essential 8 Medium has been used to scale up production of iPSC and shown to support iPSC growth for over 50 passages without any signs of karyotypic abnormalities, along with maintaining the ability of iPSC to differentiate into all three germ line lineages.

The features of Essential 8 Medium include:

- Consistent-reduced variability compared to existing feeder-free culture media
- Robust-reliable and robust cultures with a xeno-free, cGMP, 8-component medium
- Cost effective-economical and scalable PSC culture compared to other feeder-free media

E8 medium is prepared as follows:

1. Thaw E8 supplements (50X - 10 mL) overnight in 4 °C
2. Dilute in 490 mL of E8 medium (keep the extra 10 mL for cell freezing)
3. Filter all 500 mL and store in 50 mL aliquots

Aliquots can be stored for one month at 4 °C, or at -20 °C for about 6 months. When using it, **never warm up the medium at 37 °C**, just take it out of the fridge and wait until it reaches room temperature.

Cell culture plate coating As iPSC cell lines are very sensitive to their environment, we culture them in pre-coated dishes. Two coatings can be used: either Vitronectin or Matrigel (or Geltrex). The two protocols are detailed below. **Vitronectin** The optimal working concentration of vitronectin is cell line dependent. We use a final **coating concentration of 0.5** $\mu g/cm^2$ on the culture surface for human iPSC. By using a precise volume of diluted solution depending on the surface to be coated (see Table 6.1), we can work with a constant dilution of **1:100** of our stock.

1. Upon receipt, thaw the vial of vitronectin at room temperature and prepare 60 μL aliquots of vitronectin in polypropylene tubes. Freeze the aliquots at –80 °C or use immediately
2. Remove a 60 μL aliquot of vitronectin from –80 °C storage and thaw at room temperature
3. Dilute the vitronectin into sterile DPBS (without Calcium and Magnesium) at room temperature with a **1:100 ratio** (i.e. **working concentration: 5** $\mu g/mL$). Gently resuspend by pipetting the vitronectin dilution up and down
4. Incubate at room temperature for 1 hour.
   Dishes can now be used or stored at 2–8 °C wrapped in laboratory film for up to a week. Do not allow the vessel to dry. Prior to use, pre-warm the culture vessel to room temperature for at least 1 hour
5. Aspirate the diluted vitronectin solution from the culture vessel and discard.
   It is not necessary to rinse off the culture vessel after removal of vitronectin
6. Cells can be passaged directly onto the vitronectin-coated culture dish

Matrigel / Geltrex Geltrex or Matrigel at two products that reproduce a basement membrane. They are mostly composed of laminin, collagen IV, entactin, and heparin sulfate proteoglycans. In this work, we always used Geltrex™ LDEV-Free Reduced Growth Factor Basement Membrane Matrix (Ref. Thermofisher A1413202), following these rules:

1. Thaw Geltrex overnight at 4 °C
2. Dilute with cold Knock-Out DMEM/F-12 Medium with 1:1 ratio

Culture Vessel	Surface Area	Diluted VN solution (mL)
6-well plate	10 cm^2/well	1 mL/well
12-well plate	4 cm^2/well	0.4 mL/well
24-well plate	2 cm^2/well	0.2 mL/well
35-mm dish	10 cm^2	1 mL
60-mm dish	20 cm^2	2 mL
100-mm dish	60 cm^2	6 mL

Table 6.1: Required volume of diluted Vitronectin solution for each cell culture plate

3. Make 1 mL aliquots and store at -20 °C
4. The day of use, dilute these aliquots with a **1:100** ratio with cold Knock-Out DMEM/F-12 Medium (Ref. Thermofisher 12660012)
5. Fill the plates to be coated with the appropriate volume (see Table 6.2)
6. Place the dishes for 1 h in the incubator
7. Then put them in the hood about 1 h, until they reach room temperature. You can then store the dish at 4 °C for up to a week, but never allow them to dry
8. Otherwise, remove the Geltrex solution and place it in another dish to reuse it (you can do it up to three times). Replace with the cell solution in E8 medium

Culture Vessel	Surface Area	Diluted GX solution (mL)
6-well plate	10 cm^2/well	1.5 mL/well
12-well plate	4 cm^2/well	750 μL/well
24-well plate	2 cm^2/well	350 μL/well
35-mm dish	10 cm^2	1.5 mL
60-mm dish	20 cm^2	3 mL
100-mm dish	60 cm^2	6 mL

Table 6.2: Required volume of diluted Geltrex solution for each cell culture plate

Passage iPSC are a bit tricky to passage as they do not survive if separated into single-cells. A very small concentration of EDTA will enable for clump detachment and passaging.

1. Equilibrate the coated dishes, the E8 medium and some DPBS to room temperature for about an hour in the hood. All quantities are detailed in Table 6.3
2. Aspirate the medium from the cells
3. Wash twice with PBS
4. Dilute the EDTA **1:1000** in PBS to obtain a 0.5 mM solution and add to the well
5. Observe under the microscope for about 4-8 minutes until the cells start to round up, separate and the colonies appear to have holes in them
6. Aspirate the EDTA
7. Add E8 to the well and gently pipette up and down to detach the cells. Cells should remain in small clumps
8. Transfer the appropriate amount of cells into E8 and seed on the warm coated dish. Cells are usually passaged with a split ratio between **1:2 to 1:8**, that can be adjusted with time.

The iPSC must be fed every day.

Cell freezing Freeze iPSC using the passaging protocol, excepted they should be resuspended in cold E8 medium supplemented with 10% DMSO at a concentration of about half a million cells per milliliter. Quickly place the cryovials in the cryofreezing container with IPA. After 48 h at -80 °C, transfer the cryovials into liquid nitrogen for long-term storage.

Cell thawing Thaw iPSC according to the same protocol as regular cell lines, excepted that the medium used is E8, and that the dishes must be coated and warm before seeding. Cells should be pelleted at 200 g for

Culture Vessel	Approximate surface	DPBS volume per wash	0.5 mM EDTA volume	Final E8 volume
6-well plate	10 cm^2/well	2 mL/well	1 mL/well	2 mL/well
12-well plate	4 cm^2/well	1 mL/well	0.4 mL/well	1 mL/well
24-well plate	2 cm^2/well	0.5 mL/well	0.2 mL/well	0.5 mL/well
35-mm dish	10 cm^2	2 mL/well	1 mL/well	2 mL/well
60-mm dish	20 cm^2	4 mL/well	2 mL/well	4 mL/well
100-mm dish	60 cm^2	12 mL/well	6 mL/well	12 mL/well

Table 6.3: Required volumes for iPSC passaging

5 minutes after thawing and resuspended in E8 medium supplemented with 1 μM ROCK-inhibitor to promote single-cell survival.

6.1.2 Biochemistry techniques

a. Immunofluorescence

The principle of immunostaining is to use fluorescent labels to mark specific proteins and be able to see their localization and abundance in the cell sample. This method is widely used in biology and quite simple, but requires several steps and controls to be able to obtain conclusive results.

General principle In short, immunostaining requires three steps: preparation of the sample; labeling of a specific protein (we label one epitope) that we want to detect with a primary antibody; and labeling of our primary antibody with a matching secondary antibody that is conjugated with a fluorescent probe. Then we use confocal microscopy to excite the probes and observe the presence of our epitope-primary antibody-secondary antibody-fluorescent probe chain (see Figure 6.1). *NB: Sometimes the primary antibody is already coupled with a fluorescent probe; then we talk of* ***direct*** *immunostaining*

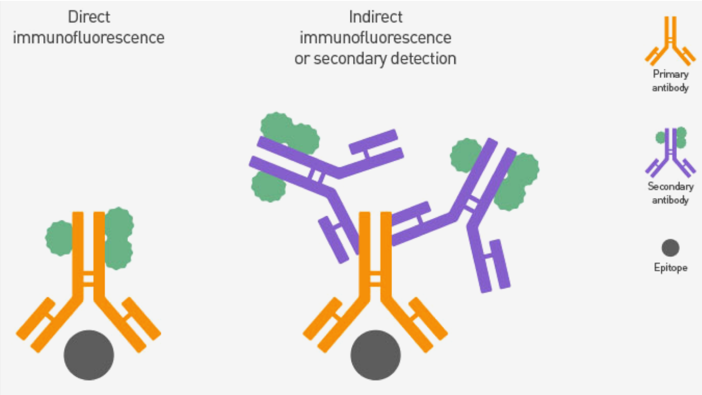

Figure 6.1: Immunostaining principle *Source: Molecular Probes*

Controls For each protein (antigen) to be stained, we must perform a positive control to be sure that our primary antibody is specific for that antigen. That means that we should stain a control sample (cells), which expresses that protein for sure, and then check that we have a coherent staining. This control means that if we observe a negative staining in our experiment, but we do not in the control experiment, then we can say for sure that we do not have a false negative (that could be due to issues with the products).

For each protein and each sample, we need to perform negative controls for both the primary and secondary antibodies. For the primary antibody, this means staining (1rst AB + 2nd AB) a sample of cells that we know do NOT express the specific protein: if we observe staining, then we know it is a false positive due to a non-specific staining of the primary antibody. Similarly, for the secondary antibody, we stain a sample of our cells with only the secondary antibody: if there is staining, then it is a false positive due to aspecific bounding of the secondary antibody to our cells.

That is why these controls are crucial for each experiment, to be able to assess whether our observations are conclusive or not. These controls were be performed for all stainings included in this thesis, even though it is not mentioned every time.

Sample preparation Before staining, cell samples need to be prepared following a succession of steps detailed below:

1. Fixation: Chemical reaction that fixes the cells in the exact state they were. This does not alter cell components, nor genes, nor proteins.
2. Blocking: To reduce aspecific bounding (as mentioned above), we perform both chemical and biological blocking of reactive sites in the cells.
3. Permeabilization: Cell membranes (and nuclei membrane) are pierced with small holes to allow the antibodies to enter the cells. This step is not required if we stain membrane markers.

Protocol

1. Fixation: cell samples are rinsed twice with warm PBS then incubated for 20 min at room temperature with a solution of paraformaldehyde, diluted to 4% in PBS. The samples are then rinsed twice with PBS and can be stored up to three months in PBS at 4 °C for further staining;
2. Chemical blocking: samples are incubated in a solution of NH_4Cl at 2.6 mg/mL for 20 min at room temperature then rinsed twice with PBS;
3. Permeabilization: samples are incubated of 5 minutes at room temperature in a solution of 0.2% vol/vol Triton-X-100 (Sigma Aldrich) in PBS;
4. Biological blocking: Biological blocking is performed with animal serum, usually 4% of BSA (Bovine Serum Albumin, Sigma Aldrich Ref.A3059), but for a better efficiency, I use some specific serum from the host in which our secondary antibodies were raised; either 5% of Donkey serum or 10% of Goat serum or both. All solutions prepared with animal serum must be filtered before use. Finally, we prepare our **blocking solution** with 0.1% vol/vol Triton-X-100 + 4% BSA wt/vol + 5% vol/vol Donkey serum and/or 10% vol/vol Goat serum . The samples are incubated for 3 hours at room temperature;
5. Primary staining: for the primary antibody staining, if we perform double staining we need to make sure that all primary antibodies were raised in different hosts. All primary antibodies are diluted in the **blocking solution** and incubated overnight at 4 °C (for dilution ratios, see Table 6.5). Afterwards, the samples are thoroughly washed (three times for 5 minutes each time);
6. Secondary staining: for the secondary antibody staining we need to make sure that no secondary antibody was raised in the same host as one of the primary antibodies and that their fluorescent probes spectra do not overlap in emission. All secondary antibodies are diluted in the **blocking solution** and incubated in the dark for 2 hours at room temperature (for dilution ratios, see Table 6.4). Afterwards, the samples are thoroughly washed (three times for 5 minutes each time);
7. Nuclei and cytoskeleton staining: samples are stained with 1 $\mu g/mL$ in PBS Hoechst 33342 (Sigma) and/or 1 μM sirActin (Spirochrome,Tebu Bio, Ref. 2515C006) for 30 min at room temperature in the dark. Afterwards, the samples are thoroughly washed (three times for 5 minutes each time);
8. Mounting and sample preservation: before mounting, the samples are rinsed with filtered deionised water to avoir PBS salts crystallization. They are then sandwiched between two glass coverslips with a drop of mounting medium (Fluoroshield, Sigma Aldrich, Ref. F6182) between the sample and each coverslip. They are sealed with transparent nailpolish and kept at 4 °C for up to one month for observation.

Observation tips During observation, we use sequential detection to separate the detection channels. I usually detect up to two fluorescent probes per sequence, with a maximum range between their spectrum *For example: Sequence 1: Hoechst + Bright Field, Seq2: Alexa Fluor 488 + Alexa Fluor 594, Seq3: AF 555 + AF 633, Seq4: AF 568 + AF 647.* I always check the image in saturation to set up the laser intensity so that no image (in all channels and all stacks) will be saturated at any point. This allows for fluorescence quantification. We never set up a gain above 100 to avoid artificially increasing the fluorescence.

Antibody	**Conjugate**	**Dilution**	**Reference**	**Company**
Donkey Anti Rabbit	AF 488	1:1000	A-21206	ThermoFisher
Donkey Anti Rabbit	AF 555	1:1000	A-31572	ThermoFisher
Donkey Anti Rabbit	AF 568	1:1000	A-10042	ThermoFisher
Donkey Anti Rabbit	AF 647	1:1000	A-31573	ThermoFisher
Donkey Anti Mouse	AF 488	1:1000	A-21202	ThermoFisher
Goat Anti Mouse IgG1	AF 488	1:250	A25536	ThermoFisher
Donkey Anti Rabbit	AF 647	1:250	A25537	ThermoFisher
Goat Anti Mouse IgG2a	AF 555	1:250	A25533	ThermoFisher

Table 6.4: Origin and dilutions used for the secondary antibodies

	Antigene	**Host**	**Dilution**	**Reference**	**Company**
Junctions	ZO-1 /TJP1	Mouse Conj: AF 488	1:100	339188	ThermoFisher
	Occludin	Mouse IgG1K	1:200	OC-3F10	ThermoFisher
	N-Cadherin	Rabbit	1:200	PA5-19486	ThermoFisher
	N-Cadherin	Mouse	1:200	33-3900	ThermoFisher
	E-Cadherin	Rabbit	1:100	701134	ThermoFisher
	VE- Cadherin	Mouse	1:100	MA1-19199	ThermoFisher
	VE-Cadherin	Rabbit	1:25	361900	ThermoFisher
Cell properties	Anti Na+/K+ ATPase alpha1	Mouse IgG1K Conj. 555	1:125	05-369X-555	ThermoFisher
	KI67	Rabbit	1:500	PA5-16785	ThermoFisher
Endothelial markers	vWf	Rabbit IgG1	1:100	PA5-16634	Thermofisher
	PECAM1	Mouse IgG1	1:100	MA1-19199	Thermofisher
	PECAM1	Rabbit IG1	1:100	ab28364	AbCam
AET II Markers	Mucin / MUC-1	Rabbit IgG	1:500	PA1-21077	ThermoFisher
	MUC5AC	Mouse	1:100	MA5-12178	ThermoFisher
	SP-A	Rabbit IgG	1:50	PA5-28480	ThermoFisher
	SFTPB	Rabbit IgG	1:200	PA5-42000	ThermoFisher
	proSP-C	Rabbit	1:1000	WRAB- 9337	Seven Hills
	NKX2.1/TTF1	Rabbit	1:1000	WRAB - 1231	Seven Hills
AET I Markers	Podoplanin (FL-162)	Rabbit IgG	1:100	sc-134482	Santa Cruz
	AQP5 (G-19)	Goat IgG	1:100	sc-9890	Santa Cruz
	Caveolin1	Rabbit IgG	1:100	PA1-064	ThermoFisher
Pluripotency markers	Nanog	Goat	1:200	AB77095	Abcam
	OCT4	Rabbit	1:100	A24867	ThermoFisher
	SSEA4	Mouse IgG3	1:100	A224866	ThermoFisher
	TRA-1-60	Mouse IgM	1:100	A24868	ThermoFisher
	SOX2	Rat	1:100	A24759	ThermoFisher
3-Germ Layer markers	TUJ1 (Beta Tubulin III)	Rabbit	1:500	A25532	ThermoFisher
	AFP (Alpha Foeto-Protein)	Mouse IgG1	1:500	A25530	ThermoFisher
	SMA (Smooth Muscle Actin)	Mouse IgG2a	1:200	A25531	ThermoFisher
Differentiation markers	CXCR4 (CD184)	Mouse IgG2a Conj. PE	1:200	MHCXCR404	LifeTech
	c-Kit	Mouse IgG1 Conj. APC	1:100	CD11705	LifeTech

Table 6.5: Origin and dilutions used for the primary antibodies

b. Flow cytometry protocol

Theory Flow cytometry is a laser-based technology used in cell sorting and analysis. Our flow cytometer (BD Accuri™ C6) does not perform sorting operations, but was used to quantify specific markers of our cells. The principle is very similar to immunofluorescence observation, as we use the same principle to label our protein of interest, and then we use a laser to detect them. Cells are detached into single-cells, flowed in front of the lasers, and their fluorescence is analyzed and counted.

Controls As detailed in the previous section, controls are required for any flow cytometry experiment. Ideally, for each sample, you would prepare several samples:

- Our sample of interest (1st ABs + 2nd ABs);
- A control without staining (No ABs);
- A control for each marker stained (1st AB + 2nd AB);
- An isotype control (or a secondary antibody control if you do not have the right type of cells).

Specific buffer preparation All staining operations are performed in a specific buffer, the **FACS buffer**, containing:

- 500 mL of D-PBS (No magnesium, no calcium);
- 5 g of BSA (Final 5% wt/vol concentration);
- 1 mL of 0.5M EDTA (Final 1mM concentration);
- 250 μL NaN3 20% (Final 0.01% concentration).

This buffer is then filtered and can be kept at 4 °C for up to a year.

Sample preparation Before staining, the cells must be collected and fixed as follows:

1. Wash the cells with warm PBS;
2. Detach the cells with Trypsin or TryplE;
3. Centrifuge the cells (5 min at 1200 rpm);
4. Discard Trypsin and add 1mL PBS. Transfer into a 1.5 mL tube;
5. Centrifuge the cells (5 min at 1200 rpm);
6. Discard PBS and add 4 % PFA for 20 min at room temperature;
7. Centrifuge the cells (5 min at 2600 rpm);
8. Resuspend cells in 0.5 mL FACS Buffer;
9. Cells can be kept at 4 °C for up to a week before staining.

Embryoid bodies specific protocol The following protocol is detailed especially for the staining of endoderm markers during alveolar differentiation. Indeed, this protocol required a long optimization process, as we need to dissociate the embryoid bodies into single cells, and our endoderm markers (CXCR4 and c-Kit) are very sensitive to shear stress. For one well of a 6-well plate:

1. Collect the EB in a 15 mL tube;
2. Wash the well with 1 mL of warm PBS and add to the tube;
3. Centrifuge the cells (2 min at 130 g);
4. Discard supernatant and wash with 2 mL PBS;
5. Centrifuge the cells (2 min at 130 g);
6. Discard PBS and add 1mL TryplE;
7. Flick the tube for about 10-15 seconds until the supernatant becomes cloudy;
8. Wait for the EBs to settle down;
9. Transfer supernatant into 2 mL of Stop Medium;
10. Add 1 mL TryplE to the EB and transfer into a small dish;
11. Place 30 seconds in the incubator;
12. Check EB dissociation under the microscope. Tap and rotate the dish if necessary;
13. Transfer cells into Stop Medium. Add excess of Wash Medium;
14. Centrifuge the cells (5 min at 300 g);
15. Discard supernantant and wash with PBS. Transfer into a 1.5 mL tube;
16. Centrifuge the cells (5 min at 300 g);
17. Discard PBS and add 0.5 mL of 4% PFA for 20 min at room temperature;
18. Centrifuge the cells (5 min at 2600 rpm);

19. Resuspend in 0.5 mL FACS buffer;
20. Cells can be kept at 4 °C for up to a week before staining.

Antibody staining We move on to staining our samples. Please remember to keep a sample (a minimum of 50 000 cells) unstained as a control. If the target protein is located inside the cell membrane, we add 0.2% vol/vol Triton-X-100 (Sigma Aldrich) to our FACS buffer before proceeding:

1. Take your sample and centrifuge the cells (5 min at 2600 rpm);
2. Aspirate the medium and resuspend in 100 µL of FACS buffer with the primary antibodies and incubate overnight at 4 % ;
3. Take your sample and centrifuge the cells (5 min at 2600 rpm);
4. Resuspend in 150 µL FACS to rinse the cells;
5. Repeat twice ;
6. If a secondary antibody is needed (SOX2 staining), incubate the cells for 2 hours at room temperature with 100 µL of FACS buffer with the secondary antibodie(s);
7. Resuspend in 150 µL FACS to rinse the cells;
8. Repeat twice and leave the sample in the fridge until analysis.

Observation Before observation, each sample is divided in three and each is observed separately to obtain the standard deviation of the measurement. The unstained condition is observed first and defines the gate to assess positively stained cells.

c. Lucifer Yellow Assay on patches

Products preparation Lucifer Yellow CH Dipotassium Salt was obtained from Sigma Aldrich (Ref.L0144-25MG) and dissolved in HOW MUCH mL sterile water and stored at -20 °C in 1mL aliquots.
Depending on the experiments, two buffers were prepared: either the **5050 White** buffer or the **LYB**.**5050 White** buffer consisted of 50% DMEM High Glucose (ThermoFisher, Ref.31053-028), 50% DPBS (ThermoFisher, Ref.14190094) with 1% Penicillin-Streptomycin (ThermoFisher, Ref.15140122) because the High Glucose Medium is at high risk of contamination. The **LYB** consists of HBSS with D-Glucose, $CaCl_2$ and $MgCl_2$ (ThermoFisher, Ref.) with 2% 1M HEPES (ThermoFisher, Ref.).

Assay preparation

- Prepare a sterile 6-well plate with integrated PDMS rings
- Fill the PDMS rings with 220 μL buffer
- Prepare a small Petri dish full of buffer (2-5mL)
- Take a patch in culture and dip it in the buffer to rinse it
- Delicately absorb the excedent of buffer by touching a clean room paper with the side of the patch
- Place the patch on a PDMS ring
- Use non-magnetic tweezers to place a magnetic-PDMS ring on top of the patch, with the circular shape towards the patch
- Elevate the plate with one hand, and with one finger keep the magnetic-PDMS ring slightly pressed against the patch with a finger
- Approach below the plate with two magnets and come below the well with the magnets on their side. Let go of them so that they flip to adhere on their right side. (This step is important because approaching directly the magnets on one specific side can move the magnetic PDMS ring and thus destroy the fibers)
- Repeat for all wells
- Place the 6-well plate on a plastic tray lined with sterile adsorbent paper (because otherwise the magnets will adhere to the shelves in the incubator)
- Take the aspiration and reduce the aspiration intensity to a minimum. Cut a 1000 µL pipette tip and fit it on the aspiration, then delicately empty all top chambers
- Fill every chamber with 220 μL of Lucifer Yellow solution (100 $\mu g/mL$ in the buffer)
- Place the tray back in the incubator for 1 hour.

Sampling and analysis

- After 1 hours take out the tray

- Collect 150 μL in each top chamber and place them in a 96-well plate (flat transparent bottom, with dark walls and an anti-evaporation lid, Corning)
- Use the previous delicate aspiration system to empty the top chambers
- Rinse them with 200 μL of buffer and aspirate again
- Delicately remove the top magnetic ring while aspirating any solution residue above the patch
- Take out the patch, rinse it by dipping it in buffer (5 mL) and place it back on its culture plate (with renewed culture medium)
- Collect 150 μL in the bottom chamber and place it in the 96-well plate
- Repeat for all patches
- Add controls in the 96-well plate: 150 μL of buffer and 150 μL of Lucifer Yellow solution
- Take the 96-well plate immediately to the plate reader (Tecan Spark) and read with the following parameters: 30 seconds of stabilization per well, Excitation 428 nm, Emission 546 nm, set Gain such as the Lucifer Yellow well is 90% of the maximal read
- Compute the permeability as: 100 x (Fluorescence of the Low Chamber - Fluorescence of the Buffer) / (Fluorescence of the Lucifer Yellow solution - Fluorescence of the Buffer)

d. Magnetic-Activated Cell Sorting

After inducing the differentiation of iPSC into endothelial progenitors, we had to sort the cells according to their CD144 (VE-Cadherin) expression. We used MACS, Magnetic-Activated Cell Sorting, a technique that can isolate live (or dead) cells with magnetic microbeads. Briefly, the beads are attached to the cells via a complex Steptavidin - Biotin - CD144 Antibody reversible chain.

DSB-X Biotin-conjugated antibodies The antibody of interest, here CD144 (VE-Cadherin) is conjuguated to DSB-X Biotin. This derivative of desthiobiotin has the ability to bind to streptavidin and avidin, just like regular biotin. However, with DSB-X Biotin, the chemical bond can be reversed quite easily. Indeed, if harsh chaotropic agents (6.0 M guanidine) and low pH (1.5) are required to break the biotin-streptavidin bond, a simple excess of D-biotin or D-desthiobiotin at room temperature and neutral pH is sufficient to break the DSB-X-streptavidin bond. The CD144 antibody was labeled with DSB-X biotin using the **DSB-X Biotin Protein Labeling Kit** from Molecular Probes (Ref.D-20655). The antibodies were then stored at -20°C before use.

Magnetic separation After marking the cells with the specific antibodies, the streptavidin- conjugated magnetic beads are introduced to the cells. The two chemicals (biotin-streptavidin) bond, and the beads are attached to the cells. A magnet helps collecting the cells, and after a few washing steps, the beads are released from the cells via the reversible process mentioned in the previous paragraph. After washing off the beads, we collect only CD144+ cells. The protocol we used was the following:

1. Magnetic labeling: we used the **Dynabeads FlowComp Flexi kit** from Invitrogen (Ref.11060D) to perform our magnetic separation. We prepared our MACS buffer as follows: 50 mL of PBS with 0.666 mL of 7.5% BSA (final concentration 0.1% wt/vol BSA) and 200 µL EDTA (final concentration 2 mM). This buffer is filtered and stored at 4 °C. We vortexed our beads for 30 seconds and resuspended 75 µL in 1 mL MACS buffer. The solution is placed on a magnet for 3 minutes then the supernatant is discarded and beads are resuspended in 75 µL MACS buffer;
2. Antibody staining (for a 60 mm dish): cells are rinsed twice with 5 mL PBS, then incubated in 2 mL Accutase 4 min at 37 °C. We add 5 mL of StemPro34 medium and pipett to detach and dissociate the cells. They are collected in a 15 mL tube, counted and centrifuged at 1000 rpm for 5 min. The supernatant is discarded and the cells are resuspended in 80 µL MACS buffer + 25 µL of DSB-X biotinylated antibody in a 100 µL tube, then placed at 4 °C on a shaking platform for 25 min;
3. Magnetic bead bonding: we then add 1 mL of MACS buffer and transfer the solution in a 1.5 mL tube, vortex it for 3 seconds and centrifuge at 350 g for 10 min **with no brakes** (this takes about 20 min). The sSupernatant is discarded and we add 1 mL of MACS buffer + 75 µL of magnetic beads then vortex again for about 3 seconds. This solution is placed at 4 °C on a shaking platform for 32 min;
4. Magnetic separation: we add 0.5 mL of MACS buffer to our cell solution and resuspend the cells to rinse them. Then we place a magnet on the side of the inclined tube (so that all the debris and non-stained cells settle down on the bottom of the tube) for 5 minutes. The medium is gently removed (and kept in another tube) without disturbing the black aggregate of beads and cells that formed alongside the

magnet, then we add 1 mL of MACS buffer. This operation is repeated two more times to wash off all the CD144- cells. The discarded cells are counted to estimate our protocol's differentiation efficiency.

5. Releasing: we resuspended the CD144+ cells with their beads in 1 mL Release Buffer from the kit and place it 4 °C on a shaking platform for 12 min. Then we pipet the solution about 10 times to mechanically help breaking the bond, place it on a magnet for about 5 minutes and transfer the supernatant to a new tube. We repeat this once more. Count the cells and centrifuge at 350 g for 10 min. Finally, resuspend in expansion medium: 3 mL of endothelial induction base medium supplemented with VEGF (to a final concentration of 50 ng/mL) and seed in a 60 mm dish.

6.1.3 Microengineered patch

Our microengineered patch is fabricated in several steps (see Figure 6.2). We first make a patterned mask to generate a resin mold by photolithography (1), then use this resin mold to make a PDMS mold (2). The PDMS molds are used to make a PEGDA frame by capillary molding (3). This frame is then coated with a gold layer (4) before deposing a network of gelatin nanofibers and cross-linking them (5).
In this work, we started with a ready-made protocol and successively modified and optimized it to obtain our final protocol. I will detail here only the first and last protocols.

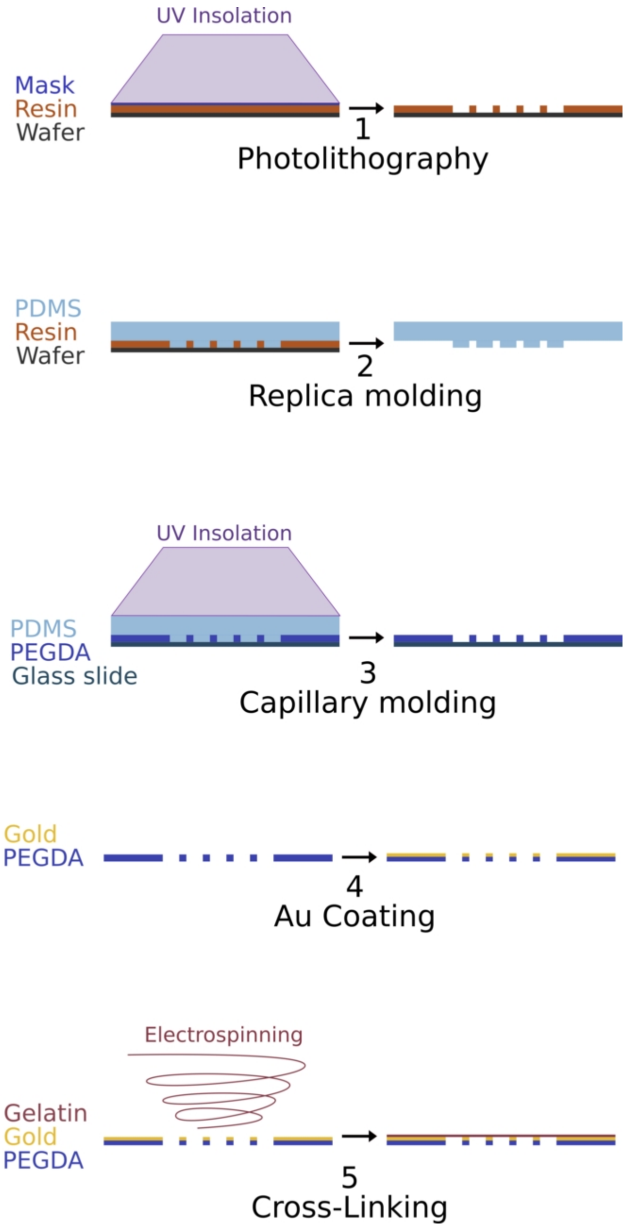

Figure 6.2: Patch fabrication process

a. Original patch

Mask preparation

1. Draft the patterns onto a .DXF file
2. Import it into the micro pattern generator *μPG* 101 (Heidelberg Instruments, precise down to 0.6 *μm*)
3. Use the diamond to cut the mask substrate (glass covered with a chrome layer and a AZ 1518 resin layer) to the appropriate size, and clean it with an airgun
4. Launch the vacuum pump
5. Place the substrate inside the generator and launch the program with expose options of 40 mW at 60%, Energy 1x1
6. Wait (around 3-4 hours for the pattern to be laser-engraved onto the resin
7. Revealed melted resin with a 1 minute bath in AZ 726 MIF Developer
8. Then use a solution of Chrome ETCH N1 to remove the chrome layer on the pattern (about 1 min)
9. Remove all residual resin with a bath in Aceton (use ultrasonic cleaner for about 30 seconds)
10. Clean the mask with water

Finally, we obtain a glass substrate with a chrome surface, except where our pattern is drafted. This will be our mask for photolithography.

Photolithography Photolithography is one of the main processes of microfabrication. It is used to transfer a 2D pattern on a substrate in a 3D volume of controled height. Briefly, substrate covered with light-sensitive resin is UV-insolated through a patterned mask, and then cured and developed with specific chemicals. Depending on the method used to print the mask, and on the resin, the resolution of the pattern can reach down to 50nm. The obtained substrate can then serve as a mold for soft lithography, with PDMS for example.

1. Take positive resin (AZ 40 XT) out of the fridge and wait until it reaches room temperature
2. Turn on vacuum pump and pre-heat the hot plates
3. Place a silica wafer in the spin-coating machine
4. Deposit some resin (AZ 40 XT) on top
5. Set the parameters of the spin-coater to obtain a layer of 10 μm (cf settings in Table 6.6)

	Step 1/2	Step 2/2
Time	15 s	20 s
Rpm	500 rpm	1500 rpm
Acc	100	300 rpm

Table 6.6: Spin-coating parameters

6. Proceed to pre-baking steps: 1 minute at 65 °C, 1 minute at 95 °C and 8 minutes to 126 °C
7. Place the mask (previsouly obtained) on top of the resin
8. Wait until reaching room temperature
9. Place the wafer is under UV light for 75 seconds.
10. Proceed to post-baking steps: 30 seconds at 65 °C, 30 seconds at 95 °C and 2 minutes at 105 °C
11. Wait until reaching room temperature
12. Wash out non-reticulated resin with a 3 minutes bath in AZ 726 MIF Developer

Finally, we obtain a wafer with our resin pattern, that is 10 μm high. It can be used to generate about a twenty PDMS molds.

PDMS Molding PDMS is one of the most used material in microfabrication applied to biology. The Polydimethylsiloxane is an organic silicon-based polymer, easily fabricated and biocompatible (inert and non-toxic). It is permeable to gas, which allows for cell culture, and optically clear, which allows for microscope imaging. In this way, we will use these temporary molds to generate our PEGDA grid, and we will be able to renew those molds when too old.

1. Perform silanization, an anti-sticking treatment by evaporation of 10 μL of Trimethylchlorosilane onto our wafer
2. Prepare a PDMS solution with a 1:10 ratio of compound A and B (curing agent) (Sylgard 184, Sigma-Aldrich)
3. Pour the PDMS on the wafer and degas it under the dessicator for about 20 minutes
4. Cure for at least 3 hours (up to overgnight) at 80 °C (70 to 90 °C)
5. Peal off the PDMS and cut out molds into a circular shape (13 mm diameter) with a metal puncher

Finally, repeat the operation to obtain about 16 PDMS mold with the negative volume of our future grid. They can be used about 20-30 times each, for no more than 6 months.
This whole process is also used to generate PDMS molds for the outer ring to place on the patch.

PEGDA solution preparation We now generate our PEGDA grid and PEGDA rings by vaccuum casting a PEGDA solution in our PDMS molds. We first prepare this solution:

1. Weight **500 mg** of the photo-initiator (2-Hydroxy-40- (2-hydroxyethoxy)-2-methylpropiophenone, Ref. Sigma 410896)
2. Dissolve in 1 mL of DMSO
3. Dilute into **11.5mL** of PEGDA (250 Mn, Ref. Sigma 475629) to obtain a final concentration of 4% photo-initiator for total volume of 12.5 mL.

This solution should be aliquoted into 1 mL aliquots (in opaque eppendorfs) and kept at 4 °C for about 6 to 9 months.

PEGDA frame reticulation The PEGDA solution is reticulated as follows:

1. Place the PDMS molds, face down, on glass slides
2. Place the dish in the dessicator for about 20 minutes
3. Rapidly take out the plate and gently drop PEDGA solution at the base of each mold

4. Wait until the solution is aspired into the molds and fills in the complete pattern. Add solution if necessary
5. Remove excess of solution
6. Place under UV light for 30 seconds to reticulate the solution
7. Remove the PDMS molds and wash them with Isopropanol (IPA) and a Nitrogen gun
8. Use the same method to generate solid rings (30 seconds UV) and detach them from the glass slide with a razor blade
9. Put about 20 μL of PEGDA solution on the ring and place it over a grid.
10. Put the ensemble under UV light for 45 seconds
11. Use a razor blade to detach the PEDGA frames from the glass slide
12. Repeat the operation until having enough frames
13. Wash all the frames with IPA at least 3 times to remove excess of photo-initiator
14. Put all the frames in water and leave them overnight

This last step is crucial: the patches need to bathe at least 12 hours in water to remove the excess of non-reticulated chemicals, otherwise the cells will die when seeded on the patch.

Gold sputtering In order to perform the electrospinning step, we need our grids to be conductive, therefore we will cover them with a thin gold layer.

1. Remove the grids from water and place them on adsorbent paper
2. Place all the grids on a petri dish so that they don't cover each other
3. Place the dish in the sputter machine (EMITECH K675X)
4. Set target B with an Au sample
5. Set up the parameters of the machine as in Table 6.7 and launch the program

Autotarget	B
Metal	Noble
Current	25 mA
Time	4 minutes
Nb of Cycles	1
Pump	No

Table 6.7: Spin-coating parameters

6. When over, remove the samples from the machine
7. Launch the vacuum shutter cycle and turn off the Sputter Coater

This operation generates a gold layer of about 1 to 5 nm on top of the PEGDA grid.

Electrospinning Electrospinning is a technique producing micro-fibers by creating an important electric force between a receiving plate and a syringe. It draws charged threads from the polymer solution in the syringe, and as the solvent evaporates, only the polymer threads are deposited onto the charged receiving plate. The result is a random heterogenous deposition of a network of micro to nano-fibers.

Before proceeding to the electrospinning, we prepare a gelatin solution as follows:

1. Prepare a small glass bottle (5 mL) with a flat bottom
2. Weight 180 mg of Gelatin (Ref. Sigma G6650, kept at 4 °C)
3. Add 500 μL of Acetic Acid
4. Add 334 μL of Ethyl Acetate
5. Add 250 μL of De-Ionised Water
6. Put on the magnetic stirrer for at least 2 hours until the solution is homogeneous

This solution should be prepared fresh before use. It can be stored at room temperature with a magnetic stirrer for about one day.

We then proceed to the electrospinning of the gelatin solution on the patch:

1. Prepare an electric generator and set it to 11 kV
2. Set up a syringe with the gelatin solution and a very long tip (¿10 cm)
3. Place it in a syringe pump with a volume rate of 0.2 mL/hour

4. Place a wafer facing the syringe, with two horizontal bands of double-sided adhesive tape 10 mm apart. Place a PEGDA frame on the adhesive
5. Place the syringe at 10 cm distance (horizontal) from the wafer
6. Pinch the positive electrode of the generator to the tip of the syringe
7. Pinch the negative electrode of the generator to the wafer
8. Launch the syringe pump and the generator for 7 minutes
9. Check fiber density under the microscope. Adapt duration in consequence
10. Place the patches in a petri dish and leave in a desiccator overnight

This step is very sensitive to weather conditions: avoid high humidity days, or be prepared to for a (much) longer electrospinning time.

Cross-linking We then prepare the cross-linking solution:

1. Weight 230 mg of NHS (N-Hydroxysuccinimide, Ref. Sigma 130672)
2. Weight 380 mg of EDC (N-(3-Dimethylaminopropyl)-N'-ethylcarbodiimide hydrochloride, Ref. Sigma 03450 (kept at -20 °C)
3. Put in a falcon and add 10 mL of Ethanol Absolute
4. Mix with a vortex machine until all products are dissolved

The solution should be prepared in sufficient quantity regarding the number of patches to be cross-linked. Count about 0.5 to 1 mL per patch. This solution should be prepared fresh before used. It can be stored at 4 °C for less than a day. We then move on to the cross-linking:

1. Place the patches in 12-well plates
2. Add the cross-linking solution to each well
3. Wait at least 4 hours (and no more than 12 h)
4. Remove the solution and rinse with Ethanol
5. Repeat the Ethanol washing step at least two times
6. Place the patches back in 12-well plates with adsorbent paper below them
7. Put in the desiccator overnight. Your patches are ready to use

Patches handling and conservation Once prepared, the patches must be kept individually (ideally in 12-well plates), placed on adsorbent paper to prevent from attaching to the plastic dish (and destroying the fiber network).

Patches should be kept for less than 3 months before use to ensure no degradation of the fibers.

Before use, the patches can be soaked in Ethanol and placed under UV-light (30 minutes on each side) for sterilization.

b. Final patch

The following protocol is the updated and optimized version of the patch fabrication protocol. This protocol differs essentially by the fact that it requires a single-step molding of the PEGDA to generate the frame, thanks to a double-layer PDMS mold. This mold is generated from PDMS replica molding of a double-layer photolithography resin mold.

Mask preparation We will prepare two masks, for each layer of photolithography. The two masks were generated with CleWin 5 (WieWeb Software) and exported in .GBR files. The masks are then directly printed onto a plastic layer with a photoplotter (Filmstar+)

Photolithography We proceed to the two-step phtolithography of two 100 μm layers as follows:

1. We prepare the wafer with an airgun to remove dust, followed by a heating step of 10 minutes at 200 °C;
2. We add a 2 μm thick pre-layer with SU8 2002 spin-coated at 3000 rpm. We proceed to the soft-baking steps: 1 minute at 65 °C, 1 min at 95 °C and 3 minutes to cool down. The layer is exposed under UV-light for 8 seconds. The post-baking steps are: 1 minute at 65 °C, 2 min at 95 °C and 3 minutes to cool down. The layer is then developed in SU8 Developer (MicroChem) for 1 minute.
3. The layer is treated with plasma at 400 mTorr for 3 minutes before moving on to the first patterned layer.

4. SU8 resin is spin-coated at 3000 rpm. We then proceed to the soft-baking steps: 1 minute at 65 °C, 20 min at 95 °C and 3 minutes to cool down. The mask is placed and the layer is exposed under UV-light for 21 seconds. The post-baking steps are: 1 minute at 65 °C, 3 min at 95 °C and 3 minutes to cool down. The layer is then developed in SU8 Developer (MicroChem) for 8 minutes.
5. For the second layer, SU8 resin is spin-coated at 3000 rpm. We then proceed to the soft-baking steps: 1 minute at 65 °C, 20 min at 95 °C and 3 minutes to cool down. The second mask is align with a MJB4 (SUSS MicroTec) and the layer is exposed under UV-light for 21 seconds. The post-baking steps are: 1 minute at 65 °C, 3 min at 95 °C and 3 minutes to cool down. The layer is then developed in SU8 Developer (MicroChem) for 8 minutes.
6. We proceed to the hard bake at 190 °C for 15 minutes and allow the wafer to cool down for 10 minutes.
7. Finally, the wafer is silanized with 10 µL TMCS for 20 minutes.

PDMS Molding The PDMS molds are obtained by direct replica molding onto our wafer, using Sylgard PDMS in a ratio 1:10 cured at 80 °C for 2 hours.

PEGDA frame reticulation We use the same PEDGA solution as the original patch and perform the following protocol, which was optimized for high-throughput production of PEGDA grid.

1. Place the PDMS molds, face down, on glass slides. Place them in touching pairs, with two pairs per slide. Place four slides in a big size Petri dish
2. Place the dish in the plasma-machine vacuum pump until reaching below 200 mbar for at least 5 minutes
3. Rapidly take out the plate and gently drop about 100 μL of PEDGA solution at the touching point of each pair of molds
4. Wait until the solution is aspired into the molds and fills in the complete pattern. Add solution if necessary
5. Remove excess of solution. Clean out solution outside the molds with clean-room specific adsorbent paper
6. Place under UV light for 50 seconds to reticulate the solution
7. Remove the PDMS molds and wash them with Isopropanol (IPA) and a Nitrogen gun
8. Use a razor blade to detach the PEDGA grids from the glass slides
9. Put all the grids into IPA for about 30 minutes to an hour
10. Repeat the operation until having enough grids
11. Wash all the grids with IPA at least 3 times to remove excess of photo-initiator
12. Wash with Millipore Water + 10 % Ethanol for 2 times
13. Place the grids inside the cover of a big size petri dish
14. Cover the outside of the bottom part of the dish with some hydrophobic parafilm and place it on top of the grids
15. Use a pipette to add water to the grids (enough to cover them all) in between the two parts of the Petri dish
16. Place a weight inside the petri dish to help keep the grids flat, as you leave them bathing in water for at least 48 hours. Ideally, renew the water after 24 hours.

Gold sputtering The patches are coated with a Gold layer using the EMITECH K675X, with a 50 seconds deposition at 125 mA. This results in a 20 nm thick Au layer on the PEGDA grid deposited on the grid side of the patch.

Electrospinning The gelatin solution is prepared with a lower concentration of gelatin, which allows for the generation of thinner fibers. Finally, we use 125 mg of Gelatin (Ref. Sigma G6650) in 500 μL of Acetic Acid with 334 μL of Ethyl Acetate and 250 μL of De-Ionised Water. The solution is stirred at room temperature for 4 hours before use.
The electrospinning is performed with the same parameters as previously (10 cm distance, 11 kV, 0.2 mL/h for 7 to 15 minutes, depending on the local humidity). However, we switched to a vertical electrospinning, in a closed enclosure (see Figure 6.3). The patches are placed on a box covered with aluminum foil, in groups of 6 to 9.

Cross-linking The solution used is unchanged (230 mg of NHS and 380 mg of EDC in 10 mL of Ethanol Absolute) and placed on the patches for 4 to 6 hours. The patches are placed in 12-well plates, with 750 µL

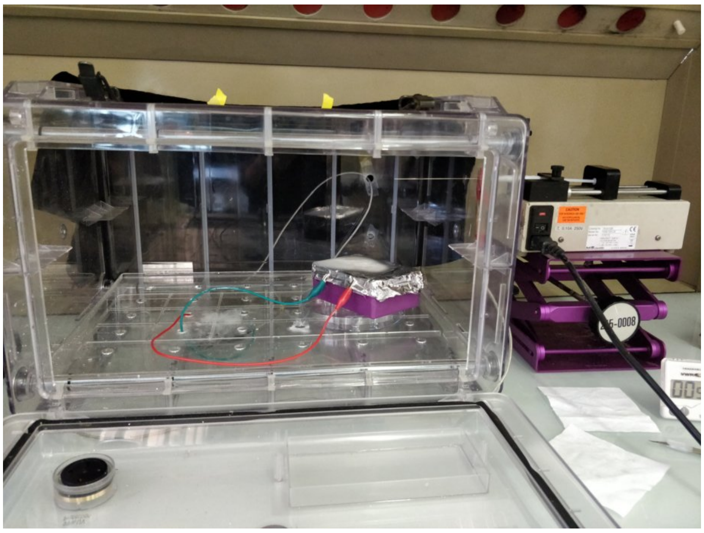

Figure 6.3: Vertical Electrospinning Setup

of solution per well. After incubation, they are rinsed three times with absolute ethanol and left to dry in the dessicator overnight.

Patches handling and conservation The patches are kept individually in 12-well plates, placed on adsorbent paper to prevent from attaching to the plastic dish (and destroying the fiber network). They should be kept for less than 3 months before use to ensure no degradation of the fibers. Before use, the patches are placed under UV-light (30 minutes on each side) for sterilization.

6.1.4 Microfluidic chip

a. 3D Printing

File generation All files were generated with the SolidWorks Software (Dassault Systemes) and exported into .STL files containing a mesh of the part. These files were opened in PreForm (FormLabs) and the parts were virtually placed on the 3D printer platform. For all prints we decided to not use any support and to print the back of the parts directly on the platform.

Printing For printing, we use the FormLabs2 with either Grey or Clear resin. The print was started when the resin was heated to 32 °C, with a resolution of 0.025 mm.

Post-treatment The parts were carefully detached from the platform with a razor blade and a metallic spatula, taking care not to scratch the platform. The parts were then placed in an IPA bath for about 5 minutes, and we used an IPA-filled wash bottle to spurt liquid into the smaller patterns and remove any resin residue. When all small patterns appear clearly (holes, egdes, etc...), we put the parts under UV light for 10 minutes on each side (beware not to let them heat, and split the UV exposures if necessary). The parts are then left one day close to a window for complete reticulation. Finally, they are bathed in water for 48 hours before use.

b. Cutter plotter

Positonning Place the PDMS sheet (Silex.co, UK) on the cutting mat, the blue layer (cover layer) face down. Use adhesive tape to maintain the sheet flat agains the mat. Manually set up the origin on the machine (Graphtec Cutting Plotter CE5000-60).

Cutting parameters We use the GraphTec Cutter Plotter with the 1.5 mm blade. The cutting parameters were optimized for the 0.1 mm sheet as: Offset=0; Velocity=4; Acceleration=1; Force=24, and Passages=3. After cutting, beware to remove any plastic residues on the PDMS parts.

1. Cut the lower layer **L4** and the patch-containing layer **PCL2**
2. Make sure that all holes are empty and that there is no residue of PDMS or plastic
3. Peel off the thin plastic cover layer of the lower layer and clean it with adhesive tape
4. Clean a 40x20 mm glass coverslip with an airgun
5. Functionalize both parts with plasma
6. Flip the PDMS part on top of the coverslip and align it
7. Gently press the PDMS against the glass starting from the center with the back of a razor blade, taking care to press on the side wall of the channels to ensure a good adherence
8. When there are no bubbles left, place the ensemble in the oven at 90 ˚C for 8-10 minutes
9. In the meantime, prepare the patch-contaning layer by laking sure that all holes are empty and that there is no residue of PDMS or plastic and clean this part with adhesive tape
10. Take the lower ensemble in the oven and remove the thick plastic supporting layer
11. Place it in the plasma with the patch-containing layer for functionalization
12. Assemble the two parts with the same technique as above. Be careful to press the PDMS around the small holes. When there are no bubbles left, place the ensemble in the oven at 90 ˚C for 8-10 minutes
13. Take the lower part in the oven and remove the thick plastic supporting layer and cover the channels with adhesive tape until use.

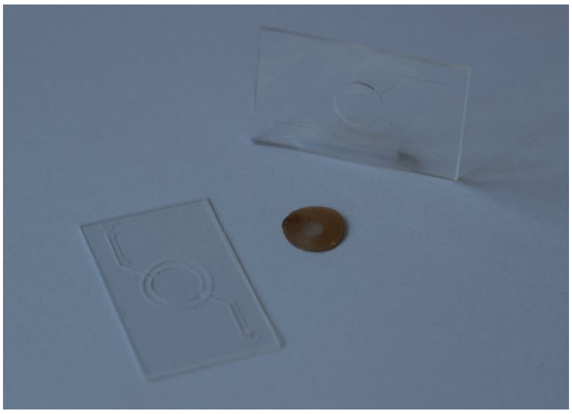

Figure 6.4: Final chip assembly

Assembling the upper part of the chip Firstly, we make the PDMS molded top part. It is replicated from a 3D-printed mold as follows:

1. Prepare PDMS in a 1:10 ratio (Sylgard)
2. Pour the PDMS on the mold to cover each part
3. Degas the PDMS under the dessicator for about 20 min
4. Gently deposit a cleaned glass slide on top of the PDMS, without generating bubbles between the glass and the PDMS
5. Align the glass slide with the pattern of the mold
6. Close the mold and apply pressure
7. Place in the oven at 80 ˚C for over 4 hours

Then, using the closing part (obtaine with the cutting plotter), we can assemble the top part in the following manner, respecting the order of the steps:

1. Take the closing layer **CL** and make sure that all holes are empty and that there is no residue of PDMS or plastic
2. Peel off the thin plastic cover layer
3. Clean this part with adhesive tape
4. Take the molded top part and pierce 0.75 mm holes in the two extremities of the channels
5. Clean the molded top part
6. Functionalize both parts with plasma
7. Flip the closing layer on top of the PDMS top part and carefully align them
8. Gently press the PDMS-sheet against the top part, starting from the center with the back of a razor blade
9. Take care to press on the side wall of the channels to ensure a good adherence
10. When there are no bubbles left, place the ensemble in the oven at 90 ˚C

11. After 8-10 minutes, peel off the thick plastic supporting layer.
12. Cover the channels with adhesive tape until use.

6.1.5 Chip assembly

The chip can be autoclaved or UV-sterilized before use. The clamp can be cleaned with ethanol. In order to insert the patch and connect the chip, there are precise operations that should be followed in this exact order:

- Clean top and bottom part with scotch tape
- Fill in the lower channels with medium
- Place the patch. You can put a drop of medium on the bottom of the patch to avoid bubbles
- Align the top with respect to the entry points for the lower channels
- Apply pressure on the surface with a tweezer to release the air and seal the parts together
- Fill two small tubes with needle pins with medium. Place them in the lower channels
- Place the chip in the lower clamp
- Thread the tubes in their respective holes in the upper clamp
- Close the upper clamp
- Fill in the input and output tubes, and connect them to the small tubes
- Place the chip in the incubator

a. Medium flow actuation

Here is the detailed protocol to install the flow in the Alveoli-on-a-chip.

Placing the patch in the chip When inserting the patch in the chip, there are a million things that could go wrong. That is why I developed an extremely detailed protocol, that may seem a bit tedious, but is actually the necessary to ensure perfect integration of the patch in the chip. I will not detail how we came up to this protocol but it was essentially by trying and failing. In order to avoid contamination, all the material used is sterile. Microfabricated parts are also cleaned from dust using adhesive tape. Then the protocol is as follows:

1. Take some warm medium (see **A** in Figure 6.5) and fill the channels of the lower part (**E**)
2. Deposit 12 μL of medium (approximately the volume of the lower chamber) on the glass coverslip, in the lower chamber (**E**)
3. Take a patch outside of its culture plate (**G**)
4. With the edge of the patch, gently touch a sterile gauze (**H**) to remove any excess of medium
5. Place the patch carefully in the medium chamber on top of the medium. *NB: if the patch is too big to fit in the patch-containing layer (due to a manufacturing defect) you can take sterile scissors to delicately reduce its outer diameter.*

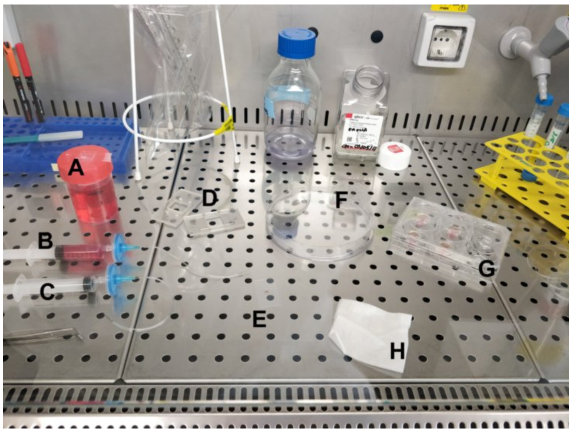

Figure 6.5: Integration of the patch in the chip

6. Take a sterile gauze (**H**) to remove any excess of medium that would have leaked outside the lower chamber (**E**)
7. Take the top PDMS part with two tweezers (each holding a short edge), and come above the patch
8. Delicately put down the top part starting with the center and use the back of a tweezer to smooth the top part and remove any bubble between the two PDMS parts
9. Prepare two Tygon tubes of about 5 cm long, with a metallic pins to one of their extremities and place them delicately at the lower channel input and output (see Figure 6.6)
10. Place the ensemble in the lower clamp (see Figure 6.6)

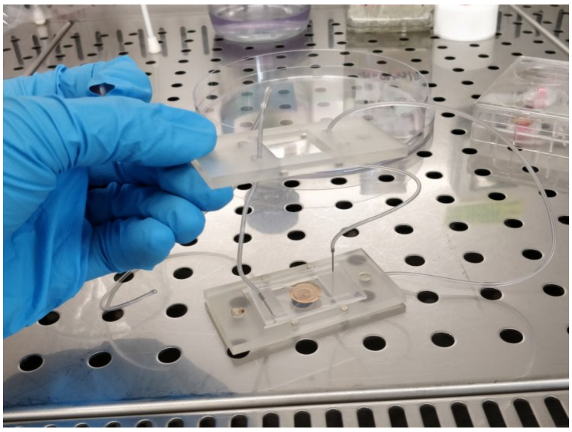

Figure 6.6: Integration of the chip in the clamp

10. Thread the two Tygon tubes through the top part of the clamp and gently close it (see Figure 6.6)
11. Once the clamp closed, take one 5 cm long tube and connect it to a syringe containing some medium (equipped with a 0.22 µ*m* filter) (**B**)
12. Plug the other tube (5 cm long) to an empty syringe with a filter (**C**)
13. Hold the clamp vertical, with the exit channel up
14. Gently push medium in with the syringe (**B**) and gently aspirate with the empty syringe (**C**)
15. Continue until all bubbles are removed
16. Place the chip and its clamp (**D+E**) in a big Petri dish (**F**) to prevent leakages
17. Place the ensemble in the incubator for static culture, or move on to the actuation protocol

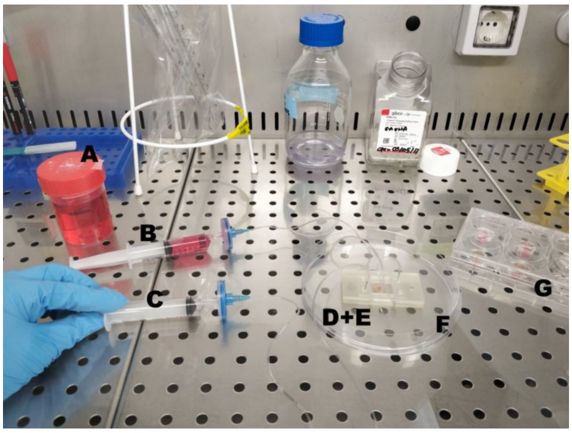

Figure 6.7: Removing the bubbles in the lower part of the chip

Preparing the flow actuator Before we can connect the chip to the flow actuator, we need to carefully prepare the whole setup. Here we detail the protocol to connect 4 chips in parallel. Firstly we need to prepare the medium input:

1. Prepare four sterile Tygon tubes of about 1 meter long, with metallic pins at one of their extremities (see **N** on Figure 6.8)
2. Prepare a 50 mL syringe (**I**) filled with medium (usually ECGM with Dexamethasone) and place a 0.22 µ*m* filter at its tip
3. Connect it to a microfluidic distributor (**K**) (1 input and 4 output channels) with a sterile tube
4. At each output, place a sterile connector (**L**) (female-female) and a syringe tip (**M**) and connect the Tygon tubes (**N**)
5. Leave free about 50 cm of tube and roll up the extra length of each tube in a small coil (**O**), leaving about 15 cm of length after the coil, where the metal pin is
6. Mark the input and the output of each 1 m tube for easier handling of the chips

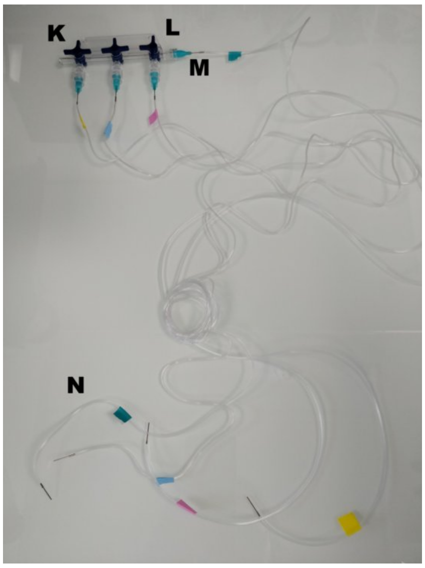

Figure 6.8: Medium distribution system

The second step is to prepare a setup collecting the medium flowing through the chip into reservoirs:

1. Prepare four sterile 50 mL Falcon tubes (see (**Q**) on Figure 6.9)
2. Prepare a sterile tube holder and put the Falcons inside (**R**)
3. Pierce 1 mm wide holes in the cap of the Falcon tubes **S** with a mechanical drill
4. Clean the caps from any dust
5. Prepare four 30 cm long Tygon tubes with a metal pin on one extremity (**P**)
6. Thread the tubes (**P**) in the caps (**S**) and place them back on the tubes

Figure 6.9: Preparing the reservoirs for medium collection

Connect the chip to the flow actuator In order to connect the chips to continuous medium perfusion, there are a few other steps to take. Here is the protocol for one chip, to be repeated with the other ones.

1. Place a patch inside the chip and close them with the clamp according to the protocol detailed above (see Figure 6.7)
2. Take the chip (**D+E**) in its dish (**F**) out of the biological hood and come next to the incubator
3. Take the tube holder (**R**) with a Falcon tube (**Q**) and connect the 30 cm tube (**P**) to the output tube of the chip
4. Press on the big 50 mL syringe (**I**) until the medium input tube **N** is filled and start dripping at the end of the coil (**O**)
5. Connect it to a chip with the 5 cm entry tube
6. Take the tube holder (**R**) and the Petri dish (**F**) containing the chips and place them in the incubator (see Figure 6.11)
7. Place the dish on the top shelf and the tube holder right below (see Figure 6.11)
8. Take all input tubes and use a tape to fix them to the outside of the incubator, just above the glass door, so that they do not fall into the door hinge
9. Start the actuator, here a syringe pump (**J**)

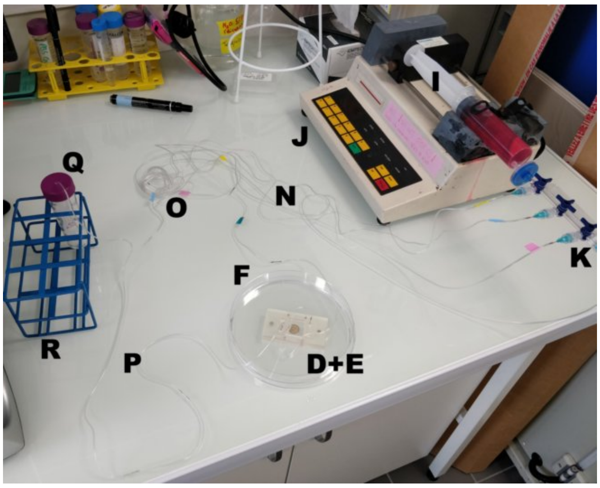

Figure 6.10: Example of a single chip connected to the complete medium circuit

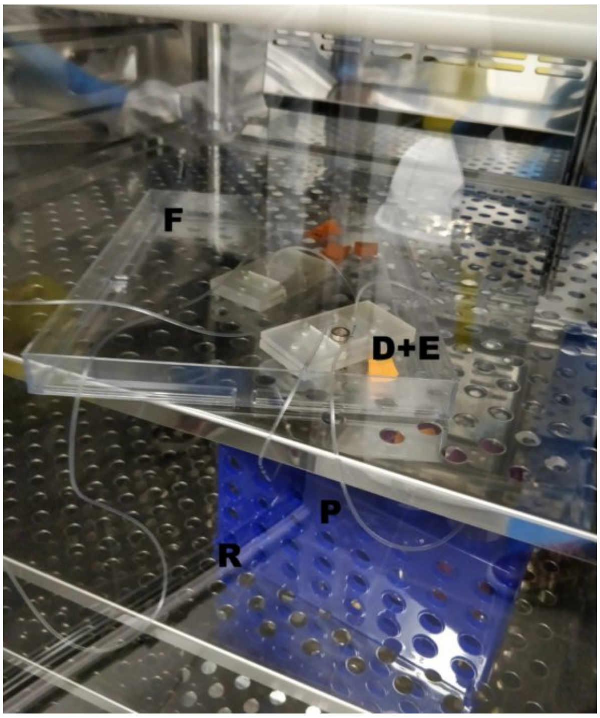

Figure 6.11: Two Alveoli-on-a-chip and their reservoirs in the incubator

Long-term flow maintenance Once the chips in place and fully connected, there are a few things to take care of. Firstly, the 50 mL syringe(s) should be protected with aluminum foil to protect it from the light. The medium is not warmed but it will heat gradually as it passes inside the coil that is placed in the incubator. Moreover, as the syringe pump heats up when used, the medium is not extremely cold in the first place.

It is important to monitor the flow rate to know when the Falcon tubes in the incubator will be full (and therefore change them). Similarly, the 50 mL syringe should be changed regularly. Each time, we used new tubes and new syringes to avoid contaminations.

6.2 Supplementary Figures

6.2.1 Technical drawings: CAD specifications

In this section are all the CAD drawings of the Chapter 3, in bigger scale for improved reading.

a. Low channels

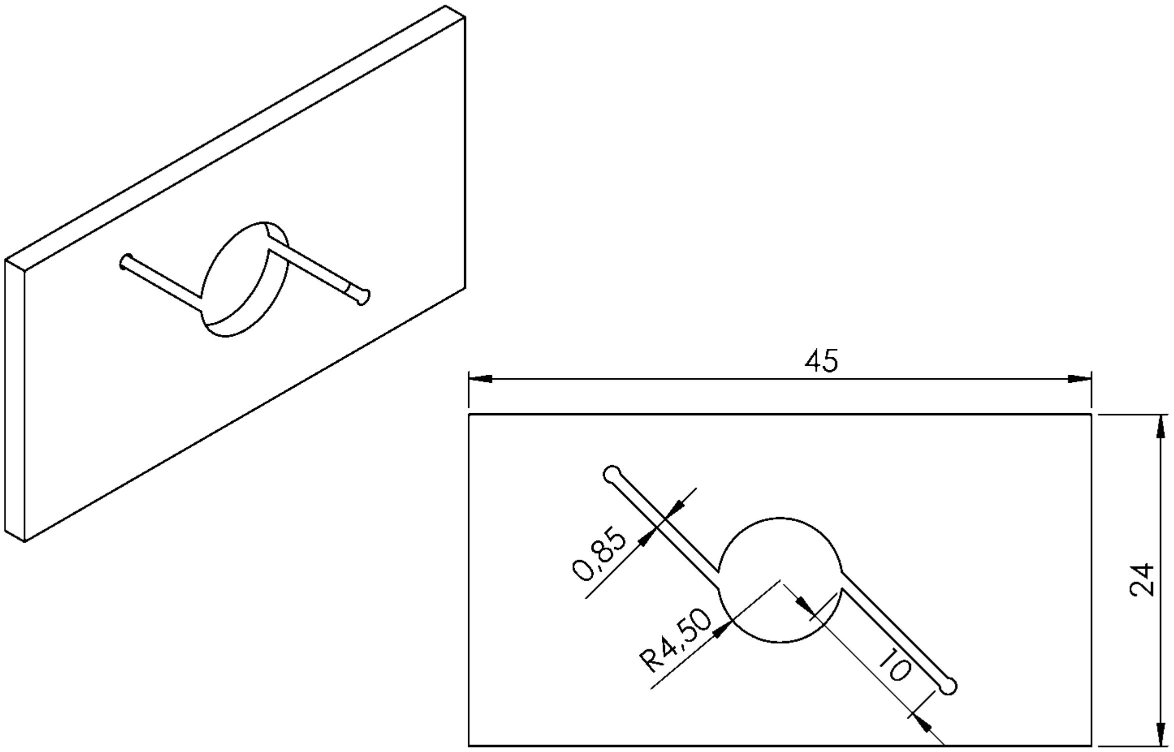

Figure 6.12: Low channels **L1**

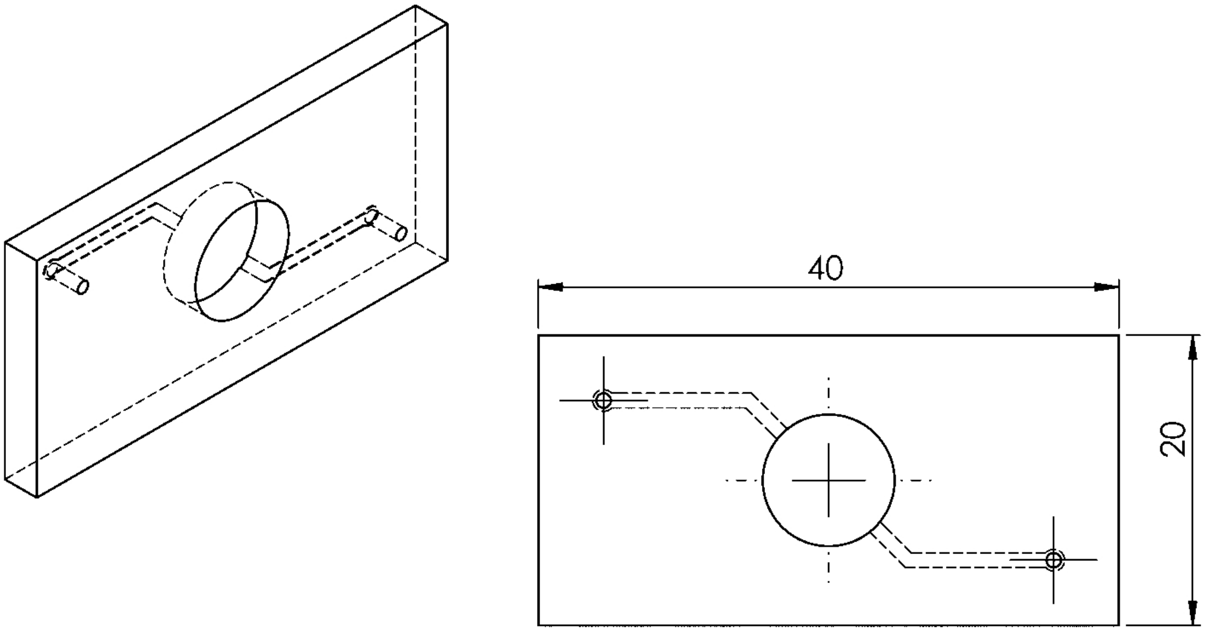

Figure 6.13: Low channels **L2**

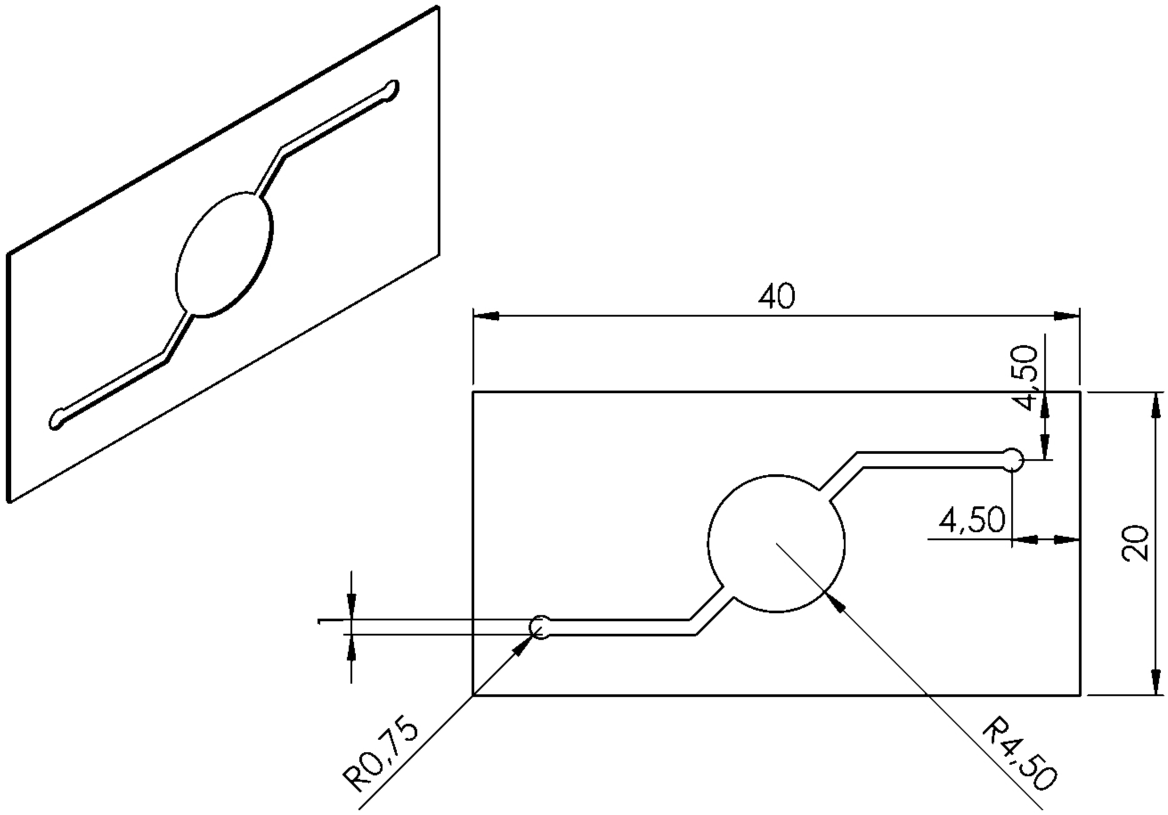

Figure 6.14: Low channels **L4**

b. Middle layers

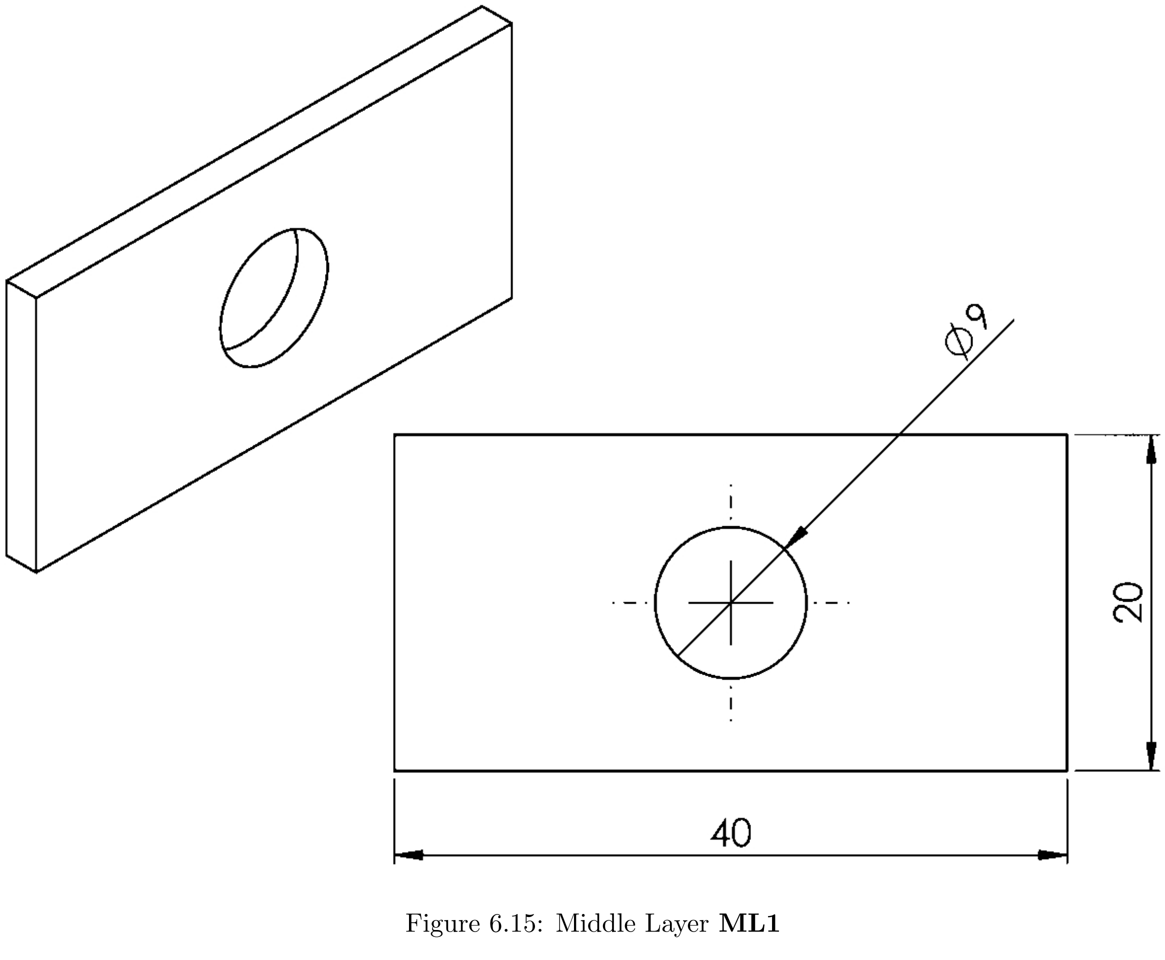

Figure 6.15: Middle Layer **ML1**

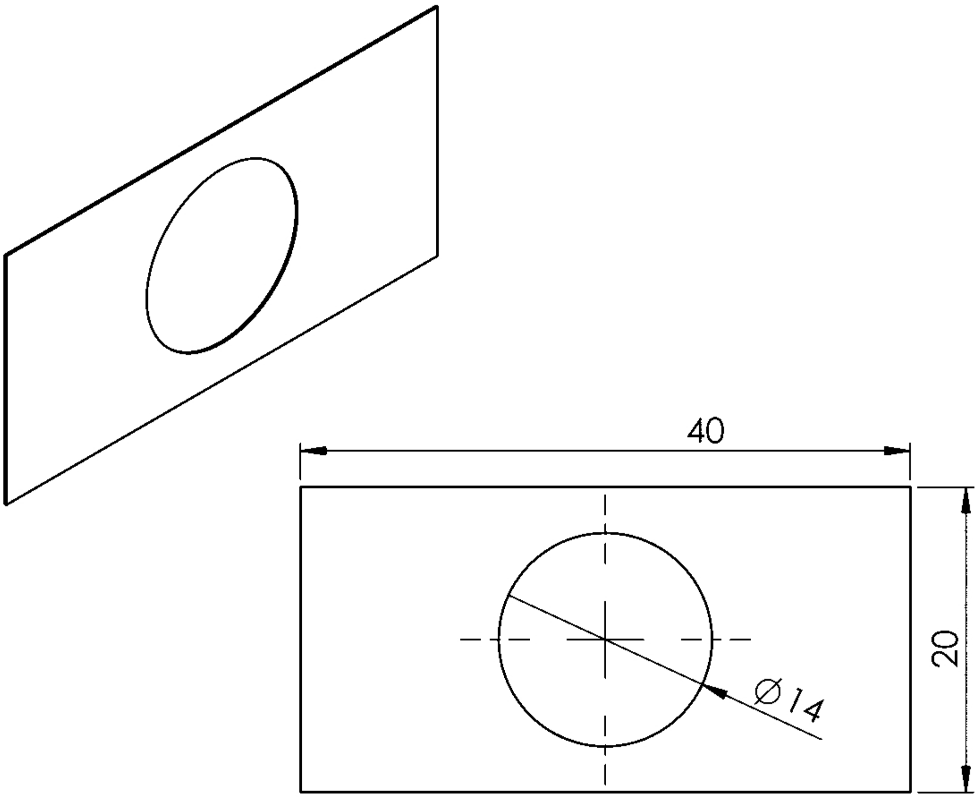

Figure 6.16: Patch-Containing Layer **PCL1**

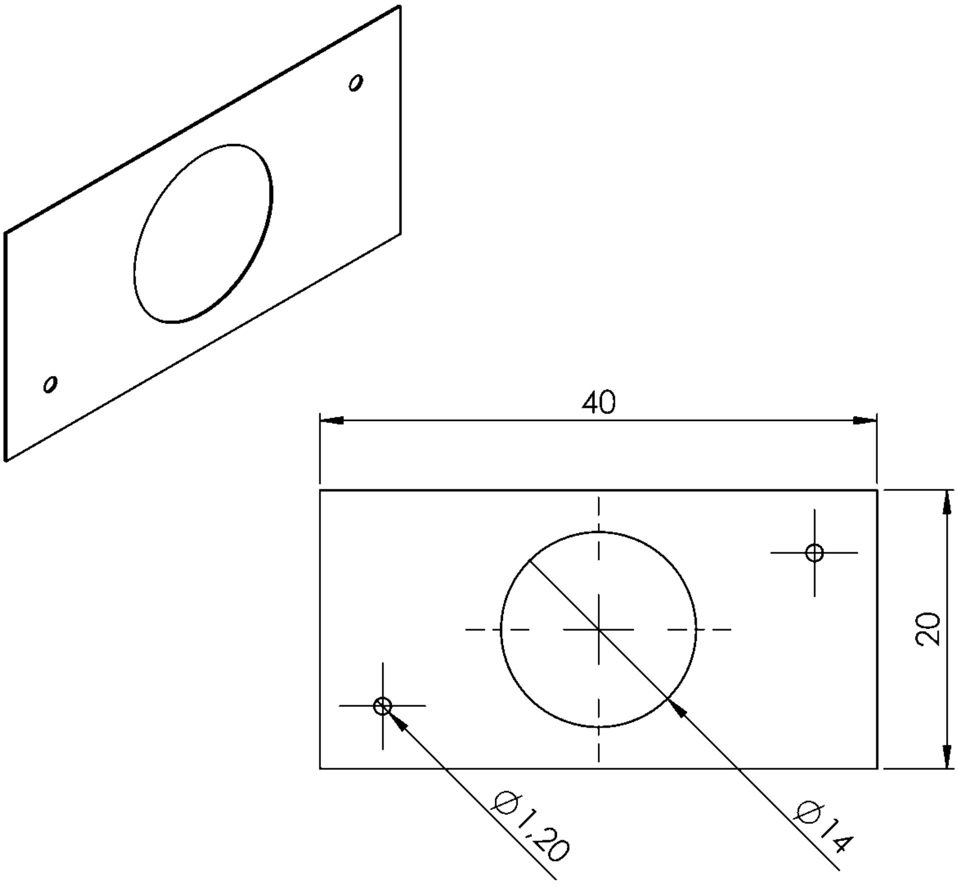

Figure 6.17: Patch-Containing Layer **PCL2**

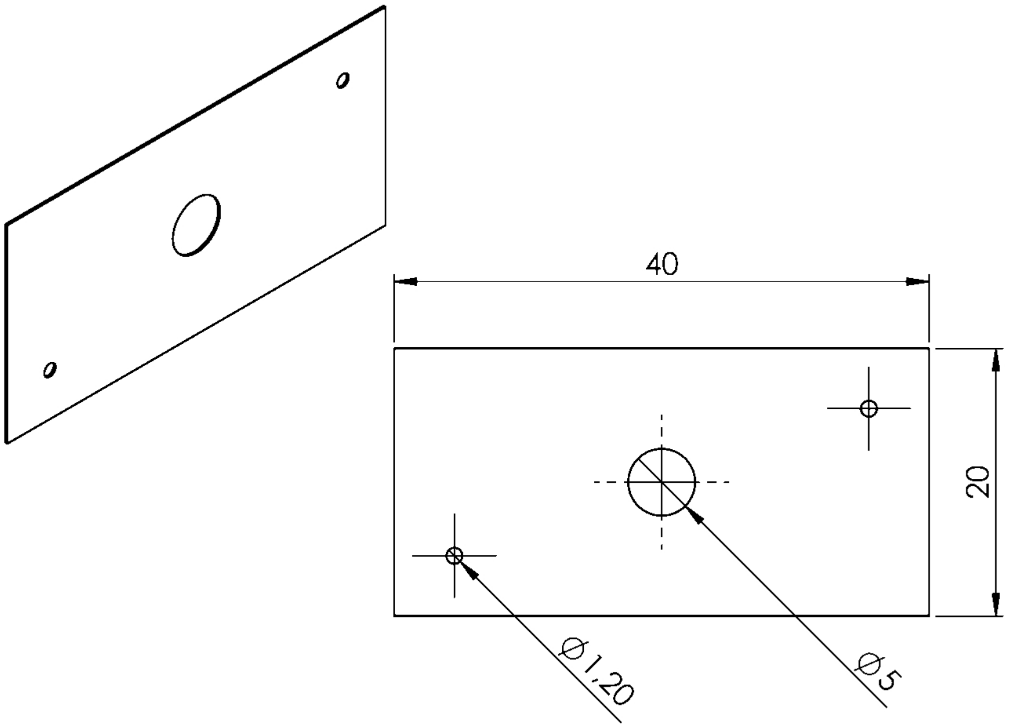

Figure 6.18: Closing Layer **CL2**

c. Top channels

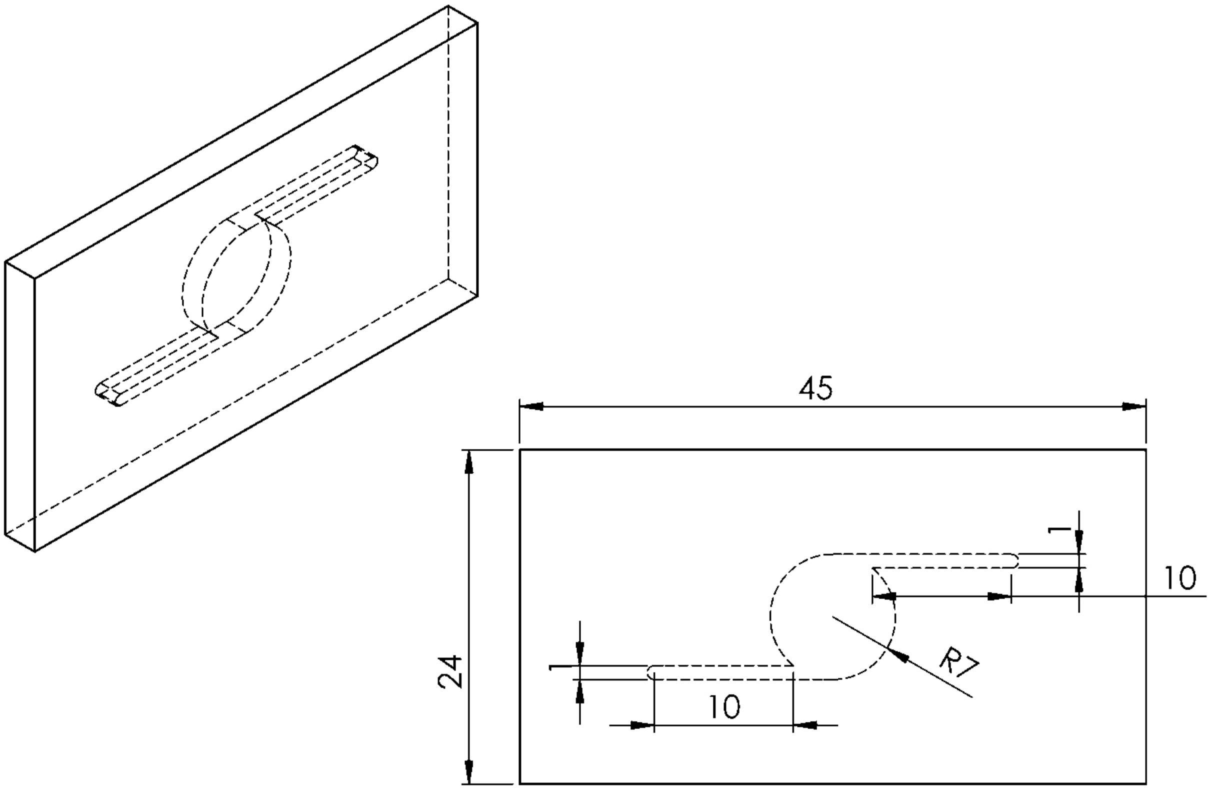

Figure 6.19: Top channels **T1**

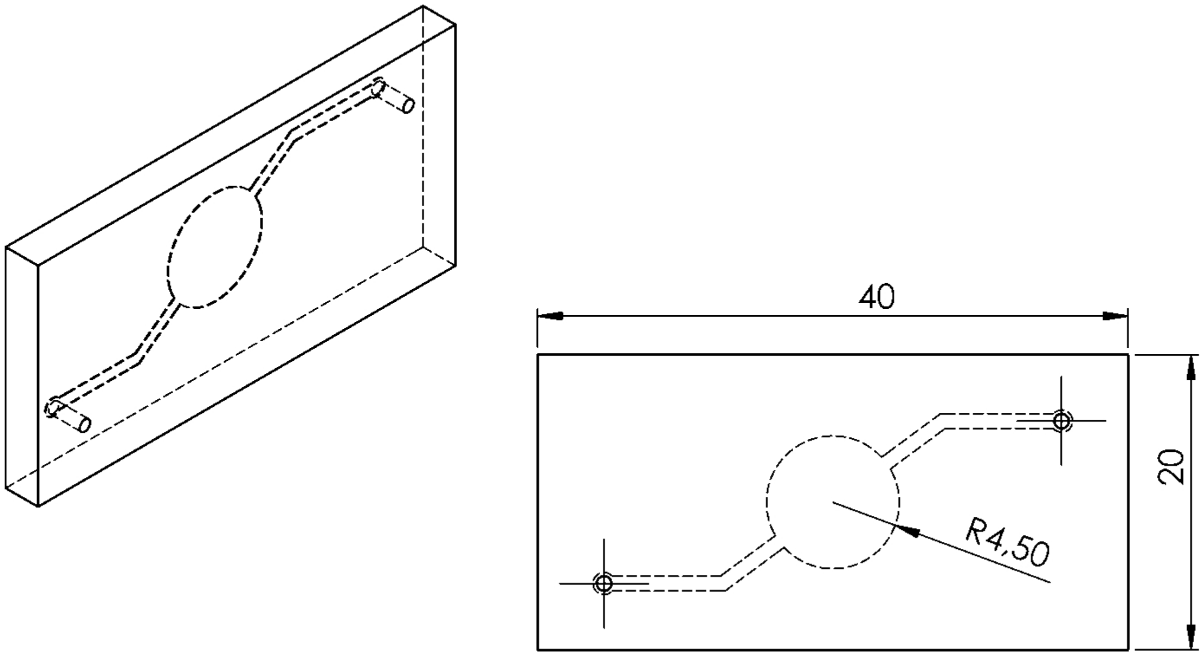

Figure 6.20: Top channels **T2**

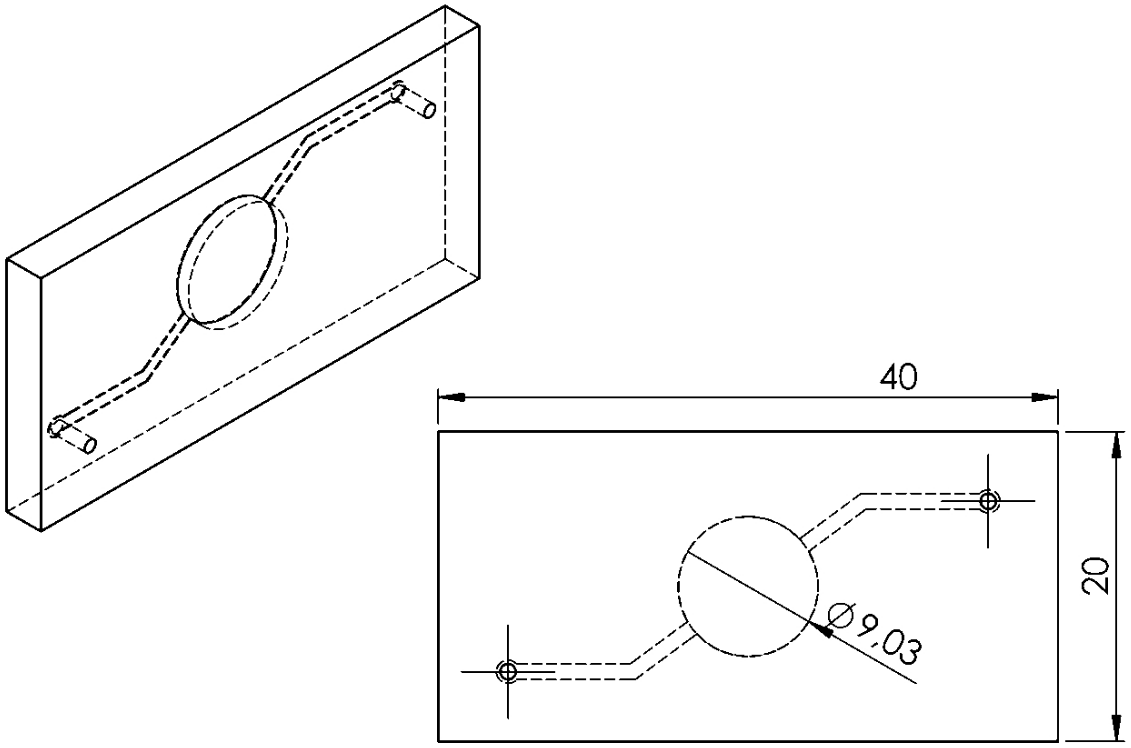

Figure 6.21: Top channels **T3**

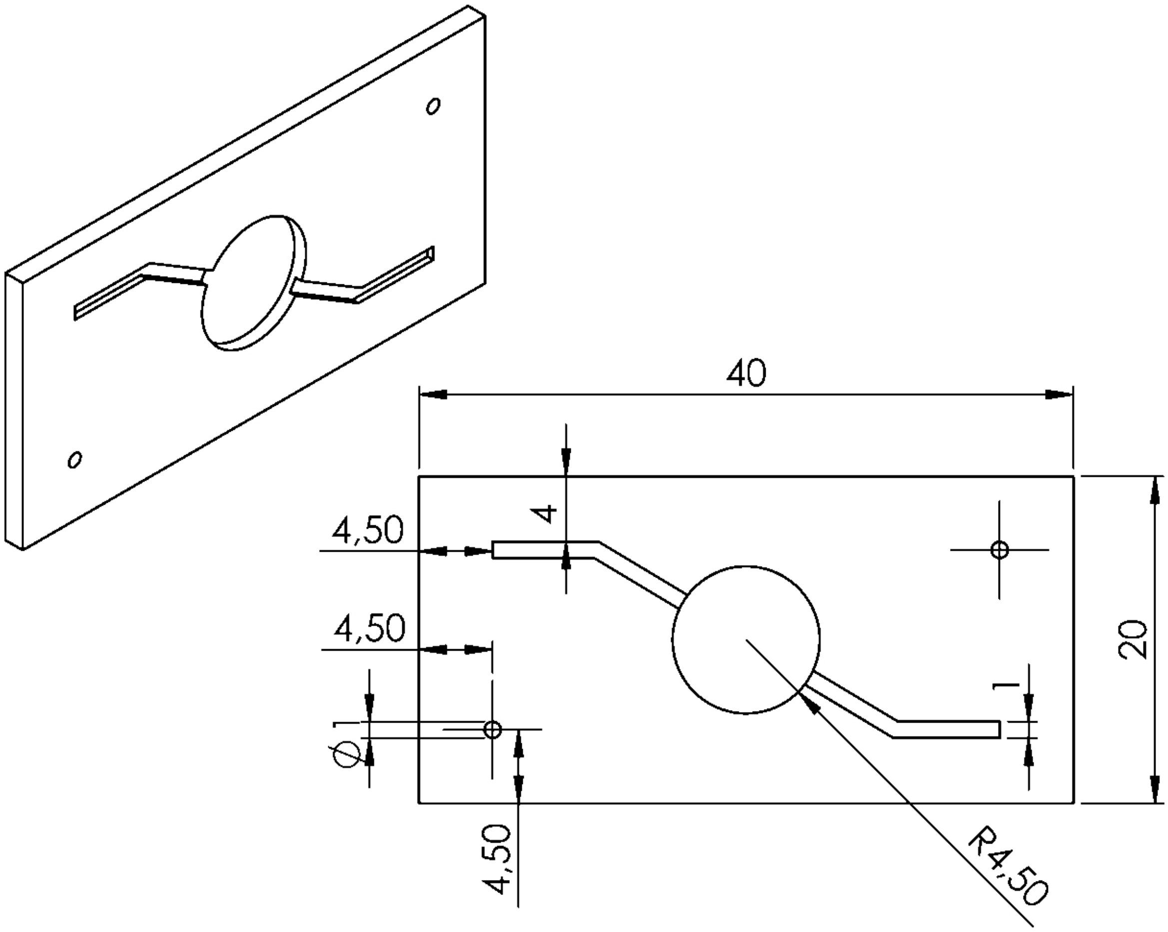

Figure 6.22: Top channels **T4**

d. Clamps

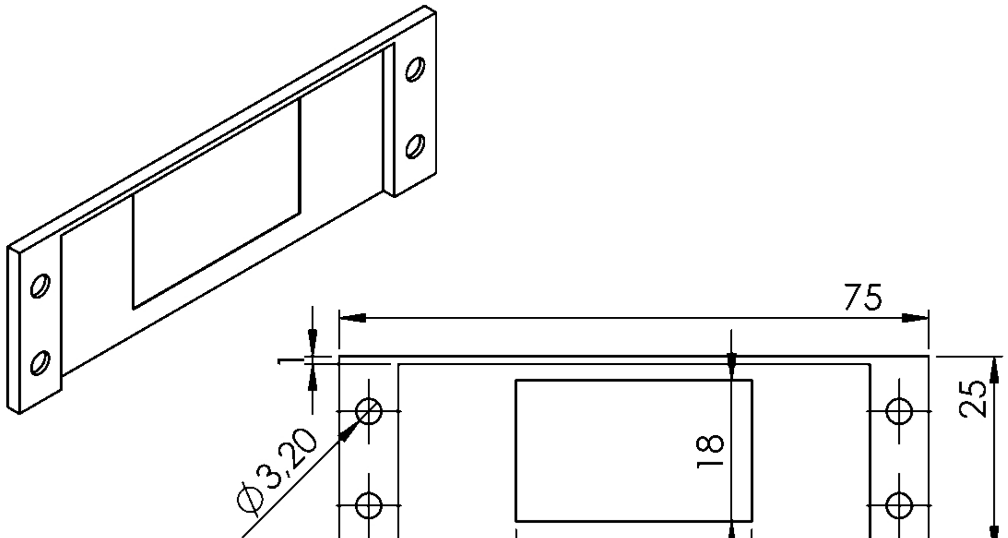

Figure 6.23: First Clamp, Low part **C1 Low**

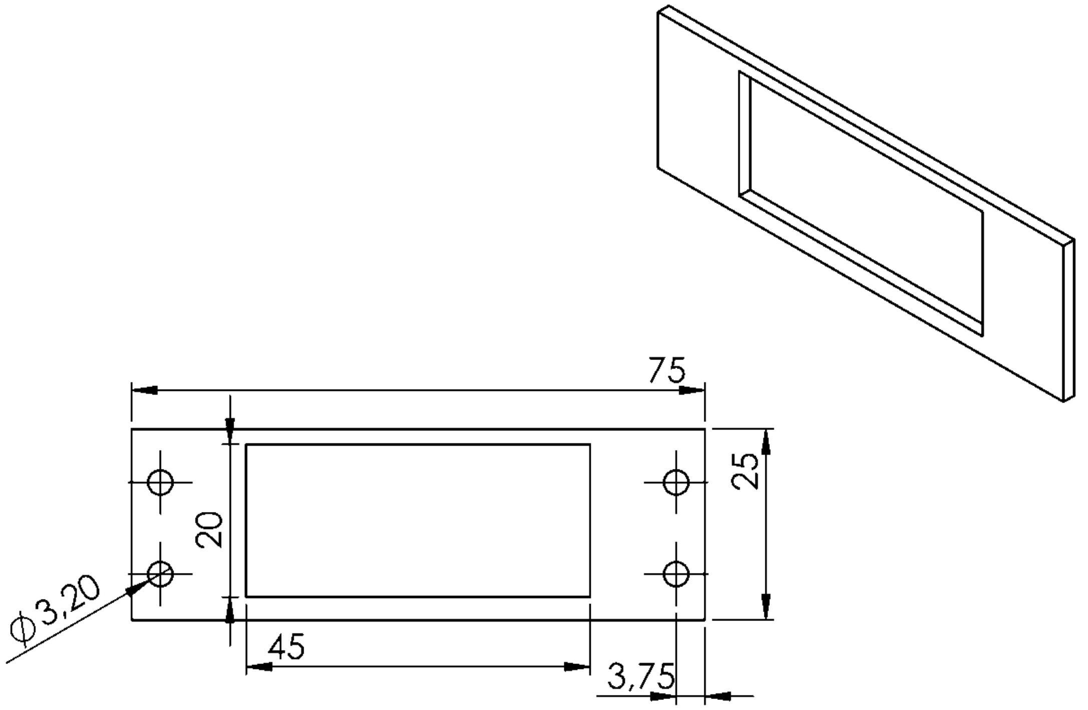

Figure 6.24: First Clamp, Top part **C1 Top**

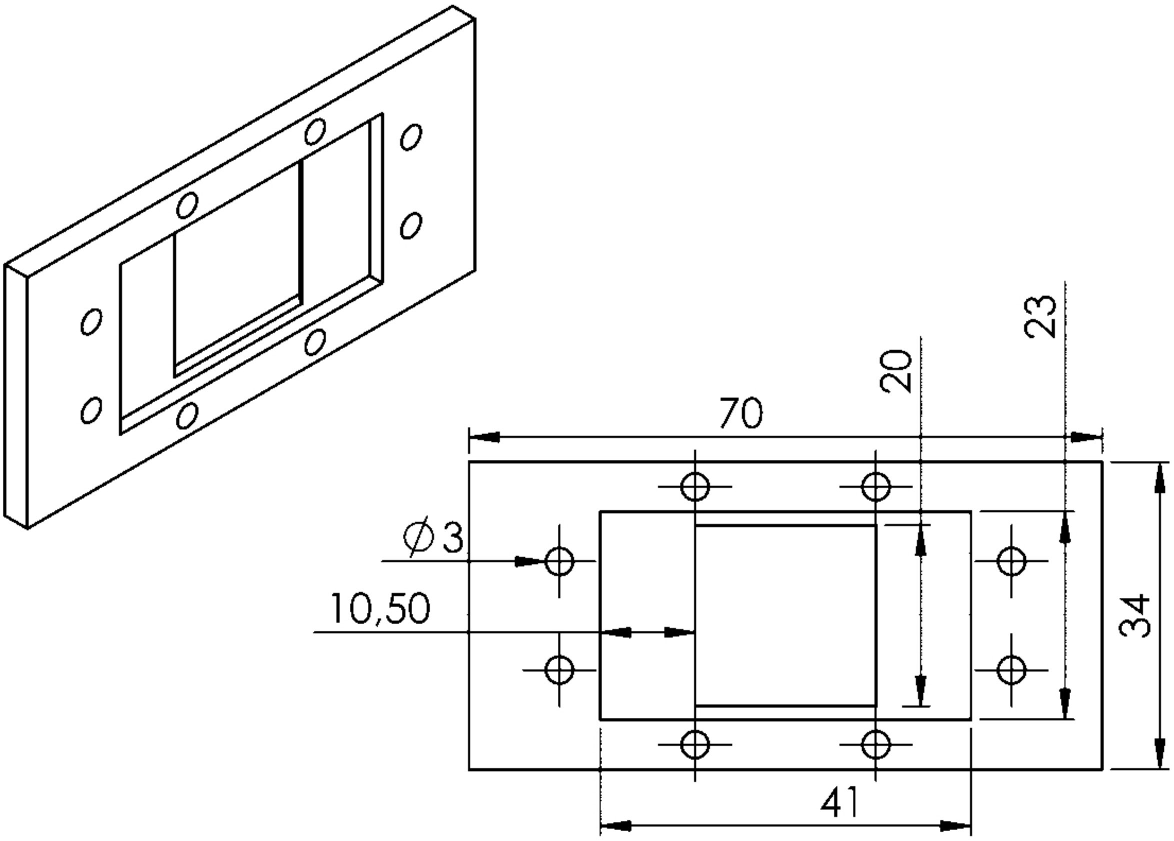

Figure 6.25: Second Clamp, Low part **C2 Low**

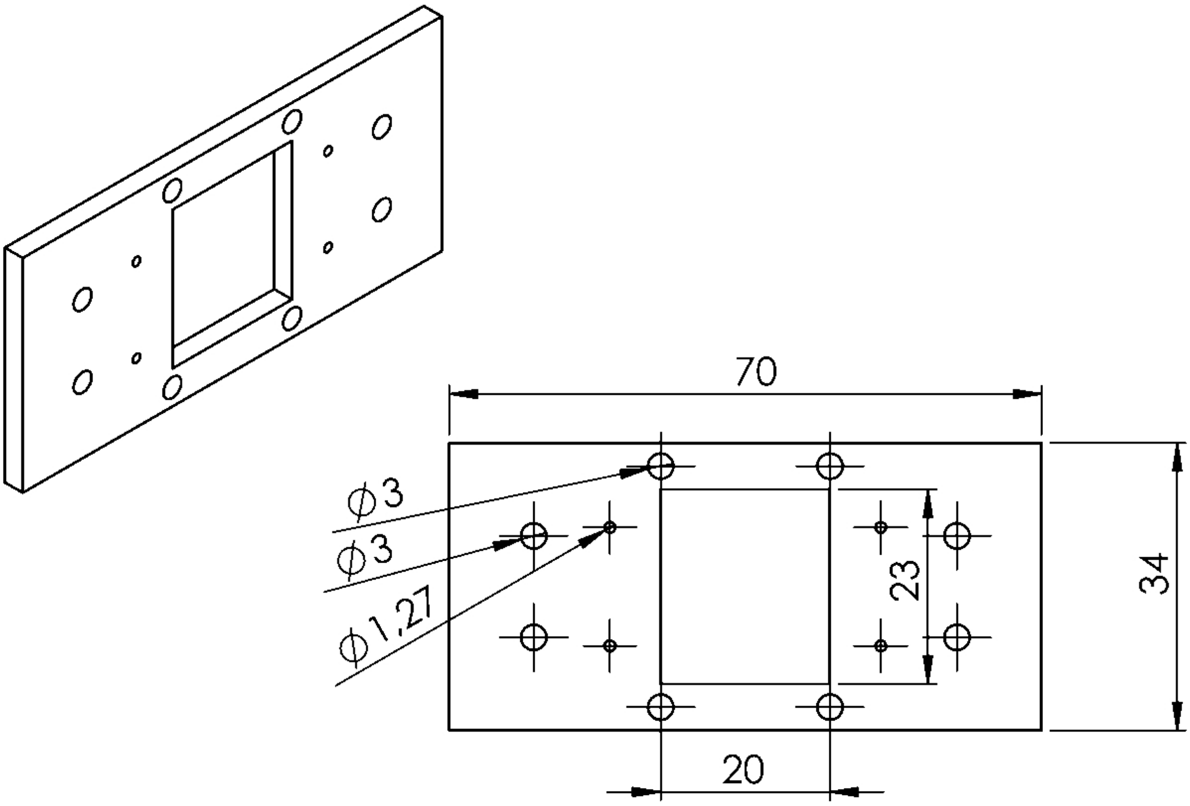

Figure 6.26: Second Clamp, Top part **C2 Top**

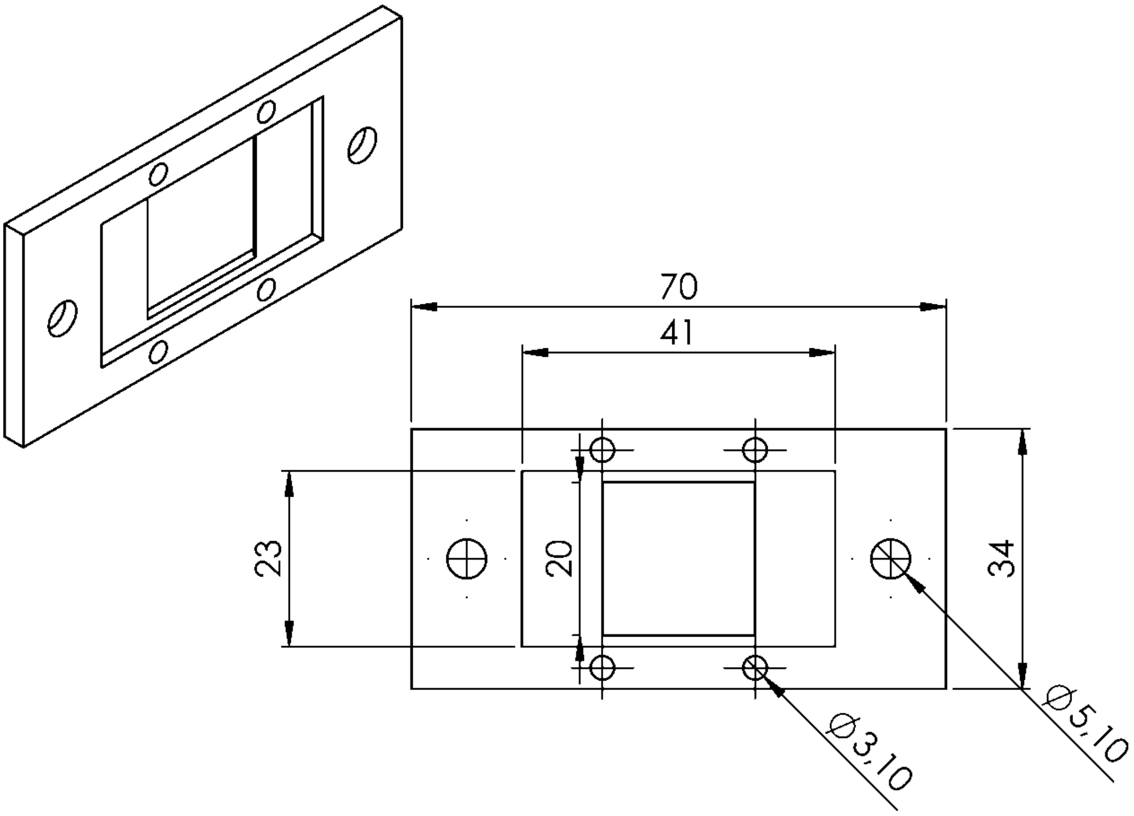

Figure 6.27: Final Clamp, Low part **C3 Low**

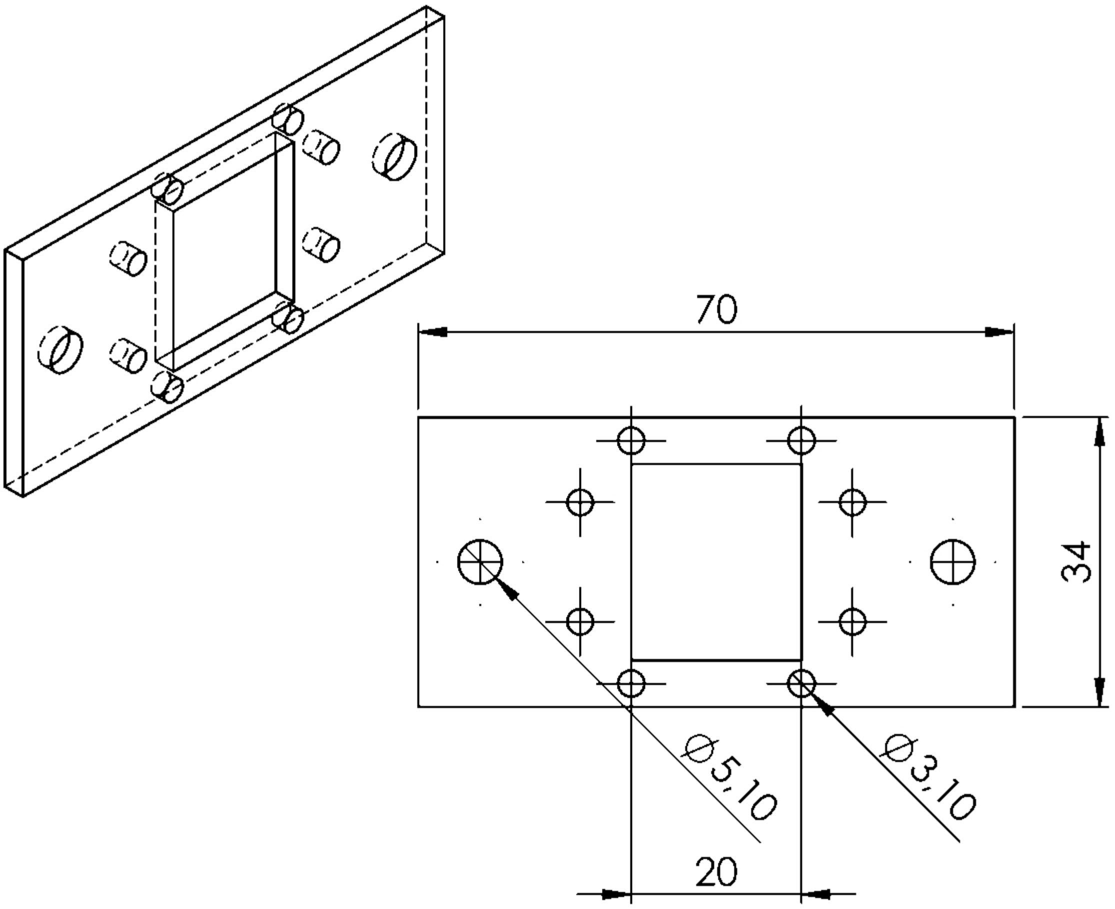

Figure 6.28: Final Clamp, Top part **C3 Top**

e. PDMS Molds

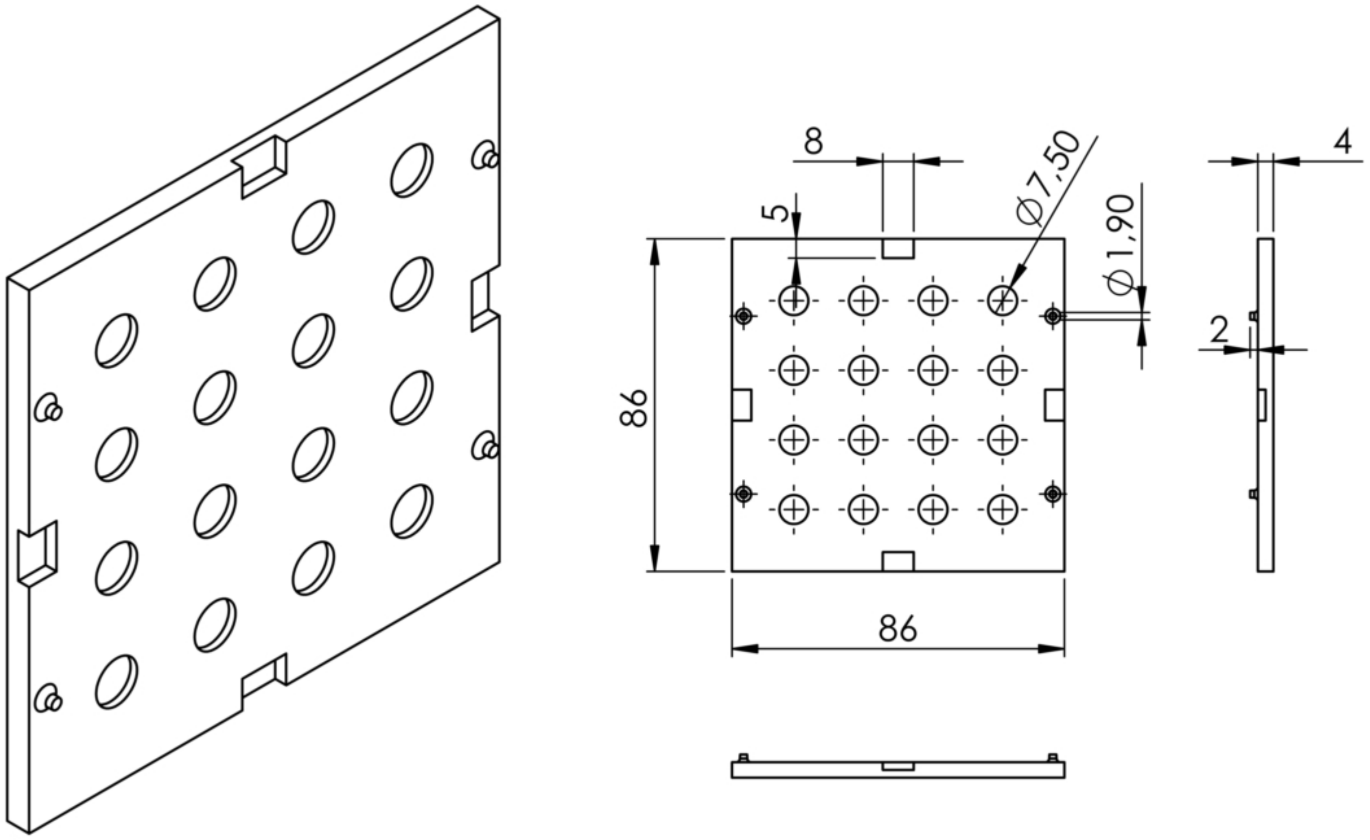

Figure 6.29: PDMS ring mold, Low part

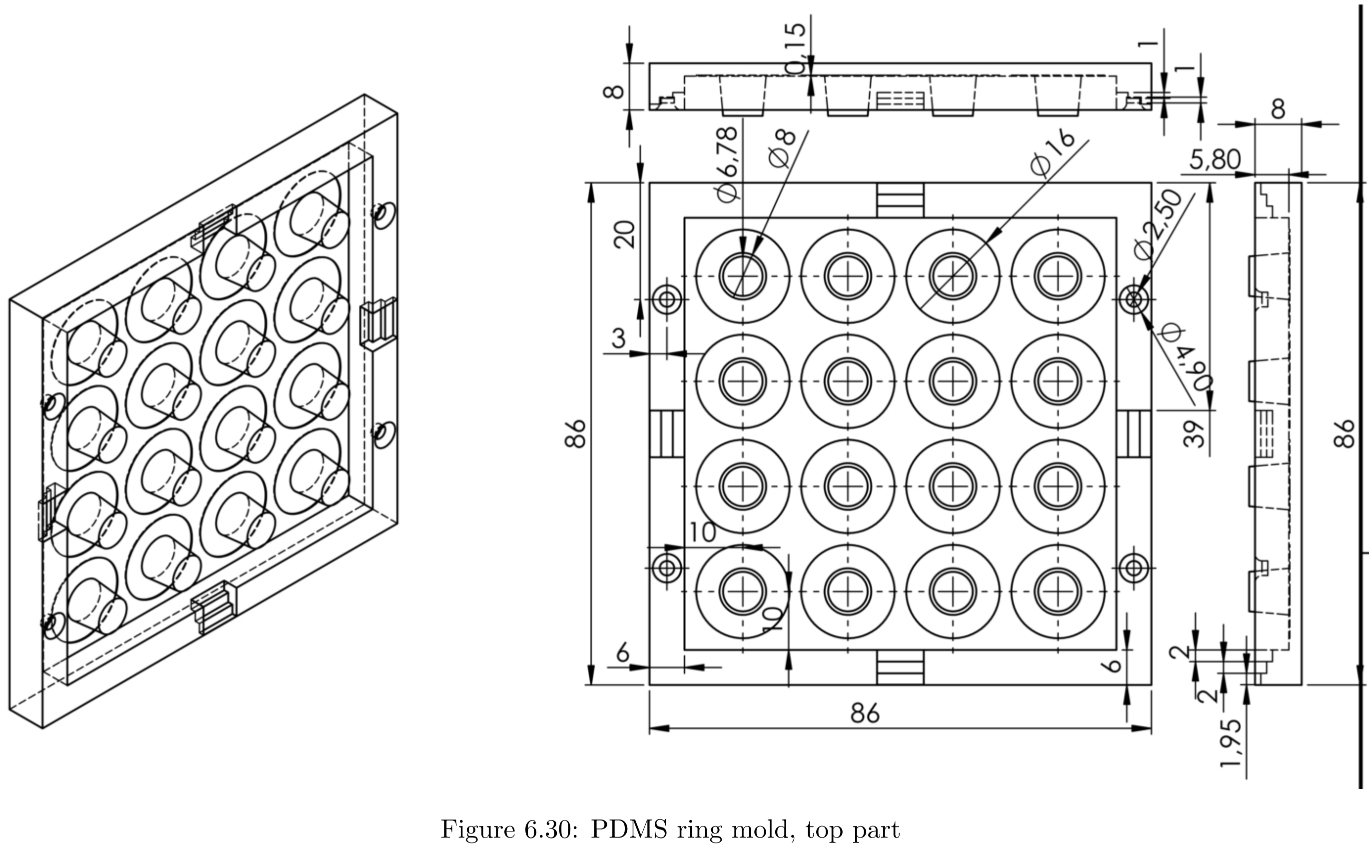

Figure 6.30: PDMS ring mold, top part

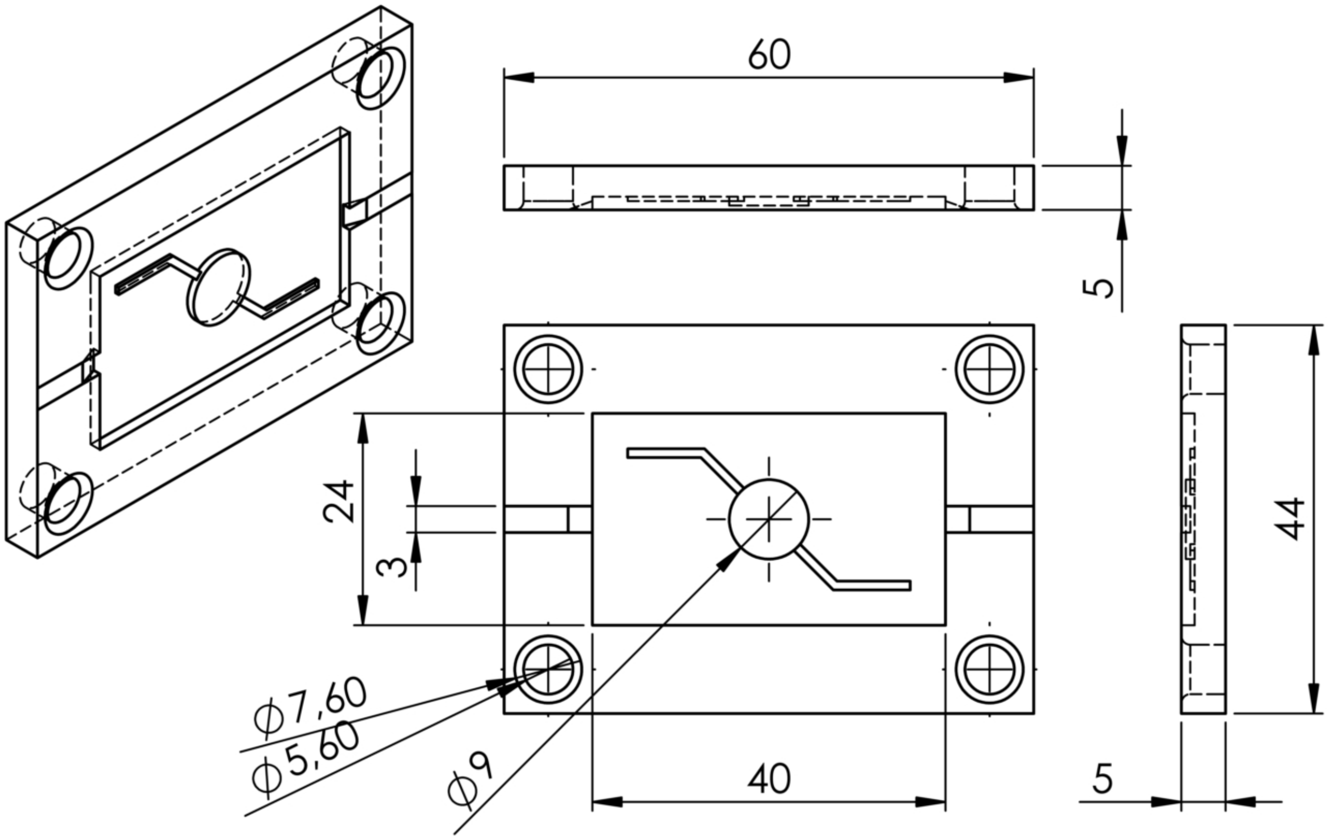

Figure 6.31: Mold for the PDMS top part of the microfluidic chip **M1**

6.2.2 More data on iPSC

a. Detailed explanation of the method used for iPSC discovery

In their paper published in 2006[137], Pr. Yamanaka and Pr. Takahashi (Kyoto University) reported the generation of pluripotent stem cells from fibroblast cultures in mice. The original and straightforward method that they used for this discovery is fascinating.

1. They selected 24 genes as candidates for factors inducing pluripotency in somatic cells (based on the hypothesis that they also play pivotal roles in the maintenance of embryonic stem cell (ESC) identity).
2. They inserted a gene for resistance to G418 (an antibiotic) into the *Fbx15* gene (a gene expressed in mouse ESC and early embryos, but which is dispensable for maintenance of pluripotency and mouse development) by homologous recombination. Therefore, only cells where the *Fbx15* locus was activated (*i.e.* ESCs) would resist to G418.
3. Then they introduced each of the 24 genes separately in Mouse Embryonic Fibroblasts (MEFs) in the *Fbx15* modified cells. None resisted G418, indicating that a single of these gene is not enough to activate the *Fbx15* locus.
4. However, when introducing all of the 24 genes together, they obtained some surviving colonies. From these colonies, after selection of the clones with ESC morphologies (round shape, large nucleoli and scant cytoplasm), they obtained a stable colony of proliferative cells expressing typical ESC genetic markers: *Oct3/4, Nanog, E-Ras, Cripto, Dax1, Fgf4* and *Zfp296.* This indicates that in these 24 genes, some are sufficient to induce cell pluripotency.
5. Then they examined the effect on the formation of G418-resistant colonies when withdrawing the 24 genes one at a time. For 10 genes, the removal resulted in zero or little colonies: these genes were therefore seen as essential.
6. The combination of these 10 genes produced more colonies than the combination of the previous 24 genes. From hereafter, the cells were produced with this pool of 10 genes.
7. As in step 5, they examined the withdrawal of individual factors from the 10-factor pool transduced into MEFs. Removing *Oct3/4* or *Klf4* resulted in no colonies. Removing *Sox2* resulted in very little colonies left. *c-Myc* removal still produced some colonies but these did not have an ESC-like morphology. These four factors were then considered crucial to induce pluripotent stem cells.

8. When using these 4 factors they obtained a similar number of colonies as with the pool of 10 genes. No combination of 2 factors produced as many colonies. Removal of either *Klf4* or *Oct3/4* produced only one colony that could not be maintained in culture. However, removal of *c-Myc* or *Sox2* produced numerous colonies, but these did not exhibit ESC-like morphologies.
9. These newly generated cells (with 3 factors) were then introduced in a mouse for teratoma formation. Not all of the clones produced endoderm, mesoderm and ectoderm. This indicated that, although *Oct3/4*, *c-Myc* and *Klf4* can induce the expression of ESC markers, they are not sufficient to induce pluripotency. The four factors (c-My*Sox2* included) were then considered both sufficient and necessary.
10. Cells transduced with the four factors produced iPSC that were positive for alkaline phosphatase (an enzyme highly present on undifferentiated pluripotent stem cells membranes) and that could differentiate into all three germ layers in vitro. These four factors were concluded to be the minimum essential for induced pluripotent stem cell generations.

b. Detailed reprogramming methods

Reprogramming methods In order to obtain pluripotent cells, we need to reprogram adult cells to a stem cell state. To this day, there are three different methods to reprogram somatic cells: nuclear transfer, cell fusion and direct reprogramming.

Nuclear transfer The Somatic Cell Nuclear Transfer is a manual technique that consists in removing the DNA of an oocyte and injecting new DNA in its place ([142] , [143]). To obtain pluripotent stem cells, we use the DNA of a zygote. This technique has the advantage to produce cells that are identical to embryonic stem cells (ESCs), but it is highly technical and requires oocytes and zygotes as a source material, which raises both ethical and cost concerns.

Cell fusion The cell fusion method consists in fusing a fibroblast and an embryonic stem cell in order to obtain an ESC-like cell [144]. This process is relatively easy, but produces tetraploid cells, which limits the use for clinical purposes. Moreover, it seems that the hybrid cells might be preferentially committed to the lineage of the somatic cells that were fused with the pluripotent cells under differentiation-inducing conditions.

Direct reprogramming Finally the direct reprogramming method is the transformation of somatic cells into stem cells by direct modification of the cell's genome through genetic material encoding for an pluripotent stem cell state. Several genetic materials can be used: reprogramming protein factors [104], recombinant proteins [145], microRNA [146], self-replicating polycistronic RNA [200] and low-molecular weight biologically active substances [201]. There are several techniques to transfect the type of genetic material chosen into the donor cells. I will detail here several techniques for direct reprogramming. These are high-efficiency techniques that are used for generating large banks of reprogrammed cells.

c. Comparison of direct reprogramming techniques

Adenoviruses and lentiviruses iPSC discovery was made through the use of reprogramming protein factors transfected via an adenovirus. However, adenovirus is a relatively low efficiency method of generating iPSC, so researchers turned to more efficient retroviruses or lentiviruses. Indeed, lentiviruses randomly insert the reprogramming genes in the host's genome, forcing the expression of the Yamanaka factors. This technique is very reproducible and is effective in reprogramming even the hardest-to-reprogram somatic cells.
This technique is however limited because it integrates DNA into the host cell's genome, which can be problematic for subsequent experiments planned with the iPSC. Indeed, the reprogramming factors are produced by genes which, on mature differentiated cells, are oncogenes. Therefore DNA reprogramming via these viruses is a high-efficiency technique, but cannot be used for clinical grade research.
N.B: Researchers at EMD Millipore are currently working on a method with a lentiviral-based stem cell reprogramming system, that offers the option to excise the four Yamanaka factors out of the genome after iPSC generation.

Episomal DNA Reprogramming by delivering episomal DNA (*i.e.* DNA that will not be inserted in the genome) for the expression of the Yamanaka factors is a nearly integration-free means of generating iPSC. These DNA plasmids are virus-free, without the risk of transgenic sequences inserted into the target cell genome. Indeed the replication is stable, and takes place outside the nuclei. Generally, only a small number of transfections are necessary, and the chance of integration into the host cell genome is slight. However, these reprogramming plasmids have a low efficiency, (especially when cells are not cultured on MEFs) and the chance of genomic integration using episomal DNA is not zero, which means that in such cases, cells should not be used for clinical purposes.

Sendai Virus This respiratory virus (originating from the mouse and the rat) is a single-stranded RNA virus that can be used on all types of cells. Contrarily to other viruses, Sendai is non-integrating and replication-deficient. It is easy to use, has a high efficiency and is free of genetic perturbation as the virus cannot enter the nucleus. Sendai viral vectors also reprogram cells with relatively high efficiency, which helps diminish its important cost.

The Sendai virus system is ideal for reprogramming blood cells, an area of growing interest due to the ease of obtaining these samples from patients. Additionally, there are many epidemiological studies that have large banks of blood samples in stock that can now be reprogrammed with Sendai virus – where mRNA has not been shown to efficiently reprogram (hematopoietic) blood cells.

mRNA delivery This last method is both non-integrative and non-viral, which is especially important for future therapeutic applications. It consists in delivering mRNA (one for each of the four reprogramming factors) to the cells and wait for their automatic replication. This method is highly efficient (with 1 to 2% of cells reprogrammed) and does not leave any residue inside the cells. However, it does not work for all types of cells, and requires 17 days of reprogramming with a constant supply of mRNA. This induces a high cost in biological material, even though its efficiency ultimately reduces the total cost for iPSC generation.

Researchers at Stemgent are currently trying to adapt the method to reprogramm blood cells. mRNA delivery could then become the dominant technology for reprogramming.